APPROACHES TO MACROMOLECULAR AND SUPRAMOLECULAR STRUCTURE DETERMINATION

THESIS

by

DAVID ANDREW AGARD

In Partial Fulfillment of the Requirements
for the Degree of
Doctor of Philosophy

California Institute of Technology
Pasadena, California

1981
(Submitted July, 11, 1980)

"Nothing can satisfy but

what confounds"

Edward Young

TO

MY GRANDMOTHER

ACKNOWLEDGEMENTS:

I wish to thank my fellow graduate students and colleagues, John Chambers, Mel Jones, Monty Krieger, Mike Ross and Steve Spencer for their help and valuable discussions. I would also like to thank F.M. Richards, T.A. Steitz, R.J. Fletterick, and H.W. Wyckoff who initially sparked my interest in structural biology and who have been advisors ever since.

I am most grateful to both Dee Barr and Ric Bornstein for their invaluable assistance in the preparation of both this thesis and the manuscripts presented in the Appendix.

I thank the National Science Foundation for financial support during the first three years of my graduate study.

My special thanks go to my family, my uncle and to Karen for their unflagging moral support and constant good humor.

My collaboration with J.W. Sedat has proven to be exciting and enlightening and reinforces my feelings on the importance of scientific communication and collaboration.

And finally, my sincerest thanks goes to my advisor and friend, R.M. Stroud for his constant help and encouragement. Working with him has been a most unique and rewarding experience.

ABSTRACT

All of the common techniques for obtaining structural information from macromolecular and supramolecular objects suffer from one type of drawback or another. X-ray and neutron diffraction methods have the phase problem (only the amplitude and not the phase angle of the complex diffraction vector can be experimentally observed). Low-dose 3-dimensional electron microscopy suffers from the inability to collect a complete data set due to instrumental limitations. Although light microscopy allows the sample to be kept under biological conditions (compare with standard electron microscopic techniques), the low resolution has limited its appeal to more qualitative aspects of ultrastructure analysis.

All of these limitations can be considered as a lack of information in the Fourier space domain. A generalized mathematical approach is presented where global real-space constraints are utilized to ameliorate this loss of information. In simple cases (one-dimensional analysis) it is possible to solve the phase problem, and in more complex cases (two- and three-dimensional analyses) the added real-space information is used to augment the experimentally derived data. The iterative Fourier refinement scheme was chosen as it represents the most versatile means for incorporating global knowledge concerning the real-space behavior of the object.

This approach was used to solve the three-dimensional x-ray structure of the snake polypeptide neurotoxin α-Bungarotoxin, the one-dimensional transmembrane electron density profile for acetylcholine receptor containing membranes, and to solve the missing cone problem of electron microscopic structure

analysis.

Real-space constraints were also incorporated into an iterative deconvolution scheme used both for image processing and for the quantitative analysis of overlapping gel electrophoretogram peaks. None of this work would have been possible if the information supplied by real-space constraints had not been utilized. The approaches presented to these problems are general ones and should be applicable to other systems.

TABLE OF CONTENTS

Contents cont.

INTRODUCTION

The work presented in this thesis is organized not chronologically but so as to emphasize the common thematic elements that underlie each of the research projects discussed. The order of presentation is one of increasing size: from atomic to microscopic; decreasing resolution: from 3.5 Å to greater than 1000 Å; and decreasing specimen order: from 3-dimensional crystals of a pure protein to in-vivo supramolecular structures composed of protein and nucleic acid complexes. The theme is one of utilizing physical constraints as a source of information. This information is then used to improve the quality of the structure determination.

All of the common techniques for obtaining 3-dimensional structural information suffer from one type of drawback or another. X-ray and neutron diffraction methods have the phase problem (only the amplitude and not the phase angle of the complex diffraction vector can be experimentally observed). Low-dose 3-dimensional electron microscopy (a new technique pioneered by Henderson & Unwin (1, 2)) suffers from the inability to collect a complete data set due to instrumental limitations. Although light microscopy allows the sample to be kept under biological conditions (compare with standard electron microscopic techniques), the low resolution has limited its appeal to the more qualitative aspects of ultra-structure analysis.

The limitations of these various physical techniques are perhaps best considered in the Fourier transform (reciprocal space) domain. X-ray and neutron diffraction techniques can provide high resolution diffraction amplitudes but the phase information is missing. In high-resolution 3-dimensional electron microscopy both phase information (from low-dose

unstained images) and amplitude information (from electron diffraction patterns) are available. Instrumental limitations on tilt angle (the sample can be tilted to only about ± 60° from the horizontal) limits the region of reciprocal space where data can be collected. Thus a conical region of half-angle 30° about the axis normal to the grid is missing from the observed data. In the optical microscope, amplitude and phase information are again available, but only to quite limited resolution. Although not an intrinsic limitation of the optical microscope, beyond stereo pairs very little use has been made of its 3-dimensional imaging capabilities.

It can thus be seen that each of these limitations can be ascribed to incompleteness of the observed data in the Fourier space domain. In some cases (such as macromolecular crystallography) experimental techniques exist for deriving the missing information based on multiple observations of samples perturbed in some relatively simple manner (e.g. the multiple isomorphous replacement method (3)). In all cases, however, it is possible to at least partially compensate for the missing information in the reciprocal space domain by using known properties of the object in the real-space domain. The iterative Fourier refinement scheme (Figure 1) has proven to be the most versatile means for incorporating both real-space information (density constraints, non-crystallographic symmetry, etc.) as well as knowledge of which aspects of the Fourier space data are most incorrect. This approach, be it used independently as in the solution x-ray diffraction analysis (chapter III, appendices IV, V), the missing cone studies (chapter II, appendix III), or micrograph image processing (chapter IV, appendices VI, VII); or in conjunction with other experimental

data such as with the large-cell MIR data for α-Bungarotoxin (chapter I, appendices I, II), forms the basis of the approach to structural problems presented in the ensuing chapters. Although the work presented in the last appendix on the mathematical resolution enhancement of electrophoresis gel profiles does not relate to structural problems, the underlying mathematics are indeed quite similar to that presented in previous chapers. The chapters serve as introductory material for the relevant manuscripts which appear in the appendices.

REFERENCES:

1. Unwin, P.N.T. and Henderson, R. (1975) J.M.B. 94, 425-440.

2. Henderson, R. and Unwin, P.T. (1975) Nature 257, 28-32.

3. Green, D.W., Ingram, U.M. and Perutz, M.F. (1954) Proc. Roy. Soc. A225, 287-307.

FIGURE LEGENDS

Figure 1.

The generalized Fourier refinement scheme. Starting with an object or density function, ρ, real-space density constraints are applied to generate a modified ρ'. This is then Fourier transformed to yield a set of amplitudes F_c and phases ϕ_c which are then constrained to provide to current best guess F,ϕ to the true structure factor. Fourier transformation of F,ϕ leads to the current guess for the structure. The entire process is cycled until convergence is reached. The nature of the real-space and reciprocal space constraints depends on the particular problem being investigated.

FIGURE 1

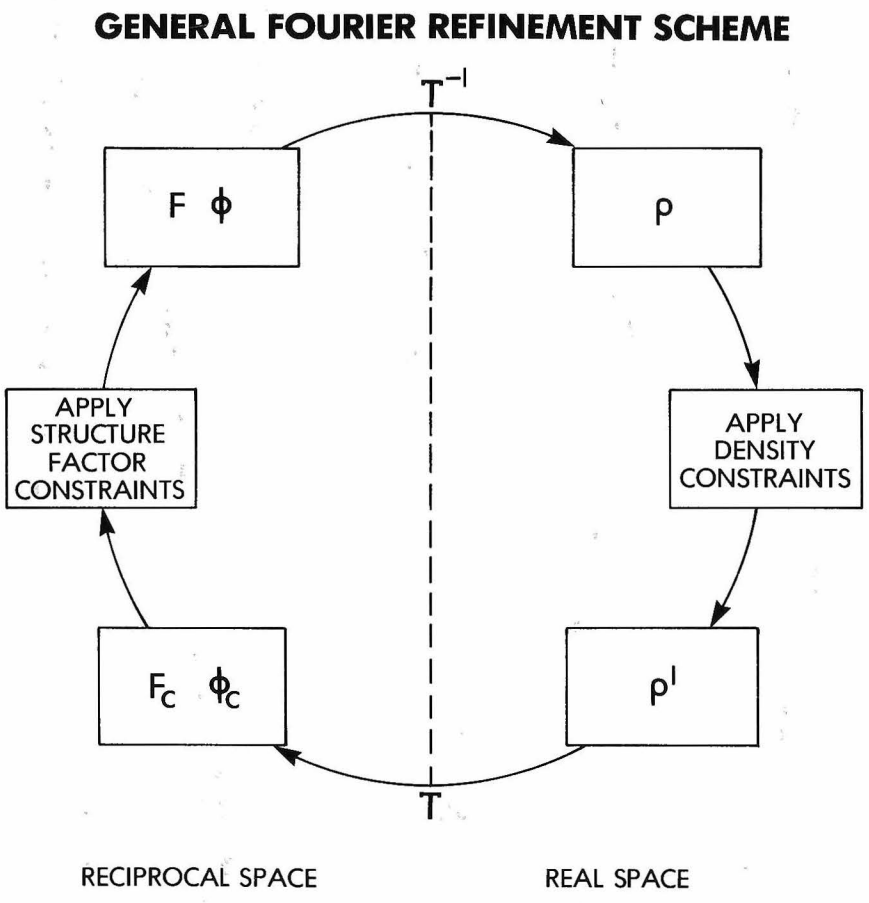
GENERAL FOURIER REFINEMENT SCHEME
T⁻¹
F ϕ
ρ
APPLY STRUCTURE FACTOR CONSTRAINTS
APPLY DENSITY CONSTRAINTS
Fc ϕc
ρ'
T
RECIPROCAL SPACE
REAL SPACE

CHAPTER I

The 3-dimensional X-ray Crystal Structure of α-Bungarotoxin at 3.5 Å Resolution

This is an example of a relatively high resolution three-dimensional structural analysis of a single macromolecule. The protein can be crystallized and conventional techniques can be used to help solve the phase problem. In this case, however, there are extenuating circumstances that preclude the possibility of an atomic interpretation. Using knowledge about crystal packing and the global behavior of the electron density, it was possible to substantially improve the quality of the experimentally derived phases. The resultant electron density map was of sufficient quality to permit an atomic interpretation. A molecular model was built and refined to a crystallographic residual of 21% at 3.5 Å resolution.

Snakes feed by either killing or paralyzing their prey with an injection of a highly toxic venom. This venom has evolved to contain many extremely toxic components ranging from small molecules of about 300 d molecular weight to phospholipase A-like enzymes of about 26000 d. In general, these components act synergistically to augment to total toxic effect. The major toxic component of the venom of elapidae snakes is a pre-synaptic curare-mimetic polypeptide α-toxin. This class of proteins acts by binding tightly to the nicotinic acetylcholine receptor, blocking the depolarizing action of acetylcholine; thereby producing paralysis and death due to respiratory collapse. The α-neurotoxins (so named for α-Bungarotoxin) fall into two classes: long (71-75 residues; 5 disulfide bridges) and short (60-62 residues; 4 disulfide bridges). At the time of writing the amino acid sequences were known for 18 long toxins and 25 short toxins (1).

α-Bungarotoxin, first isolated by Chang and Lee (2) is a member of the long class with 74 residues and a molecular weight 7900 d. Owing to its

nearly irreversible binding to the nicotinic acetylcholine receptor (k_d 10^{-10}), this toxin has played an important role in the biochemical studies of the receptor (3, 4, 5).

The structural study of α-Bungarotoxin was begun in Stroud's lab in 1974 by S.A. Spencer (thesis project, Department of Chemistry, California Institute of Technology) as part of the structural investigation of the membrane bound acetylcholine receptor from the electroplax of Torpedo californica. It was felt that the tight binding between toxin and receptor could not be the result of a simple 1 or 2 point interaction, but rather could arise only from the large contact area afforded by the precise alignment of complementary surfaces. An analysis of the toxin structure, it was hoped, would provide valuable insights into the structure of the receptor at a higher resolution than obtainable with other techniques.

Spencer purified α-Bungarotoxin from the venom of Bungarus multicinctus according to the procedure of Chang & Lee (2), grew crystals and collected native and derivative data. He was also able to produce a low-resolution density map. Owing to pseudo-symmetry and twinning problems (see below) it was not possible to extend the analysis beyond 5 Å resolution; obviating the possibility of an atomic interpretation. Although a detailed description of the problems surrounding the low-resolution determination is to be found in Spencer's thesis (1977), those points relevant to the final solution of the structure will be recapitulated here.

Two crystal forms of the toxin have so far been obtained: a "large cell" form (a=69.9 Å, b=76.7 Å, c=44.8 Å, α=β=γ=90°) with 16 molecules per unit cell and a "small cell" for (a'(a)=67.8 Å, b'(b)=78.4 Å, c'(c/2)=22.4 Å,

$\alpha=\beta=\gamma=90°$) with 8 molecules per unit cell. Both crystal forms show mmm diffraction symmetry. Crystals of the large cell form are only stable below pH 4.4 and below 14°C. Small cell crystals (room temperature, pH >7) suitable for data collection have not yet been obtained. Raising the temperature of the large cell crystals above 14°C generally results in crystal destruction (as always happens with pH elevation). On rare occasions, however, a conversion to the small cell form occurs. At least partial conversion can be induced by some heavy-atom derivatives. The large cell form diffracts well to at least 2 Å resolution and all derivative data were collected on this form. One 3.5 Å resolution native data set was collected on a crystal that survived temperature conversion.

The diffraction pattern for the $h\phi\ell$ projection of the large cell form is shown in Figure 1. An examination of the intensity as a function of ℓ reveals that at low angles the $\ell=2n+1$ rows are substantially weaker than the $\ell=2n$ rows. This distinction vanishes at high angles. A plot of ℓ_{odd}/ℓ_{even} is shown in Figure 2. This is indicative of a unit cell composed of nearly identical halves. The native Patterson map shows two prominent features (Figure 3). The first, a very strong bimodal peak at uvw= .47c & .53c, supports the cell halving hypothesis. When integrated, this peak has the same intensity as the origin, indicating that for every atom there is a corresponding atom related by either ± .47c. The displacement from uvw= .5c indicates that the molecules in the upper half cell are shifted by ± .03c with respect to those in the lower half cell. The other dramatic feature of the native large cell Patterson map is a peak at uvw= .416a, 341b, .28c. Upon integration, this peak also corresponds to the

full height of the origin, providing indication of additional non-crystallographic symmetry.

At low resolution (below 5 Å) the ℓ_{odd} rows are sufficiently weak that they can be ignored. Using only the ℓ_{even} rows corresponds to averaging the contents of the upper and lower half cells. The averaged half-cell can then be re-indexed to correspond to a c axis length of 22.4 Å. In this averaged half cell the non-crystallographic symmetry peak falls exactly on c= .5 (.416a, .341b, .5c).

Spencer was only able to solve the heavy atom derivatives in the averaged half cell and only in the space group $P2_12_12_1$. This observation was confirmed by both J.L. Chambers and myself. The dilemma raised by this finding results from the fact that the stacking of two slightly different $P2_12_12_1$ unit cells leads to a large cell with at most $P2_1$ symmetry (see Figure 4); yet the diffraction data shows mmm symmetry for all reflections. (Because the half cells are $P2_12_12_1$ symmetric, the ℓ_{even} rows are expected to possess mmm symmetry but the ℓ_{odd} cannot.)

A situation similar to α-Bungarotoxin has recently been reported in the co-crystallization of histidine and aspartic acid (6). The authors correctly point out that two-fold rotational twinning where the $hk\ell$ and $\bar{h}\bar{k}\ell$ reflections are precisely superimposed would give rise to the observed diffraction symmetry. We also believe that the large cell Bungarotoxin crystals are twinned. In our case, however, the temperature-induced conversion from a twinned to a non-twinned state precludes the existence of such rotational twinning. Another very attractive possibility is that since only one of the 2_1 axes (either along a or b) can survive

in the large cell form, the twinning results from the co-existence of domains having the unique 2_1 axis along either a or b. This possibility is being further investigated. In any event, it seems unlikely that the large cell form, in spite of its high-resolution diffraction, will prove to be useful during the refinement of the existing model.

The starting point for my work on this project was the low-resolution (5 Å) electron density map from the averaged half cell MIR analysis as well as the one native 3.5 Å resolution data set taken from a tempterature converted small cell crystal. At that time, the nature of the twinning was not understood. Initially, I attempted to solve both the averaged half cell and small cell crystal forms using molecular replacement methods. The search molecule was the short (62 residues; 4 disulfides) α-toxin erabutoxin b. This structure was solved independently and virtually simultaneously by Tsernoglou & Petsko (7) and Low et al., (8). The coordinates used were those from Tsernoglou & Petsko. The sequences were examined and where different, atoms were removed from the erabutoxin starting model. Thus a ser-thr transition (erabutoxin to bungarotoxin) was left as a ser whereas a thr-ser was converted to a ser. Dissimilar residues were truncated at the β carbon. Rotation searches were performed using the approaches of Crowther (9), Lattman (10), and Huber (11). All of the rotation functions showed very poor discrimination and had very few peaks in common. The top dozen peaks were screened by behavior during translation searches. Instead of using a conventional Patterson space translation search procedure (12), I developed a fast reciprocal space method (see appendix I) that has a much higher signal-to-noise ratio. This is a direct consequence of using

the phase information inherent in the model to separate the inter-molecular vectors from the contaminating intra-molecular vectors. The results were quite disappointing and this approach was abandoned. After solving the α-Bungarotoxin structure (see appendices I & II) the erabutoxin coordinates were best fit to those of Bungarotoxin and structure factors were calculated. The standard crystallographic residual: $R = \Sigma||F_o|-|F_c||/\Sigma|F_o|$ providing an assay for the equivalence of the two structures was 57% at 3.5 Å resolution. This explains the difficulty encountered with the molecular replacement approach. A more detailed comparison of erabutoxin b to α-Bungarotoxin is presented in appendix II.

The α-Bungarotoxin structure was solved by transferring the MIR phase information from the averaged half cell form to the small cell form and then refining the phases in the small cell using the constraint that the two molecules in the asymmetric unit must be identical (see appendix I). The assumption of equivalence places a powerful joint constraint on the phase terms. In addition, solvent regions surrounding each molecule were set to zero electron density and both upper and lower limits were placed on the allowed electron density values within the molecular volume. The net effect is to use this wealth of real space information concerning the nature of the electron density within the unit cell as a mathematical constraint with which the phases must be consistent. The iterative Fourier refinement procedure enforces this consistency.

As part of the non-crystallographic phase refinement, a new approach was developed for averaging the density from translationally related molecules. It was recognized that averaging in the real-space domain is a

superposition operation and hence can be performed more efficiently in reciprocal space as a multiplication. The approach does not require any interpolations (as does Bricogne's (13, 14) methods) and is thus much faster and more accurate. The increase in accuracy is quite important when only two molecules are being averaged. A complete discussion of this method and the phase refinement scheme is presented in appendix I.

REFERENCES:

1. Karlsson, E. (1979) in Handbook of Experimental Pharmacology Vol. 52 (C-Y. Lee, Ed.) Springer-Verlag, N.Y., pp. 159-212.
2. Chang, C.C. & Lee, C.Y. (1963) Arch. Int. Pharmacodyn 144, 241-257.
3. Changeux, J-P., Kasai, M., Lee, C-Y. (1970) PNAS 67, 1241-1243.
4. Miledi, R., Molinoff, P., Potter, C.T. (1971) Nature 229, 554-557.
5. Raftery, M.A., Schmidt, J., Vandlen, R. and Moody, T. (1974) Neurochemistry of Cholinergic Receptors, pp. 5-18.
6. Bhat, T.N. and Vijayan, M. (1979) Acta Cryst. B34, 2556-2565.
7. Tsernoglou, D. and Petsko, G.A. (1976) FEBS Lett. 68, 1-4.
8. Low, B.W., Preston, H.S., Sato, A., Rosen, L.S., Searl, J.E., Rudho, A.D. and Richardson, J.S. (1976) PNAS 73, 2991-2994.
9. Crowther, R.A. (1972) in The Molecular Replacement Method (Rossmann, M.G., Ed.) International Science Review Series, Vol. 13, Gordon & Breach, N.Y., pp. 174-178.
10. Lattmann, F.E. and Love, W.E. (1970) Acta Cryst. B26, 1854-1857.
11. Bode, W., Feblhammer, M. and Huber, R. (1976) J.M.B. 106, 325-335.
12. Crowther, R.A., Blow, D.M. (1967) Acta Cryst. 23, 544-548.
13. Bricogne, G. (1974) Acta Cryst. A30, 395-405.
14. Bricogne, G. (1976) Acta Cryst. A32, 832-847.

FIGURE LEGENDS

Figure 1.

An $h\phi\ell$ precession diffraction pattern from a large cell α-Bungarotoxin crystal. Note the weak ℓ_{odd} rows.

Figure 2.

A plot of ℓ_{odd}/ℓ_{even} out to a resolution of 2.5 Å using 3-dimensional native data from the large cell α-Bungarotoxin crystal form.

Figure 3.

Two regions of the native large cell Patterson function indicating the presence of translational non-crystallographic symmetry within the unit cell. The peak corresponding to the approximate cell halving (o,o,±.47) is shown in a) and the other non-crystallographic translation vector (.416, .341, .28) is shown in b). Plot regions are: a) u = 0; V = -.25, .25; w = 0,1; w is vertical and b) u = 0, .5; v = 0, .5; w = .28; v is vertical.

Figure 4.

A packing diagram for the two interconvertable crystal forms of α-Bungarotoxin. The large cell form is known to be composed of two nearly

Figure 4 (cont.)

identical halves. On conversion to the small cell form, the space group is $P2_12_12_1$. The large cell must have $P2_1$ symmetry, with the 2_1 axis either along x or along y. z is vertical only; y is horizontal.

FIGURE 1

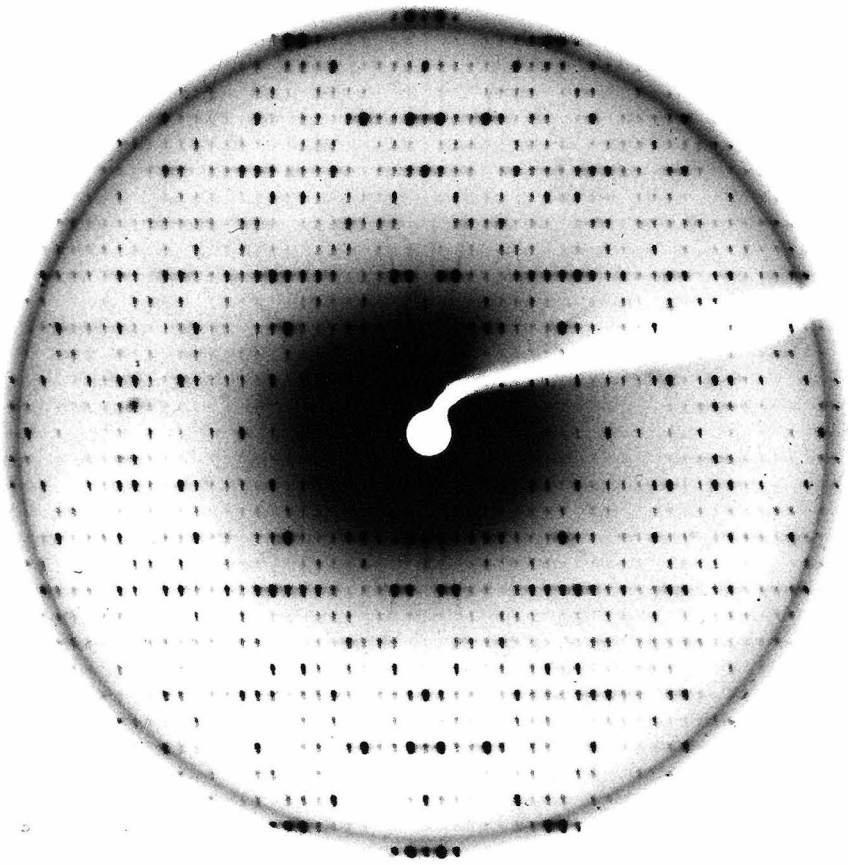

FIGURE 2

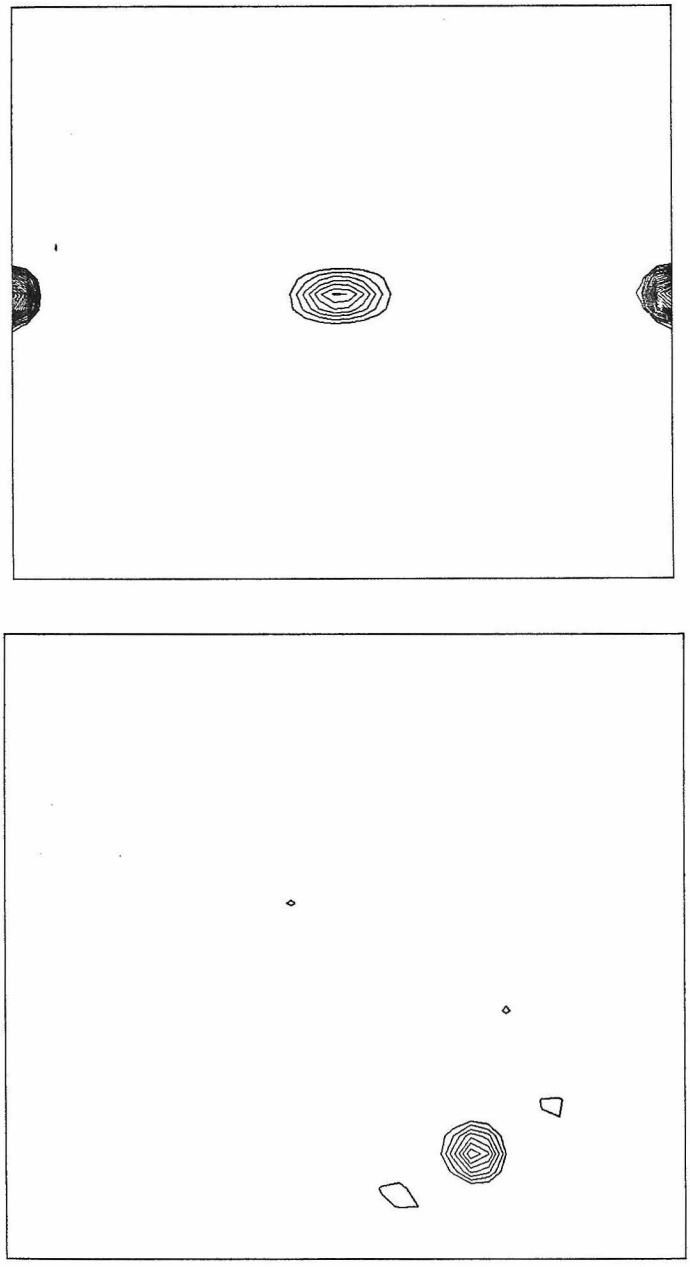

FIGURE 3

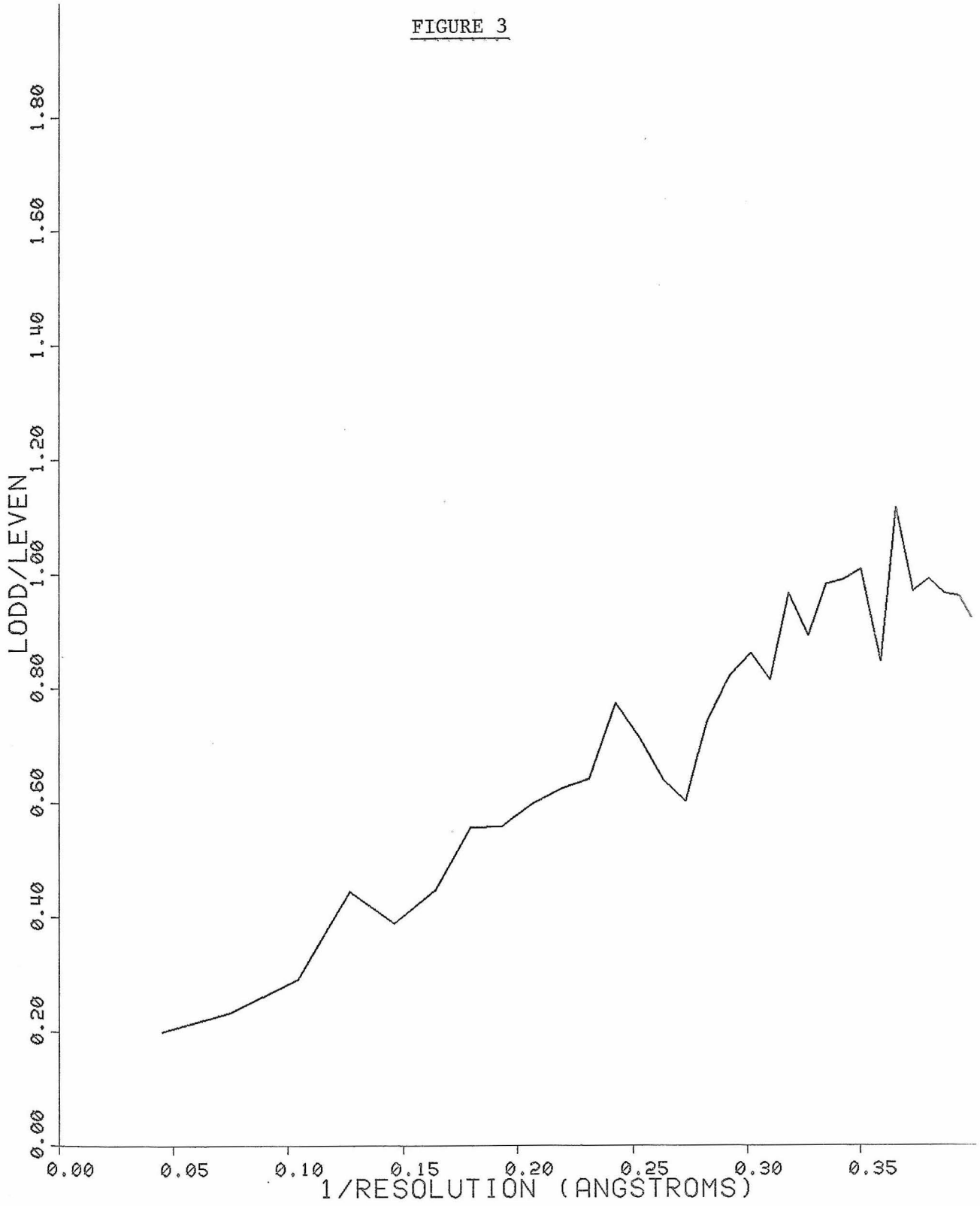
LODD/LEVEN
0.00
0.20
0.40
0.60
0.80
1.00
1.20
1.40
1.60
1.80
0.00
0.05
0.10
0.15
0.20
0.25
0.30
0.35
1/RESOLUTION (ANGSTROMS)

FIGURE 4

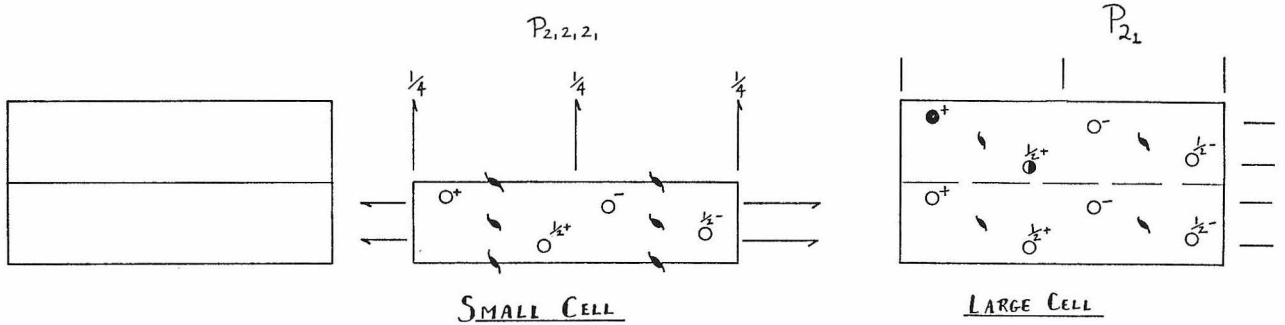

CHAPTER II

Finding the Linker Regions in Bacteriorhodopsin: A Solution to the Missing Cone Problem

Three-dimensional electron microscopic structural analysis requires the recombination of many different tilted views of the same specimen. The inability to tilt the sample to angles greater than 60° on most instruments or without severe distortion due to different focal distances across the specimen implies that the observable range of electron diffraction data is limited to this range of angles. Thus, it is not generally possible to observe the diffraction maxima which lie within a conical region of reciprocal space around the direction perpendicular to the electron microscope grid. The absence of data in this region leads to a predictable distortion in the object, and makes the resolution essentially twice as bad in the direction perpendicular to the grid as it is for the in-plane image.

This problem can be solved by an iterative Fourier refinement scheme that uses the properties of limited spatial extent and non-negativity in the object domain to extrapolate into the missing cone region in Fourier space. Thus Fourier space data are generated in the missing region so as to rectify the object's inconsistency with the applied real-space constraints. In the case of the moderate resolution analysis of Bacteriorhodopsin, this processing rendered visible the regions of polypeptide chain connecting the α-helices.

The bacteriorhodopsin molecule (BR) functions both as a photosensory receptor (1) and, under anaerobic conditions, as an energy transducer. Acting as a light-driven proton pump, BR directly converts incident light energy into the chemical energy of a hydrogen ion gradient (2). In support of the Mitchell chemi-osmotic hypothesis (3), the stored proton gradient is depleted to drive ATP synthesis (4) and other energy requiring processes such

as active ion translocation, active transport, etc. The direct involvement of the proton gradient in ATP generation is well established, and simultaneous monitoring of proton influx and photophosphorylation has revealed a proton per ATP ratio of 3 (5).

Bacteriorhodopsin is an integral membrane protein of about 26,000 d molecular weight containing a light absorbing chromophore (retinal) bound to the protein in a 1:1 ratio via a Schiff's-base linkage to a lysine side chain (6). The amino acid sequence has recently been reported by several workers (7, 8).

I strongly feel that understanding the bacteriorhodopsin structure will have general implications above and beyond those related simply to BR. Certainly understanding the energy transduction mechanism of BR will be important in the study of other light-activated systems such as photosynthetic centers and quantum-detectors like rhodopsin. Furthermore, it should significantly advance our knowledge concerning the structure of integral membrane proteins as a class. Comparison of the interactions within the molecule and with its hydrophobic environment to those normally found in soluble proteins should shed new light on the role of solvent (both hydrophobic and hydrophilic) in protein folding. Currently this is the only integral membrane protein that is truly amenable to high-resolution structural analysis.

Although 3-dimensional crystals of BR suitable for high resolution x-ray analysis have not yet been obtained, the molecule naturally exists in large 2-dimensional crystalline patches within the cytoplasmic membrane (9). These 2-dimensional crystals are of suitable quality to make BR amenable to high-

resolution structural analysis using the elegant low-dose electron microscopic techniques pioneered by Unwin and Henderson (10, 11). Electron diffraction data (in projection) haverecently been recorded to 2.5 Å resolution by Glaeser and colleagues using a low temperature stage (Hayward, unpublished) indicating the high degree of inherent crystallinity. Unfortunately, distortions introduced by the objective lens as well as signal-to-noise limitations have made it impossible to record images that diffract to better than about 6-7 Å with currently available instrumentation. In the analysis procedure, phases derived from the image are coupled with the observed electron diffraction amplitudes to yield a potential density map of the BR molecule. Thus the unavailability of experimentally derived phases beyond about 7 Å has limited the resolution of the calculated map to this value. The result of such an electron microscopic analysis (10, 11) reveals that each BR molecule consists of 7 α-helical segments running nearly perpendicular to the plane of the membrane and extending from one side to the other (approx. 45 Å). Three such molecules are clustered around the crystallographic three-fold axis, the remaining space in the unit cell (approx. 25% by weight) being occupied by lipid molecules (Figure 1).

An implicit requirement for the structure determination is knowledge of which residues are in which helix. In the current 7 Å structure (11), the linker regions cannot be visualized, only the helical segments are visible. This is partly, if not entirely, a consequence of the unavailability of diffraction data in a conical region about the z* axis. This results from the inability to tilt the sample to angles steeper than about 60° from the horizontal. The lack of data about the z* axis (the

missing cone problem) introduces a systematic distortion into the calculated structure: each point in the potential density map is convoluted with a function similar to a prolate ellipsoid having an axial ratio of about 2:1 (elongated about the z axis). The density values are thus smeared out in the z direction (smoothing and elongating the helices) and washed out in the other directions (tending to obliterate the connecting regions).

The work presented in appendix III indicates that the judicial application of real-space constraints in an iterative Fourier refinement scheme can lead to an enhanced potential density map where many of the linker regions are visible. This map would then serve as the starting point for further structural studies where model α-helices and linkers would be built into the low-resolution density and refined against higher resolution diffraction amplitudes.

REFERENCES:

1. Stoeckenius, W., Lozier, R.H., and Bogomolni, R.A. (1979) BBA 505, 215-278.

2. Oesterhelt, D. and Stoeckenius, W. (1973) PNAS 70, 2853-2857.

3. Mitchell, P. (1972) Bioenergetics 4, 265-293.

4. Racker, E. and Stoeckenius, W. (1974) J. Biol. Chem. 249, 662-663.

5. Bogomolni, R.A., Baker, R.A., Lozier, R.M., and Stoeckenius, W. (1976), BBA 440, 68-88.

6. Bridgen, J. and Walker, I.D. (1976) Biochemistry 15, 792-798.

7. Ovchinnikov, Yu. A., Abdulaev, H.G., Feigina, M. Yu., Kiselev, A.V., Labanov, N.A., and Nasimov, I.V. (1978) Bioorg. Khim. 4, 1573-1574.

8. Gerber, G.E., Adneregg, R.J., Herlihy, W.C., Gray, C.P., Biemann, K., and Khorana, H.G. (1979) PNAS, 75, 227-231.

9. Blaurock, A.E. and Stoeckenius, W. (1971) Nature New Biology 233, 152-155.

10. Unwin, P.N.T. and Henderson, R. (1975) J. Mol. Biol. 94, 425-440.

11. Henderson, R. and Unwin, P.N.T. (1975) Nature 257, 28-32.

FIGURE LEGENDS

Figure 1.

The 7 α-helical rods of Bacteriorhodopsin as determined by Unwin & Henderson (11). Because of the missing cone problem, the regions of polypeptide chain that connect the rods cannot be seen. Figure taken from reference 11.

FIGURE 1

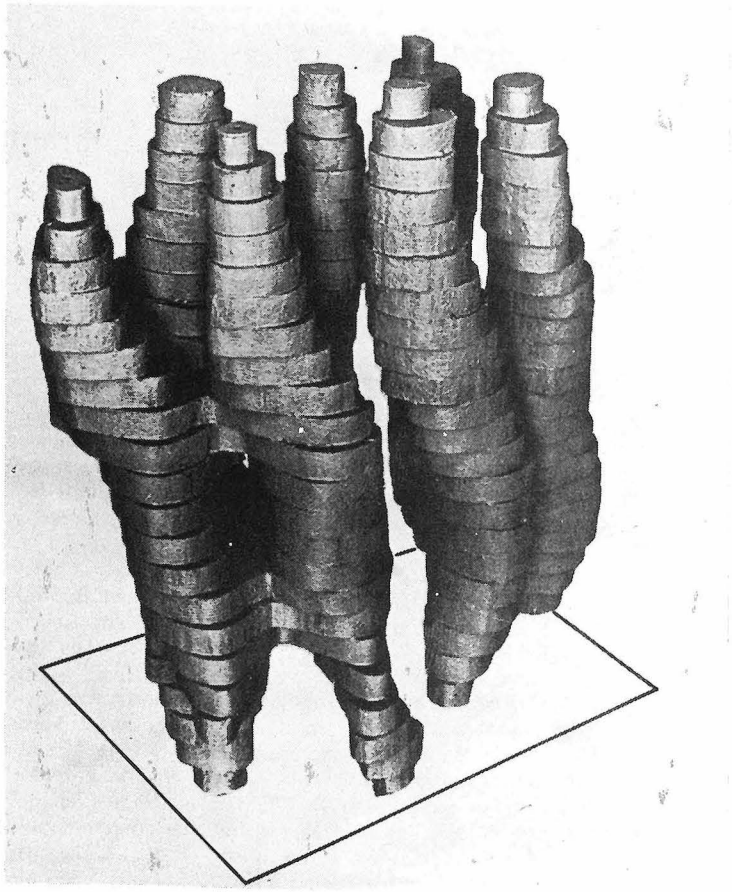

CHAPTER III

X-ray Diffraction Analysis of Acetylcholine Receptor Membranes: A Solution to the One-Dimensional Phase Problem

Biological membranes represent a two-dimensional assemblage of protein within a fluid lipid bilayer. With the possible exception of Bacteriorhodopsin (1), membrane proteins have not been crystallized in a manner suitable for three-dimensional x-ray diffraction studies. The majority of membrane systems do not show the inherent two-dimensional crystallinity that is also characteristic of Bacteriorhodopsin (2). As a consequence, it has not been possible to structurally study most membrane-protein systems using either high-resolution, low dose electron microscopic or single crystal diffraction methods.

Solution diffraction from either suspensions or oriented pellets of membranes can provide valuable information concerning the distribution of protein components with respect to the lipid bilayer. When there is in-plane diffraction (as occurs with the acetylcholine receptor, appendix V, orienting the membranes allows the in-plane and normal diffraction components to be separated. The observed data in either case represent the continuous Fourier transform of the membrane projected onto an axis perpendicular to the membrane plane. In this simple one-dimensional case, one is again confronted with the phase problem: the amplitudes of the complex structure factors are observable, the phases are not. It is possible to utilize the knowledge of how thick the membrane is (limited spatial extent) to generate a solution to the phase problem. The technique of choice is again an iterative Fourier refinement scheme where limited spatial extent serves as the real-space constraint. In many cases, the resultant electron density profile represents a unique solution to the phase problem. Otherwise, members of the limited family of mathe-

matically allowed solutions can be found, and some eliminated on the grounds of chemical unreasonableness.

Appendix IV concerns the development of the technique, its performance using both synthetic and real data, and a comparison to other methods. Appendix V discusses the utilization of this procedure in the study of a membrane bound acetylcholine receptor from electroplax tissue of Torpedo californica. The trans-membrane electron density profile derived from the observed diffraction amplitudes suggests that the acetylcholine receptor spans the lipid bilayer, is 110 Å long, and is situated asymmetrically with respect to the bilayer. In a separate experiment, analysis of high-angle diffraction data indicates that the receptor is composed of long stretches of α-helix (∿80 Å) oriented roughly normal to the membrane plane. The electron density profile has since been confirmed by direct electron microscopic observation of edge-views from folded receptor membranes (3).

REFERENCES:

1. Michel, H. and Oesterhelt, D. (1980) PNAS 77, 1283-1285.

2. Blaurock, A.E. and Stoeckenius, W. (1971) Nature New Biology 233, 152-155.

3. Klymkowsky, M.W. and Stroud, R.M. (1979) J.M.B. 128 319-334.

CHAPTER IV

Examination of Chromosome Structure

The study of supramolecular structure especially at the level of cellular architecture can both confound and intrigue the structural investigator. Such structures although perhaps built following regular structural principles, are invariably not sufficiently crystalline to allow study using methodologies based on repeating objects. One is thus left to consider large, complex, three-dimensional, non-crystalline objects. The investigative tools available for such studies are either electron or optical microscopy depending on the desired resolution range and specimen size. Optical microscopy offers the advantages of studying the specimen in a hydrated, defined ionic environment at one atmosphere pressure. Unfortunately, because of its relatively low resolving power, it has generally been relegated to qualitative instead of quantitative investigations. While electron microscopy (especially using high voltage microscopes) resolves the resolution problem, the need for dried, in vacuo samples may preclude the study of environment-sensitive structures in their native state.

The work discussed in this chapter and in appendix VI has all been done in collaboration with Dr. J.W. Sedat (Biochemistry & Biophysics Department, University of California at San Francisco). Long involved in the study of nuclear architecture, Dr. Sedat has recently begun investigations using the fluorescent, DNA-specific, non-intercalative dye Hoechst 33258. This dye has the properties of only fluorescing when bound, only binding to DNA, and because it does not intercalate, little or no perturbations are introduced into the chromosome structure. Furthermore, the use of a specific dye means that only a specific molecular species (in this case DNA) is imaged.

Both sperm heads and mitotic chromosomes from Drosophila have been under investigation as they represent well-defined stages of highly-condensed DNA. Drosophila was chosen because it is a rather simple system (four chromosomes) with well characterized genetics. Using image processing and reconstruction techniques, we plan to examine the higher-order levels of DNA condensation and packaging in these two systems. The goal is to treat the problem of chromosome architecture in a manner analogous to macromolecular architecture: first, solve its three-dimensional structure: then, build and refine a model. Three-dimensional data would be collected using either tilted views or optical sections and processed to yield an enhanced three-dimensional image. The image would be interpreted by model building much as would an electron density map. Parameters of the model would then be refined and questions concerning structure-function relationships posed. It would also be hoped that the model could be extended to higher resolution using high-voltage electron microscopy and potentially even solution x-ray scattering.

The first steps in this project have been accomplished. Two-dimensional fluorescent images of both sperm heads and mitotic chromosomes have been taken and analyzed to reveal that they have well defined sub-structures. Various image processing methods have been investigated for their ability to enhance fluorescent images (mainly by correcting the gaussian emitter effect). Three-dimensional data from sperm heads has also been collected, but not yet processed. The details of the results obtained to date are presented in manuscript form in appendix VI.

This general approach is essentially tomography at the cellular level.

It is hoped that techniques developed in the course of studying chromosome architecture will be of general use for investigating very large, non-crystalline biological objects.

APPENDIX I

A Rapid Method for Averaging Non-crystallographically, Translationally Related Molecules with Application to α-Bungarotoxin

A RAPID METHOD FOR AVERAGING ELECTRON DENSITY OF NON-CRYSTALLOGRAPHICALLY, TRANSLATIONALLY-RELATED MOLECULES WITH APPLICATION TO α-BUNGAROTOXIN

David A. Agard

&

Robert M. Stroud

University of California, S.F.
Department of Biochemistry & Biophysics
San Francisco, California 94143

ABSTRACT:

In macromolecular crystallography multiple and independent images of the same chemical species are often present in the crystallographic asymmetric unit. Averaging of density for non-crystallographically related molecules is a powerful technique both for improvement of the density image, and for subsequent phase refinement. Surprisingly often, a non-crystallographic axis of symmetry lies parallel to a crystallographic axis. In such cases, the averaged electron density map can be computed simply and directly from the observed structure factors without subsequent interpolation or averaging in the molecular density map. The procedure described is much more efficient than averaging with consequent interpolation in the real space domain.

The same algorithm can be used in reverse both for very rapid computation of the Fourier transform $F_c(\underline{s})$ of a unit cell based on replacement of the "averaged" density image for the non-crystallographically related molecules, and consequently for a rapid translation function search based on minimization of $R=\Sigma||F_o|-|F_c||/\Sigma|F_o|$ directly. This residual is much more sensitive than any "Patterson" search technique where there is overlap between inter- and intra-molecular vectors.

Jointly these rapid analytic techniques for density averaging and subsequent computation of calculated structure factors from the averaged density map were used to solve and refine the crystal structure of α-Bungarotoxin. The rapid translation search procedure was crucial to the solution of the α-Bungarotoxin structure which is described.

INTRODUCTION:

Many examples now exist where macromolecules crystallize with more than one molecule per crystallographic asymmetric unit (asu); the most striking instance perhaps being the regular icosahedral or helical viruses (Harrison et al., 1978; Bloomer et al., 1978). If each of the molecules in the asu are identical, the resultant non-crystallographic symmetry (NCS) implies a powerful joint relationship amongst the phases. Both Rossmann and co-workers (Rossmann & Blow, 1963; Main & Rossmann, 1966) and Bricogne (1974, 1976) have developed formalisms for utilizing the real-space redundancy to constrain or refine experimentally-derived phases. Bricogne's approach has proven to be the most useful for macromolecular structural problems. The principle behind both methods derives from the fact that inaccuracies in the experimentally determined, or even refined phase terms will cause the electron density calculated for the NCS-related molecules to be non-equivalent. An improved estimation of the "true" molecular density distribution can be obtained by averaging the related density for NCS-related molecules. A new set of phases can then be derived by back-transforming the density map using "averaged" density images for the NCS molecules. The improved phases are associated with observed amplitudes and a new density map computed. The entire process is reiterated until convergence is reached, generating an improved set of phases consistent with the constraints implied by non-crystallographic symmetry. The coherent identical components of the density are reinforced while incoherent or non-identical noise components are diminished at each cycle. For a detailed description of this approach, see Bricogne (1974, 1976).

In those cases where the rotational part of the NCS is parallel to a crystallographic axis and a subset of the Laue symmetry about that axis (e.g. a 2-fold NCS rotation in a cell of space group $P2_12_12_1$ as in Bungarotoxin) the NCS can be considered as arising from pure translationally related molecules. Where all or part of the NCS can be considered as purely translational (e.g., in crystals of α-Bungarotoxin (Spencer, 1977), lac repressor core (Steitz, personal communication), glutamine sythetase (Heidner, et al., 1978), melitin, (Eisenberg -personal communication), a more efficient approach to molecular averaging than the real-space method suggested by Bricogne (1974) can be utilized. Described here, along with application to the low-resolution structure determination of the snake neurotoxin α-Bungarotoxin, is a technique where the averaging is performed as a simple multiplication in reciprocal-space. For pure translations of the kind described above no interpolations are required with this approach so affording significant increases in speed and accuracy over conventional methods.

Theory of the Method

(i) The Translation Operation

Let $\rho_m(\underline{r})$ represent the electron density distribution of one molecule and $F_m(\underline{s})$ be its Fourier transform as defined by

$$F_m(\underline{s}) = \int_{V_m} \rho_m(\underline{r}) e^{2\pi i(\underline{r}\cdot\underline{s})} d\underline{r} \qquad (1)$$

where V_m is the volume containing the density for the molecule m, and

where $\underline{r}$, $\underline{s}$ represent real and reciprocal space vectors respectively. Translation of $\rho_m(\underline{r})$ by a vector $\underline{\Delta}$ causes the phase of $F_m(\underline{s})$ to be shifted by $2\Pi\underline{\Delta}\cdot\underline{s}$ while leaving the amplitude unchanged:

$$F_m'(\underline{s}) = \int_{V_m} \rho_m(\underline{r})\ e^{2\pi i(\underline{r} + \underline{\Delta})\cdot\ \underline{s}}\ dr$$

$$F_m'(\underline{s}) = F_m(\underline{s})\ e^{2\Pi i(\underline{\Delta}\cdot\underline{s})} \qquad (2)$$

The Fourier transform of a collection of N equivalent molecules related by N translations $\underline{\Delta}_j$ for j = 1-N can be described in terms of the Fourier transform of a single molecule $F_m(\underline{s})$ by expansion of equation 2.

$$F(\underline{s}) = F_m(\underline{s}) \sum_{j=1}^{N} e^{2\Pi i(\underline{\Delta}_j\cdot\underline{s})} \qquad (3)$$

$$F(\underline{s}) = F_m(\underline{s})\ F_t(\underline{s})$$

where now

$$F_t(\underline{s}) = \sum_{j=1}^{N} e^{2\Pi i(\underline{\Delta}_j\cdot\underline{s})}$$

$F_t(\underline{s})$ is independent of the molecular transform and arises solely from the non-crystallographic symmetry.

From another viewpoint, the reciprocal-space multiplication implied by equation 3 is equivalent to a real-space convolution of ρ_m with N delta functions appropriately located in the unit cell (i.e., at the

positions $\underline{\Delta}_j$ for j=1-N). This equivalence is exploited in the averaging method.

(ii) Density Averaging.

If an observed set of amplitudes $|F_o(\underline{s})|$ and phases $\phi(\underline{s})$ have been obtained, the electron density for the unit cell is given by

$$\rho_o(\underline{r}) = \sum_{\underline{s}} F_o(\underline{s})\, e^{-2\pi i \underline{r}\cdot\underline{s}} \qquad (4)$$

where

$$F_o(\underline{s}) = |F_o(\underline{s})| e^{i\phi(\underline{s})}$$

This map will contain N different images of the molecule at positions $\underline{\Delta}_j$. It is convenient to set $\underline{\Delta}_1=0$ so fixing the origin: i.e., $\rho_m(\underline{r})_{(j=1)}$ corresponds to the density for the first molecule with respect to the unit cell origin at $\underline{r} = 0$. Translation of the entire unit cell density map by $-\underline{\Delta}_j$ leads to superposition of the experimentally determined images for the j^{th} and first molecule. Thus, the ourier transform of

$$F_o(\underline{s})[1 + e^{+2\pi i\, \underline{\Delta}_j\cdot\underline{s}}] \qquad (5)$$

will superimpose and add density for the j^{th} and first molecule at the position of the first molecule. Outside of the molecular volume V_m the superposition will be of non-equivalent (non-NCS related) parts of the unit cell, and will be meaningless. All NCS molecules may be summed,

and averaged by:

$$\bar{\rho}_o(\underline{r}) = \frac{1}{N} \sum_{\underline{s}} F_o(\underline{s}) \left(\sum_{j=1}^{N} e^{-2\pi i \, \underline{\Delta}_j \cdot \underline{s}} \right) \cdot e^{-2\pi i \underline{r} \cdot \underline{s}} \qquad (6)$$

where $\underline{\Delta} = 0$. Thus, $\bar{\rho}_o(\underline{r})$ is given directly as the Fourier transform of the modified coefficients

$$F_o(\underline{s}) \left(\sum_{j=1}^{N} e^{-2\pi i \, \underline{\Delta}_j \cdot \underline{s}} \right) \qquad (7)$$

$\bar{\rho}_o(\underline{r})$ now contains the averaged density for all NCS related molecules, with incoherent overlap contributing to other regions of the map everywhere else. It must be emphasized that this procedure does not depend on knowing anything about V_m, or the volume shape of each molecule. Indeed, the $\bar{\rho}_o(\underline{r})$ maps will be the means of best defining V_m. The $\underline{\Delta}_j$ are readily obtained from the native Patterson map and can be refined later using the rapid translation/R factor search described below.

Since the averaged map $\bar{\rho}_o(\underline{r})$ (Equation 6) will contain only one copy of the averaged molecule, it will always be of triclinic (P_1) symmetry, no matter what the space group of the crystals is. Correspondingly, the modified $F(\underline{s})$ produced in Equation 3 must be calculated for all h, k, and for $\ell > o$. This increase in the number of input $F(\underline{s})$ to a triclinic (P_1) Fast Fourier Transform is compensated for by the fact that it is only necessary to compute $\bar{\rho}_o(\underline{r})$over the volume of a single molecule. Because the averaging is performed in reciprocal-space the

translations are analytically incorporated; hence, no interpolations are required. The result is a dramatic increase in the speed and accuracy over a conventional approach (e.g. involving averaging by interpolation in the real-space domain). Only the first molecule, over which all others have been placed will be properly averaged, the remainder of the density map outside V_m will be completely scrambled. This is a direct consequence of translating the entire unit cell by the local translational symmetry between molecules.

Since the averaging process does not require the definition of a molecular boundary, solvent regions immediately surrounding the molecule, if they are represented around each molecule, are correctly averaged. Iterative phase refinement, however, does require that the molecular envelope be defined, a task simplified by using the averaged density map.

(iii) Crystallographic Symmetry and Calculation of $F_c(\underline{s})$

For efficiency in the total NCS refinement procedure, and for application of the molecular density transform to rapid translation search, it is necessary to build the calculated structure factor $F_c(\underline{s})$ for the entire unit cell, directly from the transform of one averaged molecular image,

$$F_m(\underline{s}) = \int_{V_m} \bar{\rho}_o(\underline{r})\ e^{2\pi i \underline{r}\cdot\underline{s}}\ d\underline{r} \qquad (8)$$

The contributions from shifted and symmetry related molecules are added vectorally to $F_c(\underline{s})$ as follows:

The coordinate transformation corresponding to the ith crystallographic symmetry element is described by a rotation matrix A_i and a translator vector $\underline{t}_i$, for M symmetry related molecules. Thus by analogy with Equation 5, $F_m''(\underline{s})$ -the transform of crystallographic symmetry related, and translated molecules becomes:

$$F_m''(\underline{s}) = \sum_{i=1}^{M} F_m\,(A_i^{-1}\cdot\underline{s})\; e^{2\pi i[\underline{t}_i\cdot\underline{s}]} \qquad (9)$$

where A^{-1} is the inverse of matrix A.

Finally, including N_j non-crystallographic translations $(\underline{\Delta}_j)$ which apply among each of the M crystallographically related sets of molecules, the transform of the whole unit cell $F_c(\underline{s})$ becomes:

$$F_c(\underline{s}) = \sum_{i=1}^{M} F_m(A_i^{-1}\cdot\underline{s}) \sum_{j=1}^{N} e^{2\pi i[(A_i\underline{\Delta}_j + \underline{t}_i)\cdot\underline{s}]}$$

or

$$F_c(\underline{s}) = \sum_{i=1}^{M} F_{m_i}\,(\underline{s})\; F_{t_i}\,(\underline{s}) \qquad (10)$$

where now

$$F_{m_i}(\underline{s}) = F_m(A_i^{-1}\cdot\underline{s})$$

and (11)

$$F_{t_i}(\underline{s}) = \sum_{j=1}^{N} e^{2\pi i[A_i\underline{\Delta}_j + \underline{t}_i]\cdot\underline{s}}$$

$F_{t_i}(\underline{s})$ is easily calculated, and for crystallographic rotations the values $F_{m_i}(\underline{s})$ are already contained in $F_m(\underline{s})$ (i.e, $= F_m(A_i^{-1}\cdot\underline{s})$ computed in equation 9.

(iv) Optimal Translation Search

The separation of terms F_m and F_t in Equation 10 provides great simplification in the calculation of $F_c(\underline{s})$ from the density for a single image, and provides the basis for rapid translation search where changes in $\underline{\Delta}_j$ of F_t are assayed directly in the conventional crystallographic residual. This procedure was crucial to the solution of both α-Bungarotoxin and Cobrotoxin in our laboratory.

The translation function search was developed independently from that described by Nixon & North (1976) though it is of similar form. The values of $\underline{\Delta}_j$ can be refined to minimize the residual

$$R = \Sigma\,\big|\,|F_o(\underline{s})| - |F_c(\underline{s})|\,\big| / \Sigma |F_o(\underline{s})| \qquad (12)$$

by the simple computation of $F_{t_i}(\underline{s})$ ($F_{m_i}(\underline{s})$ is only calculated once) for all $\underline{\Delta}_j$. This "reciprocal space" translation function has a much higher signal-to-noise ratio than Patterson search techniques since it searches only for inter-molecular vectors, where a Patterson search implies a search for intermolecular vectors in a map which includes both inter- and intra-molecular vectors.

(v) Density Map Refinement

The separation of terms in Equations 6,7 & 10,11 permits density map refinement without any interpolation. Rapid density averaging (Eq. 6,7) leads to the initial averaged density map. $\bar{\rho}_m(\underline{s})$ is extracted from $\bar{\rho}_o(r)$ with a boundary function $g(\underline{r})$ that has values of unity inside V_m and zero outside. Next, this average density for a single molecule is Fourier transformed to yield $F_m(\underline{s})$ (Eq. 8) which is used in equation 10 to reconstruct the structure factors of the unit cell. Lastly, the phases of $F_c(\underline{s})$, are associated with the observed $|F_o(\underline{s})|$ (using a weighting scheme if desired), and Fourier transformed to provide a new electron density map. These operations can be reiterated until no further improvement in the electron density map is observable. Since no interpolations are required, substantial improvements in accuracy and computation time can be achieved.

APPLICATION TO α-BUNGAROTOXIN:

α-Bungarotoxin is a polypeptide α-neurotoxin isolated from the venom of the banded krait Bungarus multicinctus (Chang & Lee, 1963).

Two orthorhombic crystal forms have been obtained by Spencer & Stroud, (Spencer, 1977), a "large-cell" form (a=69.9 Å, b=76.7 Å, c=44.8 Å) with 4 molecules per asymmetric unit and a "small-cell" form, (a'(≃a)=67.8 Å, b'(≃b)=78.4 Å, c(≃c/2)=22.4 Å) with 2 molecules per asymmetric unit.

The native Patterson function for the large cell form shows that four molecules within the unit cell are related by pure translational non-crystallographic symmetry. The small cell form obtained under slightly different conditions has almost identical a and b cell dimensions, and half size c dimension. Thus, the native Patterson for the small cell form, and the NCS vectors show that packing in the small cell form is almost identical to that in the large cell form. The large cell consists of two almost equivalent halves in the c direction, which become truly equivalent in the small cell form. The NCS translational vector between pairs of molecules in the small cell is (uvw)= 0.416a-0.341b + 0.5c. (The additional pure - translational NCS vector in the large cell is parallel to the c axis, (uvw)= 0.53c.)

The structure was solved initially to 5 Å resolution for the averaged half-cell, in the large cell form, by multiple isomorphous replacement methods, Spencer & Stroud (Spencer, 1977). The assumption of equivalence between the two halves becomes invalid beyond about 5 Å resolution. Since this assumption is required to achieve the solution, analysis of this form is restricted to 5 Å resolution. To circumvent this problem, attention was turned to the small cell form: this was solved by placement - and refinement of the "averaged" density map obtained from the large cell form.

The final 5 Å averaged denisty map for the large cell form was calculated using eq. 6. NCS vectors $\underline{\Delta}_j$ and the correct placement of molecules for the small cell form were refined using this 5 Å MIR density map, instead of an atomic model via the translational search. (Eqns. 10, 11, 12).

The initial phases for the small cell form were defined by three cycles of non-crystallographic averaging and phase refinement. The net result was a much improved 5 Å resolution density map computed from the small cell data. The calculated data were compared to the observed $|F_o(\underline{s})|$ using the standard crystallographic residual (Equation 12) which dropped from 40% to 30%. A section through the translation function showing the correct location (-.004, .008, .023; R=40%) is shown in Figure 1. The final averaged 5 Å density map is shown in Fig. 2.

In an effort to extend the structural analysis to higher resolution, MIR phases were calculated for the averaged half-cell in the large cell form to 4 Å. Since the assumption of equivalence between the two halves in the large cell form is invalid beyond 5 Å, these calculated phases were greatly in error. Using the positions and molecular boundary defined by the 5 Å analysis, the 4 Å phases were transferred to the small cell form. The electron density map calculated using these phases and the small-cell $|F_o|$ (Fig. 3) became the starting point for three cycles of non-crystallographic phase averaging using the procedures described above. Throughout the refinement process, new averaged electron density maps were computed using Sim's weighted (Sim, 1959) $2|F_o|-|F_c|$ amplitudes.

The correct molecular boundary was redefined and three more cycles

of density map refinement using the refined $\underline{\Delta}_j$ reduced the residual from 35% to 20% and gave the much improved map shown in Fig. 4.

The main chain connectivity, was unambiguously established from this map as well as the location of the 5 disulphide cross-bridges and many of the larger side-chains. A Lab-Quip molecular model was built to the map using a Richard's box (Richards, 1968). Subsequently, 3.5 Å data were included and the structure refined using the difference Fourier method (Chambers & Stroud, 1977, 1979) to a residual of 23%. A section through the 3.5 Å averaged $2F_o-F_c$ map is shown in Fig. 5a. The α-carbon structure is presented in Fig. 5b.

DISCUSSION:

The power of this method is emphasized by the fact that the structure analysis of Bungarotoxin has withstood attack by conventional MIR methods, by use of Patterson search and rotation function analysis using the structure of erabutoxin (Tsernoglou & Petsko, 1976, Low et al., 1976) and by all attempts to build a correct model to the 5 Å MIR map (which in this application was the starting point for the successful scheme outlined).

The existence of non-crystallographic symmetry implies that the crystallographic phase terms are not independent. They are coupled in a complex manner reflecting the duplicate copies of a single structure at different locations within the asymmetric unit. This joint relationship amongst the phases can be exploited to improve the experimentally determined values. In many instances, all or part of the NCS can be interpreted as arising from translationally related molecules. When this occurs, our hybrid real-reciprocal space approach to phase refinement

is more accurate and computationally efficient than either the exclusively real-space (Bricogne) or exclusively reciprocal-space (Rossmann) approaches previously described. With our method, the averaging and unit cell reconstruction steps are recognized to be convolutions in real-space. These convolutions are more conveniently performed in reciprocal-space as multiplications where the translations are incorporated analytically; hence, no interpolations are required. The imposition of a molecular boundary (necessary for phase refinement) is performed in real-space as a simple multiplication instead of in reciprocal-space as a convolution (Rossman), again resulting in significant time savings.

In this paper the mathematics required to perform these operations have been developed and applied to the low-resolution structure determination of α-Bungarotoxin. The problem here was to transfer phases from one crystal form to another by molecular replacement methods and to subsequently refine the phases in the new unit cell (containing two copies of the molecule per asu). The resultant 5 Å electron density map is a significant improvement over the starting map. Since there are only two α-Bungarotoxin molecules per asu, accurate averaging and reconstruction are crucial for refinement.

For those cases where part of the non-crystallographic symmetry is translational and part is rotational about an <u>arbitrary</u> axis, interpolations must be performed with any refinement scheme. The translational component can always be dealt with as described here. The remaining rotational NCS is probably best treated in real-space as described by Bricogne (1974, 1976), although it is possible to use generalized rotations

(Equation 10, requiring interpolations) in the reciprocal-space approach. Where applicable, however, the methods described here represent significant improvements in speed and accuracy.

ACKNOWLEDGEMENTS

This work was supported by the National Institutes of Health, Grant #GM 24485 and by the National Science Foundation, Grant PCM77-25407.

REFERENCES:

Bloomer, A.C., Champness, S.J., Bricogne, G., Staden, R., Klug, A. (1978). Nature 276, 362-368.

Bricogne, G. (1974). Acta Cryst. A30, 395-405.

Bricogne, G. (1976). Acta Cryst. A32, 832-847.

Chambers, J. & Stroud, R.M. (1979). Acta Cryst. B35, 1861-1874.

Chambers, J.L., Stroud, R.M. (1977). Acta Cryst. B33, 1824-1837.

Chang, C.C. & Lee, C.Y. (1963), Arch. Int. Pharmacodyn. 144, 241-257.

Harrison, S.C., Olson, A.J., Schutt, C.E., Winkler, F.K., Bricogne, G. (1978). Nature 276, 368-373.

Heidner, E.G., Frey, T.G., Held, J., Weissman, L.J., Fenna, R.E., Lei, M., Harel, M., Kabsch, H., Sweet, R.M. and Eisenberg, D. (1978), J.M.B. 122, 163-173.

Main, P. and Rossmann, M.G. (1966), Acta Cryst. 21, 67-72.

Nixon, P.E., North, A.C.T. (1976) Acta Cryst. A32, 320-332.

Richards, R.M. (1968) "Richard's Folly", J.M.B. 37, 225-230.

Rossmann, M.G. & Blow, R.M. (1963) Acta Cryst. 16, 39-45.

Sim, G.A. (1959), Acta Cryst. 12, 813-815.

Spencer, S.A. (1977), Ph.D. Thesis, Department of Chemistry, California Institute of Technology, Pasadena, California.

Tsernoglou, D. and Petsko, G.A. (1976), FEBS Lett. 68, 1-4.

FIGURE CAPTIONS:

Figure 1.: A region through the final averaged 5 Å small-cell maps shown in stereo (x= .23-.73, y=.38-.69, z=.8-1.3; x -horizontal, y -vertical).

Figure 2.: A section through the translation function relating the electron density from the averaged half-cell to the small cell form (x=.-12-.12, y= .008, z= -.35-.35; x horizontal, z vertical). The peak corresponding to a crystallographic residual of about 40% indicates a fractional translation of (-.004, .008, .023). Contour levels are at 1% intervals; the function 1-R is plotted to show the correct location as a peak.

Figure 3.: Stereo plots of three different regions through the starting 4 Å map in the small cell. a) x=.18-.75, y=.53-.6, b) x=.18-.75, y=.59-.67, z=0-1.4, sectioned down y, z horizontal, c) x=.23-.7, y=.3-.8, z=.3-.6; sectioned down z, x horizontal.

Figure 4.: Stereo plots of the same three regions shown in Fig. 3 but after the non-crystallographic symmetry averaging/ phase refinement process was completed.

Figure 5.: A stereo plot of a region of the final $2F_o-F_c$ 3.5 Å map showing the non-crystallographic diad axis is seen in (a). Three strands of the 4-stranded anti-parallel β-structure spanning the intermolecular interface are also shown. The complete α-carbon diagram is shown in stereo in (b).

FIGURE I

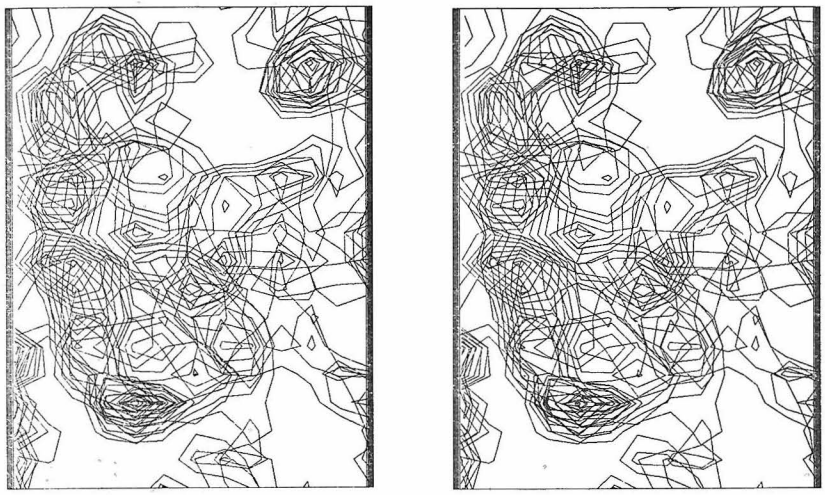

FIGURE 2

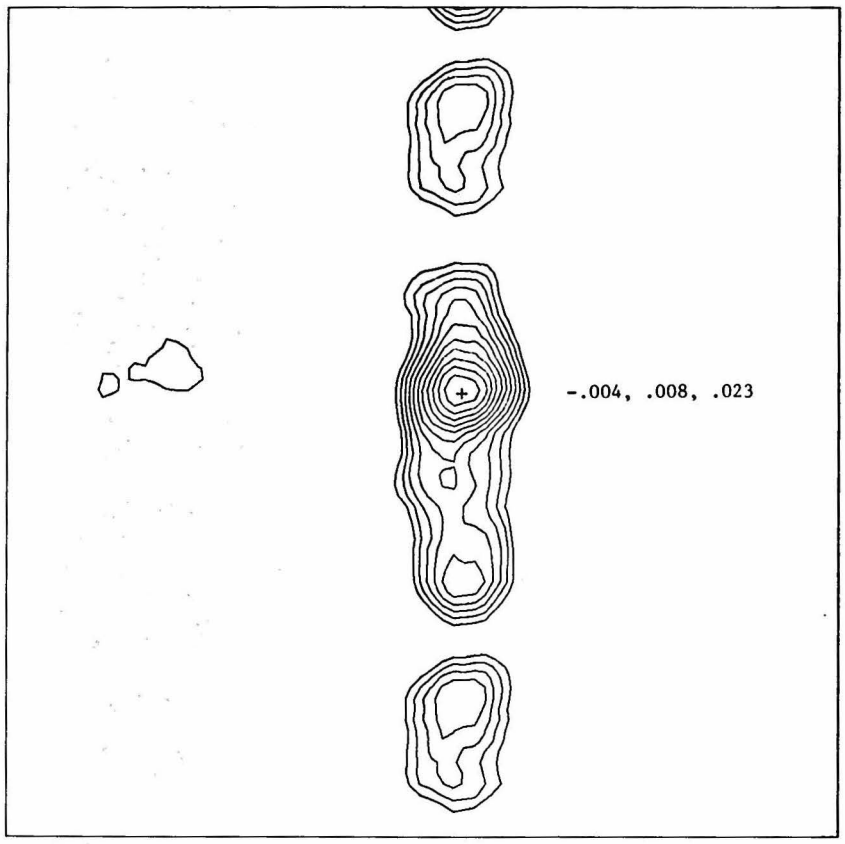

FIGURE 3

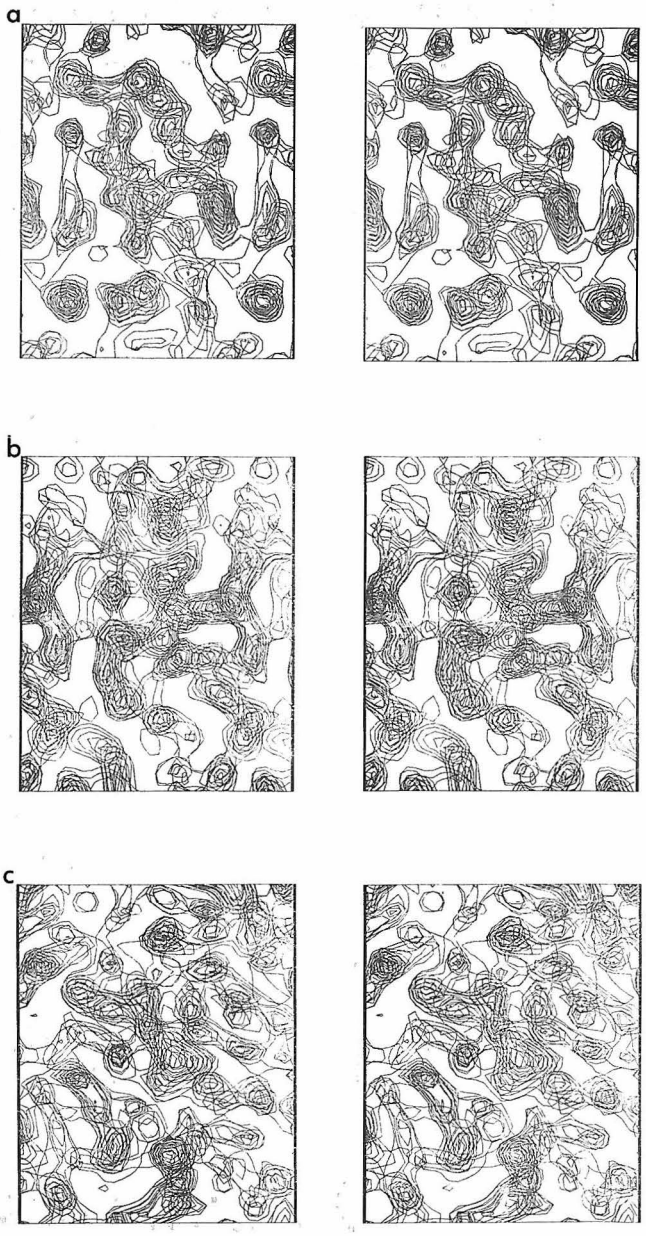

FIGURE 4

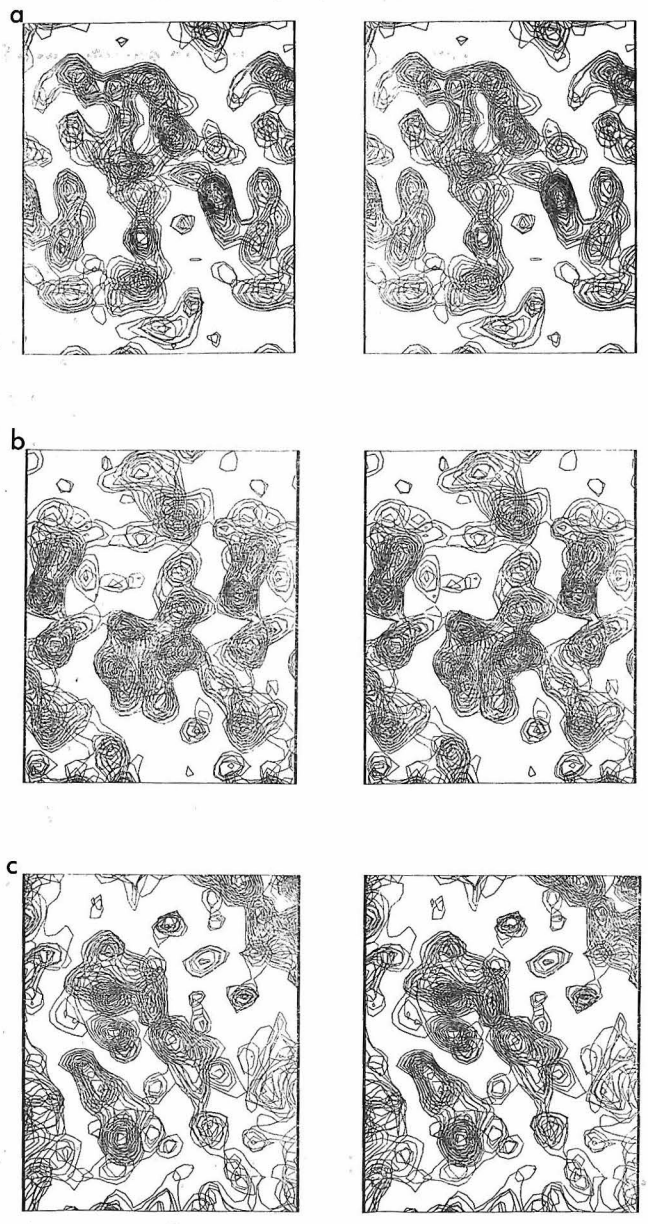

FIGURE 5

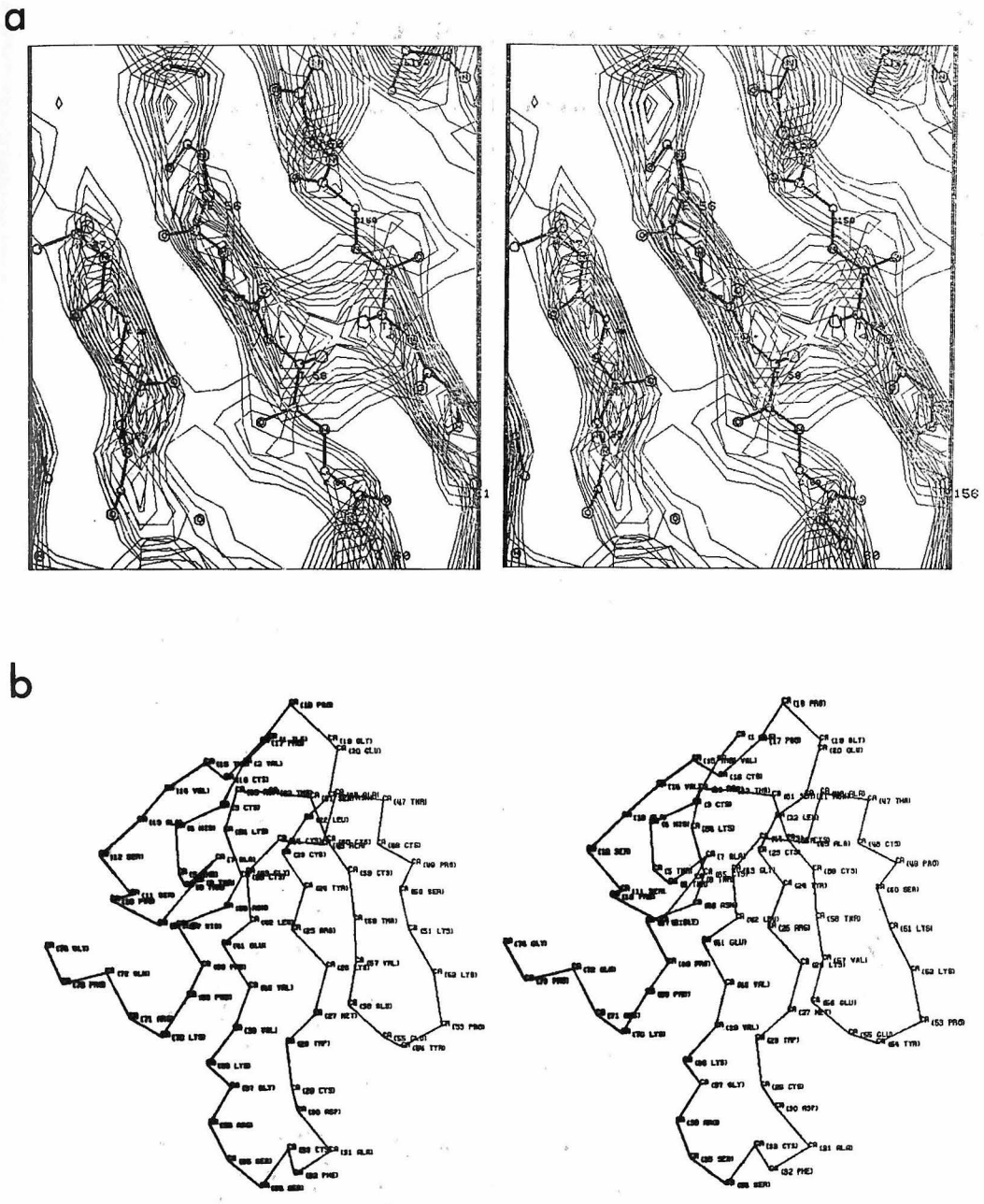

APPENDIX II

Evolution of a Molecular Surface Interaction: The Structure of α-Bungarotoxin

EVOLUTION OF A MOLECULAR SURFACE INTERACTION:

THE STRUCTURE OF α-BUNGAROTOXIN

Key words: (Neurotoxin/acetylcholine receptor/x-ray crystallography)

by

DAVID A. AGARD, STEVEN A. SPENCER

and ROBERT M. STROUD

Department of Biochemistry
University of California
Medical Center
San Francisco, California 94143

Communicated by: Walther Stoeckenius

ABSTRACT

The structure of α-Bungarotoxin was solved by x-ray crystallographic methods and refined to a standard crystallographic residual of 21% at 3.5 Å resolution. Two interconvertible crystal forms were used to obtain the solution. Multiple isomorphous replacement methods led to solution of one form obtained at pH 4, 8°C to 5 Å resolution. The density image so obtained was transferred to the second crystal form obtained at 20°C and refined using constraints of positivity of electron density, non-crystallographic symmetry, and volume of the molecules. Subsequently a molecular interpretation was made from a 4 Å map prior to difference Fourier refinement which gave the final residual of R=21% at 3.5 Å resolution.

Comparison with other related post-synaptic neurotoxin structures reveals that these structures are variable in conformation and most probably evolved a binding surface for the target acetylcholine receptor which allows for some refolding upon formation of the receptor-toxin complex.

α-Bungarotoxin is one of the neurotoxic components in the venom of the formosan banded Krait, Bungarus multicinctus. The alpha toxins from several families of snakes produce a non-depolarizing post-synaptic block at neuromuscular junctions by binding to the acetylcholine receptor (1). This class of toxins has received attention because of the tight specific binding to nicotinic acetylcholine receptors from mammalian neuromuscular junctions and the electric organs of electric fish (2-6). They are small, highly basic and extremely stable proteins with isoelectric points generally around 9 (the isoelectric point for α-Bungarotoxin is 9.19 (7)). The stability is partly due to the presence of 4 or 5 disulfide cross-links. Cobrotoxin, for example, retained 25% activity after heating at 100°C for 30 minutes (8) whereas erabutoxins a and b from Laticauda semifasciata retained full activity under the same conditions over the pH range from 1 to 11 (9). Cobrotoxin retained full activity in 8 M urea (10) and Naje haje toxin 1 retained full activity after treatment in anhydrous formic acid or 1 M HCl for 100 minutes (11).

More than 56 α toxin sequences have been determined and they fall into two classes: The type 1 or short neurotoxins contain 60-62 amino acids and 4 disulfide bonds. The type 2 or long neurotoxins, are comprised of 71-74 amino acids cross-linked by 5 disulfide bonds. Sequence comparisons show that all are homologous and presumably arose from a common ancestor (12). α-Bungarotoxin and α-Cobratoxin (13,14) are examples of type 1, while erabutoxin b and cobrotoxin are of type 2. The x-ray crystal structures of a small neurotoxin (erabutoxin b)(15,16) and of

another long type 2 neurotoxin α-Cobratoxin (13, 14) have been determined and are compared with the structure reported here.

METHODS

Lyophilized venom from Bungarus multicinctus was obtained from Miami Serpentarium laboratories (Lots #BM 1E and BM 2 ETL). α-Bungarotoxin was purified using procedures similar to those of Clark et al., (7) followed by further chromatography on CM-52 and Sephadex G-50 (fine) equilibrated with 0.1 M acetic acid. α-Bungarotoxin eluted from the G-50 column just ahead of the salt fractions and the peak was skewed toward higher molecular weight which seems to be characteristic for this toxin. This could be due to dimerization in the concentrated solution supplied to the column followed by gradual dissociation of species as the toxin was diluted by the eluant. The material was lyophilized, and shown to bind specifically to the acetylcholine receptor using a standard assay (7). It was the main component in the venom out of 18 components total assayed by absorbance at 280 nm.

Crystallization. Crystallization conditions were defined by the free-diffusion technique of Salemme (17). Batch crystallization was from α-Bungarotoxin (32.8 mg/ml) dissolved in 0.25 saturated NaCl, 0.1 saturated NH_4SO_4, 5 mM EDTA, 0.05 M Tris, 0.05 M glycine and sufficient glacial acetic acid to adjust the pH to 4.25. The solution was filtered and immediately placed at 10-12°C. Crystals appeared in several weeks and eventually the mother liquor was replaced by a solution of 0.3 saturated NaCl, 0.15 saturated $(NH_4)_2SO_4$, 0.05 M glycine, at pH 4.0 in which the crystals were stable indefinitely at 8°C. These crystals have cell

dimensions of a=69.86 ± .05 Å, b= 76.71 ± 0.05 Å, c= 44.75 ± 0.01 Å, and angles $\alpha = \beta = \gamma = 90.0°$. They are referred to as the large cell form and had a density of 1.29 ± .01 g per cm^3 measured by flotation in cesium chloride. The diffraction pattern had apparently perfect orthorhombic symmetry though the space group remains undetermined and the pattern reflects an intimate molecular twinning that was only appreciated much later.

Between about pH 7 and 9, a different crystal form (referred to as the small cell form), was obtained which had true orthorhombic symmetry, space group $P2_12_12_1$ with an approximately halved c cell dimension. (a= 69.4 Å, b= 77.9 Å, c= 22.4 Å). There were two molecules in the asymmetric unit (V_M= 1.89). Both crystal forms contain about 36% solvent.

Above pH 4.5 or above 12°C, the "large cell" crystal form cracked and crystalites were converted to the small cell form. Since raising either pH or temperature would favor ionization of carboxyl groups, they may be a factor in the metastable packing arrangement which allowed the "large cell" crystals to grow larger than other crystal forms. Crystals grown at room temperature, or pH above 7.0 produced only long thin crystals of the small cell form.

Diffracted x-ray intensities from native and derivatised crystals were recorded on a Syntex P_1 diffractometer using graphite monochromatised CuKα radiation, generally following the procedures described by Stroud et al., (18). Crystals of the large cell form were maintained at 8°C ± 1°C throughout data collection in a cooled cell (19).

Heavy atom derivatives of the large cell form were screened using

precession photographs. Many of the tested derivatives caused the crystals to crack, and/or converted them to the small cell crystal form. In all, ten heavy atom derivatives were solved and phases refined prior to calculation of the best 5 Å multiple isomorphous replacement density map from the averaged half cell in the large cell crystal form.

RESULTS

Crystallography

The crystallographic solution was unusually complicated by the following factors: (i) The large cell form is made up of two almost identical sets of molecules separated by ∿c/2 in the c cell direction (actually 0.53c); (ii) The asymmetric unit within the large cell form contains four molecules all related by purely translational vectors: they are all in essentially identical orientation; (iii) The translation vectors between all four molecules involve separation of either 1/4 or 1/2 cell c, plus or minus 1.32 Å. Thus, all vectors are confused with Harker peaks; (iv) The correct solution implies a space group $P2_12_12_1$ for the small cell: Thus the large cell form with a doubled c axis dimension cannot be assigned a space group in the crystallographic sense (the 2_1 related molecules in the c direction are separated by ∿ c/4 in the large cell). It is an essentially perfect, intimately twinned assembly of monoclinic layers each with angles of exactly 90°. (v) Because of the open toxin folding pattern, even relatively sophisticated application of various Patterson search methods (20-22) using erabutoxin b coordinates failed to give

any indication of the (single) orientation for all four molecules of bungarotoxin in the asymmetric unit (even when the correct solution was identified). (vi) Most heavy atom derivatives cracked the crystals, - but of those acceptable all had two or more major sites per molecule.

A diffraction pattern from the large cell crystal form is shown in Figure 1. Most effort was concentrated onto solution of this form since large crystals were obtained first and are still obtained much larger and more readily than for the other form. Systematic absences for h,k,1 odd seemed to indicate a space group $P2_12_12_1$. However, the most striking feature of the diffraction pattern was the weak intensities for the 1=odd planes of reflections, which demonstrates that the unit cell contains two almost equivalent layers in the c axis direction. An average displacement of about 1 Å between equivalent atom positions in the two layers would satisfactorily account for the gradually increasing intensity in the 1= odd planes, which become roughly equivalent to the 1= even intensities at about 3 Å resolution.

The native protein 2.5 Å Patterson map contained a major peak at (uvw) = .410, .341, .28 whose intensity (including symmetry related peaks) was essentially the same as that of the origin. This demonstrates that each molecule in the crystal is related to another by a pure translation of $\Delta x = \pm .416$, $\Delta y = \pm .341$, $\Delta z = \pm .28$ vector. A second pair of peaks (uvw) = 0,0,0.47 and (uvw)= 0,0,.53 overlap around (uvw)= 0,0,1/2. Their intensity sum was also the same as that of the origin. A

second pair of molecules is separated from the first pair by 0.47 c in one direction, 0.53 c in the opposite direction.

The approximate equivalence of the two halves of the cell was exploited in determination of the first 5 Å resolution electron density map by the multiple isomorphous replacement method. All l=odd planes were omitted from the analysis to 5 Å resolution, corresponding to solution of the averaged halves of the unit cell. The difficulty in resolving the actual difference between the almost equivalent halves of the unit cell, and ultimately the realization that this was a statistical phenomenon made solution of the large cell form beyond 5 Å resolution intractible, even though the diffraction pattern extends to at least 2 Å resolution.

At this point attention was turned to the small cell crystal form obtained by temperature-induced conversion of the large cell form. The native Patterson map again indicated a pure translation vector, of slightly different value (uvw)= 0.416, 0.341, 0.5. This vector in the small cell was almost the same as found in the large cell, except that a small shift of 1.32 Å in w placed the non-crystallographically related molecules exactly 0.5 c apart. Coupled with a crystallographic 2_1 axis parallel to c, the implication is that bungarotoxin molecules occur as dimerized pairs about non-crystallographic 2-fold axes which are also parallel to c. The averaged 5 Å density map was located in the small cell and refined using a rapid translation algorithm we described elsewhere (23), and a rapid scheme for averaging of non-crystallographically related molecular density. A molecular interpretation was made to a 4 Å map and the structure refined

using the difference Fourier procedure described by Chambers & Stroud (24,25) to a standard crystallographic residual $R = \Sigma|F_o - F_c|/\Sigma|F_o|$ of about 21% at 3.5 Å resolution. The accuracy of coordinates is estimated to be about σ = 0.5 x R x resolution (25) = ± 0.35 Å.

The Structure of α-Bungarotoxin:

The density map refinement procedure produced a 4 Å map of such quality that the main chain could be unambiguously traced. In addition, all of the disulfide bridges as well as many of the larger side chains were visible. Density in the region of the active loop (residues 29-35) was initially weak. Following inclusion of the 3.5 Å data and several cycles of crystallographic refinement, this region was omitted from the structure factor calculations. This modified model was refined for 4 more cycles and residues 29-35 were rebuilt using an averaged $2F_o - F_c$ map. During the course of refinement, a few regions developed unreasonably short close contacts and were rebuilt in a similar manner.

A portion of the final electron density map is shown in Figure 2. The structure of a single molecule is depicted in Figure 3. Very little organized secondary structure is observed in the refined model. There are no α-helical regions and only one length of extended anti-parallel β sheet: between residues 25-27 and 56-58.

The molecular packing arrangement is such that a close contact is formed between two bungarotoxin molecules related by a non-crystallographic two-fold axis. Recall that the profile obtained from the G-50 column was indicative of dimerization at high concentrations. The dimeric contact

involves anti-parallel β pleated sheet contacts between residues 55 and 59 of one molecule, with residues 59 and 56 of the two-fold relative. Thus, in the dimer 4 chains are cross-linked by anti-parallel β sheet-like hydrogen bonds. There is also a region of close contact between residues 30-35 on the one molecule and residues 35-30 from a symmetry-related molecule. As a consequence, Phe 32 which is extended in both erabutoxin b (15,16) and cobratoxin (13,14) is seen oriented into the molecule in bungarotoxin.

The basic folding pattern of the three crystallographically-determined α-toxin structures are similar although there are significant differences in detail. The polypeptide chain of these three toxins are folded into an extended 3 loop structure held together by 4 disulfide cross-links (the long neurotoxins have a 5th disulfide pinching off a region at the end of the middle loop). In spite of small insertions and deletions in the amino acid sequences, the 4 disulfide bridges common to both the long and short toxins are in the same spatial location in all three structures. The axes of all four bridges are similarly oriented in both α-bungarotoxin and α-cobratoxin (13,14), yet two are nearly perpendicular to those in erabutoxin b (15,16). Although the only well-defined secondary structure present in these toxins is anti-parallel β-sheet, the amounts differ widely between the short (≈ 75%) and long (< 40%) toxin classes. It appears as though one of the strands comprising the 3-stranded β-structure found in α-cobratoxin (13,14) is lost in Bungarotoxin upon formation of the 4-stranded intermolecular anti-parallel β-sheet found in the crystal.

Although the basic folding patterns of all three toxins are rather similar, the detailed folding specifically around residues 1-11, 27-42, and 61-68 (containing $\sim$ 50% of the conserved residues) is unexpectedly different (figure 4a). The conformation of the middle loop (containing the extra disulfide bridge) in Bungarotoxin is quite different from that predicted by Low (26) based on model building to the erabutoxin structure as well as that observed in α-cobratoxin (13,14).

DISCUSSION

One of the goals of this work is to correlate binding of the toxin to the acetylcholine receptor with the three-dimensional structure of the toxin. The very tight binding of the α-toxins to the nicotinic acetylcholine receptor ($K_d = 10^{-9} - 10^{-11}$) suggests that the binding results not from a simple one or two point interaction, but rather arises from the large contact area afforded by the precise alignment of complementary surfaces. Thus, it is expected that this binding surface would be evolutionarily conserved. Only indirectly, then, would the amino acid sequence be conserved. Chemical modification or sequence differences at the site of receptor-interacting residues would be likely to diminish, but not abolish, binding unless a structural alteration is induced. The pronounced sequence homology amongst the long and short toxins as well as the extensive chemical modification literature has prompted several investigators (26-28) to assign crucial roles to conserved residues. In addition, those conserved residues that are also present in a sequence-related, yet non-neurotoxic, family of molecules (the cardiotoxins) are generally

assigned to "structural" rather than "functional" roles. It is felt that the remaining functional residues should be considered not as absolutely required for toxin-receptor association, but as a means for defining general aspects of the interaction surface.

A comparison of the three toxin structures reveals that the side chains of certain conserved, functional residues (Typ 24, Lys 26, Asp 41, Lys 51) are all in roughly the same location and all seem to lie on one surface of the toxin molecule (Figures 4b, 4c). By contrast, the side chain of another invariant residue (Trp 29) is rotated completely away from the "binding surface" in Bungarotoxin, instead of into this surface as for erabutoxin b (15,16) and α-cobratoxin (13,14). This would suggest a role more structural than functional for this residue.

Methionine 27 and tyrosine 54 are the only other residues found protruding into the binding surface in Bungarotoxin (Figure 4c). In all of the other toxin sequences, methionine 27 is replaced by either a charged residue or a neutral hydrophilic residue. The equivalent glutamine found in erabutoxin b (15,16) is pointing away from the contact surface (Figure 4b). The tyrosyl residue of Bungarotoxin is replaced by glycine in nearly all of the other toxin sequences. The positions of both residues in the Bungarotoxin crystal structure probably represent hydrophobic contact points on the interaction surface.

The Asp 30 - Arg 36 pair of conserved residues that have been postulated to mimic acetylcholine (26-28) are also located on the postulated binding surface and are oriented towards each other in Bungarotoxin and not extended into solvent as found in the other toxin structures. The

distance between a carboxyl oxygen on the Asp and the partially positively charged ϵ-carbon in the arginine side chain is about 4.7 Å in bungarotoxin. Although this is less than the value of 5.9 Å found from crystal structures of acetylcholine analogues (29), small side-chain bond rotations could make the distances equivalent; thereby suggesting a role for these residues in directing the toxin to the acetylcholine binding site on the receptor.

Other useful information concerning the location of the binding surface comes from immunological studies (30). None of the antibodies binding sites were found to be located on the postulated interaction surface. This could be due to the lack of antigenic determinants on this surface or more interestingly it could result from raising antibodies to receptor-bound toxin in which case the contact surface would be inaccessible. If the latter explanation were true, this finding would provide further support for the hypothesized binding surface. These studies also point to significant differences between the long and short neurotoxins as there is immunological cross-reactivity only within, and not between, the toxin classes.

The structure of α-Bgt has very little conventional intra-molecular secondary structure, -perhaps only 6 β-hydrogen bonds, compared with $\sim$ 75% β in erabutoxin, < 40% β structure in α-cobratoxin. This explains several unusual chemical properties of the toxins, -such as their extra-ordinary stability: cobrotoxin retains full activity in 8 M urea (10) while Naje haje toxin 1 retains full activity after 100 minutes in anhydrous formic acid or 1 M HCl (11). Yet all three toxin structures are relatively well defined in density maps. Laser Raman and optical rotatory dispersion

spectra show loss of the β structure on reduction of the S-S bridges in cobrotoxin (31) and erabutoxin (32). The stability could be a consequence of the variability inherent in these structures since weak crystal packing forces are sufficient to produce the differences in tertiary folding found for all three structures. Circular dichrosim and NMR studies also provide evidence for a floppy, dynamic structure existing in solution (33).

The picture that emerges is that the open "hand" shaped molecule has one binding surface containing both hydrophobic and charged contact points. This 20 x 30 Å area includes the sensitive groups (Figures 4b,c) and may "refold" around the receptor binding site, involving one entire side of the molecule. The on-rates for long toxins are extremely slow, $t_{\frac{1}{2}} \sim 3$ minutes (34), which may reflect extensive refolding, and association (but not dissociation) decreases rapidly below 11°C (35) in agreement with this idea.

Thus, the toxins have a binding surface, as Low (26) suggests, (rather than a binding site), which could function to "lock" the target site so preventing conformational change of the receptor. They do not precisely mimic acetylcholine since they do not open the ion channel: they are "curarimimetic". The actual refolding necessary for receptor complexation is different from each toxin crystal structure observed so far.

Chemical modification experiments (work in progress) on toxin-receptor complexes should provide further information on which toxin residues and which acetylcholine receptor subunits participate in the toxin-receptor interaction.

REFERENCES:

1. Lee, C.Y. (1972) Ann. Rev. Pharmacol. 12, 265-286.

2. Changeux, J.-P., Kasai, M. and Lee, C.Y. (1970) PNAS 67, 1241-1247.

3. Raftery, M.A., Schmidt, J. and Clark, D.G. (1972) Arc. Biochem. Biophys. 152, 882-886.

4. Cohen, J.B. (1978) in Molecular Specialization and Symmetry in Membranes, (Solomon, A.K., ed) Harvard University Press, Cambridge, Mass.

5. Chang, C.C. and Lee, C.Y. (1963) Arch. Int. Pharmacodyn. 144, 241-257.

6. Miledi, R., Mollinoff, P., and Potter, L.T. (1971) Nature New Biology 229, 554-557.

7. Clark, D.G., Macmurchie, D.D., Elliott, E., Wolcott, R.G., Landel, A.M. and Raftery, M.A. (1972) Biochemistry 11, 1663-1668.

8. Yang, C.C. (1965) J. Biol. Chem. 240, 1616-1618.

9. Tu, A.T., Hong, B. and Solie, T.N. (1971) Biochemistry 10, 1295-1304.

10. Yang, C.C. (1967) Biochim. Biophys. Acta 133, 346-355.

11. Chicheportiche, R., Rochet, C., Sampieri, F. and Lazdunski, M. (1972) Biochemistry 11, 1681-1691.

12. Strydom, D.J. (1979) in Snake Venoms, Handbook of Experimental Pharmacology, Vol. 52, (Lee, C.-Y., ed) Springer-Verlag, New York.

13. Walkinshaw, M.D., Saenger, W., Maelicke, A. (1980) PNAS 77, 2400-2404.

14. Walkinshaw, M.D., Saenger, W. and Maelicke, A. (1980) -in press.

15. Tsernoglou, D. and Petsko, G.A. (1976) FEBS Letts. 68, 1-4.

16. Low, B.W., Preston, H.S., Sato, A., Rosen, L.S., Searl, J.E., Rudho, A.D. and Richardson, J.S. (1976) PNAS 73, 2991-2994.

17. Salemme, F.R. (1972) Arch. Biochem. Biophys. 151, 533-539.

18. Stroud, R.M., Kay, L.M., and Dickerson, R.E. (1974) J. Mol. Biol. 83, 185-208.

19. Krieger, M. and Stroud, R.M. (1976) Acta Crysta A32, 653-656.

20. Crowther, R.A. (1978) in The Molecular Replacement Method, (Rossmann, M.G., ed) International Science Review Series, Vol. 13, pp. 174-178 Gordon & Breach, New York.

21. Lattman, E.E. and Love, W.F. (1970) Acta Crysta B26, 1854-1857.

22. Bode, W., Fehlhammer, H. and Huber, R. (1976) J.M.B. 106, 325-335.

23. Agard, D.A. and Stroud, R.M. (1980) -submitted to J. Mol. Biol.

24. Chambers, J.L., Stroud, R.M. (1977) Acta Cryst B33, 1824-1837.

25. Chambers, J.L. and Stroud, R.M. (1979) Acta Cryst. B35, 1861-1874.

26. Low, B.W. (1979) in Snake Venoms, Handbook of Experimental Pharmacology, Vol. 52, (Lee, C.-Y., ed), Springer-Verlag, New York, pp. 213-257.

27. Tsernoglou, D., Petsko, G.A., Hudson, R.A. (1978) Molecular Pharmacology 14, 710-716.

28. Karlsson, E. (1979) in Snake Venoms, Handbook of Experimental Pharmacology , Vol. 52 (Lee, C.-Y., ed) Springer-Verlag, New York, pp. 159-212.

29. Beers, W.H. and Reich, E. (1970) Nature 228, 917-922.

30. Boquet, P., Poilleux, G., Dumarey, C., Izard, Y. and Ronsseray, A.M. (1973) Toxicon 11, 333-340.

31. Yang, C.C., Chang, C.C., Hayashi, K., Suzuki, T., Ideka, K. and Hamaguchi, K. (1968) Biochim Biophys Acta (Amsterdam) 168, 373-376.

32. Harada, I., Takamatsu, T., Shimanouchi, T., Miyazawa, T. and Tamiya, N. (1976) J. Phys. Chem. 80, 1153-1156.

33. Lauterwein, J., Lazdunski, M. and Wuthrich, H. (1978) Eur. J. Biochem. 92, 361-371.

34. Chicheportiche, R., Vincent, J.-P., Kopeyan, C., Schweitz, H. and Lazdunski, M. (1975) Biochemistry 14, 2081-2091.

35. Lester, M. (1971) Dissertation, Rockefeller University, New York.

FIGURE LEGENDS:

Figure 1. An $h\phi\ell$ precession diffraction pattern from a large cell α-Bungarotoxin crystal. Note that the ℓ_{odd} rows are weak.

Figure 2. A representative region of the final F_o,ϕ_c 3.5 Å density map showing residues 68-70. The crystallographic residues for the refined model is 21% at 3.5 Å.

Figure 3. A stereo plot of the entire α-Bungarotoxin molecule. The face of the molecule presented (especially in the region of the long central loop) represents the proposed binding surface.

Figure 4. Comparison of the structures of α-Bungarotoxin and erabutoxin b (15). The α-carbon diagram of erabutoxin b showing the highly conserved residues try 25, lys 27, gln 28, trp 29, asp 31, arg 33, glu 38 and lys 47 (b). The equivalent residues (tyr 24, lys 26, met 27, trp 28, asp 30, arg 36, glu 41 and lys 51) in Bungarotoxin are shown in c. The tryptophan and methionine residues are in significantly different positions in the two structures.

FIGURE I

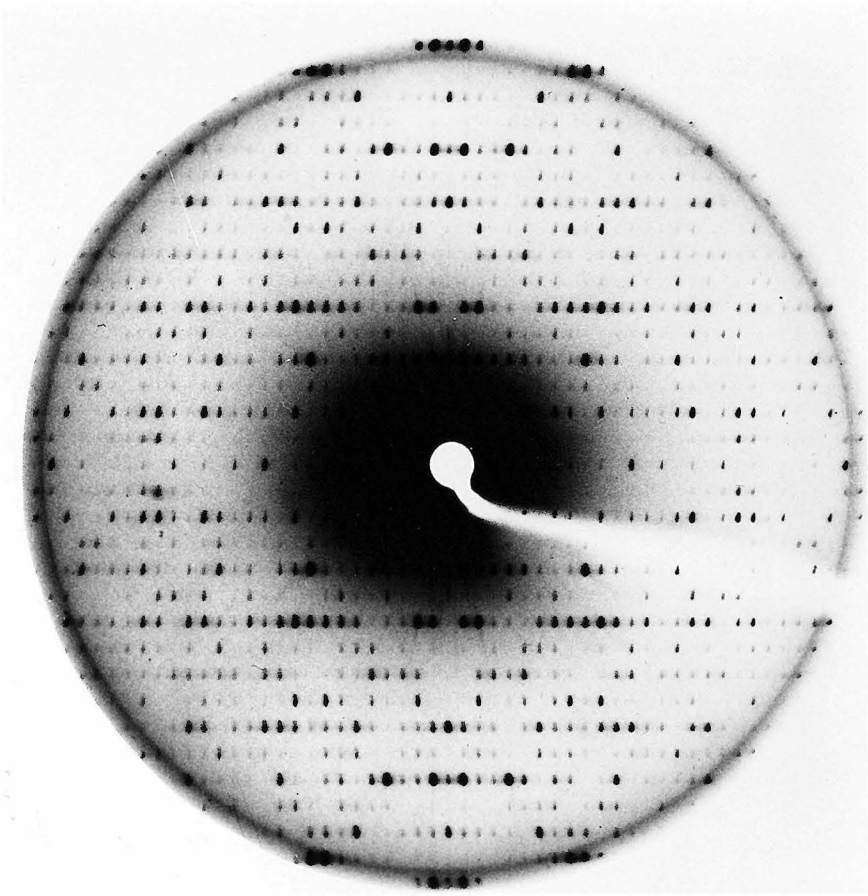

FIGURE 2

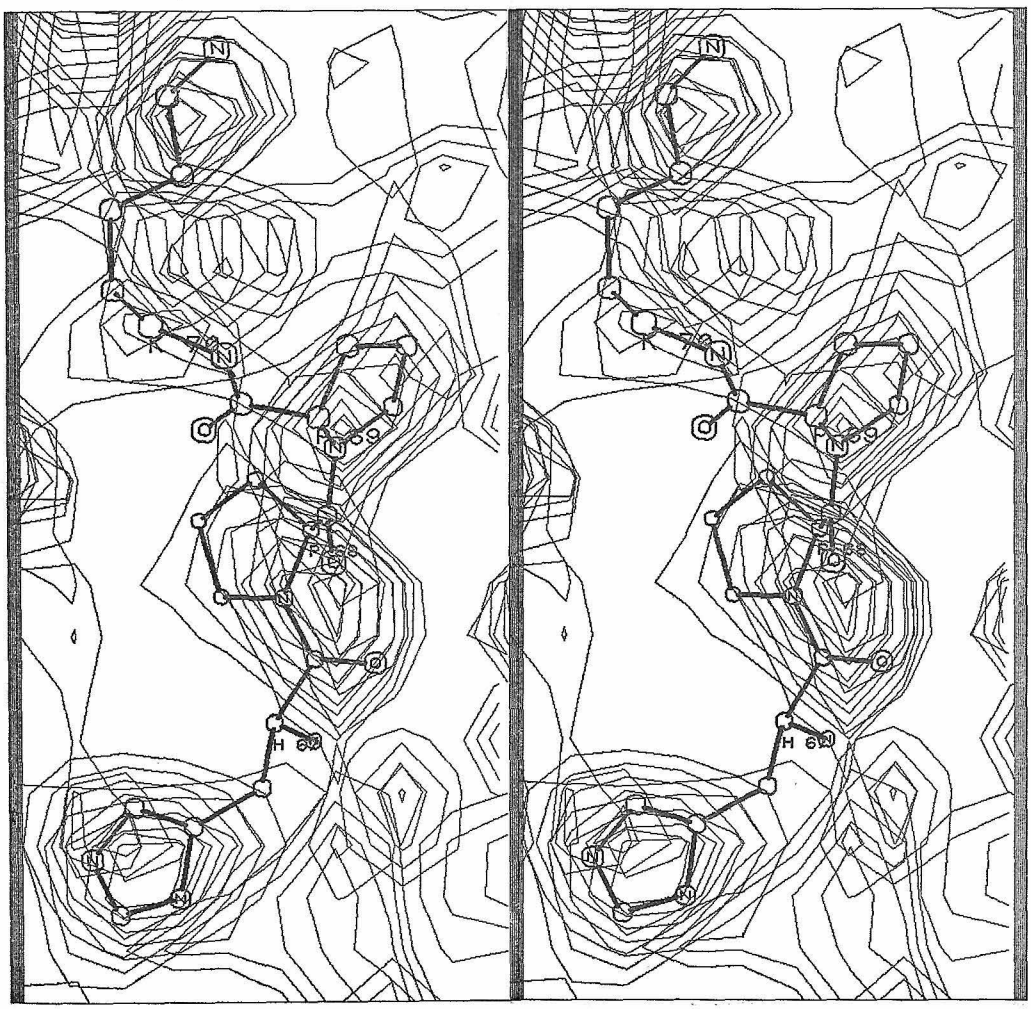

FIGURE 3

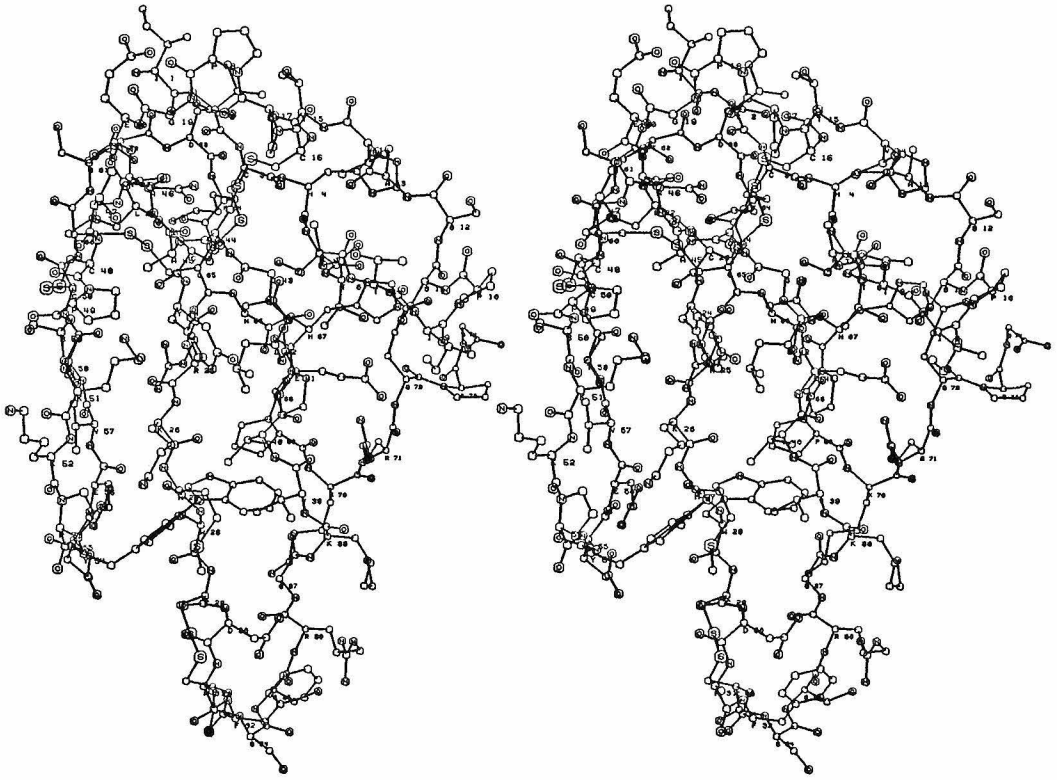

FIGURE 4a

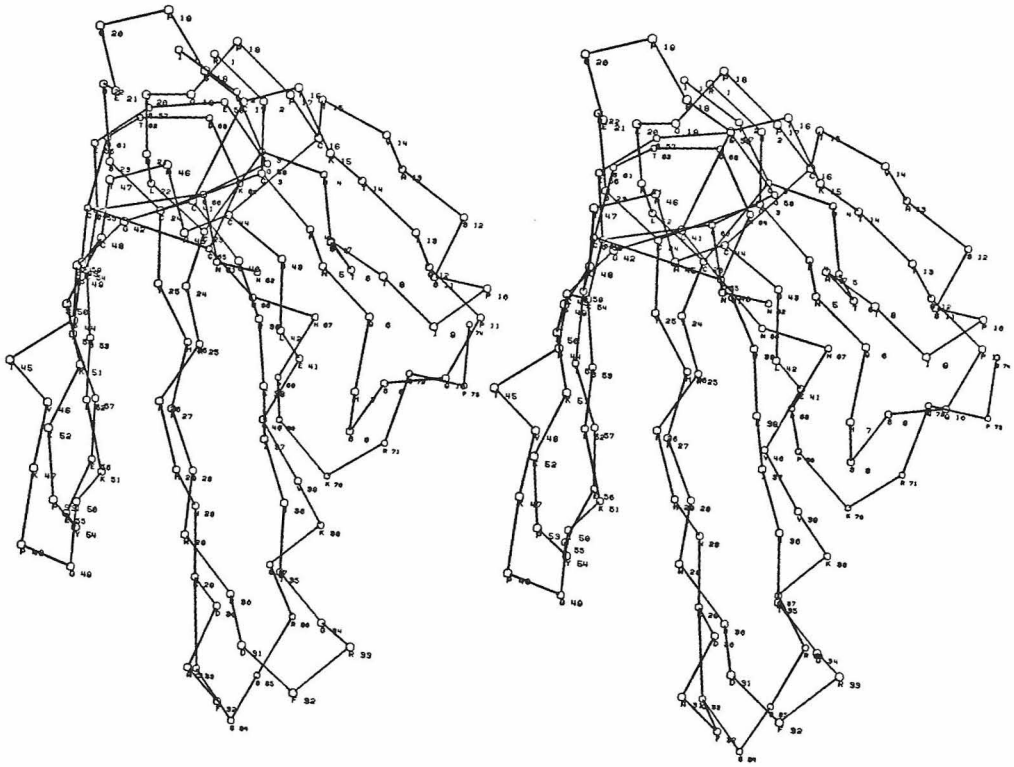

FIGURE 4b

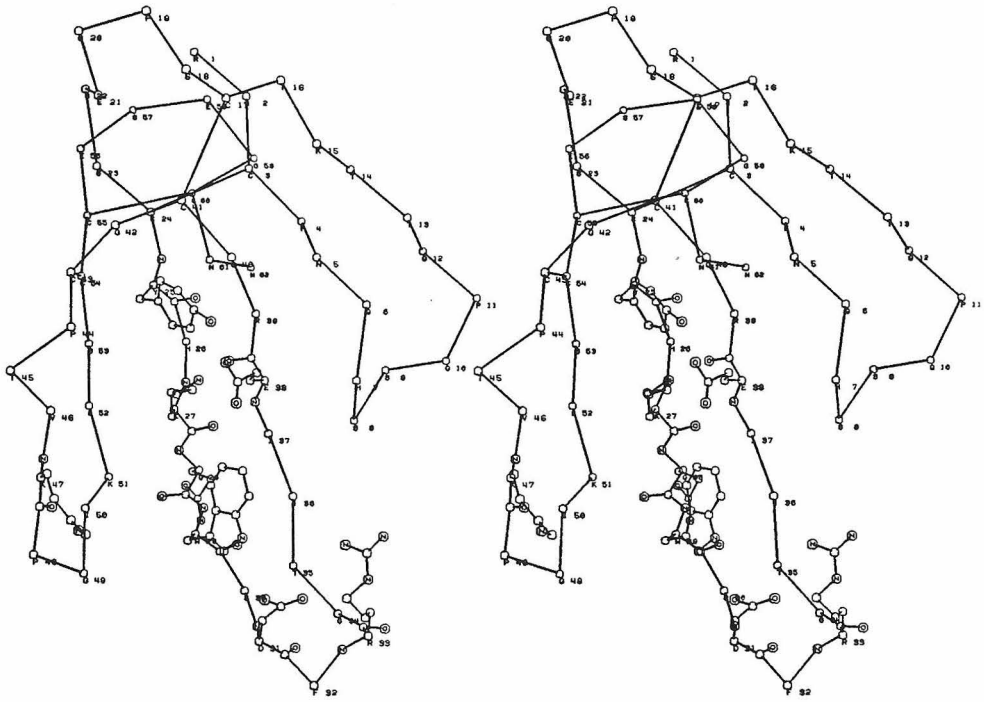

FIGURE 4c

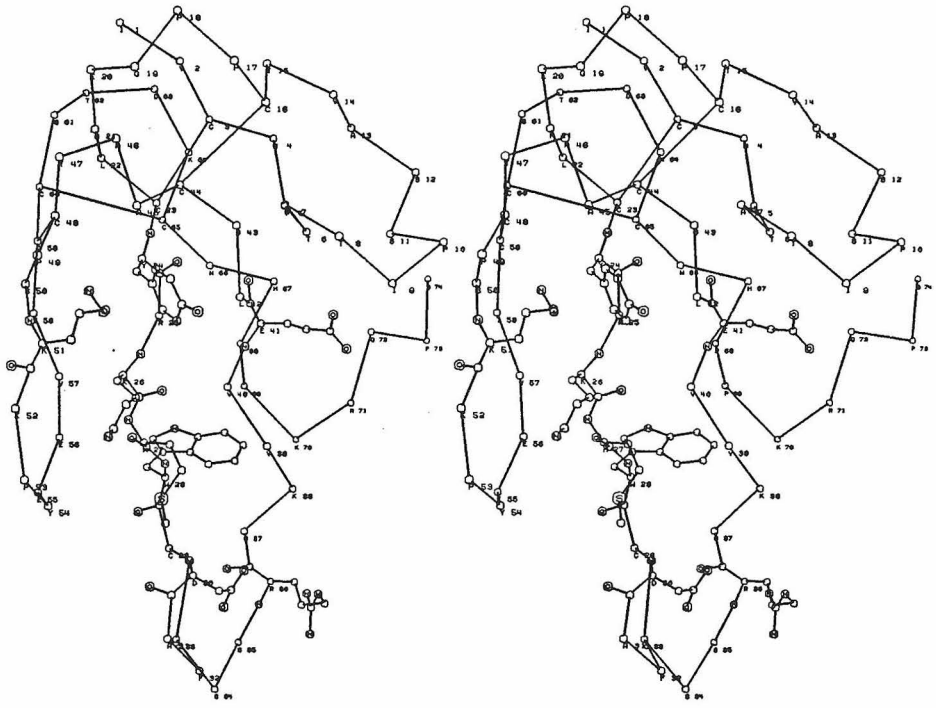

APPENDIX III

Linking Regions Between Helices in Bacteriorhodopsin Revealed

LINKING REGIONS BETWEEN HELICES IN BACTERIORHODOPSIN REVEALED

David A. Agard & Robert M. Stroud

Department of Biochemistry & Biophysics
University of California
San Francisco, CA 94143
U.S.A.

Key words: Purple membrane/electron microscopy/
limited angle/three-dimensional structure

Communicated by: _____ _____
date

ABSTRACT:

Three-dimensional electron microscopic structural analysis requires the combination of many different tilted views of the same specimen. The inability to tilt the sample to angles greater than 60° on most instruments, or without severe distortion due to different focal distances across the specimen implies that the observable range of electron diffraction data are limited to this range of angles. Thus, it is not generally possible to observe the diffraction maxima which lie within a conical region of reciprocal space around the direction perpendicular to the electron microscope grid. The absence of data in this region leads to a predictable distortion in the object, and makes the resolution essentially twice as bad in the direction perpendicular to the grid as it is for the in-plane image. Constrained density map modification and refinement methods can significantly reduce these effects. A method has been developed, tested on a model case, and applied to the electron microscopic structure determination of bacteriorhodopsin in order to visualize the location of linking regions between α-helices.

Density in the refined maps indicates the possible location of at least five of the extra-helical segments of the polypeptide. Models for the topology of linkage between regions of the model suggest a small set of possible models for bacteriorhodopsin topology.

Electron microscopic structural analysis of Bacteriorhodopsin (1, 2) showed that the molecule consists of 7 α-helices each spanning the lipid bilayer. Owing to the distortion introduced by the missing conical region of reciprocal space data, no density was visible for the polypeptide segments linking the α-helices. Following processing, four of the six linking regions

as well as the N-terminus were clearly visible. The total number of possible ways of interconnecting the α-helices was reduced from 7! (5040) to 3 most consistent possibilities.

INTRODUCTION:

The analysis of glucose sustained two-dimensional crystals of catalase and of bacteriorhodopsin by Unwin and Henderson (1), Henderson and Unwin (2), and the similar analyses of frozen hydrated specimens by Glaeser and his colleagues (3-5) have secured the role of electron microscopy for moderate resolution structural studies of biological specimens, and especially membranes where two-dimensional ordering is apparent.

Data collection for three-dimensional electron microscope image reconstruction requires that many different tilted two-dimensional projections of the same material be combined. The effects of limited tilt angle on the final reconstructed image are most easily described with respect to the three-dimensional Fourier transform $F(\underline{s})$ of the three-dimensional object $\rho(\underline{r})$(figure 1). Any given projection of the object defines a plane of the Fourier transform $F(\underline{s}')$ perpendicular to the viewing direction $\underline{s}_o$ (i.e., for $\underline{s}' \cdot \underline{s}_o = 0$), and passing through the origin $|\underline{s}| = 0$. The final reconstructed image is the inverse Fourier transform of $F(\underline{s})$. In practice, it is not generally possible to collect electron microscope data when the specimen is tilted to angles greater than about 60° from the horizontal. As a result, no diffraction data can be observed within a conical region of the reciprocal space transform $F(\underline{s})$ about the axis normal to the specimen plane. The angular restriction arises from both instrumental limitations and the large changes in focus occurring across a sample tilted to such steep angles (∿8700 Å focal change for a 1 μ long sample at 60° tilt angle).

The absence of data within this conical region introduces severe distortions into the resultant structure. Strictly, the observable diffraction

$F_o(\underline{s})$ is described in terms of the entire region of the transform space, by multiplying the entire molecular transform $F(\underline{s})$ by the observable volume $G(\underline{s})$:

$$F_o(\underline{s}) = F(\underline{s}) \cdot G(\underline{s})$$

where $G(\underline{s})$ corresponds to a sphere of radius s_{max} (corresponding to the highest observed resolution) minus a pair of conical regions of semi-angle 30° whose apices pass through $|\underline{s}| = 0$, and whose axes are perpendicular to the electron microscope grid (ℓ in figure 1a, 1b).

This product in diffraction space implies that each atom to be imaged within the structure is convoluted with the Fourier transform of $G(\underline{s})$ schematised in Figure 1c, as $\rho^*(\underline{r})$. Each atom is "blurred out" in the density map to an approximately prolate ellipsoidal shape with a major axis $\sim$1.8 x the minor axis. The resolution is consequently almost twice as bad in the "Z" direction perpendicular to the specimen. As a result, segments of chain running parallel to the Z axis tend to be elongated and smoothed by the large overlap of ellipsoidal functions $\rho^*(\underline{r})$, whereas chains parallel to the plane of the specimen can, in some cases, be obliterated. Overlap in the plane is much less and density is consequently much lower. The observation for bacteriorhodopsin (1, 2) is that there are 7 rods of density (thought to correspond to α-helices) running almost perpendicular to the membrane (approximately parallel to the Z direction). However, neither the connections between the rods nor the chromophore, whose major axis is known to lie about 23° away from the membrane plane (6), could be observed at that stage. This is precisely the type of distortion expected to arise from the

"missing cone" of information. As the mathematical nature of the distortion is known, its effects can be greatly reduced. We have applied a constrained iterative, Fourier extrapolative refinement procedure for removing this known type of distortion. The method was applied to the Bacteriorhodopsin data of Henderson and Unwin (2) with the result that 4/6 regions of density between possible ends of the helices were revealed.

The treatment presented here is directed most specifically to the electron imaging problem, though the solution is applicable in identical form to the limited angle reconstruction problem and to computer aided tomography. In a more general sense, it can be usefully employed for resolution extension, or completion of any incomplete imaging data set.

THEORY OF THE METHOD:

The approach taken is to use the observed data, and several global constraints which apply to the object, to extrapolate into the unobservable region. An iterative procedure is used to "fill in" the missing data so as to generate a structure that is consistent with the constraints, and that correctly predicts the observed $F_o(\underline{s})$. The iterative approach schematised in figure 2 was chosen over an analytic method (based on a Taylor series expansion, for example) because of the ease of incorporating constraints in either the Fourier-space or real-space domains.

All such extrapolation techniques are based in some way on the fact that each point in the Fourier transform $F(\underline{s})$ of an object derives from each point in the entire object according to:

$$F(\underline{s}) = \frac{1}{V} \int \rho(\underline{r}) e^{2\pi i \underline{r}\cdot\underline{s}} \, dV_{\underline{r}} \qquad (1)$$

Thus, there is information in the observed data $F(\underline{s})$ concerning the nature of the unobserved data, since each point in the unobserved portion of $F(\underline{s})$ derives from the same $\rho(\underline{r})$ (see for example, reference 7).

Any physically realistic object must occupy a finite volume. In the case of a membrane-bound protein in a two-dimensional lattice, the thickness of the membrane is limited, as is also the volume U in the unit cell occupied by the ordered components, i.e., single protein molecules. These constraints imply a powerful joint set of relationships among all the $F(\underline{s})$, which provides the basis for the method. This single boundary condition is very powerful and in theory, allows a unique extension of the diffraction data into unobserved regions (8, 9) since it implies that $F(\underline{s})$ is a continuous analytic function. This same kind of constraint is also sufficient to allow de novo calculation of phases for continuous diffraction data $|F(\underline{s})|$ as, for example, in our method for the determination of electron density profiles of biological membranes (10). In that case, the relevant $|F(\underline{s})|$ are observable, the phases are not. In the present application both amplitudes and phases are known for a subset $F_o(\underline{s})$.

The density map computed from the observed data alone

$$\rho_o(\underline{r}) = \int_{G(\underline{s})} F_o(\underline{s}) e^{-2\pi i \underline{r}\cdot\underline{s}} \, ds$$

is necessarily inconsistent with the known constraints of volume, thickness, etc., which apply to the real object. The unobserved portion of $F(\underline{s})$ must, therefore, account for the discrepancy between $\rho(\underline{r})$ and the known constraints. At the same time, each point within the constrained volume U computed by trans-

formation of $F(\underline{s})$ is affected by each new value of $F(\underline{s})$. There is thus a means for iterative refinement of the unknown $F(\underline{s})$, in a way which improves the density function both outside (to a constant level), and inside the constrained molecular volume. Inherent in the process is some knowledge of the molecular volume U which includes the entire non-zero part of $\rho(\underline{r})$.

Sensitivity to data errors can be substantially reduced by incorporation of additional knowledge or constraints, such as non-negativity of scattering density (a further constraint incorporated in the refinement scheme we used). Using the positivity constraint, additional error components in the extrapolated region produced by errors in the data are greatly minimized and generally lower than the errors in the observed region, making the method remarkably insensitive to data errors. These two constraints are also sufficient to allow for phase refinement-phase extension (where amplitudes are available to higher resolution than are the phases). Neither constraint alone will suffice (Agard & Stroud, unpublished).

Studies to demonstrate the efficacy of the refinement procedure were carried out first for model structures in 2 and 3 dimensions using restricted sets of calculated data and data modified by inclusion of random error in $F_o(\underline{s})$, and then applied to the experimental data for Bacteriorhodopsin. In all cases, the distortions due to the angular limitations of the data set were dramatically reduced.

TEST OF THE METHOD:

The test model was a sequence of three connected α-helices extracted from the myoglobin structure (residues 70-149, Brookhaven data bank) and

slightly modified for clarity using the Protein Interactive Graphics System developed by Dr. R. Langridge. The model was used to compute an initial set of $F(\underline{s})$ which was subsequently modified to resemble an observed set $F_o(\underline{s})$ by removal of "unobservable" data, inclusion of error, resolution cut off, etc.. For the two-dimensional studies only the main chain and β-carbon atoms were used to simplify the structure as viewed in projection. All atoms were used in the three-dimensional studies. The models were placed in either a 64 x 64 Å two-dimensional unit cell, or in a 64 x 64 x 32 Å three-dimensional unit cell. Structure factors were calculated for all reflections to either 3.5 Å (2-dimensional) or 7 Å (3-dimensional) using a temperature factor of 15 for each atom.

In order to model the angular limitations inherent in a 3-dimensional EM data set, data were omitted from a ± 30° region of $F(\underline{s})$ about what was designated the X axis in Figure 3. Under those conditions, fully 33% of the 2-dimensional data and 14% of the 3-dimensional data were "unobserved" in the starting $F_o(\underline{s})$ data set. Rough boundaries used to delineate the volume (or area) U occupied by protein were drawn so that approximately 50% of each unit cell was considered solvent. This volume approximates values found in many protein crystals and in the purple membrane unit cell. The constrained volume used is depicted in Figure 3; the projection onto the X-Y plane was used for the two-dimensional case. All density values outside the depicted

volume in the unit cell were set to 0 during each cycle of refinement. Simultaneously, a lower limit was applied to density values within the molecular boundary. In the projection experiments (3.5 Å) all values below 0 were set to 0. Because of the lower resolution used in the 3-dimensional experiments, (7 Å) and the resultant, more pronounced, series-termination ripples, slightly negative lower boundaries were employed (-50 on a scale where the peak positive value was 1200) which were dropped to -100 during the final stages of refinement.

Application to Bacteriorhodopsin

The set of three-dimensional electron microscopic data recorded by Henderson & Unwin (2) for Bacteriorhodopsin (Br) was kindly provided by R. Henderson. Although the data extend to a resolution of 7 Å in the plane of the membrane, the resolution perpendicular to the plane is only 14 Å (2). Thus, the effects of the unobserved data (53% of total 7 Å data) are more serious than for the missing cone region alone. Refinement was employed not only to extrapolate into the missing cone region but to extend the perpendicular resolution to 10 Å (47% missing). The data were sampled at an interval corresponding to a 100 Å c axis cell length.

By comparison with the model cases, the task of properly defining real-space constraints was more complex. It was necessary to use smoothed boundary functions (Figure 4), otherwise serious ripples appeared in the density functions and the procedure failed to converge. The F(000) term corresponding to the absolute density level was chosen from the extrapolated value of a Wilson plot (11) at $\underline{s} = 0$. To minimize the deleterious effects of inaccuracies

in the density levels outside the boundary function (outside of the membrane, and outside of the molecule within the bilayer) the very low angle data (>20 Å resolution) was omitted from the starting data set. This serves to decouple the density asignments in different regions outside of the boundary. Thus the constraint on density levels outside of a boundary become local instead of global in nature. Such an approach is a common feature of many two-dimensional image enhancement algorithms.

The refinement of Bacteriorhodopsin data was carried out in three stages starting with both in-plane and perpendicular volume constraints as well as a strong non-negativity constraint. After 10 cycles, the non-negativity constraint was removed, and 5 more cycles were performed. Finally, the in-plane volume constraint was removed and another 5 cycles run.

RESULTS:

Two-dimensional Model Studies

The distortions introduced into the structure as a result of placing ± 60° angular restriction on the observed 3.5 Å resolution 2-dimensional data set are shown in Figure 5a,b. Comparison with the undistorted structure in Figure 5a shows how regions of chain or helix running perpendicular to the X (horizontal) axis are almost totally obliterated. After 30 cycles of constrained refinement starting from the "observed" data shown in Figure 5b and using the boundary area shown in Figure 3, much of the original structure is restored as shown in Figure 5c. Although the restoration is certainly not perfect, the improvement is dramatic and sufficiently accurate for the polypeptide chain to be unambiguously traced.

The restoration of the missing sector of Fourier data is also shown in figure 5 by the half-tone representation of the diffraction amplitudes $|F(\underline{s})|$. The residual:

$$R = \frac{\sum_{\underline{s}} ||F_T(\underline{s})| - |F_c(\underline{s})||}{\sum_{\underline{s}} |F_T(\underline{s})|} \qquad (2)$$

provides a quantitative aasay of the mean discrepancy between the original - or true value of $F(\underline{s})$, ($F_T(\underline{s})$, Figure 5a) and the calculated values $F_c(\underline{s})$ (figure 5c). The residual for the "true" versus calculated data in the missing sector is 45.3% while the rms phase error:

$$\phi_{rms} = (\sum_{\underline{s}} (\phi_T(\underline{s}) - \phi_c(\underline{s}))^2)^{\frac{1}{2}} \qquad (3)$$

is 70°. This corresponds to a mean figure of merit $< \cos(\phi_T(\underline{s}) - \phi_c(\underline{s}))>$ of 0.52 (12). The residual calculated within the observed region is 4.7%. Although the errors for the extended region $F_c(\underline{s})$ may seem large, it is necessary to keep in mind that fully 1/3 of the total data is being predicted by the refinement. Even so, these errors are no worse than occur in the early stages of any macromolecular x-ray structure determination. The non-zero residual in the observed region results from errors introduced by the constraints: at any finite resolution there are series termination effects that imply non-positivity density values in the resolution limited map, using correct $F_T(\underline{s})$ values for $\underline{s}<$ some s_{max}. The chosen constraints do not allow for non-negative values in the refined structure. In this sense, the positivity constraint while physically correct, is not procedurally correct, however

the errors introduced are negligible, and the power of the constraint is considerable. Too much is gained, especially in the early stages of refinement, to relax this constraint and little is to be gained even in the end by altering the lower boundary.

Three-dimensional Experiments

Severe distortions are also introduced into a 3-dimensional structure when a conical region of half-angle 30° is removed from the total (true) 7 Å data set (figure 6a,b) where proper chain connectivity is lost for those segments running perpendicular to the axis of the missing conical region. The resultant distortion is less severe than in the 2-dimensional case owing to the reduced percentage of missing data (14% vs. 33%). 25 cycles of refinement led to nearly perfect restoration (figure 6c); chain connectivity is restored and the elongated regions have returned to their undistorted sizes and shapes. At convergence the residual for the predicted amplitudes was 15.3%; the rms phase error was 28.2% (a mean figure of merit of 0.92). As in the 2-dimensional case, the non-zero residual for observed data (R = 5.5%) reflects inaccuracies in the assumptions and gives an empirical estimate of the error introduced by these assumptions. These errors are slightly more severe at 7 Å than at 3.5 Å because of the larger series termination ripples. The use of a lower cut-off which acommodates series termination ripples in early stages of refinement slowed convergence; therefore the low density cut-off was modified only in the final stages.

The Effects of Data Errors

The effects of errors in the data were investigated by introducing into the "observed" data set random errors. Errors introduced into the data set

are described by a residual between modified $|F_o'(\underline{s})|$ and unmodified $|F_o(\underline{s})| = |F_T(\underline{s})|$ amplitudes (equation 2), and by an rms phase difference $\Delta\phi_{rms}$ between the two sets (equation 3). In the tests described in Table 1, random errors were introduced either into the amplitudes alone (R = 19.7%, column 2) or into both amplitudes and phases (R = 17.4%, $\Delta\phi_{rms}$ = 29°, column 3) and a conical region of semi-angle 30° was removed to generate the "observed" data sets $F_o'(\underline{s})$, $F_o''(\underline{s})$.

Ten cycles of refinement gave the results summarized in Table 1 (figure 7), which demonstrate a remarkable degree of immunity to error. When perfect error-free data were used in the observed region, the solution after 10 cycles gave residuals for extrapolated versus true data of 17.9%, ± 25.5°. Introduction of errors into the observed region resulted in residuals only very slightly worse (18.4% ± 28.0°, and 21.7% ± 25.1° for the F_o', F_o'' data sets respectively). Thus, the effective figures of merit are 0.92 - 0.94 for the derived data - even when errors of the order of 20%, ± 30° are present in the observed data set.

There is an obvious tendency for refined data in the observed region to converge toward the observed data, since at each cycle observed amplitudes and phases are reassociated with extrapolated values in the unobserved region. Nevertheless, the errors between the values computed in the final cycle and the true data in the observed region were only slightly worse (10.9% ± 12.0°, 11.2% ± 18.5°) when error-flawed data were used, than when refinement was based on error-free data (7.5% ± 9.0°). Thus, there is a powerful tendency to correct for data errors which are themselves inconsistent with the constraints. This potential for improvement of data errors is not fully used in the method

as presented here since observed values are always given full weight at each cycle. A weighting scheme would allow for some refinement of observed amplitudes and phases. This approach is also of use in refinement of early phases in protein crystallography (13).

For completeness, residuals calculated between refined and observed (i.e., error-flawed rather than true) data in the observed region are listed in Table 1. These residuals rise more rapidly than for the comparison of refined and true data as errors are introduced, again symbolic of the inconsistency between flawed data and a self-consistent result, and the tendency to minimize effects of random error.

Bacteriorhodopsin:

As was found in the model examples, the iterative Fourier refinement technique was able to minimize much of the distortion caused by the absence of observed data. The final residual for predicted data in the observed region was 11.2%. Views of a model built to the reconstructed density map showing connectivity at both the cytoplasmic and extra-cellular surfaces of the membrane are shown in Figure 8. Before processing, the helices rapidly tapered to points near the end and were only about 35 Å in length. After refinement, the helices no longer tapered and extended to both membrane surfaces. Nearly all of the new density appeared between ends of the density rods on the membrane surface. The connectivity information provided by refinement limits the possible number of ways of assigning the amino acid sequence (14, 15) to the structure from 5040 (7 !) to 3 most probable models (figure 9). The helix containing the retinal chromophore (the second or B helix) is in the same location in all three

models; this is the position found by King, et al., (16) in their neutron diffraction studies comparing deuterated and hydrogenated retinal. The helices in the model are labeled as they were by Englemann and co-workers (17) in their discussion of more probable models. Their criteria were based on the density of regions in the density maps, the proximity of charged residues, and the length of supposed linking regions between helices. Their most probable model (Figure 8a) is one of the three models consistent with the arrangement of visible linking regions. Another model (Figure 8b) is number 30 out of their most probable 35, while the third model (Figure 8c) is not among the most probable by the criteria of Englemann et al. (17). The B helix containing the chormophore remains at the same site as in their most probable model, but the arrangement of chains is anti-cyclic to their choice. This model was down-weighted in their scheme both because it did not assign the least dense of the chosen helical sequences to helices A and D, and because of a somewhat less favorable arrangement of charged residues. Since the exact termination of each helix is not known, and the apparent densities in the map may be affected by other factors, the exclusion of this as one of the possible models is not yet fully justified. Overall, the visible linking regions may help to weight the discussion in favor of an even more restricted set of structures.

Work in progress on the localization of several linker-directed heavy metal labels (18) should decide between the three allowable connection schemes. A more detailed interpretation of the Bacteriorhodopsin results, together with the results of chemical labeling will be published elsewhere.

DISCUSSION:

The refinement method presented here and tested on both a model and a real system was designed specifically to remove the distortion produced in electron microscopically determined structures as a result of the limited data set obtainable. The mathematical basis is in a sense derivative from our Fourier model refinement approach to phasing of continuous x-ray scattering from membranes (10, 19). In a more general sense, it is clear that this method is applicable to resolution extension, refinement of phases where intensities are known, or determination of some subset of the phases in the Fourier transform of any structure or image, with different, though some significant gain in each case.

Theoretically, only the volume/thickness restriction is required to extrapolate into the missing region from the observed $F_o(\underline{s})$. Methods such as those proposed by Wolter (8) or Harris (20) that rely strictly on limited spatial extent are extremely sensitive to data errors. The incorporation of the positivity constraint dramatically increases the stability of the algorithm as demonstrated by the remarkable noise immunity. An additional piece of information that could be exploited during refinement would result from incorporating the meridional scattering data obtained from small-angle solution x-ray experiments ($F(\underline{s})$ for $\underline{s}$ parallel to Z). When corrected for the absence of a constant solvent density, absent in electron microscopy, these data most accurately determine the specimen thickness (10), and provide a set of experimental data along the Z axis. This direction is otherwise the most difficult to predict since no values of $F(\underline{s})$ in this direction are obtained from electron microscopy.

It is desirable to have a quantitative relationship which would define the gain available in any given situation. There are, however, a sufficient number of variables (molecular dimensions, unit cell dimensions, resolution of $F_o(\underline{s})$, of $\phi_o(\underline{s})$, errors in $F_o(\underline{s})$, redundancy in the data, etc.) that the analytical treatment is beyond the scope of this communication.

REFERENCES

1. Unwin, N.T. and Henderson, R. (1975) J. Mol. Biol. 94, 425-440.
2. Henderson, R. and Unwin, P.N.T. (1975) Nature 257, 28-32.
3. Hayward, S., Grano, D.A., Glaeser, R.M., Fisher, K.A. (1978) PNAS 75, 4320.
4. Chiu, W. (1978) in Scanning Electron Microscopy, Vol. I, 569-580.
5. Chiu, W. and Hosoda, J. (1978) J. Mol. Biol. 122, 103-107.
6. Bogomolni, R.A., Hwang, S.-B., Tseng, Y.W., King, G.I., and Stoeckenius, W. (1977) Biophys. J. 17, 98
7. Crowther, R.A., DeRosier, D.J., D.J., Klug, A. (1970) Proc. Roy. Soc. A317, 319.
8. Wolter, H. (1961) in Progress in Optics, ed. by E. Wolf, (North-Holland Publishing Co., Amsterdam).
9. Frieden, B.R. (1975) in Topics in Applied Physics, Vol. 6, pp. 177-248.
10. Stroud, R.M. and Agard, D.A. (1979) Biophys. J. 25, 495-512.
11. Wilson, A.J.C. (1942) Nature 150, 152.
12. Blow, D.M. and Crick, F.H.C. (1959) Acta Cryst. 12, 794-802.
13. Agard, D.A. and Stroud, R.M. (1980) -submitted, J. Mol. Biol.
14. Ovchinnikov, Y., Adbulaev, N. Feigira, M., Kislev, P. and Lobanov, N. (1979) FEBS Lett. 100, 219-224.
15. Gerber, B.E., Anderegg, R.J., Herlihy, W.C., Gray, C.P., Biemann, K. and Khorana, M.G. (1979) PNAS 75, 227-231.

16. King, G.I., Mowery, P.C., Stoeckenius, W., Crespi, H.L. and Schoenborn, B.P. (1980) -submitted to Biophys. J.

17. Englemann, D.M., Henderson, R., McLachlan, A.D. and Wallace, B.A. (1980) PNAS 77, 2023-2027.

18. Katre, N., Stoeckenius, W. and Stroud, R.M. (1980) -manuscript in preparation.

19. Ross, M.J., Klymkowsky, M.W., Agard, D.A., Stroud, R.M. (1977) J. Mol. Biol. 116, 635-659.

20. Harris, J.L. (1964) J. Opt. Soc. Am. 54, 931.

FIGURE/TABLE LEGENDS

Figure 1 The limited ability to tilt the object or sample to angles greater than 60° results in a missing conical region of diffraction data - two views of this are shown in a,b. As a result, each point in the structure is convoluted with a function ρ^* which has the symmetry of a prolate ellipsoid of axial ratio $\sim$2 (shown in c).

Figure 2 Schematic diagram of the constrained refinement procedure. Here $F_c(\underline{s})$ and $\phi_c(\underline{s})$ are constrained to equal $F_o(\underline{s})$ and $\phi_o(\underline{s})$ in the observed region.

Figure 3 The region of the 3-dimensional unit cell considered as protein is depicted (shaded), the remainder being featureless solvent. The same boundary (X-Y plane) was used for the 2-dimensional experiments.

Figure 4 The mask functions used for the Bacteriorhodopsin experiments. The in-plane mask is shown contoured in (a) and the transmembrane mask is shown in (b).

Figure 5 The results of the 2-dimensional refinement. Shown are the structures and their Fourier transforms (half-tone images) for (a) the true structure, (b) before refinement indicating the severity of the distortion, and (c) following 30 cycles of constrained Fourier refinement. Note that the missing region lies along the horizontal axis.

Figure 6 Several sections through the 3-dimensional density maps for noise-free data. Panel (a) shows the true structure, (b) before refinement, and (c) following 25 cycles. As in Fig. 5, the axis of the missing cone of data is taken along the horizontal axis.

Figure 7 Same as Fig. 6, but with noise in both the amplitudes (R=17.4%) and the phases (rms phase error = 29°).

Figure 8 Two views of the model of Bacteriorhodopsin built using missing cone corrected data. The cytoplasmic surface is shown at the top of the model. The connector regions that are revealed following processing are indicated by arrows.

Figure 9 The three possible helix-helix connectivity patterns that are consistent with the model shown in Figure 8. Panels (a) and (b) correspond to choices 1 and 30, respectively, from the set of 35 most probable models chosen by Engleman et al., (17). The model in (c) is essentially anti-cyclic to (a) or without the cross-over in (b).

Table 1 Analysis of the sensitivity to data errors.

Shown are the residuals and rms phase errors for restricted data sets with no errors, errors in the amplitudes alone, and errors in both the amplitudes and the phases. The values reported are after 10 cycles of constrained refinement. There is almost no change in the accuracy of the extrapolated data when errors are incorporated into the starting data set. Since the errors themselves are inconsistent with the constraints data in the observed region refines towards error-free values. The remarkable insensitivity to data errors is readily apparent.

TABLE 1

	F_o-No error		F_o'-Errors in F_o only.		F_o"-Errors in F_o, ϕ	
	R%	$\Delta\phi^o$	R%	$\Delta\phi^o$	R%	$\Delta\phi^o$
Errors introduced in observed data	0	0^o	19.7	0^o	17.4	29^o
Unobserved region: Extrapolated versus true data:	17.9	25.5^o	18.4	28.0^o	21.7	25.1^o
Observed region: Refined versus true data:	7.5	9.0^o	10.9	12.0^o	11.2	18.5^o
Refined versus observed data:	7.5	9.0^o	15.9	12.0^o	15.4	23.5^o

FIGURE I

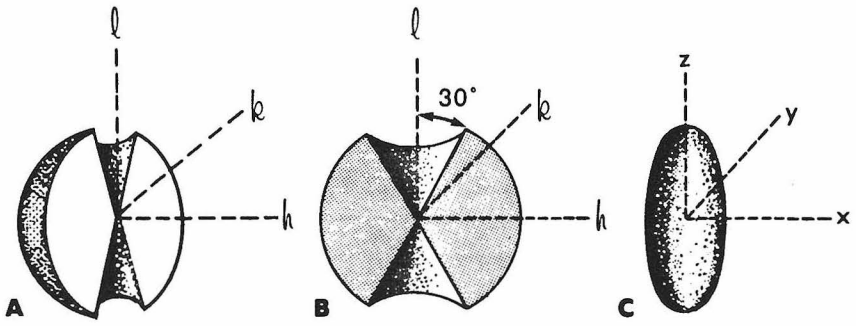

FIGURE 2

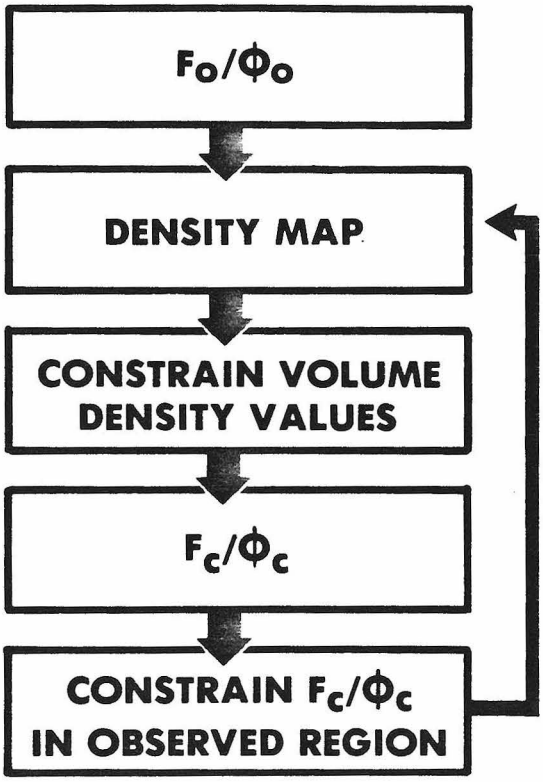
F_o/ϕ_o
DENSITY MAP
CONSTRAIN VOLUME DENSITY VALUES
F_c/ϕ_c
CONSTRAIN F_c/ϕ_c IN OBSERVED REGION

FIGURE 3

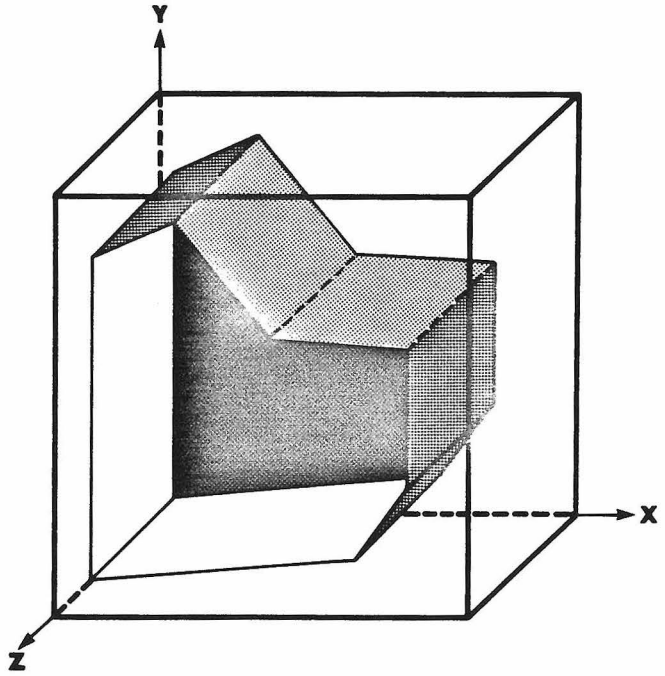

FIGURE 4

A

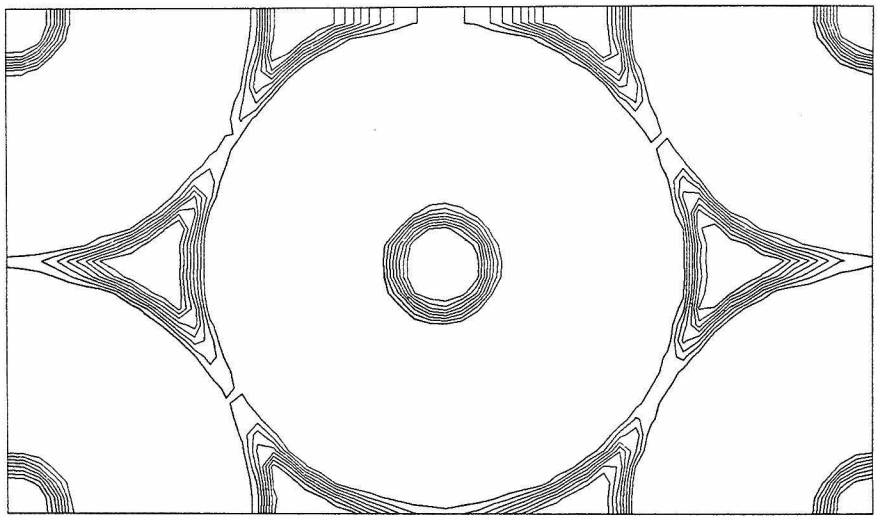

B

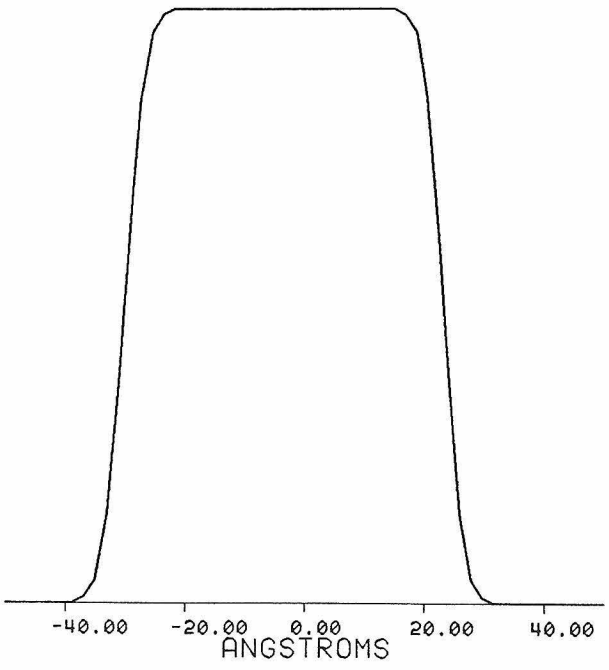

FIGURE 5

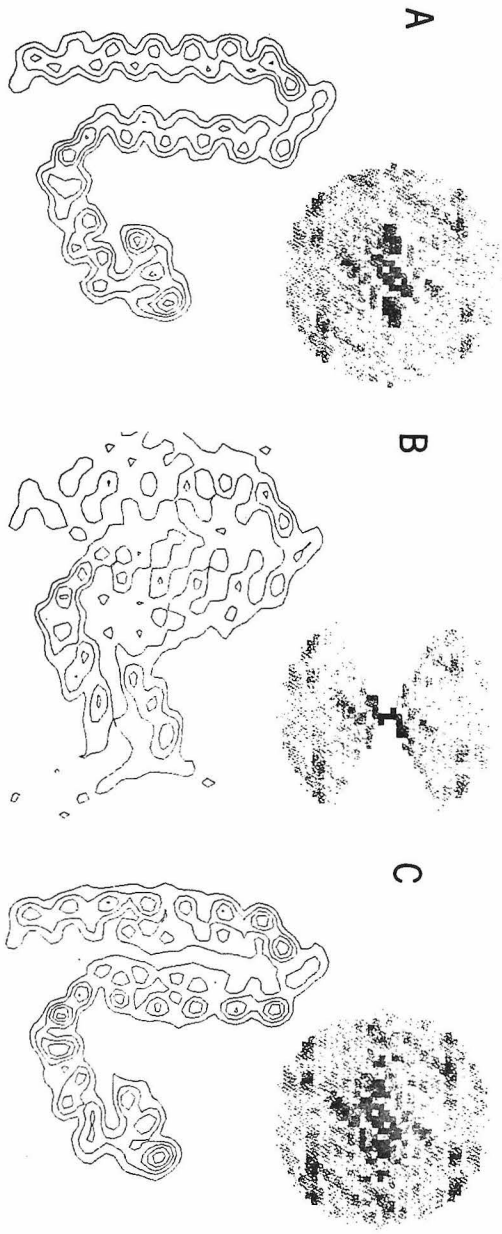

FIGURE 6

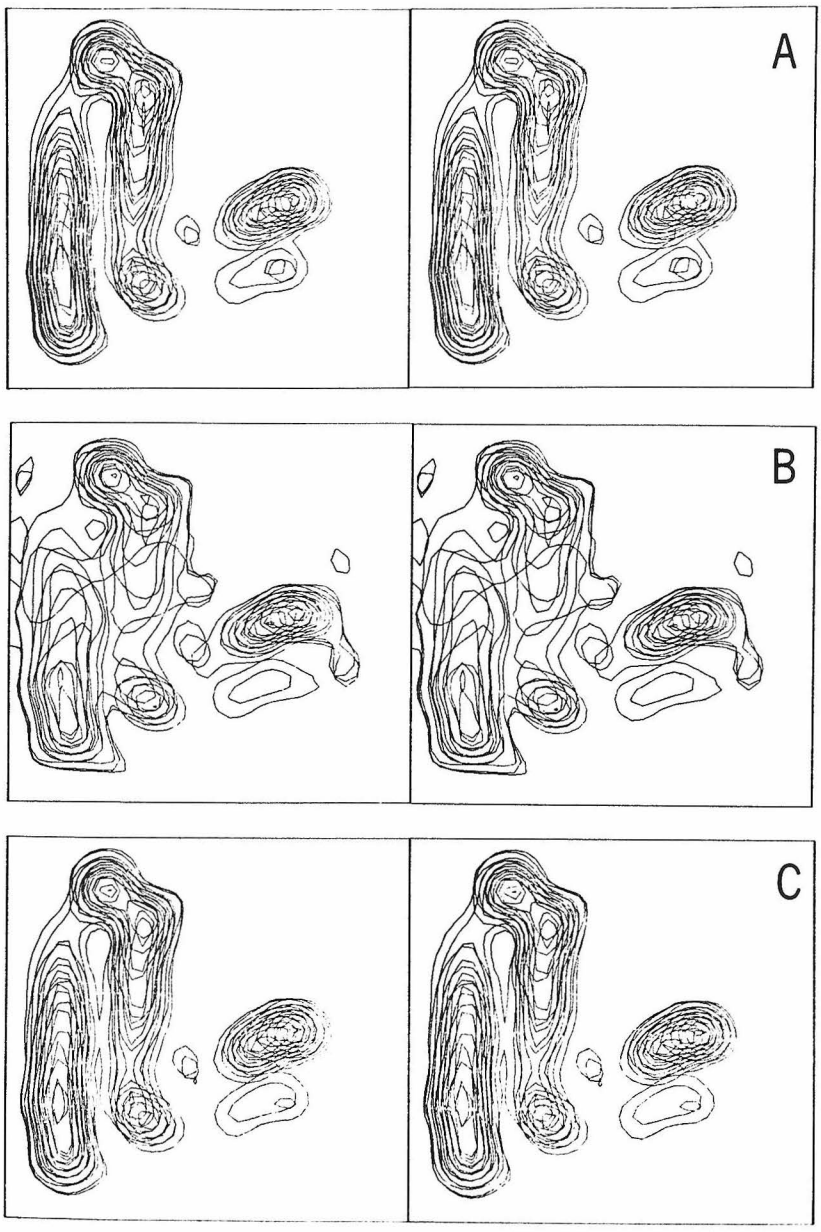

FIGURE 7

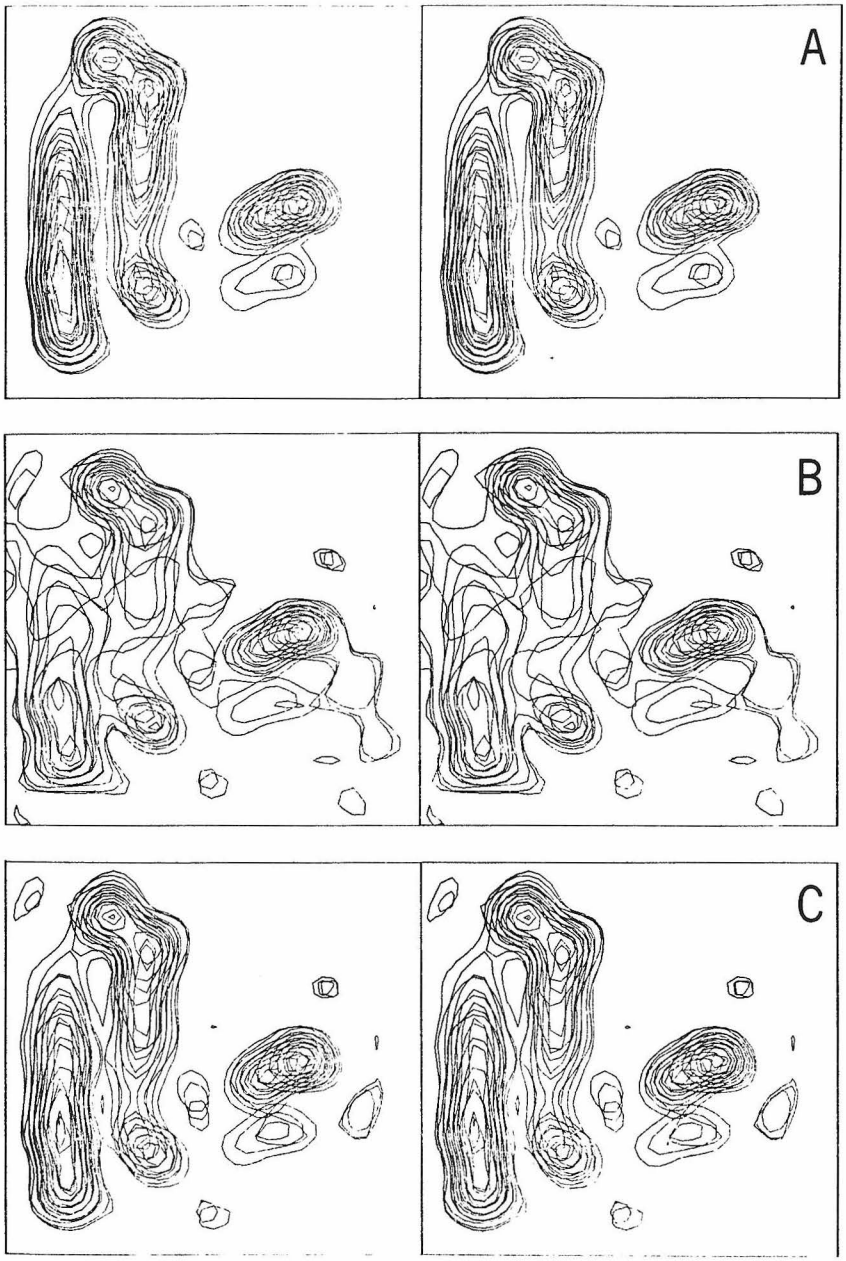

FIGURE 8

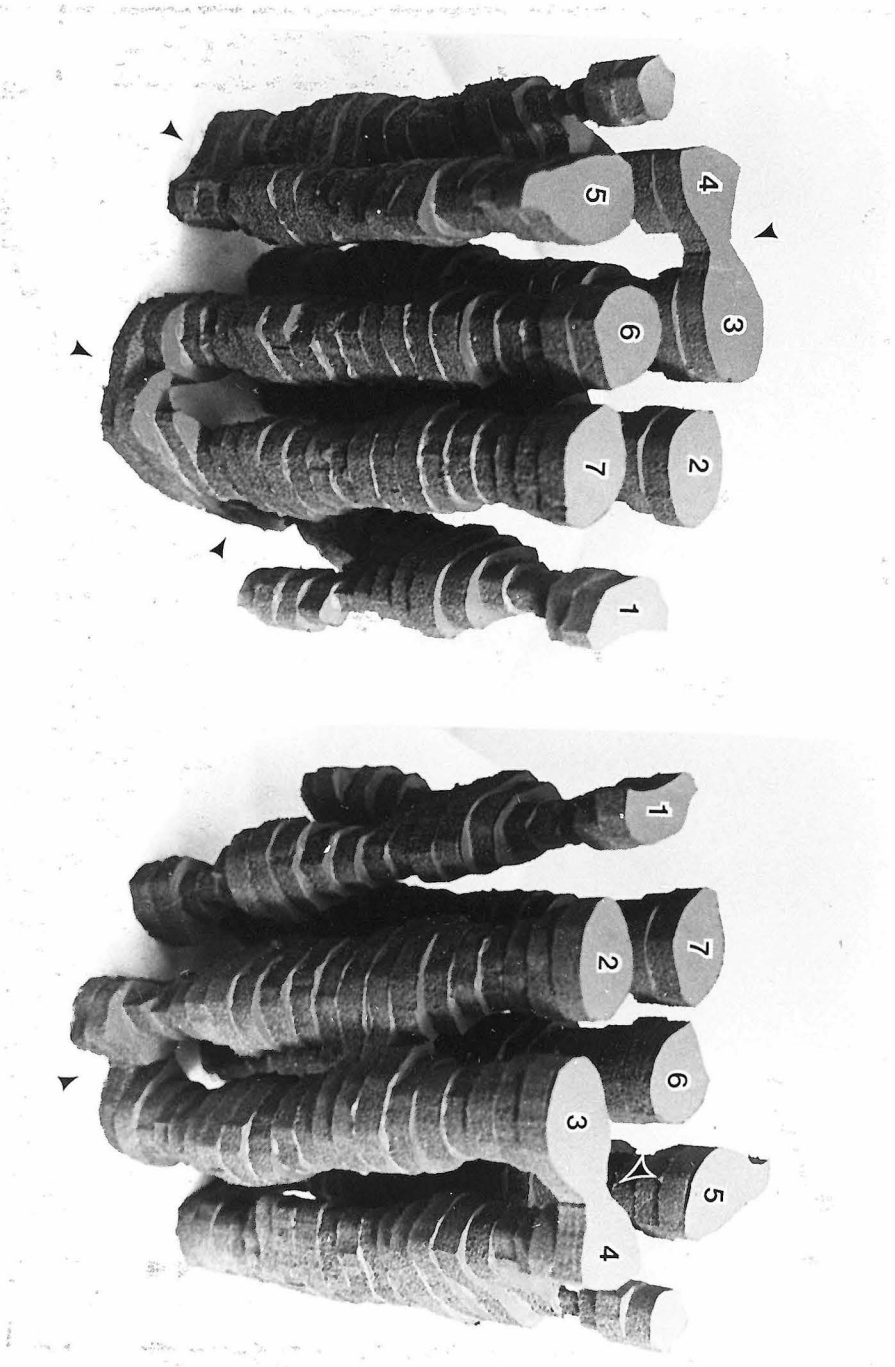

FIGURE 9

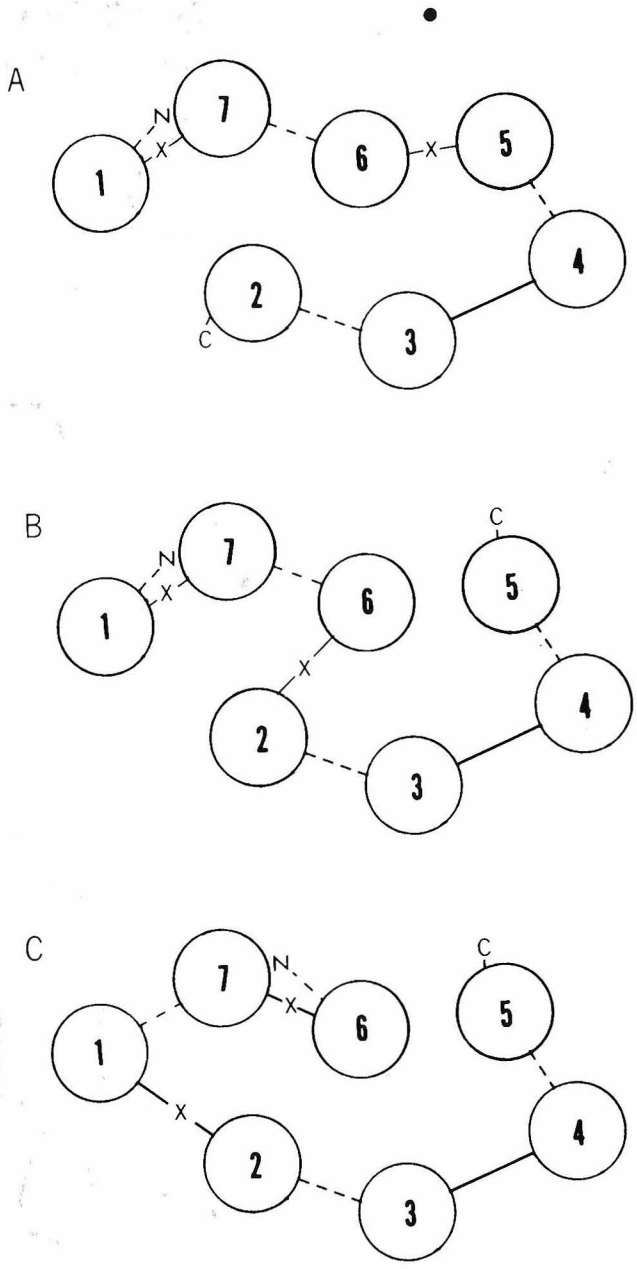

APPENDIX IV

Structure Determination of Asymmetric Membrane Profiles Using an Iterative Fourier Method

STRUCTURE DETERMINATION OF ASYMMETRIC MEMBRANE PROFILES USING AN ITERATIVE FOURIER METHOD

ROBERT M. STROUD AND DAVID A. AGARD, *Department of Biochemistry and Biophysics, University of California, San Francisco, California 94143 U.S.A.*

ABSTRACT An iterative Fourier method is applied to solving and refining the electron density profile projected onto the line perpendicular to a membrane surface. Solutions to the continuous X-ray scattering pattern derived from swelling of multilayer systems or from membrane dispersions can be obtained by this technique. The method deals directly with the observed structure factors and does not rely on deconvolution of the Patterson function. We used this method previously to derive the electron density profile for acetylcholine receptor membranes (Ross et al., 1977). The present paper is an analysis of the theoretical basis for the procedure. In addition, the technique is tested on artificially generated continuous-scattering data, on the data for frog sciatic nerve myelin derived from swelling experiments by Worthington and McIntosh (1974), and on the data for purple membrane (Blaurock and Stoeckenius, 1971). Although the method applies to asymmetric membranes, the special case of centrosymmetric profiles is also shown to be solvable by the same technique. The limitations of the method and the boundary conditions that limit the degeneracy of the solution are analyzed.

INTRODUCTION

The principles of X-ray crystallography were first developed to determine structure in repeating systems. Three-dimensional order in a crystalline specimen permits a great enhancement of the X-ray scattering expected from a single molecule or dispersion of molecules, although the scattering function is consequently sampled only at the positions determined by Bragg's law. The components of biological membranes are inherently closely packed in two dimensions, although crystalline ordering of membrane-bound protein, even in domains containing several hundred molecules, is rare. Most specialized biological membranes are inherently asymmetric structures, i.e. the distribution of protein (or other material) in a direction perpendicular to the plane of a lipid bilayer is asymmetric.

X-ray diffraction has played a major role in establishing the nature of phospholipid bilayers (Levine and Wilkins, 1971). Although phospholipid molecules in the leaflet were shown to possess no regular two-dimensional crystalline order at temperatures above the phase transition, ordering and structural repetition could be obtained in the third dimension, perpendicular to the membrane surface, by close packing of the equivalent and symmetric layers. As a result, the diffraction pattern defined along a reciprocal lattice direction **s**, where **s** is normal to the membrane surface, is contained in discrete Bragg reflections.

Robert M. Stroud is an Alfred P. Sloan Foundation Fellow. David A. Agard is a National Science Foundation Predoctoral Fellow at the California Institute of Technology, Pasadena, Calif. 91125.

BIOPHYS J. © Biophysical Society · 0006-3495/79/03/495/18 $1.00
Volume 25 March 1979 495-512

Since a small number of biological membranes, generated by folding over a cell envelope such as the myelin sheath, or rod outer segment, contain a preexistent center of symmetry, the theories of diffraction from centrosymmetric structures could be applied. Solution of the phase problem, for the signs of successive reflections in such cases, is often by deconvolution of the Patterson function or by trial, since experimental methods, such as isomorphic replacement of one component of the sample by another, have not generally been successful for membranes. Often the diffraction data can only be phased to relatively low resolution, as the correct phase choice relies to some extent on agreement with a reasonable structural model. There is no precedent for use of the finer modulations of structure (which depend on the higher resolution data) as a means of choosing between the possible signs associated with higher order terms.

In some centrosymmetric membrane structures, such as myelin sheath, the membrane multilayers may be reversibly swollen (Robertson, 1958; Moody, 1963; Blaurock, 1971; Caspar and Kirschner, 1971; Worthington and McIntosh, 1974). If the structural unit remains intact during swelling, i.e., if the function $\rho(\mathbf{r})$ (referred to as the membrane profile) does not change within the limited thickness of the leaflets and only the repeat or multilayer spacing d is assumed to vary, then the observed transform is sampled at different positions defined by $\mathbf{s}_h = \lambda h/d$, and the continuous transform can be mapped. The positions of zeros in the transform, i.e., where $|F(\mathbf{s})|^2 = I(\mathbf{s}) = 0$, provide a powerful constraint useful in defining similarities of signs for adjacent reflections that lie between the zeros in the continuous transform. However, the function $F(\mathbf{s})$ need not change sign at one of these nodes. For frog sciatic myelin (*Rana pipiens*), the mapping of the continuous transform by Worthington and McIntosh (1974) reduced the number of possible sign combinations for diffraction orders $h = 1$–12, from 2,048 to 64.

Difficult as it is to define the phases for a centrosymmetric structure, determination of general phases for asymmetric membranes is much more difficult, and this is a primary concern here. Generally, when asymmetric membranes are closely aligned one against the other, there will be no true repetition in the direction perpendicular to the sheets. The statistical distribution of membranes with alternate surfaces up or down gives rise to large statistical fluctuations in the true repeat distances in the specimen. As a result, there is a pillar of continuous scatter perpendicular to the membrane surface due to the product of the true transform of one membrane sheet, $F(\mathbf{s})$, and the transform of a statistical stacking function. The continuous scatter may show slight evidence for the minimum possible repeat distance in the stacking direction arising from the chance stacking of several layers in the same direction. Where sheets are almost symmetric in terms of the distribution of density through the membrane, the pattern may show a reasonably well-defined minimum repeat distance. This is the case for the asymmetric purple membrane from *Halobacterium halobium* (Blaurock and Stoeckenius, 1971; Henderson, 1975). But in all cases, the pattern obtained from closely packed asymmetric membrane systems is made only more complex by the close packing of successive leaflets, as it is the product of the continuous transform from one layer $F(\mathbf{s})$ and a sampling function, which may not depend on random statistics of stacking for obvious physical reasons. Since the second function is extremely difficult to derive (Burge and Draper, 1967), the first is equally difficult to extract.

A more easily obtained scattering pattern is the one from membrane dispersions or

moderately close-packed membrane sheets, where the scattering pattern $I_{obs}(\mathbf{s}) \sin^2\theta$ more nearly represents the square of the Fourier transform of a single membrane sheet $F(\mathbf{s})$ (Wilkins et al., 1971). It is also possible to orient the membrane sheets centrifugally while maintaining only moderate close packing. This allows for separation of the normal and in-plane diffraction, which is important if there is significant in-plane lattice structure.

The information present in continuous X-ray scattering patterns of these types is in one sense greater, since the transform is a continuous function often observed to moderate resolution. In many cases the transform can be shown to be unsampled by the statistical stacking disorder function (disorder of the second kind of Hosemann and Bagchi, 1962) by comparison with the diffraction pattern from membrane vesicles, for example. The continuity of the observed transform places restrictions on the solution. The main difficulty in interpreting these patterns is again determination of the phases $\phi(\mathbf{s})$ of the observed continuous transform $|F(\mathbf{s})|$.

In the case of sampled diffraction patterns, as in crystallography, Fourier refinement methods generally require a good approximation to the real solution before refinement is at all meaningful. The continuity of the observed Fourier transform partially removes this condition. One further piece of information, namely knowledge that the structure is of finite rather than infinite thickness, is sufficient to restrict the number of possible solutions to a very small number, and often to just one.

The method of refinement discussed in this paper imposes the criterion of limited physical extent (constrained thickness) during successive cycles of Fourier refinement of an electron density model to the observed continuous transform $|F_0(\mathbf{s})|$. The starting trial model used to initiate the procedure is demonstrably unimportant when a unique solution exists, since the method always leads to convergence on a solution.

Likewise, the constraining thickness is theoretically unimportant as regards obtaining a solution, providing it is larger than the actual thickness of the membrane structure. No converged solution can be obtained if the thickness used for refinement is too small. Practically, a correct choice for the constraining thickness assists in achieving more rapid convergence to a solution, and in minimizing problems associated with errors in the data, including the fact that data are necessarily of limited resolution. Resolution is limited theoretically by the wavelength of the radiation to $\lambda/2$, and practically limited by experimental conditions, or by signal-to-noise ratio.

This application of Fourier refinement can determine and refine possible solutions for the electron density function, although absolute certainty that all solutions have been obtained would require testing of a large number of possible alternatives. In practice, the number of real alternatives is limited to those consistent with the maximum and minimum electron density allowed by the chemical constituents of the system, i.e., to chemically reasonable alternatives that can in principle all be tested. The more difficult question is whether a determined solution is necessarily the correct one. If more than one solution is obtainable, identification of the correct one requires experimental evidence of a different type, such as isomorphic replacement. Thus, in reporting membrane profiles, many solutions should be sought and reported where obtainable.

To test the efficacy of the iterative refinement method, several transforms were generated from artificial model structures. The character and dimensions of the models were of the

kind that might be expected for genuine membranes, so that discussions of resolution limits, etc., may be compared with real cases. The iterative method was then applied to the generated transform data for hypothetical membrane-like structures to assess the power of boundary conditions and limitations of the method. The method was also applied to solution of the density profiles from the continuous purple membrane data of Blaurock and Stoeckenius (1971) and from the myelin data of Worthington and McIntosh (1974).[1]

The primary motivation for evaluation of the method is to apply the technique to the location of biochemically characterized components in specialized membranes.

THEORY OF THE METHOD FOR ASYMMETRIC AND SYMMETRIC STRUCTURES

Let the electron density perpendicular to the membrane be $\rho'(\mathbf{r})$ and let ρ_s be the constant electron density of the solvent. For simplicity in the ensuing discussion, it is convenient to define a solvent relative profile $\rho_0(\mathbf{r}) = \rho'(\mathbf{r}) - \rho_s$, since the transform of $\rho_0(\mathbf{r})$ is observed in a diffraction experiment. The transform of the constant density ρ_s is contained in the direct beam. For a real asymmetric structure, the choice of origin is arbitrary. Thus if the membrane is of width w, then $\rho_0(\mathbf{r})$ may be nonzero only between the limits $\mathbf{r} = a$ and $\mathbf{r} = b$, where $w = b - a$. The function $\rho_0(\mathbf{r})$ is then said to be constrained to lie within these limits. Although $\rho_0(\mathbf{r})$ will generally be largely positive, it may also be negative where, as in the center of a bilayer for example, $\rho'(\mathbf{r})$ is less than the electron density of the solvent (Levine and Wilkins, 1971).

The Fourier transform of $\rho_0(\mathbf{r})$ will be $F_0(\mathbf{s})$, where the reciprocal space vector $\mathbf{s}$ is parallel to $\mathbf{r}$. Then the observed diffraction pattern, if it can be shown to be an unsampled continuous pattern (or is the continuous data extracted from swelling experiments), will be, after suitable corrections for the experimental arrangement are applied, $I_0(\mathbf{s}) = |F_0(\mathbf{s})|^2$. Having derived the function $|F_0(\mathbf{s})|$ from the diffracted intensity, the problem is to determine solutions for $\rho(\mathbf{r})$ that obey the normal Fourier inversion relationship:

$$\rho(\mathbf{r}) = \int_{-s_1}^{s_1} F_0(\mathbf{s}) \exp(-2\pi i \mathbf{r}\cdot\mathbf{s}) d\mathbf{s}, \tag{1}$$

where

$$F_0(\mathbf{s}) = \int_{-\infty}^{\infty} \rho(\mathbf{r}) \exp(2\pi i \mathbf{r}\cdot\mathbf{s}) d\mathbf{r}, \tag{2}$$

and where s_1 defines the highest resolution ($d_{\min} = \lambda/s_1$) to which the data are measured. Data obscured by the beam stop can be interpolated by using either the sampling theorem or by curve fitting. Since the observed transform is continuous (unlike the crystallographic case), Eqs. 1 and 2 are linear integrals of a continuous function.

Any random phase function $\phi(\mathbf{s})$ associated with $|F_0(\mathbf{s})|$, such that $F_0(\mathbf{s}) = |F_0(\mathbf{s})| \exp(2\pi i \phi(\mathbf{s}))$, when transformed according to Eq. 1, will yield a function $\rho(\mathbf{r})$ that when

[1] It should be clearly noted that the objectives in these cases were to test the method against solutions obtained by these authors by using their particular data sets. The results are therefore entirely dependent on the data set, and the tests were set up this way so that solutions obtained by this method could be directly compared with those obtained by these authors.

transformed by Eq. 2 will necessarily generate the same $F(\mathbf{s})$. This is true only so long as the integration in Eq. 2 is carried out over all space ($\mathbf{r} = -\infty$ to $\mathbf{r} = +\infty$). The resulting $\rho(\mathbf{r})$ will be a function of infinite extent; i.e. $\rho(\mathbf{r})$ may be nonzero for all $\mathbf{r}$ ($-\infty < \mathbf{r} < \infty$). The solution $\rho(\mathbf{r})$ so obtained clearly has no physical meaning. Since the phases $\phi(\mathbf{s})$ were chosen at random, there are an infinite number of such solutions. Without additional information, there is no basis for determining the phases of $F_0(\mathbf{s})$ from the observed values of $|F_0(\mathbf{s})|$.

Since $\rho(\mathbf{r})$ must correspond to a real object, it cannot be of infinite extent or thickness. This alone restricts the number of solutions, no matter how they are obtained, to a small number, all of which are necessarily of the correct actual membrane thickness, without any assumption of what that thickness may be. This can be seen in the following way.

The transform of $F_0(\mathbf{s}) \cdot F_0^*(\mathbf{s})$ is the Patterson function

$$P(\mathbf{r}) = \int_{-s_1}^{s_1} |F_0(\mathbf{s})|^2 \exp(2\pi i \mathbf{r}\cdot\mathbf{s}) d\mathbf{s}, \tag{3}$$

and will always be equal to the convolution $\rho(\mathbf{r}) \widehat{\rho(-\mathbf{r})}$ (see Lipson and Taylor, 1958, for example). This convolution is termed the autocorrelation function,

$$Q(\mathbf{r}) = \int_{-\infty}^{+\infty} \rho(\mathbf{r}')\rho(\mathbf{r}' + \mathbf{r}) d\mathbf{r}'. \tag{4}$$

Thus $P(\mathbf{r}) \equiv Q(\mathbf{r})$, whatever the phase set that is applied to $|F_0(\mathbf{s})|$ in Eq. 1, providing the integrals in Eqs. 2 and 4 are carried out from $\mathbf{r} = -\infty$ to $\mathbf{r} = +\infty$.

Now consider the autocorrelation function computed from a $\rho(\mathbf{r})$ of finite extent, i.e. $\rho(\mathbf{r}) = 0$ for $\mathbf{r} < a$ or $\mathbf{r} > b$. The autocorrelation function

$$Q(\mathbf{r}) = \int_{-\infty}^{+\infty} \rho(\mathbf{r}')\rho(\mathbf{r} + \mathbf{r}') d\mathbf{r}' \text{ will be zero for all values of } |\mathbf{r}| > w,$$

(where $w = b - a$) since at least one of the terms $\rho(\mathbf{r}')$, $\rho(\mathbf{r} + \mathbf{r}')$ must be zero when $|\mathbf{r}| > w$. Conversely, if $Q(\mathbf{r}) = 0$ for $|\mathbf{r}| > w$, then any function $\rho(\mathbf{r})$ that is a solution to Eq. 4, can only be nonzero within an interval $\Delta\mathbf{r} = w$ provided that $\rho(\mathbf{r})$ is of finite extent.

If the actual (true) thickness of the membrane leaflet is w, the autocorrelation function for the structure $Q_0(\mathbf{r})$ [$\equiv P_0(\mathbf{r})$] will be zero for all $|\mathbf{r}| > w$. $P_0(\mathbf{r})$ is determined by the intensity distribution $|F_0(\mathbf{s})|^2$ alone, and not by the phases assigned to $|F_0(\mathbf{s})|$. Any function $\rho(\mathbf{r})$ of thickness $t > w$ will necessarily produce an autocorrelation function $Q(\mathbf{r})$ that has nonzero components[2] for $w < |\mathbf{r}| < t$. Therefore $Q(\mathbf{r}) \neq P_0(\mathbf{r})$, at least for $w < |\mathbf{r}| < t$, and so $\rho(\mathbf{r})$ cannot be a function derived from the observed moduli $|F_0(\mathbf{s})|$ (Eq. 1).

Thus no function $\rho(\mathbf{r})$ of finite width $t > w$ (and by similar arguments $t < w$) can be a solution to Eqs. 1 and 2. It follows that imposition of any constraining thickness, which alters Eq. 2 to

$$F_0(\mathbf{s}) = \int_a^b \rho(\mathbf{r}) \exp(2\pi i \mathbf{r}\cdot\mathbf{s}) d\mathbf{r}, \tag{5}$$

[2] In general $Q(\mathbf{r})$ will similarly be nonzero for all $|\mathbf{r}| < w$. However, there may be particular values of $\mathbf{r}$ for which all terms in Eq. 4 cancel to give a zero in $Q(\mathbf{r})$.

where $b - a > w$, only allows solutions, $\rho(\mathbf{r})$, of thickness w. In the Fourier refinement method, solutions that obey Eqs. 1 and 5 are determined in an iterative process.

By analogy with usual Fourier refinement procedures, an initial structure $\rho_i(\mathbf{r})$ is transformed according to Eq. 5, i.e., between some limits $\mathbf{r} = a$ to $\mathbf{r} = b$ to generate an initial calculated transform $F_c(\mathbf{s})$. The phases $\phi_c(\mathbf{s})$ derived from this model are then associated with the "observed" $|F_0(\mathbf{s})|$ and transformed back by using Eq. 1 to obtain a new function $\rho_i'(\mathbf{r})$. The entire process is cycled until convergence is reached (Fig. 1). All refined solutions, $\rho(\mathbf{r})$, will necessarily be of the same thickness.

If multiple solutions, $\rho(\mathbf{r})$, exist that are compatible with a thickness of w, then these will form a set of possible solutions (strictly a homometric set of solutions) that cannot be eliminated without further information by any method of treating $|F(\mathbf{s})|$. The choice of starting model $\rho_i(\mathbf{r})$ in these instances will tend to select for the solution closest to the starting model. Consequently, this approach can be used to test hypothetical structures. Obviously, if only one $\rho(\mathbf{r})$ of finite thickness exists, this procedure will converge upon that structure. In practice it seems that when multiple solutions do exist, they are often qualitatively quite similar to one another.

The boundary limits $\mathbf{r} = a$, $\mathbf{r} = b$ are unimportant as regards achieving a converged solution. The choice of a constraining thickness w that is close to the correct value for converged solutions greatly speeds up convergence.

The constrained thickness may be estimated in several ways and, therefore, is not difficult to determine accurately enough to be effective. It may be estimated: from electron microscopy of isolated protein molecules, or of thin sections cut perpendicular to close-packed membrane sheets; from the minimum close-packing distance found in X-ray scattering from densely packed specimens; or from the Patterson function, which identifies (within resolution limits) the largest vectors in the structure.

So far in our considerations we have assumed that $|F_0(\mathbf{s})|$ contains no errors. In any real case the values of $|F_0(\mathbf{s})|$ will be extracted with care to try to achieve this condition (see, for example, Ross et al., 1977). If there is independent evidence for the thickness of the leaflet

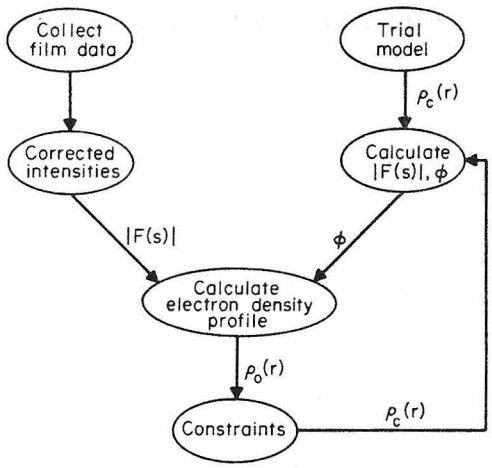

FIGURE 1 Schematic of the refinement procedure.

(of the kind mentioned above), then imposition of the boundary thickness can minimize errors in the profile introduced by errors in $|F_0(\mathbf{s})|$. If such errors in the data exist, they will be assayed by the final agreement between $|F_0(\mathbf{s})|$ and $|F_c(\mathbf{s})|$ for the constrained structure.

Systematic errors in the refined profile arise when the data are cut off at some particular resolution, s_1, such that $|F_0(\mathbf{s})|$ is nonzero for $\mathbf{s} > s_1$. This is to be expected since the "true" resolution limited structure (computed with true phases and limited in resolution to s_1) will contain Fourier series termination ripples of frequency equal to s_1. The presence of termination ripples is inconsistent with the refinement procedure used here [$\rho(\mathbf{r})$ is constrained to be zero outside the boundary thickness]. Therefore the phases of the terms $F(\mathbf{s})$ with $\mathbf{s}$ closest to s_1 will be modified, and so changed away from their true phase to best accommodate the termination ripples. In any real case, data to the highest observable resolution should be included, such that $|F_0(\mathbf{s})| \to 0$ at the resolution cutoff limit. The imposition of an artificial temperature factor $\exp(-B\mathbf{s}^2)$ is useful when this condition is not met.

Criterion for Acceptance of a Solution

The criterion for accepting a refined solution, $\rho(\mathbf{r})$, is that the amplitude of the transform $|F_c(\mathbf{s})|$ computed in Eq. 5 should agree with the observed transform $|F_0(\mathbf{s})|$. The degree to which $|F_c(\mathbf{s})|$ approximates $|F_0(\mathbf{s})|$ characterizes the extent of convergence, and indicates the degree to which the diffraction data are consistent with a structure of width $w < b - a$ in thickness. The agreement index,

$$R = \frac{\int_0^{s_1} ||F_c(\mathbf{s})| - |F_0(\mathbf{s})|| \, d\mathbf{s}}{\int_0^{s_1} |F_0(\mathbf{s})| \, d\mathbf{s}} \tag{6}$$

is typically 0.1%–1% for a solution to artificially created and purple membrane data, or about 1%–5% for measured $|F_0(\mathbf{s})|$ data from acetylcholine receptor membranes, for example, (Ross et al., 1977).

Since for any solution, $\rho(\mathbf{r})$, there will be three other trivial solutions, $-\rho(\mathbf{r})$, $\rho(-\mathbf{r})$, and $-\rho(-\mathbf{r})$, only one solution of the set for which $\int \rho(\mathbf{r}) \, d\mathbf{r} > 0$ will be considered.

TESTS OF THE METHOD

An Asymmetric Structure

A supposed (initial) electron density function shown in Fig. 2 A was used to generate the function $|F(\mathbf{s})|$, which was then regarded as an observed transform. The back transform of $F(\mathbf{s})$ at 10 Å resolution, the correct resolution-limited structure, is also shown in Figure 2 A. Attempts were then made to derive the electron density function $\rho(\mathbf{r})$ starting only from the moduli $|F(\mathbf{s})|$ by application of the refinement method. Numerous different trial models were used to initiate the procedure by using data to 10 Å resolution. These ranged from a single delta function, to several step functions, to various continuous functions. In each case convergence on the same final structure was achieved (Fig. 2 C). The boundary thickness chosen varied from 210 to 250 Å.

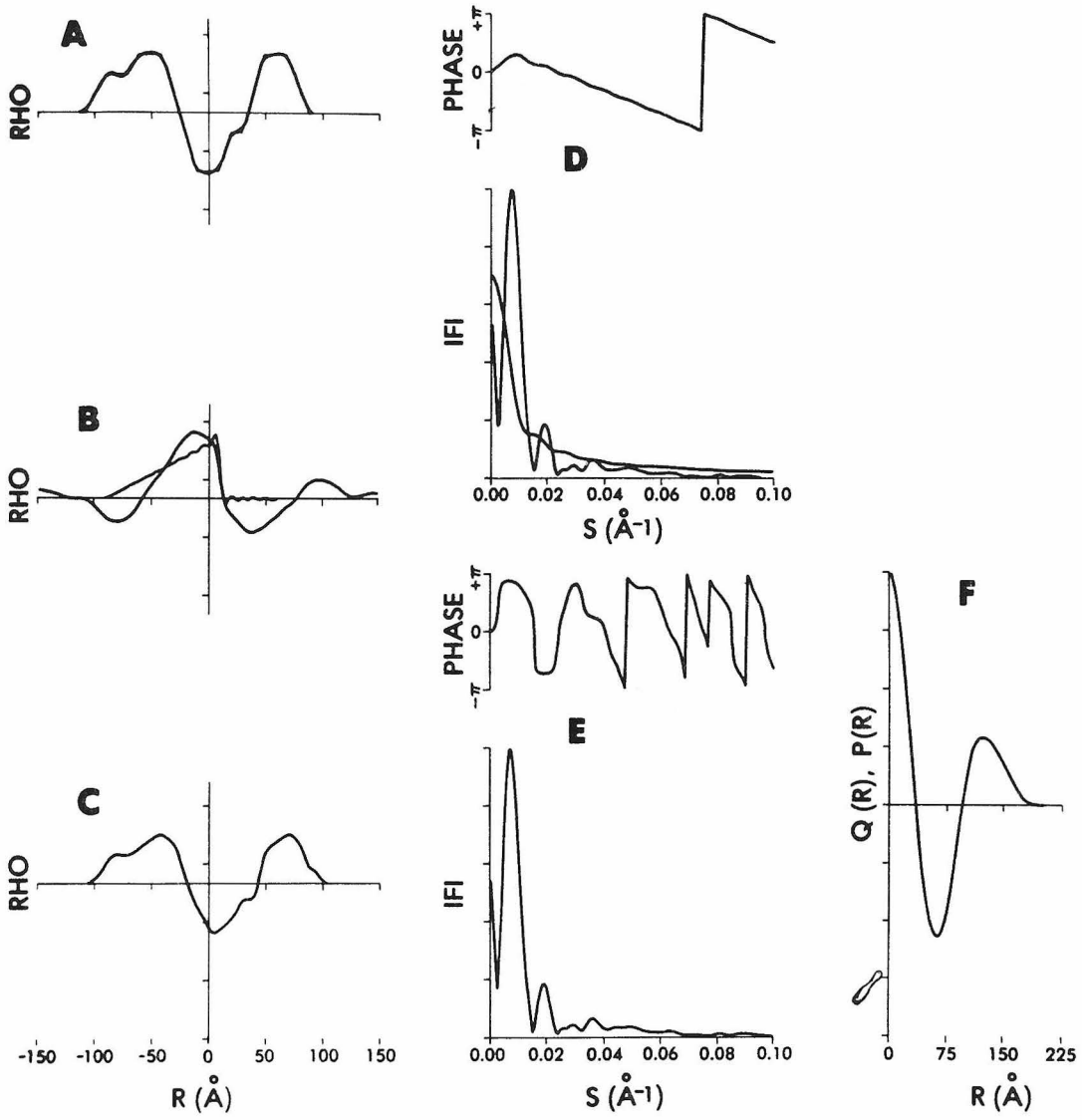

FIGURE 2 Results of refinement of an asymmetric "membrane" profile using synthetic data to 10 Å. The model used to generate the observed structure factors is shown in A. Using a ramp function for the trial structure results in the profiles depicted in B and C (1 and 30 cycles of refinement, respectively). Corresponding observed and calculated Fourier amplitudes and calculated phases are shown in D and E. A typical plot of both $Q(\mathbf{r})$ and $P(\mathbf{r})$ is shown in F. R_F and R_P factors in all refined cases are less than 1.5%.

When the structure was refined at 20 Å resolution, series termination ripples in $\rho(\mathbf{r})$ at each successive stage were forced into the structure by the refinement procedure (which eliminates ripples outside the structure) (Fig. 3 B). Later addition of higher resolution data (20–10 Å) did not immediately lead to further refinement of the 20 Å data, since subsequent refinement first tends to minimize ripples outside the boundary that at this stage are produced only by the additional data (Fig. 3 C). In this situation the additional data from

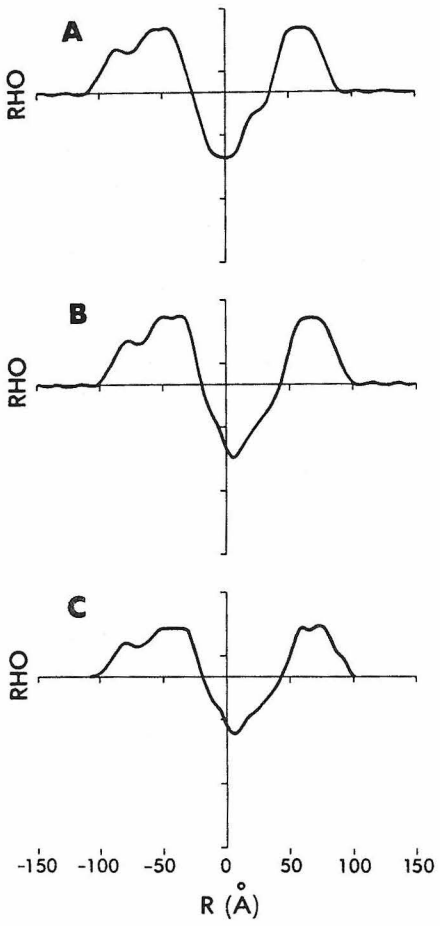

FIGURE 3

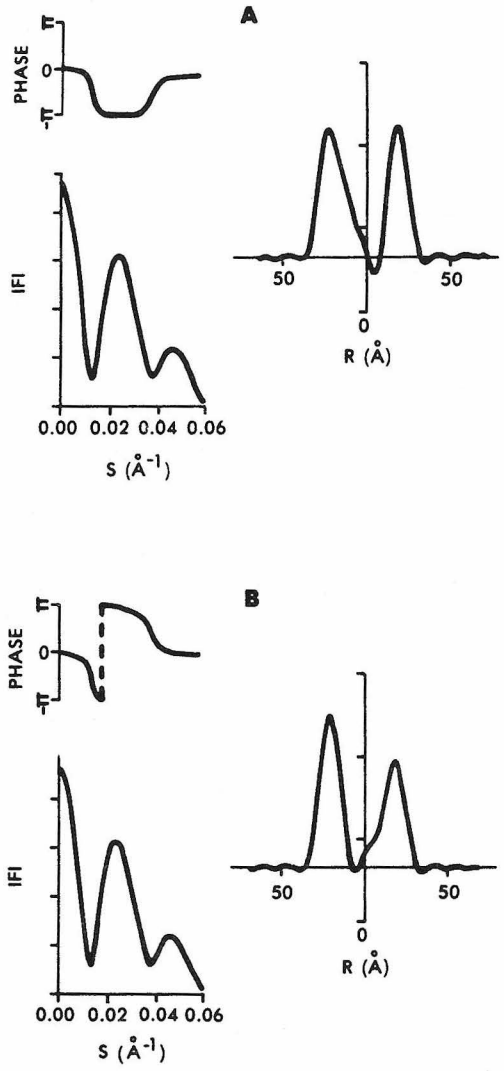

FIGURE 4

FIGURE 3 Refinement of the same profile as in Fig. 2 but at lower resolution. The true structure is depicted in A. The converged solution using 20 Å data after 20 refinement cycles appears in B. Although similar to the profile obtained with 10 Å data (Fig. 2 C), there are distinct differences resulting from forcing the series termination ripples to be accommodated within the structure. These ripples are not immediately removed by a later inclusion of the higher resolution data, as shown in C.

FIGURE 4 The two solutions (A, B) to the purple membrane continuous scattering data of Blaurock and King (obtained after 30 cycles of Fourier refinement). The left side of the figure shows the derived phase functions and the equivalence of $|F_0(s)|$ and $|F_c(s)|$ (shown superimposed). The R-factor in both cases was below 0.15%. On the right are the corresponding electron density profiles, showing the asymmetry in the protein distribution across the membrane. Many different starting models were used; however, only these two solutions could be obtained.

20 to 10 Å resolution are initially being treated as an independent data set. Only as successive changes in structure begin to affect the phases of the lower resolution data does the pressure to refine the lower resolution phases develop.

When the starting trial model $\rho_i(\mathbf{r})$ is centrosymmetric, convergence to the correct structure, which is asymmetric, requires that the centrosymmetric phase relationships (which are signs if the origin is chosen at the symmetric center) be broken. If the refined model is constrained to be concentric with the centrosymmetric starting model, it is impossible to achieve even qualitative agreement with the observed data. Convergence on the final solution is possible when the constraint to symmetry is removed by imposing a boundary size whose limits are not concentric with the starting model. The asymmetric truncation of series termination ripples allows a degree of freedom for the phases and so allows refinement to continue.

Several different initial structures were used to generate observed values of $|F(\mathbf{s})|$. The experience with the case described above was shared in other similar cases. As the complexity of the profile increased to the point where variations in $\rho(\mathbf{r})$ were of the same order as the resolution cutoff limit applied to the data, multiple solutions were obtained. These solutions were similar with differences accountable as alternative ways of phasing the lower intensity data at higher resolution while maintaining a width $\simeq w$. This is a consequence of the errors introduced by using data of limited resolution (see Theory section), and the lower pressure to phase weak-intensity data, whose contribution to $\rho(\mathbf{r})$ is least. Since the lowest intensities are found in general at highest resolution, phase errors will correspondingly be greater at higher resolution.

As another test, data from suspensions of purple membrane from *Halobacterium halobium*, kindly provided by Allen Blaurock (California Institute of Technology), were refined by using this method. Various starting models were used and only two different solutions could be obtained (Fig. 4). These solutions are identical to the two reported by Blaurock and King, 1977. The two solutions correspond to different senses of phase change $(d\phi/ds)$ between maxima in the observed transform $|F_0(\mathbf{s})|$.

Centrosymmetric Structures

A more difficult question is whether an initially centrosymmetric model $\rho(\mathbf{r})$ used to generate a transform or a centrosymmetric membrane structure will also be determined correctly, since the final phase angles must accommodate discontinuities between regions of opposite sign in the transform $F(\mathbf{s})$. This was tested first by calculation of observed transforms from symmetric models (see Fig. 5). Refinement against the data shown in Fig. 5 always led to convergence on the correct structure (Fig. 5 D). The phases changed most rapidly at the positions of sign change in the observed transform (where the computed $|F_0(\mathbf{s})|$ are smallest) and accommodated a phase change of 180° within a small range of $\Delta\mathbf{s}$.

In a second test of the method to determine centrosymmetric structures, the continuous transform for frog sciatic nerve myelin mapped from a series of swelling experiments by Worthington and McIntosh (1974) was used. The data were extracted from their Fig. 9 and digitized at intervals of 0.001 $Å^{-1}$ in reciprocal spacing to a resolution of $\mathbf{s} = 1/14$ $Å^{-1}$. Different data sets reported elsewhere, or different interpretations of what constitutes the continuous transform of myelin (considered extensively by Blaurock, 1976), would clearly give rise to different electron density profiles. Our objective was to see how closely the

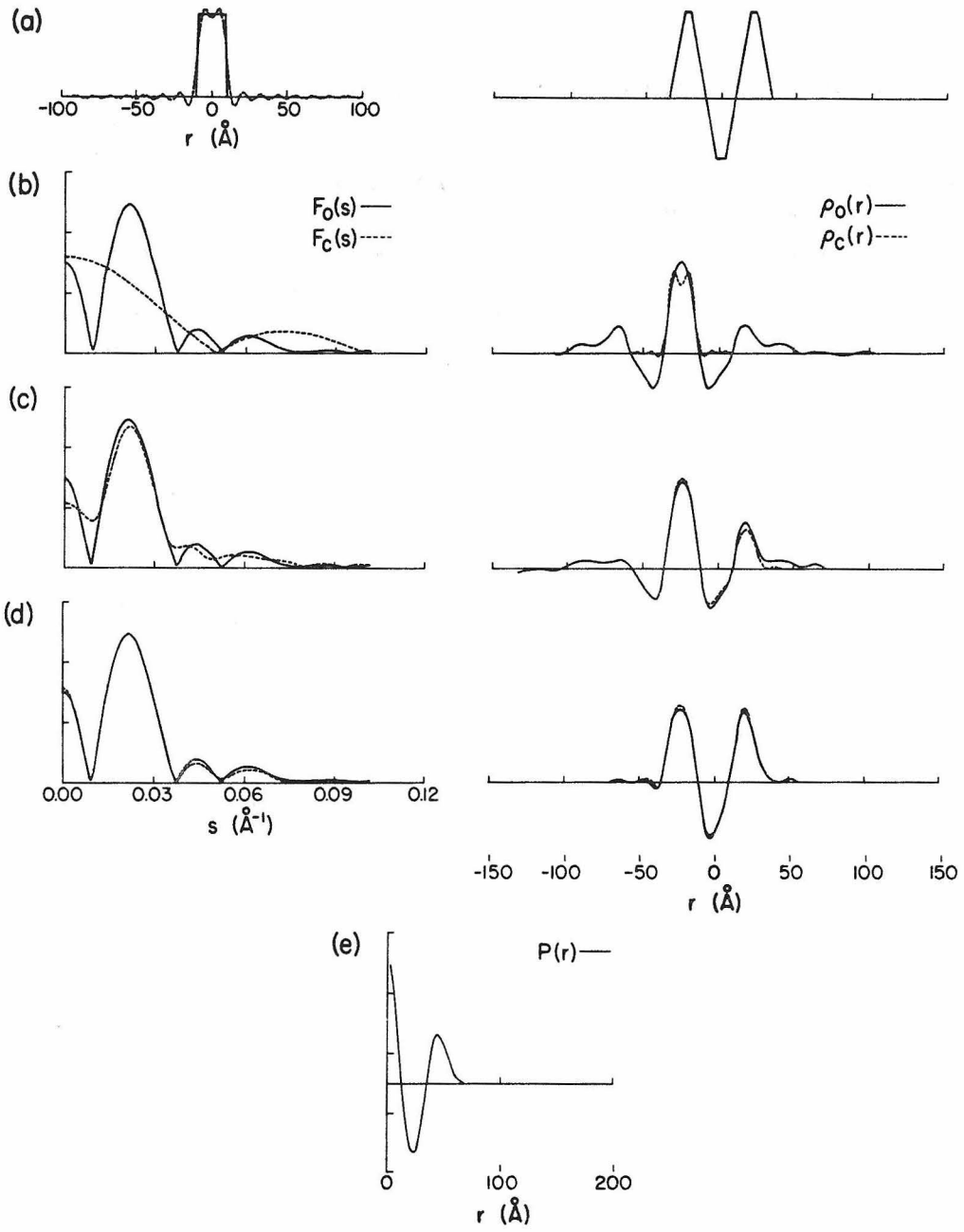

FIGURE 5 Test of solution at 10Å resolution for data generated from a centrosymmetric structure is shown in part 2 of A. The trial model used to initiate refinement was a box function (solid line in part 1 of A). Fourier transformation of the $|F_c(s)|$, $\phi_c(s)$ generated from the trial model (A), and cut off at 10 Å (- - - - - - - - in A) contains series termination ripples. At the first cycle (B) observed $|F_o(s)|$ (——) were coupled with phases calculated from the trial model (A) to generate a new model $\rho_o(r)$. This model was used to generate amplitudes $|F_c(s)|$ (- - - - - -) and phases $\phi_c(s)$. ($\rho_c(s)$ is computed from $|F_c(s)|$, $\phi_c(s)$). The procedure was iterated, and results after 4 cycles (C), and after 14 cycles (D), show convergence onto an essentially correct structure, which may be compared with A above. The agreement between the Patterson and autocorrelation function is essentially perfect (E).

solution using the Fourier method fitted the conclusions and the ambiguities derived by Worthington and McIntosh from these data.

The myelin data also represent an ideal system for illustrating the theoretical basis for the multiple solution problem. The normal frog sciatic nerve myelin structure gives rise to Bragg reflections that lie on maxima determined by the minimum multilayer repeat of **d** = 171 Å. A width of 180–190 Å was chosen as an estimate of the thickness of a single repeated unit. A width slightly larger than the true repeat Bragg spacing was chosen so as to allow a smooth truncation of series termination ripples within the boundary thickness. The Fourier refinement method was applied to several different starting models bearing no relationship to the solutions obtained by Worthington and McIntosh (1974). One solution summarized in Fig. 6 again indicates that convergence on an almost centrosymmetric struc-

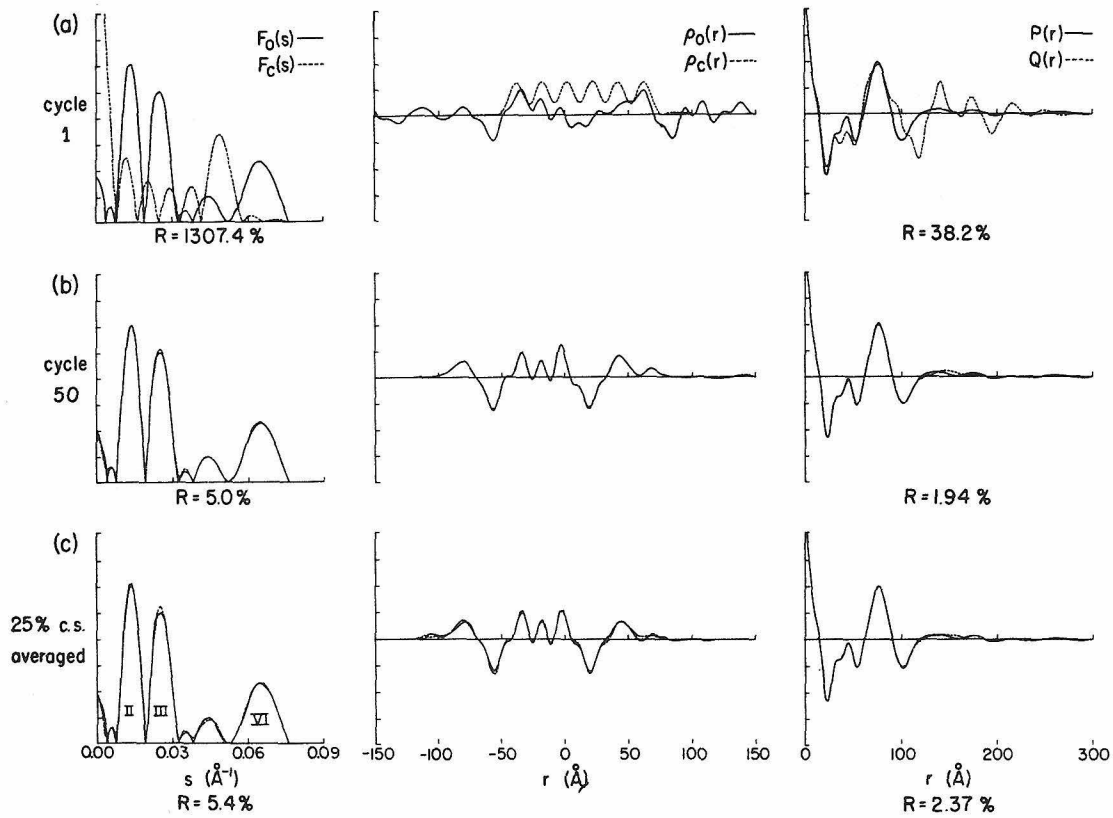

FIGURE 6 Test of solution using the continuous data $|F_0(\mathbf{s})|$ for frog sciatic nerve myelin (Worthington and McIntosh, 1974) to a resolution of $\mathbf{s} \approx 1/14$ Å^{-1}. The trial model for initiating refinement was $\rho_c(\mathbf{r})$ (- - - - - - - - in A); and at cycle 50 (B), are shown (left). The central figures show the calculated model generated by transformation of $|F_0(\mathbf{s})|$, $\phi_c(\mathbf{s})$ $[\rho_0(\mathbf{r})]$ and of $|F_c(\mathbf{s})|$, $\phi_c(\mathbf{s})$ $[\rho_c(\mathbf{r})]$ at corresponding cycles. Agreement between $P(\mathbf{r})$ and $Q(\mathbf{r})$ is indicated at the right side. Values for the residual R at each stage are indicated below each data summary. The residual values underneath the Patterson summary are R_P values. The structure $\rho_0(\mathbf{r})$ shown in B is not completely centrosymmetric, and the two sides of the structure were subjected to weighted averaging to achieve pressure toward centrosymmetricity. Weighting was 0.75 of $\rho_0(\mathbf{r})$ + 0.25 of $\rho_0(r_0 - \mathbf{r})$ with respect to a pseudocenter at the center of mass (r_0). Results are shown in C. The signs indicated for the zero order, and the six regions of the transform between zeros are (+) − + − + − + (the "alternate" structure of Worthington and McIntosh, 1974).

ture is achieved. Further refinement cycles tend to generate more perfectly centrosymmetric structures. The resulting structure (Fig. 6 B) was similar to one of the solutions obtained by Worthington and McIntosh (1974)—their "alternate" structure.

It was possible to incorporate knowledge of centrosymmetry in the final stages of refinement by defining a new $\rho(\mathbf{r})$ composed of 75% of the original value and 25% of the symmetrically related value of $\rho(\mathbf{r})$ (Fig. 6 C). This constraint allows the phases to refine to the correct values, whereas forcing them to be signs, + or −, would not.

In some cases (see Fig. 7) the myelin refinement yielded noncentrosymmetric solutions. This is to be expected in light of the greater degrees of freedom available with general phases. Application of the real-space averaging procedure (above) resulted in an alternative symmetric solution to that of Fig. 6. In all, four different centrosymmetric solutions for the myelin structure were obtained that matched our criteria for an acceptable solution. They correspond to the four possible permutations of − or + sign choices for regions V and VI of the observed transform (see below), and were similarly identified as possible ambiguities by Worthington and McIntosh (1974); two of these solutions were favored. This raises the question as to why there should be four homometric solutions, and ultimately shows that two of these structures cannot be distinguished without more information than is contained in the one continuous transform. The other two structures can in theory be

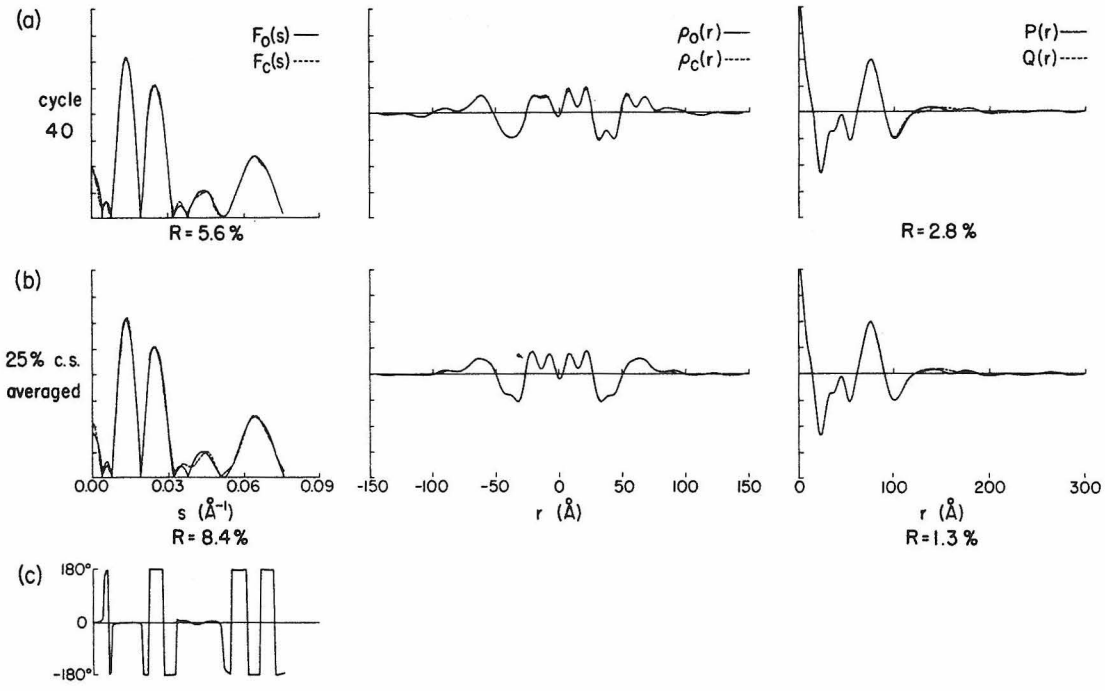

FIGURE 7 Another of the four solutions to the myelin transform, (*a*), after 40 cycles of refinement, is noncentrosymmetric, although the structure retains symmetric features of the structure permuted in cyclic order. Pressure toward centrosymmetricity (using 0.75/0.25 weights) leads to a symmetric structure with somewhat better agreement between $P(\mathbf{r})$ and $Q(\mathbf{r})$ (B), (R_P = 1.3%). The phases derived from refinement (C) indicate a sign choice (+) − + − + + − for the zero-order component, and the six transform regions between zeros.

eliminated, but this requires essentially perfect data, or data from different species as was used by Worthington and McIntosh in their analysis.

Worthington and McIntosh (1974) identified six zeros ($|F(\mathbf{s})|^2 = 0.0$) in the observed transform-out to a resolution of 7 Å ($\mathbf{s} = 1/14$ Å). They identified seven regions of the transform separated by the six zeros, which were labeled regions 0, I, II, III, IV, V, and VI. The ambiguities in solution by the iterative Fourier method are directly associated with the phases (or signs) of regions V and VI. Sign changes in the latter region cannot be discriminated without additional information beyond that contained in a single continuous transform from one species.

Each region of the continuous transform contributes a Fourier component to the electron density synthesis, and in each case, the contribution of just one region is a wave packet that resembles a cosine curve of frequency determined by the **s** value where the local value of $|F(\mathbf{s})|$ is maximum multiplied by a smooth envelope that is qualitatively like either a Gaussian or a zero-order Bessel function. Looked at another way, each region of the transform $F(\mathbf{s})$ is a delta function at the **s** value of the center of the peak, convoluted with the profile of the region. The contribution to electron density synthesis is thus the product of a cosine wave with a Gaussian-like envelope. The width of the envelope is inversely proportional to the width of the transform region. Each one of the regions 0–V of the transform is sufficiently narrow (<0.013 Å^{-1}) so that its contribution to the density synthesis extends beyond the constrained thickness of the structure. Region VI, on the other hand, is at least 0.02 Å^{-1} in width, and its contribution to the resulting electron density synthesis is confined well within the thickness (180 Å) of the profile (Fig. 6). There is no pressure on the refinement process to phase this region, since its contribution to the profile outside the boundary is too small to be significant. As a direct consequence of this fact, the autocorrelation function is the same as the Patterson synthesis for both structures when computed using either sign for the data of region VI. Worthington and McIntosh (1974) presented two structures for frog sciatic nerve myelin that differed in the same way—namely, in the choice of sign for region VI of the profile. Their results were obtained by direct methods of deconvoluting the Patterson function, based upon the theory of Hosemann and Bagchi (1962) and reconstruction methods based on the Shannon (1949) sampling theory applied to the sampled transform data. The transform of region V is approximately the same size as the total width of the double bilayer structure and because it is rather small, its sign cannot practicably be determined from a single specimen scattering pattern alone. Different sign choices from those we found (the same as discussed by Worthington and McIntosh, 1974) have been proposed earlier by Caspar and Kirschner (1971), and by Blaurock and Worthington (1969) using different data. Our analysis (which would not allow these solutions) applies strictly to the data set used.

DISCUSSION

From the applications of the Fourier method to continuous scattering data, the following generalizations can be made:

(*a*) The starting model for initiating refinement is arbitrary, and its only function is to generate a set of phases, $\phi(\mathbf{s})$, which roughly correspond to a model centered somewhere near the arbitrary $\mathbf{r}_0$. The initial model may be useful in testing different types of structure.

(*b*) Successive cycles of refinement from the starting model always lead to convergence on a solution, usually after 15–40 cycles.

(*c*) In every case we tested from artificially synthesized data, $|F(\mathbf{s})|$, one solution of a very small number was correct, suggesting that in general the number of solutions will be small. The difference between different solutions was often small and probably reflects the lower pressure to phase the lowest amplitudes in the transform $F(\mathbf{s})$, since they contribute least to the $\rho(\mathbf{r})$ synthesis (Eq. 1). Often a unique solution is found.

(*d*) If the assigned boundary condition, w, is chosen to be too small, refinement can never adequately lead to fitting even the first minimum of the transform. If w is too large (several times the correct thickness) then refinement is slower, since the pressure to produce alterations in the structure at each cycle is diminished.

(*e*) Alternate structures can be identified by the Fourier method where they exist, whereas they cannot necessarily be found by direct methods (King, 1975), or by normal methods of deconvolution of the Patterson function. In those cases where more than one solution exist, one cannot be certain that all possible solutions have been obtained when using only a limited set of starting models. It is possible, however, to test various classes of solutions by appropriate choice of starting models. Since most asymmetric membranes are based on a bilayer structure, chemical reasonableness may be a basis for preference rather than proof. Nevertheless, our concern was primarily with the location of asymmetric protein or other components at relatively low resolution in a simple structure based on a bilayer. Is the protein localized only on one side of a membrane, for example, or does the protein traverse the lipid bilayer in any particular case? The method can be extremely powerful in determining the range of possible solutions in these cases.

The essential component of the Fourier refinement method applied to continuous diffraction is the assumption that the scattering object is of finite, rather than infinite, dimension. This condition is applied by the imposition of a finite size to the density profile. This restraint allows convergence. It also explains the pressure to converge on a definite solution, since it forces all Fourier components used to calculate $\rho(\mathbf{r})$ at each cycle to account correctly for a constant solvent density outside the boundary limits. Since the calculated amplitudes $|F_c(\mathbf{s})|$ must match the observations $|F_0(\mathbf{s})|$, the phases must account for the featureless solvent region. Thus, the method is essentially refinement of the solvent density for $\mathbf{r} = -\infty$ to a; b to ∞.

Alternative Approaches to Solution

With the exception of our own studies of acetylcholine receptor membranes (Ross et al., 1977) and the work on purple membrane that is only slightly asymmetric (Blaurock and King, 1977), solutions to membrane profiles, $\rho(\mathbf{r})$, have so far only been attempted for centrosymmetric structures, i.e., cases in which the repeating unit consists of a pair of membranes generated by the folding over of a cell envelope or artificial lipid bilayers without protein.

The problems associated with phasing of lamellar diffraction from symmetric structures have been approached in several different ways. A number of methods for deriving the electron density profile have been proposed, and most of these depend on a deconvolution of the Patterson function $P(\mathbf{r})$. Several developments of the deconvolution method of Hosemann and Bagchi (1962) have been used. These and other methods have been critically analyzed by Worthington, et al. (1973). Since then Moody (1974) has proposed other methods for

achieving deconvolution in the particular case where swelling experiments can be used to map the continuous transform from multilayer systems. Luzzati et al. (1972) also proposed a pattern recognition approach based on interpretation of even higher order autoconvolutions of $F(\mathbf{h})$ in terms of higher powers of $\rho(\mathbf{r})$.

In the case of asymmetric membrane profile analysis, general deconvolution of the Patterson function has been proposed, but to this point remains untested. A direct method based on the Hilbert transform (Papoulis, 1962; King, 1975) has recently been applied successfully to the purple membrane profile, but only one of the two possible solutions could be found (Blaurock and King, 1977). A general and severe problem with these and other methods providing a single solution from a single data set is the uncertainty that always remains as to whether other solutions exist, and if so, how many might equally well fit the data.

Blaurock and King (1977) also presented a trial and error method which, as with our method, uses knowledge of the membrane thickness. The continuous transform was sampled at intervals determined by a hypothetical unit cell. By using all possible phase combinations for these "reflections," the continuous transform was reconstructed by the Shannon method (1949) and compared to the observed transform. The observed and reconstructed functions would be identical (within data errors) for a correct phase choice. This process is equivalent to choosing a combination of phases that will generate a $\rho(\mathbf{r})$ contained entirely within the "unit cell" (our constraining thickness, w). As our and their approaches employ the same physical criterion for determining a solution, they would provide identical solutions if the trial phases were sampled at infinitesimally small intervals. The method of Blaurock and King (1977) requires that all possible phase choices be tried, and thus in principle, it can obtain all solutions. Within the bounds of practicality, all phase combinations cannot be tried. In an effort to circumvent this problem, the authors chose the rather coarse interval of $\pi/8$ between trial phases to limit the number of tests. Even so, this results in 16^n Shannon reconstructions for n reflections. For purple membrane where a 50 Å "unit cell" was chosen, only two reflections were involved at the observed resolution (196 trials). When larger structures such as the acetylcholine receptor (110 Å actual thickness, Ross et al., 1977) are considered, where higher resolutions are required, or where smaller phase intervals are used, the computation involved would be prohibitive. Application to the acetylcholine receptor, for example, would require $16^9 = 6.9 \cdot 10^{10}$ trials and is clearly impractical. In our Fourier refinement technique, consistent sets of phases are jointly developed in a convergent stochastic process, and are not restricted to be multiples of $\pi/8$. In our approach it is also possible to incorporate other knowledge about the structure (e.g. limits on allowable densities, centrosymmetricity, etc.) whenever it is available.

Asymmetric Membranes and Continuous Diffraction

It is possible in many cases to prepare asymmetric membrane fractions from specialized tissue, which contain a highly enriched biochemical function. Membranes containing acetylcholine receptors, for example, have been prepared from the electric organ of the electric fish *Torpedo californica*. Other fractions prepared from the same organ show that separate patches contain other biochemical functions such as acetylcholine esterase and ATPase. In this system, at least, it would seem that specialized functions are contained within specialized regions of the synapse (Cohen et al., 1972; Duguid and Raftery, 1973). In the case of acetylcholine receptor membranes, it is clear that there is a structural asymmetry

to the membrane and that receptor molecules are all aligned in the same way, and sometimes organized into an array within each sheet (Ross et al., 1977). This type of situation is also known in bacterial systems, where the purple membrane of *Halobacterium halobium* has been shown to contain an organized, directionally polar array of bacteriorhodopsin molecules (Henderson, 1975). Thus we expect there will be a large number of systems such as these where the Fourier method of structure determination will initially provide valuable information on the distribution of macromolecules in a membrane.

The necessary X-ray data may be generated from vesicle dispersions. Such X-ray scattering patterns have been acquired in several cases for membranes isolated from cells or organelles (Engleman, 1971; Wilkins et al. 1971; Lesslauer, et al., 1971; Lesslauer and Blasie, 1972; and Blaurock, 1973). In some cases centrifugation or drying of vesicles has been used to record lamellar diffraction (Finean and Burge, 1963; Dupont, et al., 1973; and Worthington and Liu, 1973), and some of the complex problems associated with the statistical arrangement of stacked asymmetric structures were detailed in the latter presentation. The iterative Fourier method can be simply applied to continuous scattering data and avoids the complex problems of stacking disorder. It is a simple procedure and can identify and refine possible solutions for the electron density profile from either asymmetric or symmetric membranes.

Since this Fourier method deals directly with $|F_0(\mathbf{s})|$, rather than higher powers of $|F_0(\mathbf{s})|$, as in deconvolution of the Patterson function by the method of moments or recursion, the solution is less sensitive to errors in the data.

In a much broader context it is clear that any solution to structural problems using diffraction techniques can be improved when physical and chemical constraints or noncrystallographic symmetry relationships can be applied. Such constraints can best be applied in the electron density domain. Working in the Patterson synthesis, or with intensities $|F(\mathbf{s})|^2$, or with higher order convolutions of $\rho(\mathbf{r})$ inevitably makes the analysis more complex and does not easily allow for iterative improvements in the result.

This work was supported by National Institutes of Health grant GM-24485 and National Science Foundation grant PCM77-25407.

Received for publication 13 May 1977 and in revised form 18 November 1978.

REFERENCES

BLAUROCK, A. E. 1971. Structure of the nerve myelin membrane: proof of the low-resolution profile. *J. Mol. Biol.* **56**:35–52.

BLAUROCK, A. E. 1973. The structure of a lipid-cytochrome c membrane. *Biophys. J.* **13**:290–298.

BLAUROCK, A. E. 1976. Myelin X-ray patterns reconciled. *Biophys. J.* **16**:491–501.

BLAUROCK, A. E., and KING, G. I. 1977. Asymmetric structure of the purple membrane. *Science (Wash. D.C.).* **196**:1101–1104.

BLAUROCK, A. E., and W. STOECKENIUS. 1971. Structure of purple membrane. *Nat. New Biol.* **233**:152–155.

BLAUROCK, A. E., and C. R. WORTHINGTON. 1969. Low-angle X-ray diffraction patterns from a variety of myelinated nerves. *Biochim. Biophys. Acta* **173**:419–426.

BURGE, R. E., and J. C. DRAPER. 1967. The structure of the cell wall of the Gram-negative bacterium *Proteus vulgaris*. III. A lipopolysaccharide "unit membrane." *J. Mol. Biol.* **28**:205–210.

CASPAR, D. L. D., and D. A. KIRSCHNER. 1971. Myelin membrane structure at 10 Å resolution. *Nat. New Biol.* **231**:46–52.

COHEN, J. B., M. WEBER, M. HUCHET, and J. P. CHANGEUX. 1972. Purification from *Torpedo marmorata* electric tissue of membrane fragments particularly rich in cholinergic receptor protein. *FEBS (Fed. Eur. Biochem. Soc.) Lett.* **26**:43–47.

DUGUID, J. R., and M. A. RAFTERY. 1973. Fractionation and partial characterization of membrane particles from *Torpedo californica* electroplax. *Biochemistry*. **12**:3593–3597.

DUPONT, Y., S. C. HARRISON, and W. HASSELBACH. 1973. Molecular organization in the sarcoplasmic reticulum membrane studied by X-ray diffraction. *Nature (Lond.)*. **244**:555–558.

ENGLEMAN, D. M. 1971. Lipid bilayer structure in the membrane of Mycoplasma laidlawii. *J. Mol. Biol.* **58**: 153–165.

FINEAN, J. B., and R. E. BURGE. 1963. The determination of the Fourier transform of the myelin layer from a study of swelling phenomena. *J. Mol. Biol.* **7**:672–682.

HENDERSON, R. 1975. The structure of the purple membrane from *Halobacterium halobium:* analysis of the X-ray diffraction pattern. *J. Mol. Biol.* **93**:123–138.

HOSEMANN, R., and S. N. BAGCHI. 1962. Direct analysis of diffraction by matter. North-Holland Publishing Company, Amsterdam. 300–500.

KING, G. I. 1975. Direct structure determination of asymmetric membrane systems from X-ray diffraction. *Acta. Crystallogr. Sect. A.* **31**:130–135.

LESSLAUER, W., and J. K. BLASIE. 1972. Direct determination of the structure of borium stearate multilayers by X-ray diffraction. *Biophys. J.* **12**:175–191.

LESSLAUER, W., J. E. CAIN, and J. K. BLASIE. 1971. On the location of 1-anilino-8-naphthalene-sulfonate in lipid model systems. An X-ray diffraction study. *Biochim. Biophys. Acta.* **241**:547–566.

LEVINE, Y. K., and M. H. F. WILKINS. 1971. Structure of oriented lipid bilayers. *Nat. New Biol.* **230**:69–72.

LIPSON, H., and C. A. TAYLOR. 1958. Fourier transforms and x-ray diffraction. G. Bell & Sons Ltd., London. 20–27.

LUZZATI, V., A. TARDIEU, and D. TAUPIN. 1972. A pattern recognition approach to the phase problem: application to the X-ray diffraction study of biological membranes and model systems. *J. Mol. Biol.* **64**:269–286.

MOODY, M. F. 1963. X-ray diffraction pattern of nerve myelin: a method for determining the phases. *Science (Wash. D.C.)*. **142**:1173–1174.

MOODY, M. F. 1974. Structure determination of membranes in swollen lamellar systems. *Biophys. J.* **14**:697–703.

PAPOULIS, A. 1962. The Fourier integral and its applications. McGraw-Hill Book Company, New York. 192–211.

ROBERTSON, J. D. 1958. Structural alterations in nerve fibers produced by hypotonic and hypertonic solutions. *J. Biophys. Biochem. Cytol.* **4**:349–364.

ROSS, M. J., M. KLYMKOWSKY, D. A. AGARD, and R. M. STROUD. 1977. Structural studies of a membrane-bound acetylcholine receptor from *Torpedo californica*. *J. Mol. Biol.* **116**:635–659.

SHANNON, C. E. 1949. Communication in the presence of noise. *Proc. IRE.* **37**:10–21.

WILKINS, M. H. F., A. E. BLAUROCK, and D. M. ENGLEMAN. 1971. Bilayer structure in membranes. *Nat. New Biol.* **230**:72–76.

WORTHINGTON, C. R., G. I. KING, and T. J. MCINTOSH. 1973. Direct structure determination of multilayered membrane-type systems which contain fluid layers. *Biophys. J.* **13**:480–495.

WORTHINGTON, C. R., and S. C. LIU. 1973. Structure of sarcoplasmic reticulum membranes at low resolution (17Å). *Arch. Biochem. Biophys.* **157**:573–579.

WORTHINGTON, C. R., and T. J. MCINTOSH. 1974. Direct determination of the lamellar structure of peripheral nerve myelin at moderate resolution (7Å). *Biophys. J.* **14**:703–729.

APPENDIX V

Structural Studies of a Membrane-bound Acetylcholine Receptor from *Torpedo californica*

J. Mol. Biol. (1977) **116**, 635–659

Structural Studies of a Membrane-bound Acetylcholine Receptor from *Torpedo californica*

MICHAEL J. ROSS†, MICHAEL W. KLYMKOWSKY‡
DAVID A. AGARD‡ AND ROBERT M. STROUD‡

Norman W. Church Laboratory of Chemical Biology
California Institute of Technology, Pasadena, Calif. 91125, U.S.A.

(*Received 29 June 1976, and in revised form 17 June 1977*)

Membranes prepared from *Torpedo californica* electroplax containing acetylcholine receptors have been studied by X-ray diffraction and electron microscopy. X-ray diffraction data suggest that acetylcholine receptor molecules traverse the endplate membrane, extending 15 ± 5 Å on one side of the bilayer and some 55 ± 5 Å on the other, with an overall length normal to the membrane of 110 Å.

Lattices of acetylcholine receptor have the symmetry of the crystallographic plane group $p1$, with one molecule per unit cell. A low-resolution projection of the surface structure of receptor arrays was determined by reconstruction of images from electron micrographs. The resolution of the image is ~ 20Å in the plane of the membrane. The electron density profile through the membrane, derived from X-ray diffraction of vesicle dispersions and of oriented membranes, has been analyzed to resolutions of 20 and 13 Å, respectively. The high-angle X-ray scattering pattern was observed to a resolution of 1·7 Å. Maxima in the scattering pattern were analyzed in terms of the state of the lipids and secondary structure in the membranes. Sharp maxima in the scattering pattern indicate that long stretches of secondary structure are present in the receptor-containing membranes. The receptor membranes contain repeating structural units of length 80 Å (5·2 Å repeat) oriented perpendicular to the membrane plane, and uninterpreted components greater than 90 Å in length with a basic repeat of 6·3 Å.

1. Introduction

Nicotinic acetylcholine receptor molecules provide one of several mechanisms found in nature for neural transmission. AcChR§-mediated synaptic transmission depends on pre-synaptic release of the low molecular weight transmitter, acetylcholine. After the transmitter diffuses across the synaptic space, it interacts with the membrane-bound receptor and effects depolarization.

The acetylcholine receptor has been shown to operate by increasing permeability to cations in the motor endplate (Takeuchi & Takeuchi, 1960). No permeability to anions was found. The ions are presumed to be conducted through a channel which spans the endplate membrane. The lifetime of this channel was estimated to be about

† Present address: The Biological Laboratories, Harvard University, Cambridge, Mass. 02138, U.S.A.

‡ Present address: Department of Biochemistry and Biophysics, University of California, School of Medicine, San Francisco, Calif. 94143, U.S.A.

§ Abbreviation used: AcChR, nicotinic acetylcholine receptor.

1 ms when excited by actetylcholine; during this time about 5×10^4 sodium ions can pass from one side of the membrane to the other (Katz & Miledi, 1972). The channel is presumably at least 5 Å across, since it has been shown to conduct cations as large as isopropyl ammonium (Furukawa & Furukawa, 1959).

Membrane fragments rich in AcChR have been purified from several species of electric eel and skate (Cohen *et al.*, 1972; Duguid & Raftery, 1973). The fact that membranes containing AcChR, acetylcholinesterase, or ATPase can be separated by sucrose gradient centrifugation suggests that the different proteins are localized in different regions of the postsynaptic membrane. Further purification of AcChR isolated from membranes by detergent extraction has been accomplished and the molecular weight of these isolated molecules estimated at 330,000 for AcChR from the species *Torpedo marmarota* and *T. californica* by Edelstein *et al.* (1975) and 380,000 for AcChR from *T. californica* by Vandlen & Raftery (1977).

Gel electrophoresis in the presence of sodium dodecylsulfate and crosslinking experiments have established a tentative subunit structure for AcChR; four different subunits have been identified (Weill *et al.*, 1974; Vandlen & Raftery, 1977). The stoichiometry of these subunits is estimated as A_4B_2CD, where A has a molecular weight of 41,000; B, 51,000; C, 60,000; and D, 64,000 (Vandlen & Raftery, 1977).

Studies reported here are concerned with the structure and organization of a membrane-bound acetylcholine receptor from the electric skate *T. californica*. Three major questions are considered: (i) the distribution of protein relative to the lipid leaflet in AcChR membranes; (ii) the secondary structure present within the membrane proteins and the thermodynamic state of the lipids; and (iii) the structure of the molecules at low resolution.

2. Materials and Methods

(a) *Sample preparation*

Samples of AcChR membranes were prepared by M. A. Raftery, R. Vandlen and collaborators as described by Reed *et al.* (1975). Argon or nitrogen-saturated buffers, low temperatures and added anti-oxidants (e.g. 3,5-di-*tert*-butyl-4-hydroxy-benzyl alcohol) were used to minimize lipid oxidation; phenylmethanesulfonyl fluoride (10^{-4} M) and EDTA (10^{-3} M) were added to inhibit proteolytic degradation (Vandlen & Raftery, 1977).

(b) *X-ray diffraction*

The X-ray camera used for both low- and high-angle pictures was designed by two of us (M.J.R. and R.M.S.). The source was a rotating anode generator (Elliott Neutron Division GX-6) run at either 1·6 kW with a 2·0 mm × 0·2 mm focus, or 0·6 kW with a 1·0 mm × 0·1 mm focus. The anode was viewed through a nickel filter at a takeoff angle of 3° to 6° to provide an approximately square image of the target. The beam was focused on to the film plane by 2 perpendicular, elliptically bent silica mirrors (Franks, 1955), and passed through a 1-mm hole in the center of the film into the direct beam trap. The sample was kept at 2°C in an atmosphere of hydrated nitrogen (for wet samples) or dry helium (for dried samples). Two 0·001-in Mylar® windows were used to isolate the sample chamber from both the room atmosphere and the dry helium which filled the remainder of the camera length. The films (2 per pack) were flat and oriented perpendicular to the beam; camera lengths from 1·0 to 19·7 cm were used; exposure times varied from 4 to 48 h.

Samples for diffraction analysis included dispersions of membrane vesicles, oriented membrane pellets of varying degrees of hydration, and dried pellets. Membranes were concentrated by centrifugation into specially designed polycarbonate sample holders contained in celluose nitrate preparative ultracentrifuge tubes. The sample holders allow for

collection of circularly averaged in-plane (equatorial) diffraction from the membranes, or for recording lamellar (meridional) and sectioned equatorial diffraction data.

In attempts to generate oriented pellets of membrane fragments, samples containing about 0·2 mg of protein were added to argon saturated buffer and were centrifuged at 120×10^3 to 300×10^3 *g* for 2 to 48 h in either Beckman SW-65L-Ti or SW-41-Ti rotors. Some samples were subjected to 3 freeze–thaw cycles (between − 80°C and + 5°C) immediately before centrifugation. This empirical procedure was found to assist in close-packing the pellets by breaking up the vesicles in the dispersions. Excess buffer was removed from the pellet with absorbant paper. Omitting this step allowed the membrane pellet to swell, and the orientation of the bilayers was lost. This resulted in an unoriented membrane dispersion.

(c) *Densitometry of X-ray films*

Films were digitized on a Syntex AD-1 autodensitometer and optical density measurements were corrected for film non-linearity using a logarithmic correction (Morimoto & Uyede, 1963). Intensities were obtained by annular averaging of optical densities within sectors around either the meridian or equator (Ross & Stroud, 1977). During the process of data analysis, it proved necessary to locate the center of the film to within ± 100 μm, and when sharp reflections were present to within ± 20 μm. The center was refined using iterative calculations based on the positions of pairs of equivalent reflections located on opposite sides of the film center.

(d) *X-ray data reduction*

Continuous diffraction data were obtained from partially ordered membrane pellets (see section (b) above), and from vesicle dispersions. The scattering from vesicle dispersions should represent the square of the transform of a single AcChR membrane, $F(s)$, multiplied by the transform of the vesicle shape and distribution. The effects of vesicle size and curvature should be small perturbations only on the observed transform since the vesicles are quite large (~ 1 μm) (Lesslauer *et al.*, 1971; Moody, 1975). Meridional scattering (i.e. perpendicular to the membrane sheets) from partially ordered membrane sheets was corrected for background scatter by subtracting the equatorial from the meridional scattering. Observed intensities were then corrected for finite beam size, beam divergence and degree of orientation in the sample. The amount of orientation present in the sample was estimated from the angular width at half-maximum of peaks in the meridional scattering pattern. This angular width was typically ± 12° to ± 40°.

The background function for the unoriented vesicle data was more difficult to obtain and required a separate, shorter exposure from a much lower sample concentration. The scattering pattern from a more dilute vesicle dispersion should contain a smaller component of $F(s)$ in proportion to the background scatter $B(s)$, and the presumption is that the background scatter should be of the same form. In order to obtain a measure of $I(s) = |F(s)|^2$, the two scattering patterns $I_1(s)$ from the concentrated solutions and $I_2(s)$ from the dilute dispersions were scaled together. First, the constant density level on the films at high angles ($s^{-1} < 10$ Å) was subtracted both from $I_1(s)$ and from $I_2(s)$, on the assumption that such scattering contains little or no component from $F(s)$. After this background was subtracted, the scattering from the more dilute sample $I_2(s)$ was scaled up by a constant multiplicative factor c such that $I_1(s) \geq I_2'(s)$ for all values of s. $I_2'(s)$ equalled $I_1(s)$ at only one value of $s^{-1} = 22{\cdot}7$ Å, where $F(s)$ had its lowest minimum. The modulus of the transform, $|F(s)|$, was then approximated as $|F(s)| = \sin\theta\,(I_1(s) - cI_2(s))^{\frac{1}{2}}$. The appropriate geometric factor of $\sin\theta$ was derived by Levine & Wilkins (1971).

Fourier refinement of electron density profiles against $|F(s)|$ was carried out by the method of Stroud & Agard (1977) (see section (e)).

(e) *Determination of asymmetric membrane profiles*

An iterative Fourier refinement method was developed and used to calculate electron density profiles for asymmetric membranes, projected onto a line perpendicular to the membrane surface. The method is described in detail by Stroud & Agard (unpublished work) and a short description only is given here.

The method relies on Fourier refinement of an electron density function $\rho(r)$ against the continuous transform $F_0(s)$ derived from continuous X-ray scattering patterns. In this procedure an arbitrary starting model $\rho'(r)$ is used to calculate $F'(s)$ according to

$$F'(s) = \int_{r=-\infty}^{+\infty} \rho'(r) \exp(2\pi i r.s)\, \mathrm{d}r \tag{1}$$

where r and s are perpendicular to the membrane surface and i is $\sqrt{-1}$. The phases of $F'(s)$ are associated with the observed $F_0(s)$ to give $F_0'(s)$ and back transformed according to

$$\rho''(r) = \int_{s=-s_1}^{s_1} F_0'(s) \exp(-2\pi i r.s)\, \mathrm{d}s \tag{2}$$

where s_1 is the limiting maximum resolution to which the scattering pattern is observed. The function $\rho''(r)$ is constrained to lie within some estimated boundary thickness $a<r<b$ such that $\rho''(r) = 0$ for $a>r>b$, and the process is repeated beginning with equation (1) until convergence is achieved, which typically involved ~ 30 cycles.

The chosen boundary thickness $t = b - a$ is unimportant in determining the final solution, provided that it is greater than the true membrane thickness and less than ∞. No converged solution can be obtained if the boundary thickness is chosen to be smaller than the true thickness. The actual thickness of the membrane leaflet is determined by the solution obtained. This can be shown as follows. Any converged solution obtained will necessarily obey the normal Fourier inversion relationships

$$\rho(r) = \int_{s=-s_1}^{s} F_0(s) \exp(-2\pi i r.s)\, \mathrm{d}s \tag{3}$$

and

$$F_0(s) = \int_{r=-\infty}^{+\infty} \rho(r) \exp(2\pi i r.s)\, \mathrm{d}r. \tag{4}$$

The autocorrelation function

$$Q(r) = \int_{r'=-\infty}^{+\infty} \rho(r')\, \rho(r' + r)\, \mathrm{d}r' = \widehat{\rho(r)\rho(-r)}$$

and the Patterson function

$$P(r) = \int_{s=-s_1}^{s_1} |F_0(s)|^2 \exp(2\pi i r.s)\, \mathrm{d}s$$

(which is uniquely determined by the observables $|F_0(s)|$ will necessarily be exactly equivalent, $P(r) = Q(r)$ (Lipson & Taylor, 1958). Since the Patterson function $P(r)$ will be 0 for $r>w$, where w is the true thickness of the membrane, any solution $\rho(r)$ which is of less than infinite extent must be bounded within the thickness w. If $\rho(r)$ were of any other thickness, the convolution product $Q(r) = \widehat{\rho(r)\rho(-r)}$ could not match $P(r)$, and $\rho(r)$ could not be a converged solution to equations (3) and (4). Therefore, all refined solutions will necessarily be of the same thickness, w.

The imposition of a boundary thickness serves only: (a) to eliminate the trivial solutions for which $\rho(r)$ is of infinite extent, obtained by applying any random set of phases to $|F_0(s)|$; and (b) to accelerate convergence to a solution. If more than one solution, $\rho(r)$, exists which is compatible with a thickness of w, then these will form a set of possible solutions which cannot be eliminated without further information, by any method of treating $|F_0(s)|$ (Stroud & Agard, unpublished work). The choice of starting model $\rho'(r)$ in these instances will tend to select for the solution closest to the starting model. Consequently, this approach can be used to test hypothetical structures. Obviously, if only one $\rho(r)$ exists, this procedure will converge upon that structure regardless of the starting model used. In practice it seems that when multiple solutions do exist they are often qualitatively quite similar to one another. In most of the simpler membrane-like trial structures tested by Stroud & Agard (unpublished work) and in the case of acetylcholine receptor membranes considered here, it appears that the solution is unique. The method was also tested on the asymmetric purple membrane from *Halobacterium halobium* using the data of Blaurock & Stoeckenius (1971). Only two solutions were obtained which were identical to those of

Blaurock & King (1977). It was also tested on one set of myelin data of Worthington & McIntosh (1974) for the centrosymmetric myelin structure. In this case 4 solutions were obtained, 2 of which coincided with those of Worthington & McIntosh (1974).

Our considerations here have assumed that $|F_0(s)|$ contains no error. The effects of data errors are considered by Stroud & Agard (unpublished work). In practice the values of $|F_0(s)|$ should be extracted with care to try to achieve this condition. If there is independent evidence for the thickness of the leaflet, then imposition of the boundary thickness can serve to minimize possible errors introduced by certain kinds of data errors. These include the kind of errors which contribute to the Patterson function $P(r)$ at $r>w$. If such errors in the data exist, they will be assayed by the final agreement between $|F_0(s)|$ and $|F_c(s)|$. The agreement index

$$R = \frac{\int_{s=0}^{s_1} ||F_c(s)| - |F_0(s)|| \, ds}{\int_{s=0}^{s_1} |F_0(s)| \, ds}$$

was used as an index of the extent of convergence, and typically refined to a value of 0·3 to 1% for artificially created test data, or 1 to 5% for acetylcholine receptor membranes.

If the data $|F_0(s)|$ are cut off at some particular resolution, the final structure $\rho(r)$—and the Patterson function $P(r)$—will contain series termination ripples which could be potentially misleading. In any real case data to the highest observable resolution should be included, such that $|F_0(s)| \to 0$ at the resolution cutoff limit.

This method is efficient and can be applied to the continuous scattering profiles for symmetric or asymmetric membranes. Continuous scattering profiles may be derived either from dispersions of membranes, or extracted from a series of swelling experiments applied to close-packed sheets, as for example was carried out by Worthington & McIntosh (1974) for myelin. For asymmetric structures the X-ray scattering pattern from close-packed sheets is made only more complex by statistically ordered stacking. Since the overall scattering pattern is sampled by a statistical stacking function which is exceedingly difficult to derive, the transform of a single membrane sheet is equally difficult to derive. Therefore, continuous scattering patterns derived from membrane dispersions are intrinsically more manageable, and also contain a greater degree of information due to the continuity of the function $F(s)$.

This application of Fourier refinement is capable of determining and refining all possible solutions for the electron density function, although absolute certainty that all solutions have been obtained would require testing of a large number of possible alternatives. In practice, the number of real alternatives is limited to those consistent with the maximum and minimum electron density allowed by the chemical constituents of the system, i.e. to chemically reasonable alternatives which can in principle all be tested. The more difficult question is whether a determined solution is *necessarily* the correct one. If more than one solution is obtainable, it can be shown that identification of the correct one requires experimental evidence of a different type (Stroud & Agard, unpublished work), such as isomorphic replacement. Thus, in reporting membrane profiles many solutions should be sought and reported where obtainable.

(f) *Electron microscopy*

Negatively stained samples were prepared and imaged as described by Klymkowsky *et al.* (unpublished work). Images were also recorded on a tilting stage in a Philips EM301 electron microscope. This allowed for recording views of up to 60° from the normal to the membrane surface.

Thin sections of pellets used for X-ray diffraction were embedded, stained and analyzed by electron microscopy as follows: the pellets were glutaraldehyde/formaldehyde fixed (4% formaldehyde, 5% glutaraldehyde in 0·05 M-sodium/potassium phosphate buffer, pH 7·4) for 2 h and washed overnight in phosphate buffer. The pellets were further fixed in 1% osmium tetroxide also buffered in 0·05 M-phosphate buffer (pH 7·4) for 2 h, dehydrated and embedded in Epon 812 epoxy resin (Luft, 1961). Thin (silver gray) sections were cut parallel to the direction of sedimentation using a freshly made glass knife, and lead citrate post-stained before viewing (Reynolds, 1963). No change in pellet thickness

occurred during the fixation or embedding. Micrographs were taken on a Philips EM301 at 80 kV. Acetylcholine receptor protein was positively identified in the microscope by use of receptor-specific antibodies (Klymkowsky & Stroud, unpublished work).

(g) *Image reconstruction*

Well-ordered areas on the micrographs were identified by visual inspection and assayed for degree of perfection by optical diffraction or by computer transform. Optical diffraction was carried out on an optical diffractometer (Markham, 1968) using He–Ne laser illumination (Hughes, model no. 3599H) and an oil-filled film gate.

Areas of electron micrographs of negatively stained samples containing an ordered array were digitized using a Syntex AD-1 flatbed scanner. Data were collected using a 32 μm $\times$ 32 μm illuminating aperture and a 32 μm step-size. This step-size corresponds to a spacing of 2 to 4 Å in the micrographs of arrays that were analyzed.

Selected areas were densitometered and Fourier transformed using a 2-dimensional fast Fourier algorithm (Cooley & Tukey, 1965)†. For image reconstructions, the mean O.D. of the area was subtracted from all picture elements, and the digitized image was "floated" in borders equal to half of the original image size in all directions (DeRosier & Moore, 1970). After Fourier transformation, the reciprocal lattice parameters were refined by a weighted least-squares procedure, and the patterns indexed according to the distribution of intensities in the pattern, such that $F_{(10)} > F_{(01)} > F_{(1\bar{1})}$.

Each lattice chosen for reconstruction was checked by examining the deviation of the positions of the observed maxima in the Fourier transform from their expected positions. Any lattice with an overall standard deviation of greater than $\pm$ 0·75 (scan area)$^{-1}$ was rejected. The magnitudes of the Fourier coefficients at each diffraction maximum were examined and those lattices containing split peaks (indicative of a distorted lattice Klymkowsky *et al.*, unpublished work) were also rejected. Phases of the stronger reflections were examined for discontinuities within the region of a diffraction maximum. If phase incoherence was found, the lattice was rejected.

Two courses of action were taken with respect to the reconstruction of the final image. A digital process, formally identical to the optical filtering techniques developed by Klug & DeRosier (1966), was used to take the masked Fourier transform and back-transform it into real space. This pseudo-optical masking suffers from 2 disadvantages when applied to AcChR membrane lattices in that: (i) low frequency components of the noise, corresponding to repeats greater than the inverse of the mask aperture used around each diffraction spot, are not removed (Erickson, 1974); and (ii) whatever lack of phase coherence exists across each reflection remains. These low frequency terms are sometimes quite large and are mainly due to stain variations on the sample. Compared with stained 3-dimensional crystals (e.g. catalase) the signal-to-noise ratio in the diffraction pattern for AcChR membrane was about 5 times worse. In addition, the pseudo-optical process leads to an ordered image even when applied to an area of incoherent noise in the Fourier transform (Klug & DeRosier, 1966; Gibbs & Rowe, 1973). The test of phase consistency places a further constraint on the choice of acceptable intensities in the diffraction pattern, and consequently provides a measure of reliability for the image.

The second method was an averaging procedure where amplitudes $F_{(hk)}$ for each reflection were generated by integration of the peaks. Phases $\phi_{(hk)}$ were calculated as the weighted average across the peak. Weighting was according to the square of the amplitude at points in a 3 $\times$ 3 or 5 $\times$ 5 array surrounding the lattice points, thus

$$\phi_{(hk)} = \tan^{-1}\left(\frac{\sum_{ij} F_{ij}^2 \sin(\phi_{ij})}{\sum_{ij} F_{ij}^2 \cos(\phi_{ij})}\right)_{(hk)}.$$

The averaged structure factors were placed at the refined reciprocal lattice points.

† All calculations were done on a Data General NOVA800 computer with 32k words of core, a Syntex Analytical Instruments floating point processor, a 2·5 M byte disk, and two 800 BPI 9-track tape units. Times for transform calculations using the program written by one of us (M.J.R.) are: 128 $\times$ 128 transform, 3 min; 256 $\times$ 256 transform, 13 min; 512 $\times$ 512 transform, 1 h 10 min. If a real-hermite transform is calculated instead of a complex–complex transform, these times are halved.

As a quantitative measure of the quality of each reconstruction, the weighted average phase for each reflection was compared to each of the individual phases that went into calculating this average. The weighted mean phase angle discrepancy and the weighted mean cosine of this angle ("figure of merit") were calculated for each reflection according to

$$\Delta\phi_{(hk)} = \left(\frac{\sum_{ij} F_{ij}^2 \, (\phi_{ij} - \bar{\phi})}{\sum_{ij} F_{ij}^2} \right)_{(hk)}$$

$$m_{(hk)} = \left(\frac{\sum_{ij} F_{ij}^2 \cos(\phi_{ij} - \bar{\phi})}{\sum_{ij} F_{ij}^2} \right)_{(hk)}.$$

An overall figure of merit was also calculated for the entire diffraction pattern:

$$m = \frac{\sum_{hk} F_{(hk)}^2 \, m_{(hk)}}{\sum_{hk} F_{(hk)}^2}.$$

The possibility of reinforcing errors in the averaging procedure is perhaps greater than in the pseudo-optical case, since the reconstructed image is perfectly repeating by definition. Thus, the figure of merit becomes a very important measure of the validity of each reconstruction. A good AcChR reconstruction gave an overall figure of merit of 0·95 to 0·99 with no reflection below 0·80. In comparison the overall figure of merit for reconstruction on an unordered area or using incorrect lattice parameters ranged from 0·2 to 0·8 with individual figures of merit as low as 0·05 to 0·3.

3. Results

(a) *Membrane profile analysis*

In an attempt to characterize the distribution of protein and lipid in the membranes, the continuous X-ray scattering profiles from pelleted samples were analyzed. The X-ray scattering pattern shown in Figure 1 is typical of those generated from partially oriented pellets. There is no indication of regular stacking in the meridional direction, or of regular order in the plane of the membranes. Such order would give rise to equatorial diffraction (horizontal in Fig. 1). This is consistent with our observation that most of the sample ($> 99\%$) does not contain arrayed structures (Klymkowsky *et al.*, unpublished work). (Further close packing of the membranes results in a much more complex problem of analysis (Stroud & Agard, unpublished work) due to statistical sampling, therefore such patterns were not used for profile structure determination.)

The meridional pattern from hydrated pellets showed a continuous scattering profile, with the first minimum at $d = 110$ Å, and maxima at d spacings of about 76 Å and 37 Å. Meridional scattering from oriented dried pellets showed a broad maximum centred at $d = 59$ Å, presumably due to the scattering function of the denatured membranes (see Fig. 2). Oriented patterns provided a means of separating the meridional scattering pattern from the equatorial scattering. The meridional scattering function $|F(s)|$ was calculated.

In view of the possibility that the oriented patterns such as those shown in Figure 1 contain sampling due to close-packing within the pellet, $|F(s)|$ was also derived from vesicle dispersions.

Electron density profiles through the membrane were determined by Fourier refinement (see Materials and Methods, section (e)). In order to speed convergence, and to minimize the effect of data errors, a rough estimate of the membrane thickness was estimated as follows.

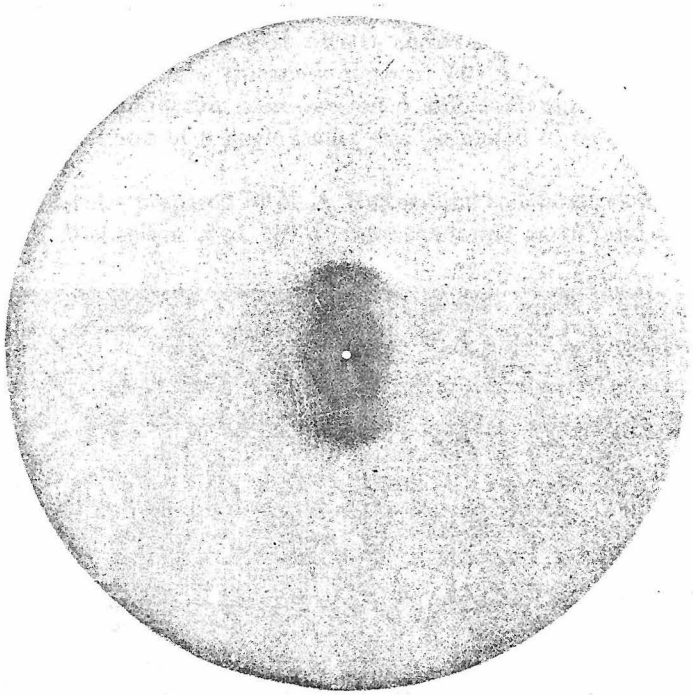

FIG. 1. Typical small-angle scattering pattern from partially oriented pellets of AcChR-rich membranes shows meridional diffraction with maxima at spacings of 76 Å and 37 Å. Angular dispersion of the peaks is about ± 22° (relative humidity 100%).

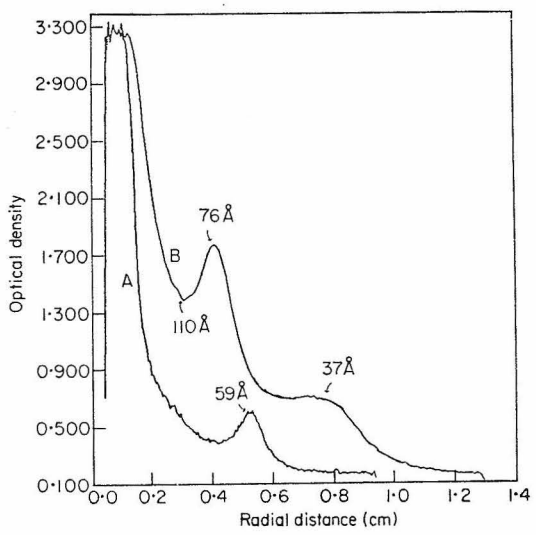

FIG. 2. Densitometer tracings of small-angle X-ray films of partially oriented pellets of AcChR membranes computed from annular integrations within an angular spread of ± 20° of the meridian. Curve A, tracing derived from a 2-h exposure of a dried pellet; curve B, integrated data from the film shown in Fig. 1.

(i) The Patterson function $P(r) = \int F^2(s) \cos(2\pi rs)ds$ calculated from vesicle dispersion data gave an indication of the largest vectors across the membrane leaflet, which indicated a minimum membrane thickness of about 110 Å.

(ii) Pellets used for X-ray diffraction were sectioned and analyzed by electron microscopy (Fig. 3). The thickness of a single leaflet was estimated to be about 100 $\pm$ 25 Å.

(iii) Isolated AcChR molecules prepared by M. A. Raftery and collaborators according to the procedures of Michaelson *et al.* (1974) were shadowed at 15° and at 45°

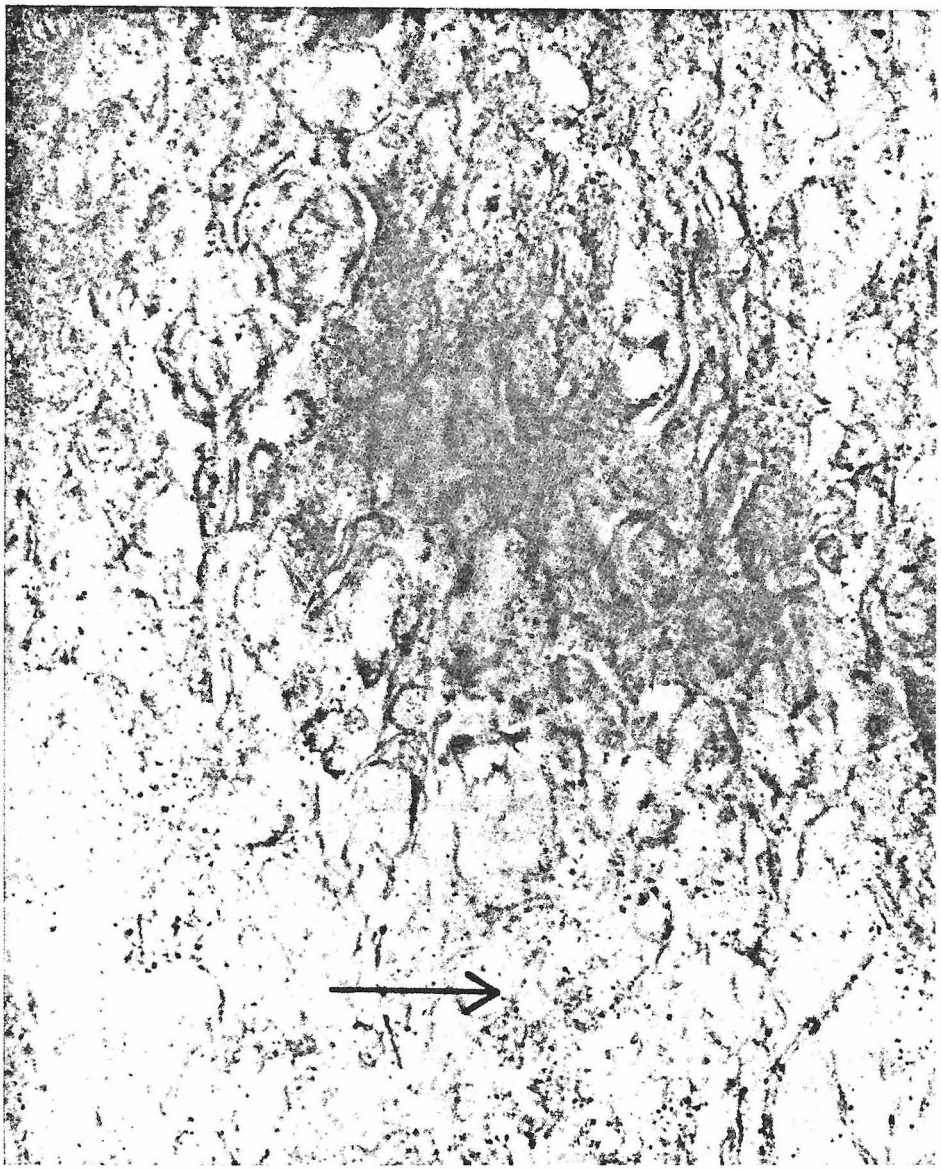

FIG. 3. Thin section of a partially oriented pellet of AcChR membrane vesicles. The direction of sedimentation in the pellet is indicated by the arrow. Membranes appear as dark lines with an average thickness of ~100 Å. The arrow represents a distance of 7600 Å on the micrograph.

with platinum (Kent & Stroud, unpublished results, 1974). Particles seen in the electron microscope were equidimensional with diameters of approximately 85 to 125 Å.

The corrected scattering function $|F(s)|$ from vesicle dispersions (Fig. 4(a)) and the corrected meridional scattering from partially oriented samples (Fig. 4(d)) were used as a basis for one-dimensional electron density refinement. After 40 cycles of refinement from many different starting models, the structures shown in Figure 4(b) and (e) were obtained. A boundary thickness of 115 Å was used to refine the electron density profile obtained from the vesicle data. Narrower boundaries do not permit a solution to be obtained, and wider boundaries slow convergence to the same solution.

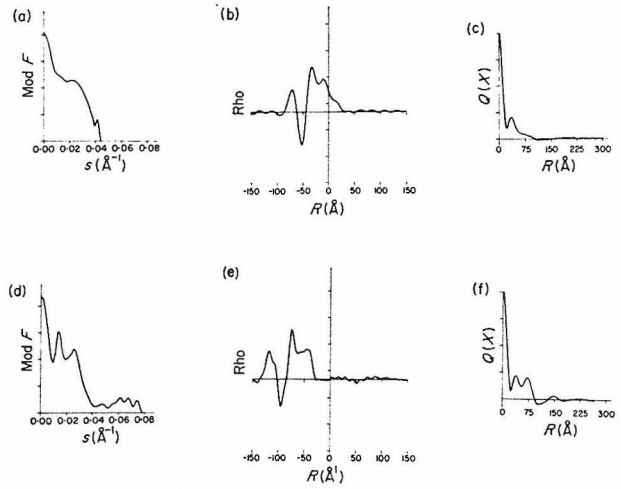

FIG. 4. Results of Fourier refinement of diffraction data from vesicle dispersions ((a) (b) and (c) to a resolution of 22Å, and from partially oriented membranes ((d), (e) and (f)) to a resolution of 13Å. Starting models included rectangular box functions, a delta function, and linear ramp functions. All gave the same results. Calculated and observed continuous scattering patterns for each of these data sets are shown superimposed in (a) and (d). The electron density profiles computed from these X-ray data are seen in (b) and (e). (c) and (f) Each contain superimpositions of the autocorrelation and Patterson functions ($R_P = 2{\cdot}3\%$ and $R_P = 1{\cdot}1\%$, respectively). (Solutions $\rho(r) = \pm\rho(\pm r)$ are mathematically equivalent. Only one for which $\tilde{\rho}(r) > 0$ is shown, since solutions where $\tilde{\rho}(r) < 0$ are chemically unreasonable.)

Application of the Fourier refinement method to the diffraction data from the partially oriented sample indicated that these data are also inconsistent with a structure narrower than 110 Å. Using a boundary width of 120 Å, the agreement between observed and calculated $|F(s)|$, and the Patterson and autocorrelation functions was considerably worse than found for the vesicle data. However, if the boundary was then relaxed to 300 Å, agreement was radically improved, and the results shown in Figure 4(e) and (f) were obtained. It is important to note that the membrane profile itself did not change significantly.

The agreement between observed and calculated scattering functions after refinement are indicated in Figure 4(a) ($R = 2{\cdot}3\%$) and (d) ($R = 1{\cdot}25\%$). The Patterson and autocorrelation functions in the two cases, as shown in Figure 4(c) and (f), are also in excellent agreement, and this provides a second indication that a converged solution has been obtained.

The two structures shown in Figure 4(b) and 4 (e) are surprisingly similar in general features, although they differ in nominal resolutions ($1/s_{max} = 22$ Å for vesicle data

and 13 Å for oriented patterns). Both profiles have characteristics of a bilayer structure in that the distance between the highest peaks on either side of the negative density region was 40 ± 3 Å. The negative density relative to solvent is interpreted as the center of a bilayer. Both profiles also indicate an extension of density on one side of the bilayer by some 55 ± 5 Å. The height of the peak for phosphatidyl head groups on the other side is lower, and may be due to insertion of a greater proportion of lower density material, i.e. protein or solvent, on that side. It therefore seems that protein extends mostly on one side of the membrane (~55 Å) and very little (~15 Å) on the other (see Discussion).

It must be noted that there is a difference between the oriented and vesicle-scattering profiles, and between the Patterson syntheses calculated in the two cases. This is primarily reflected in the peak at $d = 76$ Å, which is a shoulder in the vesicle profile (see Fig. 4(a) and (d). The difference may be due to the lower intensity, and therefore lower accuracy, of the radially smeared vesicle-scattering function, or may be due to a stacking disorder in the oriented pattern. The second explanation seems most reasonable since the refined electron density function from oriented sample seems to contain a second "ghost" membrane profile of much weaker amplitude, as would be expected if there was a small amount of close packing in the specimen (Stroud & Agard, 1977).

A thin section of partially ordered membrane pellet shows a degree of ordering in the pellet qualitatively consistent with the small-angle X-ray results (Fig. 3). The average intermembrane distance (in the pelleting direction) is ~800 Å; however, the membranes occasionally appear as pairs with much closer spacings between the two sheets in a pair. The bilayers in each close pair of membranes are an average of 225 Å apart (center to center) with a standard deviation of ± 90 Å, and approach as close as ~105 Å. This could account for the small amount of statistical sampling implied in the X-ray pattern of partially ordered pellets.

(b) *Image enhancement*

The nature of negative staining makes interpretation of stained images less than straightforward. According to current models (Horne & Whittaker, 1962), the heavy metals form an amorphous glass over the specimen, filling in uneven features on the surface of the membrane. Stain density should therefore be inversely proportional to the surface relief of the membrane-bound components. Multiple-tilted views of each specimen are required to obtain unequivocal information about the distribution of stain in the third dimension.

Some membrane fragments contained areas of extended lattice organization which allowed the application of image enhancement techniques to certain areas (Klymkowsky *et al.*, unpublished work; and Fig. 5). The contrast transfer function (Erickson & Klug, 1971) was evaluated from the image transforms. All images were underfocused to achieve maximum contrast. The first phase change in the transfer function occurred at about 15 to 18 Å resolution. All maxima in transforms used for reconstruction were of lower resolution than the first node in the transfer function, thereby eliminating the need for phase correction.

The transform to 20 Å resolution contained 32 independent (hk) reflections out to the fourth order ($h = 4$) for each latticed array (see Fig. 6). Typically 18 to 23 reflections had enough significant intensity and phase coherence for inclusion in the reconstruction.

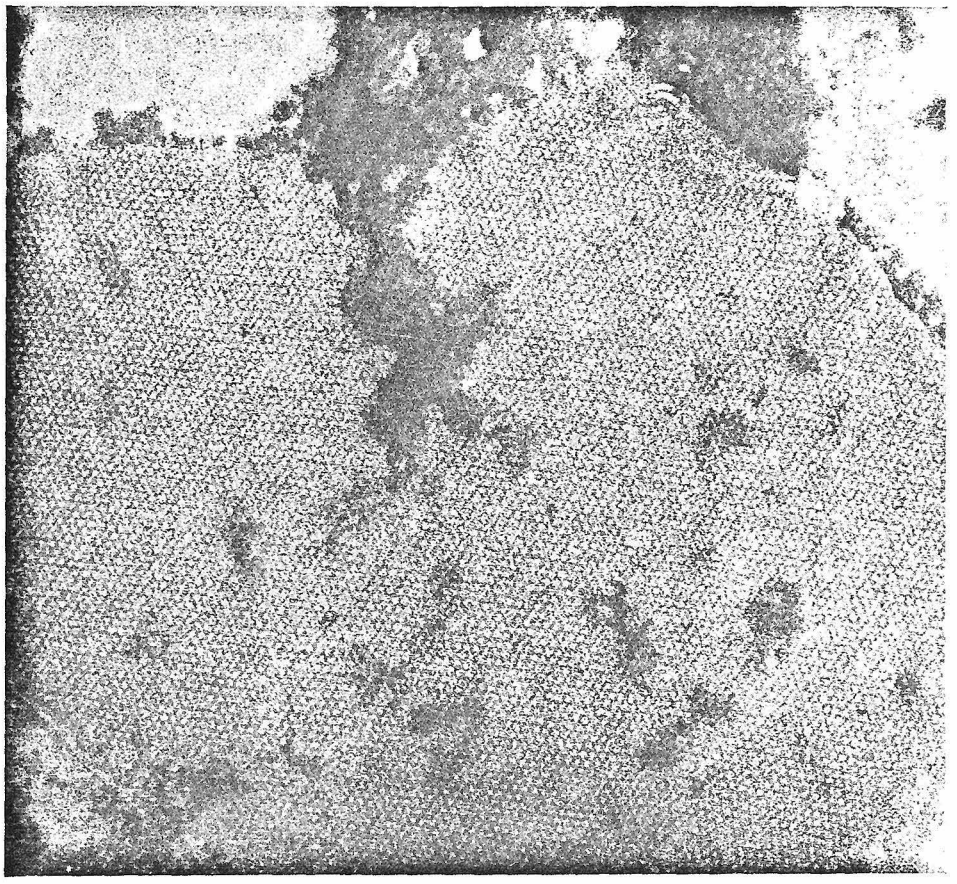

FIG. 5. Negatively stained (1% phosphotungstate, 0·1% uranyl acetate, pH 6) AcChR-rich membrane with a high degree of ordering. Electron optical magnification 98,000×.

Many images contained two or more ordered arrays. These were separated in the Fourier transform and treated separately. Reconstructed images from the separated lattices of two-layer structures (stained with uranyl acetate) consistently gave either of two different views of the receptor ((a) and (b) in Figs. 7, 8 and 9). One of these views indicated that the stain penetrated a well in the center of the molecule. The reconstructed molecule looked like the isolated particles seen in vesicles (Klymkowsky *et al.*, unpublished work; also (a) in Figs. 7, 8 and 9). The alternative view consistently showed a groove part of the way across the molecule, with a shallower central well ((b) in Figs. 7, 8 and 9). The presence of these two different views from alternate layers of moiré patterned images suggests a different distribution of stain in the upper layer and the layer in contact with the grid. The particles seen in reconstructed images (with either phosphotungstate or uranyl acetate staining) are not centrosymmetric, even at lower resolution (90 Å), indicating that the phases are inconsistent with the oblique plane lattice $p2$. The lattice therefore has $p1$ symmetry.

Reconstructed images from phosphotungstate-stained material indicated much weaker staining of the central well than was seen with uranyl acetate, and this may be due to some degree of positive staining with uranyl cations in this area, which is

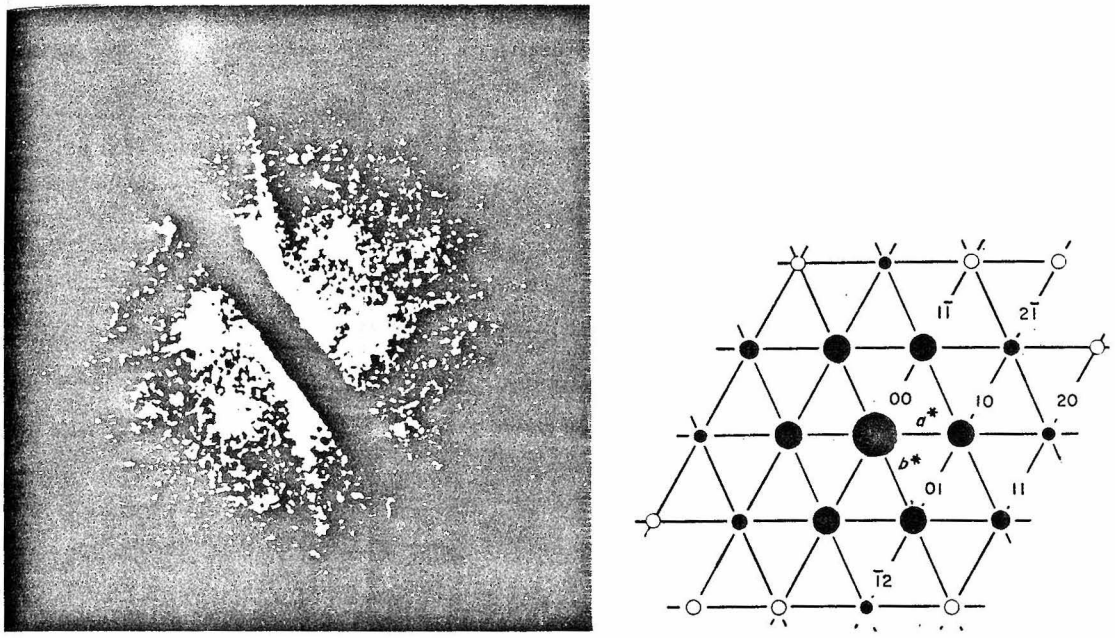

(a) (b)

(c)

FIG. 6. (a) Optical diffraction pattern showing intensities from an array.
(b) Schematic of the reciprocal lattice in (a).
(c) A computed transform showing amplitudes $|F_{hk}|$ masked according to the aperture sizes used in Fig. 7.

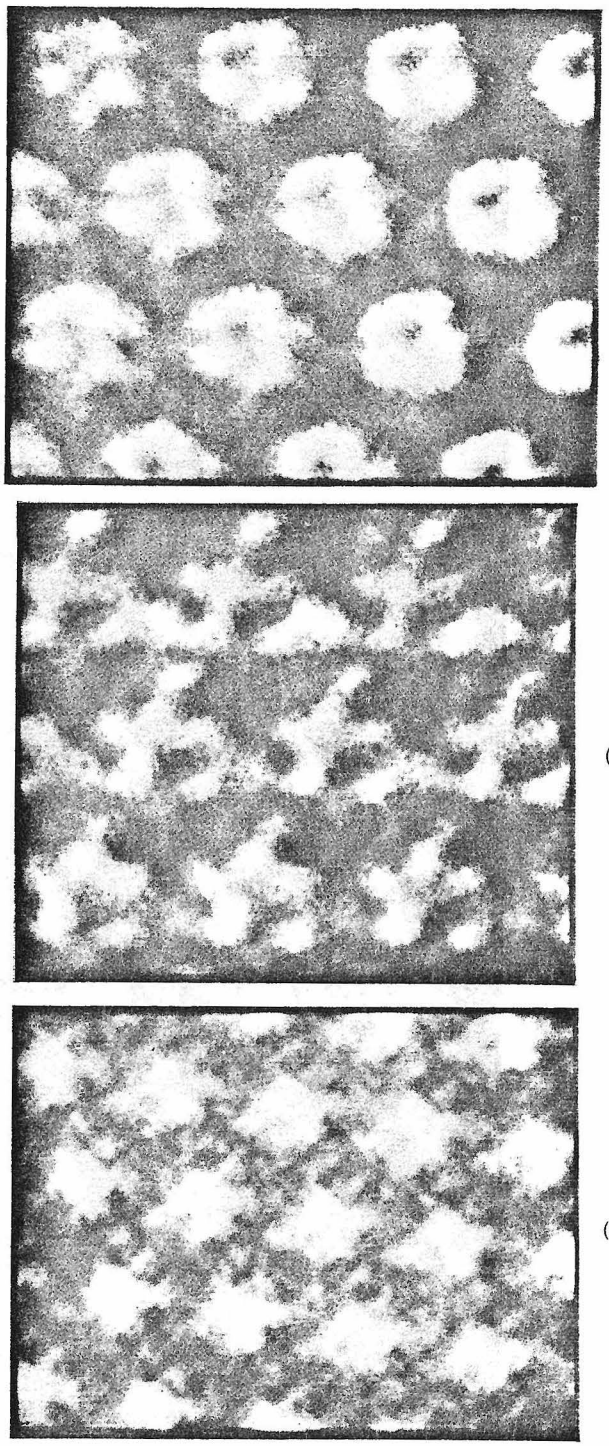

FIG. 7. Pseudo-optically enhanced images. Stain is dark.

(a) and (b) Typical uranyl acetate stained images from alternate sheets of 2 overlaid AcChR membranes. Separate reconstructions were carried out on each of the moiréd lattices by masking of the 32 independent reflections from each lattice (resolution 20 Å).

(c) Phosphotungstate-stained image of one sheet of AcChR membrane. 23 independent reflections were masked and used in reconstruction (resolution 20 Å).

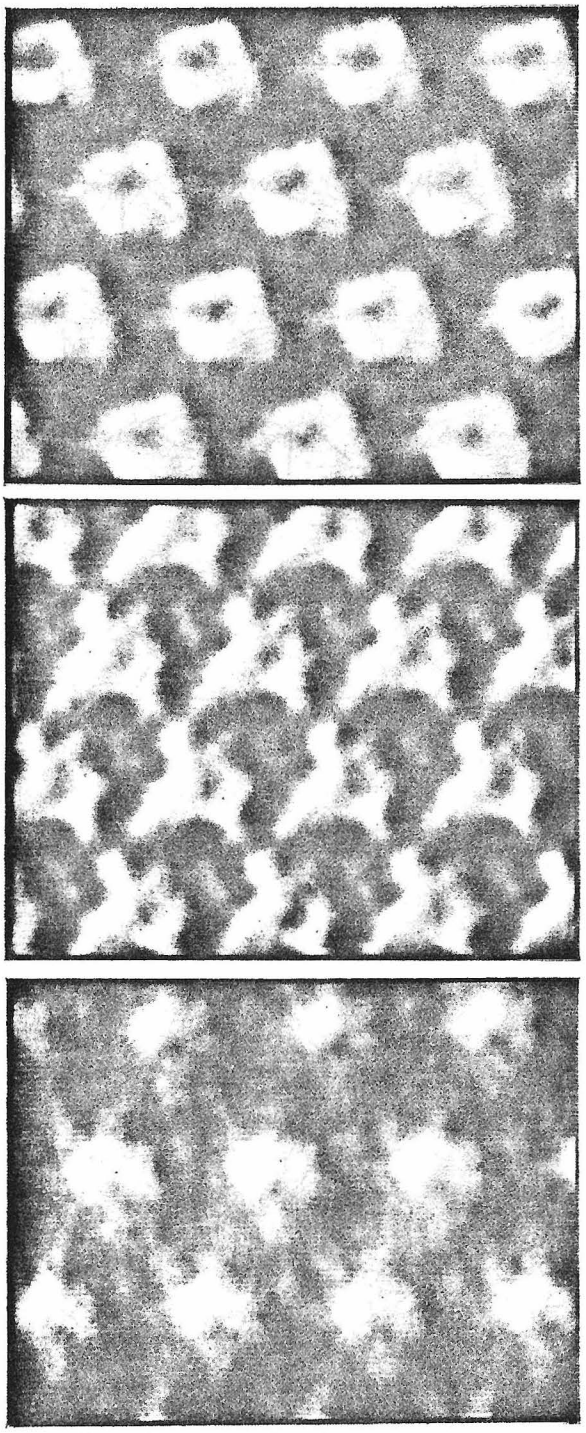

FIG. 8. Images enhanced by phase averaging show: (a) and (b) the 2 characteristic images from alternate layers of double-layered structures, stained with uranyl acetate; (c) the characteristic pattern seen with phosphotungstate stain (stain is dark).

(a) 18 independent reflections phase-averaged. Average overall positional error in diffraction centers was $x = 0{\cdot}57$, $y = 0{\cdot}41$ (scan area)$^{-1}$ from calculated lattice positions. First-order maxima were at a spacing of $\sim$25 (scan area)$^{-1}$. Overall figure of merit = 0·96.

(b) 22 independent reflections used. Averaged overall error in $x = 0{\cdot}47$, $y = 0{\cdot}43$ (scan area)$^{-1}$ from calculated lattice positions. Overall figure of merit = 0·90.

(c) 18 independent reflections used. Average overall error $x = 0{\cdot}54$, $y = 0{\cdot}60$ (scan area)$^{-1}$. Overall figure of merit = 0·96.

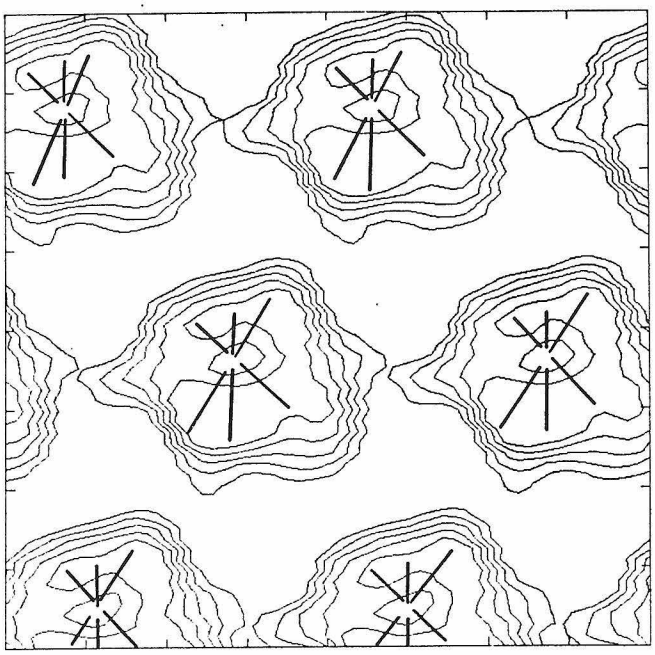

(a)

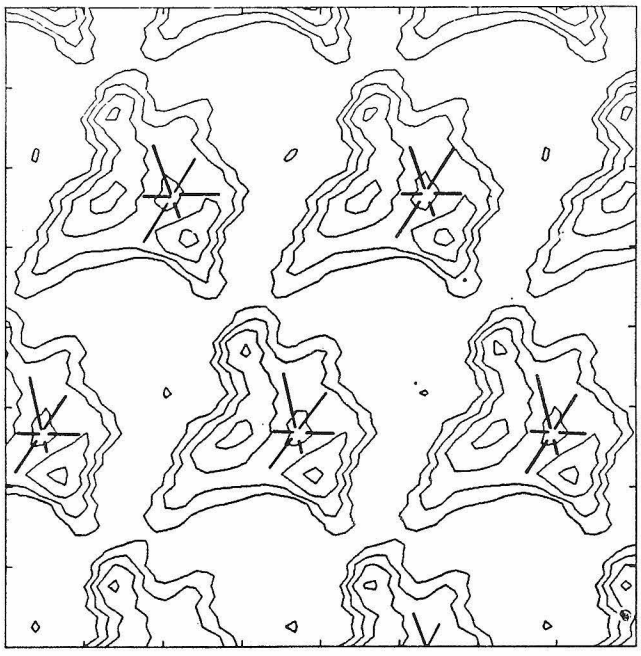

(b)

FIG. 9

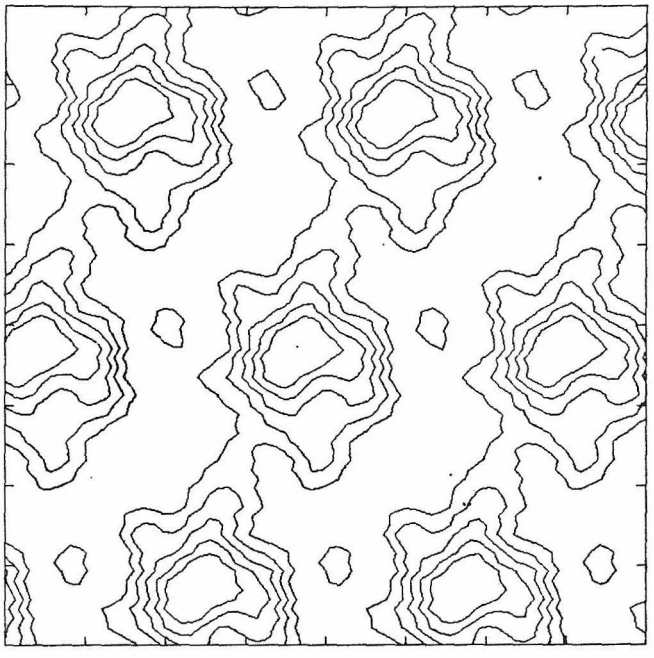

(c)

FIG. 9. Contoured plots of phase-averaged images. The images shown in Fig. 8(a), (b) and (c) were contoured at isodensity levels to indicate the overall molecular shape and lattice contacts present in AcChR membranes. (a) and (b) Uranyl acetate; (c) phosphotungstate.

not matched by phosphotungstate anions. This is not unreasonable if the central well constitutes an ion channel, since the channel transports only positive ions.

(c) *Secondary structure*

High-angle X-ray diffraction photographs of AcChR-rich membrane vesicles reveal several broad maxima characteristic of lipid or water spacings (Fig. 10(a) and (b)). A broad band centred at d-spacing of 4·6 Å is characteristic of the inter-hydrocarbon chain spacings in lipids above the fluid–crystalline phase transition (Luzzati *et al.*, 1960). A sharper maximum at $d = 4{\cdot}2$ Å is expected for the crystalline lipid phase (Dervichian, 1964). High-angle vesicle patterns recorded at either 2°C or 20°C (relative humidity 100%) indicate that a small proportion of the lipids are in the crystalline phase. The phase transition is broad, and this is not surprising in view of the temperatures of the natural habitat of *Torpedo*.

As a quantitative assay for the orientation of these rings, a difference plot of the equatorial pattern subtracted from the meridional pattern was calculated (Fig. 11). 4·2 Å diffraction appeared in both meridional and equatorial scans; however, the diffraction from fluid phase lipids at 4·6 Å was strongly equatorially oriented. This would suggest that most of the lipids contained in the oriented vesicles are above their phase transition temperature (at 2°C), but that part of the sample contains crystalline lipids. These are presumably not in vesicles or sheets and thus do not orient during pelleting.

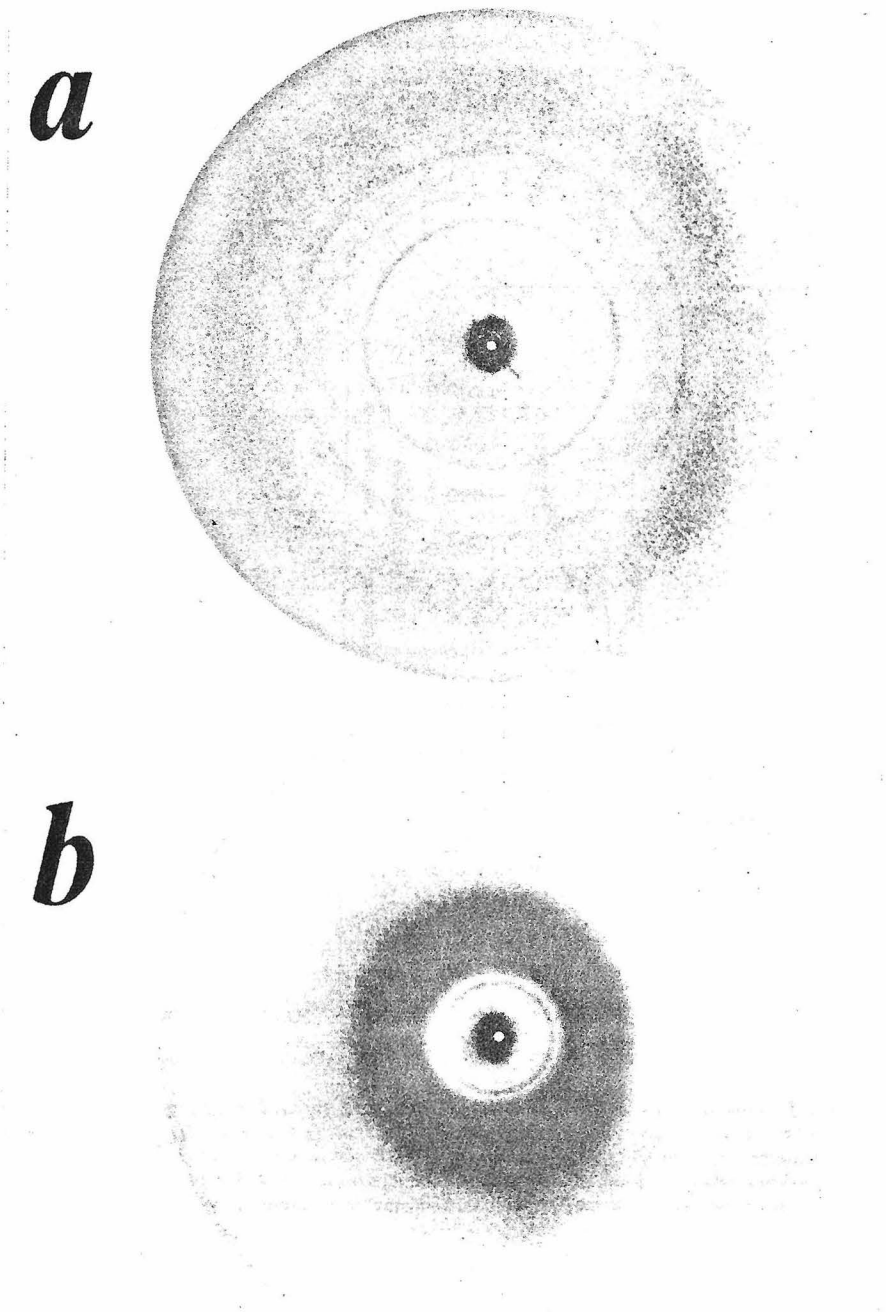

FIG. 10. High-angle X-ray diffraction from partially oriented membrane samples (meridian vertical).

(a) Camera length was 4·66 cm. Exposure time was 15 h. X-ray focus 0·2 mm × 2 mm.

(b) Camera length was 2·0 cm. Exposure time was 20 h. X-ray focus 0·1 × 1 mm.

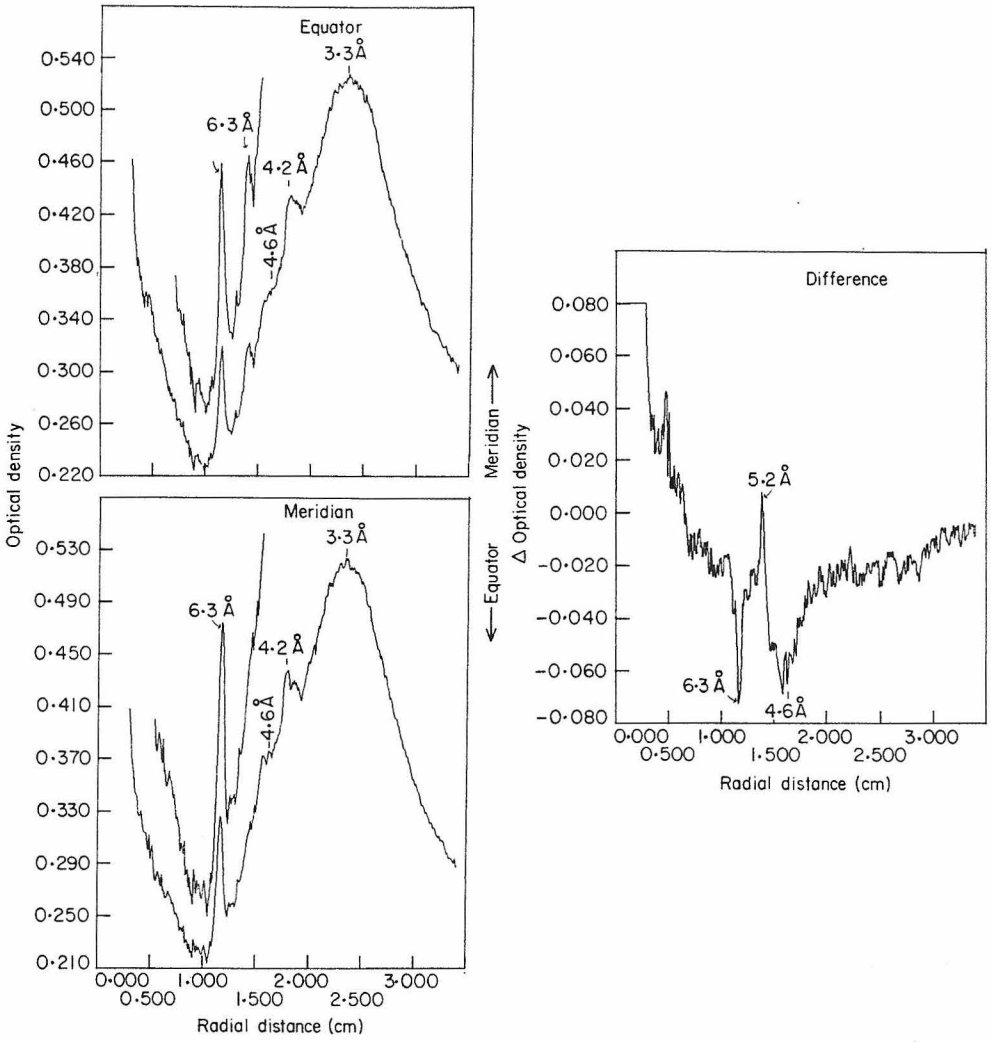

FIG. 11. Densitometer tracings of high-angle scattering from AcChR-rich membranes. Equatorial (a) and meridional (b) integrations from the film shown in Fig. 10 were carried out with angular acceptance limits of ± 50°. Insets on the equatorial and meridional figures are expansions which show the sharp 6·3 Å and 5·2 Å reflections. A difference curve (c) displaying the meridional minus equatorial density is shown. Peaks with meridional orientation are positive; those with equatorial are negative on this plot.

There is a broad peak centred at $d = 3{\cdot}3$ Å characteristic of water scattering. The degree of hydration of the sample can be estimated from the height of the water peak. There are two sharp reflections at spacings $d = 5{\cdot}2$ Å and $d = 6{\cdot}3$ Å in the high-angle pattern of hydrated AcChR membranes. In addition there is a maximum at $d = 4{\cdot}06$ Å (Fig. 11) and a broad maximum at $d = 2{\cdot}2$ Å (Fig. 10).

The maximum at $d = 5{\cdot}2$ Å is highly oriented towards the meridian, while the 6·3 Å reflection is slightly oriented toward the equator. Both the 5·2 Å and the 6·3 Å reflections are extremely sharp. The ratio of the width of these rings at half-height

to their radial position from the film center is an index of the length of the structural feature giving rise to the diffraction. These ratios are 1/18 for the 5·2 Å reflection, and 1/17 for the 6·3 Å reflection, indicating that the 5·2 Å reflection is caused by a stretch of secondary structure ~ 80 Å in length running perpendicular to the membrane, and that the 6·3 Å reflection is caused by structures of ~ 90 Å in length. The angular reflection width of the 5·2 Å reflection was analyzed and compared to the angular width of the small-angle diffraction maxima in the same pattern; the 5·2 Å reflection had an angular peak width about twice that of the low-angle maxima.

4. Discussion

(a) *Contents of the unit cell*

The subunit stoichiometry of this acetylcholine receptor has been estimated to be $A_4B_2C_1D_1$ (Vandlen & Raftery, 1977), which is inconsistent with a three- or sixfold symmetry within the molecule. Therefore, any symmetry higher than that of a primitive lattice cannot be assumed. A careful analysis of likely errors in the intensities and phases of the transform, and comparison with similar studies of the hexagonal arrays found in gap junctions (Klymkowsky *et al.*, unpublished work), render our results inconsistent with any type of lattice other than a plane lattice of oblique symmetry (plane group $p1$). The lattice type may be important to the function of this receptor, if it were shown to be present at the synapse.

The averaged values of unit cell parameters were obtained from ten different arrays, and were found to be $a = 90{\cdot}8 \pm 4{\cdot}1$ Å, $c = 91{\cdot}0 \pm 4{\cdot}3$ Å, and $\beta = 118 \pm 4°$. The average area of one projected unit cell was found to be 7300 ± 200 Å^2. While the unit cell angles are close to 120°, the lattice cannot be described as a hexagonal or trigonal arrangement of molecules, since both intensities (see Fig. 6) and phases in the lattice transforms are far from symmetric. The unit cell contains one molecule, and a symmetric lattice arrangement would require that the molecule had internal symmetry. The unit cell area would imply a volume of 805,000 Å^3 for a 110 Å thick "unit cell". Each cell contains one molecule of AcChR oligomer, of estimated molecular weight 370,000. Assuming a $\bar{v}$ for the protein of 0·74 cm^3 g^{-1} (Matthews, 1968), the protein would occupy a volume of 450,000 Å^3.

Based on the image analyses (Fig. 9), we estimate that no more than half of the area of each unit cell may be lipid. The number of lipid molecules present in such an area can be estimated by dividing the lipid area of each unit cell (less than 3700 Å^2) by the estimated area per lipid molecule. Assuming a value of 62·7 Å^2 per lipid molecule (obtained by Levine & Wilkins (1971) for lecithin bilayers at 100% relative humidity), 60×2 lipid molecules would be contained in bilayer structure per unit cell. The volume occupied by the lipids would be $3700 \times 40 = 148{,}000$ Å^3 (taking 40 Å as the bilayer thickness in hydrated lecithin bilayers (Levine & Wilkins, 1971)). Thus the protein and lipid would account for a total of 600,000 Å^3 or about 74% of the unit cell.

It must be emphasized that the three unit cell parameters, a, b, and c, are never observed simultaneously, since no estimate of the thickness of one layer b is obtained from the microscopy of single or multilayered arrays used to define a and c. Conversely, since the bulk of the sample contains membranes with close-packed, but not highly-ordered arrays of molecules, the X-ray diffraction studies used to define the b dimension do not allow for an estimate of the in-plane lattice dimensions.

(b) *Receptor arrays*

It seems likely that the acetylcholine receptor exists as an arrayed structure *in vivo*, since a wide range of preparative conditions has been used, and these are certainly not expected to be conducive to "crystallization" of the membrane-bound protein. Nor have we been able to alter the frequency with which crystalline arrays are observed by changing conditions of pretreatment. The lateral motion of AcChR in membranes of developing muscle fibers has been studied by fluorescence photobleaching recovery (Axelrod *et al.*, 1976). In this system it was found that there were two coexisting classes of AcChR on non-innervated rat myotubes. One class was relatively mobile with a diffusion constant of 5×10^{11} cm^2/s at 22°C, while the other class was immobile and occurred in dense patches. It may be that the immobile patches detected in these experiments correspond to the arrayed structures seen in our studies. This kind of organization *in vivo* might simply represent an energetically favorable system for concentrating receptor activity at the tips of postsynaptic membranes, or might be functionally important for molecule–molecule co-operativity (Levitski, 1974). Such mechanisms offer attractive hypotheses for the efficient and error-free repetitive action of neuroreceptors.

(c) *Distribution of lipid and protein*

The electron density profile perpendicular to the membrane surface indicates that the membranes are 110 Å thick. The resolution of the profiles are nominally 22 Å and 13 Å, although by the Rayleigh criterion actual resolution should be 11 Å and 6·5 Å, respectively. From the solutions indicated in Figure 4, we presume that the main minimum in the function lies at the center of a lipid bilayer. Thus, it appears that the protein extends considerably on one side, ~55 Å, and little on the other, ~15 Å. The two maxima in the electron density profile on either side of the lowest minimum were ~40 ± 3 Å apart, i.e. about equal to the separation between the electron-dense phosphatidyl head groups in artificial lipid bilayers (Levine & Wilkins, 1971; Lesslauer *et al.*, 1972). Many different model profiles were tested using the method of Stroud & Agard (unpublished work), and no other models were found which were compatible with the continuous scattering profiles.

The profile solutions shown in Figure 4 represent the averaged profile for all membranes in the specimen. Thus, the density of AcChR protein within the membranes will affect the relative scale of those features of the profile due to protein, with respect to those due to a lipid bilayer. Also, any membrane-bound protein other than AcChR in the preparations will be represented according to its relative contribution of electron density.

These membranes have been chemically characterized by Reed *et al.* (1975), who showed that the protein subunits and their relative stoichiometry in the membranes are closely similar to that of Triton-extracted AcChR from the membranes after purification by affinity chromatographic procedures.

The molecular weights of subunits found in the membranes were the same as for AcChR, with the addition of a small amount of a 105,000 molecular weight component which appears in varying proportions between preparations. The stain density for the A subunit of AcChR (M_r~41,000) is also increased by the presence of actin monomers (M_r~42,000) which are also found in the solubilized membranes (M. Raftery, personal communication). Actin filaments were also observed occasionally in electron micrographs, however it is unlikely that the presence of randomly oriented

actin filaments would contribute significantly to the profile structure since they are not integral to the membranes. While the total electron content of proteins other than AcChR is relatively quite small, they could cause perturbations in the final profile if they were membrane bound. In fact, the differences between electron density profiles from different preparations were very small.

In the electron microscope, the AcChR membrane fragments typically occurred as vesicles several microns across. The structures visible in the vesicles appeared as "doughnut-like" structures which were densely close-packed (although generally not arrayed) in the membranes. These structures resemble the structures seen in negatively stained fields of isolated AcChR (Kent & Stroud, unpublished data) and are easily distinguished from the particles seen in membranes enriched in AcCh esterase from the same source (Reed *et al.*, 1975). Thus almost all discernible structures within the AcChR membranes appear to be the same doughnut-like particles, generally held to be AcChR molecules (Nichol & Potter, 1973; Cartaud *et al.*, 1973; Reed *et al.*, 1975), and positively identified as such immunologically (Klymkowsky & Stroud, unpublished work).

Some membrane vesicles seen in the AcChR-rich fraction do not contain any discernible structures (10 to 20%). It seems unlikely that these vesicles contain phospholipid alone, since they band at the same density as the AcChR membranes (1·17 g/ml). However, if they were lipid vesicles, they would perturb the "average" profile, de-emphasizing the features due to protein alone. More likely is the possibility that these are smooth-side-out AcChR vesicles sealed to negative stain. In this case the electron density profile would be unaffected, although little contrast would be seen in the micrographs.

The electron density profile can best be analyzed in terms of a lipid bilayer plus protein (which may or may not be 100% AcChR) plus solvent. The electron density of protein ($\rho \sim 0{\cdot}40$ eÅ^{-3}) is close to that of phosphatidyl head groups ($\rho \sim 0{\cdot}45$ eÅ^{-3}). Therefore, the highest positive density in the profile should be due to the densest arrangement of phosphatidyl head groups plus protein, and the lowest negative trough due to terminal methyl groups in the center of the bilayer.

The electron density of water is 0·334 eÅ^{-3}. Electron densities for hydrated protein are about 0·40 eÅ^{-3}, or 0·44 eÅ^{-3} for anhydrous protein. Electron densities estimated for phosphatidyl head groups are typically $\rho \sim 0{\cdot}45$ eÅ^{-3}; close to that of protein. For methylene groups $\rho \sim 0{\cdot}32$ eÅ^{-3} is close to that of water. Densities for terminal methyl groups in the center of a bilayer vary from about 0·18 eÅ^{-3} (Engleman, 1971) to about 0·27 eÅ^{-3} (Caspar & Kirschner, 1971).

The electron density scale for AcChR membranes is relative, but can be scaled assuming that the highest peak corresponds to protein plus phosphatidyl head groups $\rho \sim 0{\cdot}43$ eÅ^{-3}, the constant density outside the membrane being that of water, 0·334 eÅ^{-3}. The density at the center of the bilayer would be $\rho = (0{\cdot}26)\dagger\ 0{\cdot}27 \pm 0{\cdot}01$ eÅ^{-3}, which could represent 0 to 40% protein at the bilayer center (depending on which methyl group density is assumed). The protein density on the right of the profile is $\rho \sim (0{\cdot}40)\ 0{\cdot}39 \pm 0{\cdot}01$ eÅ^{-3}, and indicates that hydrated protein is reasonably close-packed immediately above the membrane surface, and this is consistent with electron micrographs which show densely packed particles in the plane of the membrane.

† Values in parentheses are from the membrane dispersion profiles (Fig. 4(b)); other values are for the higher resolution profiles (Fig. 4(e)) from partially oriented membranes.

The lower head group peak on the left side of the profile $\rho\sim(0{\cdot}38)$ $0{\cdot}39 \pm 0{\cdot}01$ eÅ^{-3} could be explained by a higher protein concentration at that surface of the bilayer, with the possibility that solvent trapped in a protein pore could also contribute to the lowered density there. Thus, the profile suggests that protein extends ~55 Å on one side of the bilayer and little, ~10 to 15 Å, on the other; that protein is present on both sides; and most probably in the center of the bilayer. Stronger evidence that AcChR molecules indeed span the bilayer derives from the 80 Å long stretches of secondary structure (most probably α helices) which run perpendicular to the membrane surface. Thus, the X-ray evidence suggests the AcChR is an integral membrane protein which spans the endplate membrane, and this is consistent with its operation as an ionophoretic channel.

The membrane thickness (110 Å) determined from this X-ray analysis is closely similar to that found by Rosenbluth (1975) by electron microscopy of thin-sectioned and freeze-fractured electrocyte membranes from *Torpedo* (~120 Å). Rosenbluth (1975) also found that particles within these membranes project (~60 Å) into the junctional cleft, and little on the other side. Thus, the side which contains peripheral protein is presumably the synaptic side of the endplate, and might therefore be reasonably expected to contain the ligand, or toxin-binding sites, located on the A_4 subunits.

(d) *Secondary structure*

Henderson (1975) discussed evidence for α-helical structure in other transmembrane proteins, and argued that the α-helix satisfies the hydrogen-bonding requirements of a polypeptide chain in a hydrophobic environment. It is notable that AcChR membranes give rise to a sharp reflection at $d = 5{\cdot}2$ Å, a spacing characteristic of α helices in the coiled-coil conformation. Whatever this arises from, the corresponding structural features are of average length ~80 Å, and oriented perpendicular to the membrane surface. The most probable explanation is that these are α helices.

Two other structures which might represent an energetically acceptable way to define a channel of dimensions ~5 to 10 Å would be: (i) a large diameter coil of polypeptide, crosslinked as a parallel β-sheet structure, and (ii) a barrel formed by twisted antiparallel β sheet. This latter structure has been found in several proteins. Either of these two structures might account for the 6·3 Å reflection.

The antiparallel-pleated sheet gives rise to a chain repeat of 7 Å, with 4·75 Å between chains running in alternate directions (as found for silk (Marsh *et al.*, 1955)). A twisted-pleated sheet might reduce the chain repeat to 6·3 Å.

The parallel β-sheet arrangement was suggested for β-keratin (Pauling & Corey, 1951), and gives rise to a 6·5 Å chain repeat, with 4·85 Å separation between chains. The sharpness of the 6·3 Å reflection is nevertheless surprising, and it is difficult to see how a coiled chain could account for the apparently large number of repetitions. The 6·3 Å reflection was observed in the X-ray patterns of other membranes prepared from *Torpedo* and *Electrophorus electricus* including those enriched in acetylcholine esterase, or ATPase. Therefore, there is at least the possibility in this case that the 6·3 Å reflection arises from some regular lipid phase in the membranes.

5. Conclusion

The acetylcholine receptor from *T. californica* is an integral membrane protein, which traverses the endplate membrane. The protein extends some 55 Å on one side

of the lipid bilayer and little on the other. This receptor occurs in an ordered lattice which is maintained by protein–protein interactions, and contains long 80 Å stretches of secondary structure tentatively identified as α helices, oriented perpendicular to the membrane surface. The center of each molecule is more accessible to uranyl stain than other parts of the molecule, and this well is tentatively identified as the ionophoretic channel. Further low-resolution studies are aimed at: (i) locating binding sites for macromolecular toxins such as α-Bungarotoxin which bind tightly to the receptor; and (ii) assaying for ligand-induced conformational change. The single crystal structure analysis of α-Bungarotoxin is nearing completion in our laboratory, and it is hoped that details of toxin binding may be obtained from the high resolution structure of the α toxin.

This work was carried out with the support of the National Institutes of Health grant no. GM-19984 and the National Science Foundation grant no. BMS75-04105, whose help is gratefully aknowledged. One of us (R.M.S.) is the recipient of a National Institutes of Health Career Development Award, and is a Sloan Foundation Fellow. Another author (M.J.R.) is the recipient of a National Institutes of Health Predoctoral Traineeship, a third author (D.A.A.) is the recipient of a National Science Foundation Predoctoral Fellowship, and the fourth author (M.W.K.) is the recipient of a California Foundation Fellowship for Biochemical Research. This is contribution no. 5370 from the Norman W. Church Laboratory of Chemical Biology, California Institute of Technology. We are grateful to Dr M. A. Raftery for valuable discussion and advice.

REFERENCES

Axelrod, D., Ravdin, P., Koppel, D. E., Schlessinger, J., Webb, W. W., Elson, E. L. & Podleski, T. R. (1976). *Proc. Nat. Acad. Sci., U.S.A.* **73,** 4594–4598.

Blaurock, A. E. & King, G. I. (1977). *Science,* **196,** 1101–1104.

Blaurock, A. E. & Stoeckenius, W. (1971). *Nature New Biol.* **233,** 152–157.

Cartaud, E. L., Benedetti, L., Cohen, J. B., Meunier, J-C. & Changeux, J-P. (1973). *FEBS Letters,* **33,** 109–113.

Caspar, D. L. D. & Kirschner, D. A. (1971). *Nature New Biol.* **231,** 46–52.

Cohen, J. B., Weber, M., Huchet, M. & Changeux, J-P. (1972). *FEBS Letters,* **26,** 43–47.

Cooley, J. W. & Tukey, J. W. (1965). *Math. Comput.* **19,** 297–301.

DeRosier, D. J. & Moore, P. B. (1970). *J. Mol. Biol.* **52,** 355–369.

Dervichian, D. B. (1964). *Prog. Biophys. Mol. Biol.* **14,** 263–342.

Duguid, J. R. & Raftery, M. A. (1973). *Biochemistry,* **12,** 3593–3597.

Edelstein, S. J., Beyer, W. B., Edelfrawi, A. T. & Edelfrawi, M. E. (1975). *J. Biol. Chem.* **250,** 6101–6106.

Engleman, D. M. (1971). *J. Mol. Biol.* **58,** 153–165.

Erickson, H. P. (1974). *Eighth Internat. Congr. Electron Microscopy, Canberra,* pp. 310–311.

Erickson, H. P. & Klug, A. (1971). *Phil. Trans. Roy. Soc. ser. B,* **261,** 105–118.

Franks, A. (1955). *Proc. Phys. Soc. (Lond.) B,* **68,** 1054–1064.

Furukawa, T. & Furukawa, A. (1959). *Jap. J. Physiol.* **9,** 130–142.

Gibbs, A. J. & Rowe, A. J. (1973). *Nature (London),* **246,** 509–511.

Henderson, R. (1975). *J. Mol. Biol.* **93,** 123–138.

Horne, R. W. & Whittaker, V. P. (1962). *Z. Zellfor. Microsk. Anat.* **58,** 1–22.

Katz, B. & Miledi, R. (1972). *J. Physiol. (London),* **224,** 665–699.

Klug, A. & DeRosier, D. J. (1966). *Nature (London),* **212,** 29–32.

Klymkowsky, M. W., Ross, M. J. & Stroud, R. M. (1977). *J. Cell Biol.,* submitted.

Lesslauer, W., Cain, J. & Blasie, J. K. (1971). *Biochim. Biophys. Acta,* **241,** 547–566.

Lesslauer, W., Cain, J. E. & Blasie, J. K. (1972). *Proc. Nat. Acad. Sci., U.S.A.* **69,** 1499–1503.

Levine, Y. K. & Wilkins, M. H. F. (1971). *Nature New Biol.* **230,** 69–72.

Levitski, A. (1974). *J. Theoret. Biol.* **44,** 367–372.

Lipson, H. & Taylor, C. A. (1958). *Fourier Transforms and X-ray Diffraction*, G. Bell and Sons, Ltd., London.

Luft, J. H. (1961). *J. Biophys. Biochem. Cytol.* **9,** 409–414.

Luzzati, V., Mustacchi, H., Skoulos, A. & Husson, F. (1960). *Acta Crystallogr.* **13,** 660–667.

Markham, R. (1968). *Meth. Virol.* **4,** 503–529.

Marsh, R. E., Corey, R. B. & Pauling, L. (1955). *Biochim. Biophys. Acta,* **16,** 1–34.

Matthews, B. W. (1968). *J. Mol. Biol.* **33,** 491–497.

Michaelson, D., Vandlen, R., Bode, J., Moody, T., Schmidt, J. & Raftery, M. A. (1974). *Arch. Biochem. Biophys.* **165,** 796–804.

Moody, M. F. (1975). *Acta Crystallogr. sect. A,* **31,** 8–15.

Morimoto, H. & Uyeda, R. (1963). *Acta Crystallogr.* **16,** 1107–1119.

Nichol, E. & Potter, L. T. (1973). *Brain Res.* **57,** 508–517.

Pauling, L. & Corey, R. B. (1951). *Proc. Nat. Acad. Sci., U.S.A.* **37,** 729–740.

Reed, K., Vandlen, R., Bode, J., Duguid, J. & Raftery, M. A. (1975). *Arch. Biochem. Biophys.* **167,** 138–144.

Reynolds, E. S. (1963). *J. Cell Biol.* **17,** 208–212.

Rosenbluth, J. (1975). *J. Neurocytol.* **4,** 697–712.

Ross, M. J. & Stroud, R. M. (1977). *Acta Crystallogr. sect. A,* **33,** 500–508.

Takeuchi, A. & Takeuchi, N. (1960). *J. Physiol. (London),* **154,** 52–67.

Vandlen, R. & Raftery, M. A. (1977). *Arch Biochem. Biophys.*, in the press.

Weill, C. L., McNamee, M. G. & Karlin, A. (1974). *Biochem. Biophys. Res. Commun.* **61,** 997–1003.

Worthington, C. R. & McIntosh, T. J. (1974). *Biophys. J.* **14,** 703–729.

APPENDIX VI

Towards Cellular Tomography; Insights into Chromosome Architecture

TOWARDS CELLULAR TOMOGRAPHY:

INSIGHTS INTO CHROMOSOME ARCHITECTURE

David A. Agard and John W. Sedat

Department of Biochemistry and Biophysics
University of California, San Francisco
San Francisco, CA 94143

ABSTRACT

Examination of supramolecular structures at the level of whole cells presents several major problems that can be solved using three-dimensional reconstruction and image enhancement techniques. Presented here is a first step towards this goal of cellular tomography. General methodologies for extraction of additional information from biological objects by computational procedures are described. These image processing techniques are suited for studying large non-crystalline objects by either optical or electron microscopy. The ultrastructural architecture of both Drosophila sperm heads and mitotic chromosomes within early embryos have been investigated in projection. These examples of highly-condensed DNA appear to have a defined architecture based on regular (helical) structural principles.

INTRODUCTION

A central problem in modern biology today is the problem of structural organization at the level of whole cells, portions of cells or subcellular organelles. Structures in this size class confront the investigator using optical and electron microscopic techniques with three major problems. First, these three-dimensional structures are generally so thick as to require either physically or optically sectioning the sample; thereby studying it in planes. This is unfortunate since interpretation of one part of the object is dependent on planes both above and below the sample. Second, the structures are usually packed or constructed in a very dense and complicated fashion making it difficult to arrive at a solution since the information in one plane is, in effect, obscured by the details in other planes. Third, while there may be some order or regularity in their architecture they are not so regularly constructed as to be crystalline; hence structural methodologies formulated for completely ordered objects cannot be employed.

The purpose of this communication is to present a straightforward methodological route for the investigation of three-dimensional structures in whole cells which adequately satisfies the conditions listed above. As a first approach towards accomplishing these goals, data taken from subcellular objects, in projection, are presented to show that additional structural information can be obtained by these techniques.

Of all the subcellular organelles one of the least understood is the cell nucleus in spite of the fact that within the chromosomes resides the DNA coding for the entire developmental program. Certainly

much effort and progress has been made in understanding the organization and sequence of the DNA yet so little is known concerning the relationship between structure and function. We have for some time studied the interphase nucleus and sub-nuclear structures such as mitotic chromosomes (Sedat and Manuelidis, 1977), focusing primarily on two questions. First, is there a unified principle of interphase chromosome architecture that would give some insights into their diversified functions and second, is there an overall three-dimensional packing or folding of these interphase chromosomes into a determined arrangement such that each nucleus is similar (conceivably identical) to nuclei in neighboring cells?

We have used as a biological system Drosophila with its well known genetics and extensive literature. The early embryo state is a source of strictly diploid interphase and mitotic chromosomes and represents as well a defined karyotype and developmental (synchronous) entity. It was recognized from the beginning that it was extremely important to attempt to control for preparation artifacts and distortions; therefore, we have studied most nuclear events in situ. A primary consideration for this work has been the hypothesis that the structure and function of nuclear components are interlocked; and once these structures are analyzed many of the loose ends and ill understood aspects of genetics could be put into perspective. Furthermore, additional questions could then be posed in light of a structural model.

Initially, extensive use of optical fluorescence microscopy has been used as a schema for recording data from nuclear structures in whole cells or embryos. Optical microscopy, uniquely, allows study in a

hydrated, defined ionic environment at one atmospheric pressure and in many cases, in living cells. In addition, optical sectioning, sample tilting, and other procedures for investigating large three-dimensional objects can be used. New staining procedures allow an enormous specificity in highlighting the visual information, thus the arrangement of biologically defined components can be investigated. Dyes such as Hoechst 33258 specifically fluoresce upon binding to DNA (but not RNA). As a consequence, only nuclear structures are imaged, vastly simplifying interpretation. Monoclonal antibodies can now be made to interesting proteins, fluorescently labelled, and used to highlight specific regions or topologically strategic antigen locations. Fluorescent microscopy does suffer from the fact that the fluorescence emanates from a volume emitter (known as a gaussian body); this aberration results in a glow surrounding the object which will tend to obscure details and blur edges.

In spite of the use of in situ labelling and study schemes, it is still necessary to control for preparation or distortion artifacts. We have tried several independent preparation procedures using fixed or unfixed tissues, in an attempt to reveal such problems and thereby lead to preparation-independent conclusions.

It should be clear that once data have been collected and interpreted at the level of light microscopy it should be possible to use electron microscopy, especially high voltage eletron microscopy (HVEM) with thick tissues, to extend the analysis into areas of higher resolution. The present scheme proposes a path for this transition.

Image processing techniques may be used to minimize the two major drawbacks inherent with epi-fluorescent optical imaging: the glow effect and the relatively limited resolution intrinsic to optical systems. Approaches employing computer manipulation of digital images have become well developed over the past decade mainly for the enhancement of astronomical images (Lorre and Lynn, 1978; Frieden, 1975; Nathan, 1968; O'Handley and Green, 1972). Unlike the methods developed by Klug and co-workers for biological specimens (Crowther and Klug, 1975), these approaches make no assumption of sample order. This point is very important. An error in the assumed object symmetry will inevitably lead to an enhancement of that symmetry component in the processed object (Gibbs and Rowe, 1973). The astronomical techniques were designed to work with arbitrary objects and involve global manipulations of either the image directly, or indirectly via its Fourier transform (FT). None of the information in the image is ever removed, it is merely re-arranged so as to counteract the deleterious effects of instrumental distortions. By contrast, the techniques used by Klug and co-workers all involve the selection of "reflections" in the Fourier transform domain, and the removal of all non-reflection data. Such an approach, while ideal for a regular crystalline object, is inappropriate for dealing with any image of unknown symmetry.

MATERIALS AND METHODS

Biological Specimens

Drosophila melanogaster testes or spermatotheca from male or female adult flies respectively were hand dissected into buffer A (Burgoyne, et. al., 1971) at room temperature. These organs were transferred into buffer A + 10µg Hoechst 33258 dye (American Hoechst, New Jersey) and immediately squashed, gently, with a cover glass or incubated without pressure damage. After various periods of staining (0.1 -1 hour), samples were examined by fluorescent microscopy.

Drosophila early embryos ($\leq$ 1 hour after deposition) were collected and decorionated by the standard Clorox treatment. Permeabilization of the vitelline membrane was accomplished by a modification of the Zalokar and Erk (1976) procedure. The embryos were shaken with an equal mixture of heptane and buffer A + 0.1% formaldehyde + 0.1M dithiothreitol at 25°C for 15 minutes followed by removal of the heptane by rinsing of the embryos onto a metal or nylon screen and then further washing with buffer A. The embryos were stained with Hoechst 33258 to fluorescently label the DNA by incubation of the embryos with a final concentration of 10µg/of dye in buffer A after 15 to 30 minutes.

Optical and Electron Microscopy

The basic procedures are given in Sedat and Manuelidis, 1977. With these large organs and structures it is possible to optically section, by variation of the focus, so that objects such as sperm can be image processed without distortion in the interior.

Digitization

Photographic images were digitized with a Perkin-Elmer PDS microdensitometer using a 10μ spot size. This digitizer was chosen primarily for its high quality and backlash-free scanning features that proved essential when using the deconvolution and bandpass filter image processing routines.

Computation

A 16 bit minicomputer, Data General S-230, with 10MB disk memory and 64K words core was used for computation. All programs were written in the Fortran language and are available on request. Computation time for a 512 x 512 FFT is 20 minutes.

Analysis of Drosophila Sperm Heads

In order to examine the efficacy of the image processing schemes outlined below, a suitable biological specimen had to be chosen. Initially, Drosophila sperm heads, whose DNA was made fluorescent by the dye Hoechst 33258, were investigated based on three considerations. First, these biological objects can be prepared with minimal internal damage by dissecting and opening the testes or spermatotheca (in case of the female). Thus the structures examined are most likely in their native state. Secondly, there is polarization microscopy evidence from cave cricket (Inoué and Sato, 1964) as well as Drosophila sperm showing that insect sperm heads are highly ordered (birefringent), elongated specimens. The helical architecture inferred from these polarization studies could be compared with the results from the procedures used here. In essence, the Drosophila sperm head with dimensions of 10 by

0.3μ and containing 0.15pg of DNA represents the usual limits of light microscopy.

Various enhancement methods were applied to particular aspects of the analysis of sperm images; in later sections these techniques will be employed in the study of Drosophila mitotic chromosomes.

An epi-fluorescent image of a Hoechst 33258 stained Drosophila sperm head is shown in Figure 1a. A similar image was digitized on a Perkin-Elmer PDS scanner and is shown displayed on a raster scan video system for comparison purposes (Figure 1b). The first step in the image processing procedure was to calculate the Fourier transform (a complex function, F) of the image using a two-dimensional Fast Fourier transform algorithm (Brenner, 1969). Although this procedure is precisely analogous to generating an optical diffraction pattern, the ease with which the FT can be manipulated makes the digital approach the technique of choice.

Displaying the modulus of the FT ($|F| = FF^*$, where F^* is the complex conjugate of F) reveals that in spite of the rather featureless appearance of the original image, the sperm is a highly ordered object since the FT contains "reflections" (Figure 2a). To better resolve the higher-order reflections, Figure 2a was treated as an image to be processed. A very powerful non-linear technique called median filter enhancement was used. This method used by Lorre at the Pasadena Jet Propulsion Laboratory (Arp and Lorre, 1976) for processing star photos has the property of removing slowly-varying broad backgrounds from the image while leaving smaller objects such as reflections (or stars) unperturbed. After processing (Figure 2b) the individual reflections

can be clearly seen. Falling onto bessel function-like layer lines these reflections are highly indicative of a helical structure. From the layer line spacing and the presence of a meridional reflection on the second layer line the basic helical parameters can be derived: two turns per linear repeat distance of 1.3 microns. One turn thus occurs every 6500Å. The difference in diffraction intensity for the two arms of the helical cross pattern (Figure 2a) could arise from internal scattering in the object which acts to reduce the recorded information from the bottom side of the helical structure. Another explanation based on the calculations of Tinoco (private communication), indicates that this might be a consequence of the interaction of partially polarized light with the highly ordered sperm head.

In the diffraction pattern shown in Figure 2a, the very low angle regions (near the center) are considerably more intense (20-50x) than the remainder of the transform. This is probably a consequence of the fluorescence volume emitter effect. Light is emitted from all parts of the sample not just the surface; hence emitted light from one part of the object is scattered by remainder of the sample. This is roughly equivalent to viewing the sample through a diffusing screen, the overall shape is visible but the fine details are obscured. Since the low angle terms in the FT correspond to the overall shape information they are considerably stronger than the high angle terms that provide the detailed information.

Although it is obvious from Figure 2a that the Fourier transform contains fine structure information, the low angle terms so dominate that details are not apparent in the image. The magnitude of the prob-

lem is seen in the pseudo three-dimensional contour plot of the diffraction amplitudes $|F|$ (Figure 3a). A very useful solution to this problem is to multiply the FT amplitudes by the smooth function:

$$1 - e^{-\alpha s^2} \qquad (1)$$

(s is the radial distance from the center of the FT, α is an adjustable parameter) which will minimize the discrepancy between the low and high angle terms. Enhancement of the high angle terms, however, leads to an increase in the apparent amount of noise in the image. Since most of the noise is confined to extremely high angles, it is possible to suppress the noise without seriously degrading the image. The result is a bandpass filter defined by:

$$(1 - e^{-\alpha s^2})e^{-\beta s2} \qquad (2)$$

The parameters α, β are adjusted to provide maximum enhancement with a minimum of noise. Applying the filter given by equation 2 to the FT of the sperm head gives the modified transform shown in Figure 3b. It is now possible to see that the transform contains information beyond the central peak.

An inverse Fourier transform computed using the modified amplitudes (using equation 2) produces the greatly enhanced image shown in Figure 4a. Performing the same operation using unmodified amplitudes would regenerate the original image. Evidence for the coiled nature of the sperm is now apparent (see inset). Because this structure is so highly

ordered, all of the useful information is contained within the region containing the reflections. Suppressing those regions outside this area in conjunction with the bandpass filter results in a further enhancement of the image (Figure 4b).

Inherent to any observational system are certain distortions (resolution limits, chromatic aberration, gaussian emmiter effect, etc.) that introduce errors into the recorded image. Mathematically (using a one-dimensional image for simplicity), the observed image $o(x)$ can be considered as arising from a convolution of the "true" image $\rho(x)$ with some distortion function $s(x)$ that serves to smear out the details in the image:

$$o(x) = \int \rho(x-v)s(v)dv \qquad (3)$$

What is desired is some way to reverse this convolution, thereby deconvoluting $o(x)$ to yield the true undistored image $\rho(x)$. This requires some knowledge of the smearing function $s(x)$. Since the major form of distortion inherent in the fluorescent imaging case results from the gaussian emitter effect, $s(x)$ was chosen to model this problem. In principle $s(x)$ can be experimentally determined by imaging a point source, in which case essentially all of the instrumental distortions can be removed. Although many techniques exist for accomplishing this deconvolution operation (see Frieden, 1975) the best seems to be a modification of the Jansson-Van Cittert iterative constrained deconvolution technique (Jansson, 1970).

The presence of noise in the observed profile $o(x)$ can lead to an inaccurately deconvoluted image. This technique uses the knowledge that $\rho(x)$ must be everywhere positive to help solve this problem. That is, since one knows that negative optical densities are physically meaningless (although they are mathematically allowed), this information can be inserted into the deconvolution procedure. The result is a greatly reduced sensitivity to noise.

The basic Jansson-Van Cittert algorithm (after Frieden, 1975) is:

$$\begin{aligned} &\text{i)} \quad o^k(x) = \rho^k(x) * s(x) \\ &\text{ii)} \quad \rho^{k+1}(x) = \rho^k(x) + \gamma(x)[o(x) - o^k(x)] \qquad (4) \\ &\text{iii)} \quad k = k+1 \end{aligned}$$

$$\text{and} \qquad \gamma(x) = 1 - A\left|o^k(x) - A\right|$$

where A is a constant and * denotes the convolution operation of equation 3. In equation 4 the starting point for the refinement is k=0 and $\rho^o(x) = o(x)$. The current guess $\rho^k(x)$ is smeared by convolution with the blurring function $s(x)$ (step i). A new guess $\rho^{k+1}(x)$ to the correct $\rho(x)$ is then generated by comparison of the broadened $\rho^k(x) (= o^k(x))$ with the observed image $o(x)$ in step ii. The entire procedure is iterated until there is no significant difference between $o^k(x)$ and $o(x)$. At this point, $\rho^k(x)$ becomes an equivalent to $\rho(x)$. The $\gamma(x)$ function is used to apply both non-negativity and maximum positivity constraints. In practice the parameter A is set to twice some reasonable approximation of the maximum optical density (accurate selection of this parameter is not required).

The original deconvolution method was modified in two important ways: the convolution operation indicated in step i is actually performed as a multiplication in Fourier transform space, thereby speeding the algorithm about 500 fold, and second the sensititity to noise was further reduced by smoothing $\rho^k(x)$ every 10 iterations. The convolution theorem shows that the convolution operation of step i is equivalent to Fourier transforming $\rho^k(x)$ and $s(x)$ according to equation 5 and taking the inverse Fourier transform of their product as in equation 6.

$$P^k(X) = \int \rho^k(x)\, e^{2\pi i x X} dx \qquad (5)$$

$$S(X) = \int s(x) e^{2\pi i x X} dx$$

$$o^k(x) = \int P^k(X) S(X) e^{-2\pi i x X} dX \qquad (6)$$

Using the Fast Fourier transform algorithm developed by Cooley and Tukey (1968) results in the great increase in speed. Also, it is only necessary to calculate $S(X)$ once.

Concomitant with increasing the resolution of the image occurs an increase in the apparent amount of noise. As with the bandpass filtration method there must be a trade off between the degree of resolution enhancement and the maximum noise level that can be tolerated in the resultant structure. No provision was made for this in the original deconvolution scheme. A simple way of accomplishing this added noise suppression is to smooth $\rho(x)$ by coupling adjacent points.

$$\rho'(x) = \alpha\rho(x) + \beta[\rho(x-1) + \rho(x+1)] + \gamma[\rho(x-2) + \rho(x+2)] \qquad (7)$$

where α, β, γ are adjustable constants and $\alpha + 2\beta + 2\gamma = 1$. Thus for each point in the image $\rho(x)$ a new value is computed based on the weighted sum of it, its first ($\rho(x-1)$, $\rho(x+1)$) and second neighbors ($\rho(x-2)$, $\rho(x+2)$). For maximal efficiency this smoothing operation should only be applied after every 5-10 cycles of the deconvolution scheme. In the example presented here α, β and γ were chosen to correspond to a limited gaussian function, and smoothing was applied every 10 cycles.

The results after 60 cycles of constrained deconvolution are shown in Figure 5. As with the bandpass filter Figure 4a, fine structural details are now visible. In general the deconvoluted image is of higher quality than the bandpass filtered image. Use of a more exact smearing function should provide even better results.

The median filter enhancement approach was also tried. While the resultant image did indicate the presence of periodic fine structure, much less of the coiling that was apparent using other processing methods could be seen.

The presence of reflections in the Fourier transform are indicative of a highly ordered object. That these reflections appear to lie on Bessel-function type layer lines argues that the sperm is built along helical principles. Furthermore, it is possible to extract detailed information from the layer line spacing, the presence of a meridional reflection on the second layer line and the angle between the arms of cross. The result is that a Drosophila sperm head is a helical object

made up of continous strands, having a radius of .136μ, and two turns per linear repeat distance of 1.3μ. Alternatively, the meridional reflection could arise from two intertwined strands having a 1.3μ periodicity. Futher analysis requiring that smooth functions be fit to background corrected layer line data is now in progress. It should be emphasized that the median filtration procedure was invaluable for the interpretation of the Fourier transform.

From analysis of deconvoluted and bandpass-filtered images it is seen that the sperm is a complex multi-stranded object; probably flattened to have an oval cross-section. Although strands can be traced in several regions, the oval cross section causes the tracings in other regions to be obscured in a projected view.

The observed architecture for Drosophila is remarkably like that deduced for cave cricket sperm heads by Inoué and Sato, (1964). Although the Drosophila sperm head was too small to be analyzed by the polarization birefringence procedure, Inoué's analysis of polarized UV microbeam-induced damage suggested that the two structures were topologically similar but having different dimensions.

Mitotic chromosomes

Another example of a supramolecular structure containing highly condensed DNA is the mitotic chromosome; which was also examined using image processing techniques. Drosophila embryos begin development with a synticial (synchronous) nuclear division which takes place in the interior as shown in stereo in Figure 6a (Hoechst 33258 DNA fluorescent staining). After nine divisions (with 512 nuclei) migration of the

nuclei to the periphery occurs, and the synchronous divisions continue for five more rounds. Thereafter, cellular membranes form around the elongated nuclei and the state known as cellular blastoderm progresses (∿6000 nuclei). This state, marked by the onset of massive transcription in the nuclei, denotes the point of nuclear determination. Figure 6b shows an embryo, fluorescently labelled and viewed through the vitelline membrane and nucleoplasm, just before the formation of the cell membranes. In such preparations it is possible to pick out embryos that are in mitosis; the mitotic chromosome arms can be seen in Figure 6c. Analogous to the sperm head studies these can be subjected to the image enhancement techniques.

An arm from a mitotic chromosome was randomly selected and digitized (Figure 7a). The results after bandpass filtering using two different β values (eqn 2) are shown in Figures 7b,c. An interpretation is shown in Figure 7d. Like the sperm, the mitotic chromosome also appears to be a flattened helical structure. The DNA is organized into a ribbon-like structure approximately 1400Å wide which is then coiled to form the mitotic chromosome. Both the diameter of this helix (about 4000Å) and its pitch (∿5700Å) can be measured from the processed micrographs. Although the ribbon appears to show substructural details, especially in Figure 7c, it is not yet possible to interpret these features with confidence. Similarly, there are some weak indications that the mitotic chromosomes might be double stranded which cannot yet be discounted. Some of the features present in the enhanced micrographs can also be recognized in the uprocessed image.

HVEM

While light microscopy, especially that utilizing fluorescence, is ideal for the investigation of large wet objects there are limitations on the ultimate resolution that can be achieved. Thus, it was important to search for a technique that would bridge light microscopy with higher resolution techniques. High voltage electron microscopy seems to fulfill this need. It is possible using HVEM with electron beams of 1.0 MEV or higher to penetrate and image quite thick samples, e.g. $\gtrsim 5\mu$, provided the samples are critical point dried. Entire Drosophila or human diploid nuclei can be imaged, in focus, at a resolution of approximately 20Å. This would be impossible for conventional transmission electron microscopy, although such performance might be approached with Scanning Transmission EM (Beer, 1976; Costa, et al., 1979). Conventional tilting techniques over a range of $\pm$ 60° would allow data to be collected from three-dimensional objects. In addition, there may be less radiation damage with HVEM (Isaacson, et al., 1973).

Even using HVEM techniques, the density and complexity of these specimens has made the task of interpretation quite difficult. In an effort to minimize the problems associated with interpreting thick specimens, HVEM micrographs of nuclear structures can be processed using the same procedures described above.

To illustrate the advantages of using image processing techniques on HVEM micrographs, an edge of a whole Drosophila diploid, critical-point dried nucleus was chosen for analysis, Figure 8a. Using the HVEM enables the entire 3-4μ thick sample to be imaged in focus. The results

after using a bandpass filter are shown in Figure 8b. Thick strands measuring 300-500Å in diameter are seen to be wrapped around one another; such detail can only be observed in the processed micrographs.

DISCUSSION

In the case of biological specimens of the type considered here, it is important to chose image processing techniques that make no assumptions concerning the intrinsic specimen symmetry. Thus the diffraction masking methods (Crowther and Klug, 1975) that have proven so successful for ordered specimens, were in general not employed here. Several processing methods were investigated for their ability to enhance micrographs (both fluorescent optical and high voltage electron) of potentially poorly ordered objects.

Although the iterative constrained deconvolution technique is the most versatile - it is possible to correct for virtually any type of instrumental distortion - the great computational expense limits its general applicability. By contrast, the bandpass filter approach was shown to be a very powerful, yet simple, technique that can rapidly provide a greatly enhanced image of the object under study. Since the Fourier space manipulations used are global instead of local, there is no possibility of artificially introducing order into the processed image. While any function could substitute for the bandpass filter given in equation 3, the use of gaussian functions is preferred. Since the Fourier transform of a gaussian is also a gaussian, no contrast reversals are introduced into the processed image. This would not be true if an arbitrarily shaped bandpass filter were chosen. Further, because of its simplicity, this method readily lends itself to proc-

essing three-dimensional images. The median filter enhancement technique is most useful for removing broad backgrounds from complex images as seen when processing the sperm FT (Figure 2) and the optical thick sections from mitotic chromosome preparations (not shown). This approach proves to be less satisfactory for dealing with the sperm images (although aspects of the underlying structure could be seen); in this regard the bandpass filter was far superior.

A few simple biological and structural statements can be made on the basis of the data presented in this paper, which were highlighted using image processing techniques. Sperm heads and mitotic chromosomes as examples of supramolecular structures containing highly-condensed DNA appear to have a defined architecture based on regular structural principles. The order seen here is reminiscent of that found in well studied biological systems such as muscle and collagen. The high degree of regularity in construction supports the elegant polarization microscopy and interpretational studies on insect sperm heads by Inoué and Sato as well as data previously collected in this laboratory on polytene bands, interband and mitotic chromosomes utilizing light microscopy (polarization, differential interference and fluorescence) and various forms of electron microscopy (Sedat and Manuelidis, 1977). Recent work using Fourier transforms made from these micrographs reveals the presence of reflections providing direct evidence for the inherent order in nuclear structures (Sedat et. al., 1980). The essential underlying form of the chromosomal architecture at several different levels of organization seems to be based on a helix. It is interesting to note

that the topology and average shape of the Drosophila sperm heads determined using image processing methods are very similar to those derived by Inoué and his colleagues for cave cricket sperm heads.

The finding that mitotic chromosomes are helical at least at the final, highest level of folding is in keeping with an enormous volume of observational data from the past 80 years (for example, Kuwada, 1939; Matsura, 1938). Likewise, it is strongly supportive of the interphase chromosome model based on defined hierarchical (sequential) helical coiling previously presented (Sedat et. al., 1980). The helical structure for mitotic chromosomes differs from the model with protein scaffolds in the interior of mitotic chromosomes of Laemmli and coworkers (Laemmli et. al., 1977). Definitive statements on the architecture at still finer levels of organization will rest on a full three-dimensional structure currently in progress; only then will it be possible to consider any structure-function aspects.

It is gratifying to see that the results of completely independent processing techniques converge on a similar structure. Therefore, based on the results of median filtration (real space), bandpass filtration (FT space), and constrained deconvolution (both real and FT space) taken together with controls and data from unprocessed images makes it extremely unlikely that our interpretations are artifactually derived.

The initial steps with the image processing relied on analysis of two-dimensional projections. Naturally, interpretation of thick complicated structures within cells or in thick sections, for example, is difficult in projection as details from many different levels in the

specimen overlap to produce confused images. A unique solution to these problems will evolve only from the direct solution of the three-dimensional structure.

Three-dimensional structural analysis requires the recombination of many different views of the same object. This can be accomplished using either a wide range of tilted views as was done in the pioneering work of Henderson and Unwin (1975) or using a few tilted views in conjunction with optical sectioning (images taken at different focal planes). Either approach is well within the technological limits of existing microscopes (± 60° tilt with electron microscopes or ± 55° tilts with an optical microscope equipped with a capillary specimen holder). Combining many views of the same object has an added advantage that the sensitivity to noise in the images is substantially reduced. Although using an incomplete set of tilted views can lead to a distorted structure as a region of Fourier space information is missing, it is possible to mathematically correct this type of distortion (Agard and Stroud, 1980).

The three-dimensional analysis approach essentially represents tomography carried out at the cellular level. Furthermore, it is possible to combine the image processing techniques described here for two-dimensional images with three-dimensional reconstruction methods. Such work is now under way in our laboratory. The resultant procedure should be a very powerful addition to the existing array of structural techniques and especially useful in the study of supramolecular structure.

In summary, a general scheme patterned after macromolecular crystallographic analysis procedures is envisioned for the study of generalized cellular architecture. Three-dimensional data (either optical or electron microscopic) would be collected and processed to generate an enhanced three-dimensional image. This image would then be interpreted in terms of a structural model whose parameters can subsequently be refined (as in x-ray crystallography) to best fit the observed data. The refined model would then serve as the basis for further investigations into supramolecular structure-function cognates.

ACKNOWLEDGEMENTS

We would like to especially thank Dr. Alan Blumenthal for advice on, and expertise with the dissections, and also Dr. R.M. Stroud for valuable discussions on the structural aspects of this work. This investigation was supported by NIH Grant GM25101-02.

FIGURE LEGENDS

Figure 1. Fluorescence Microscopy of Hoechst 33258 stained Drosophila sperm heads. (A) is a fluorescent micrograph taken with a Zeiss 100x/1.3N.A. Neofluar objective. (B) is the video raster display of a digitized image (512 x 200 pixels) from a similar sperm head on a fluorescent micrograph negative.

Figure 2. Fourier transforms from a Drosophila sperm head. The modulus of the Fourier transform of the image in Figure 1B is displayed in (A). Median filtration enhancement of A results in the image displayed in B.

Figure 3. A psuedo-three-dimensional representation of a sperm head Fourier transform. The unprocessed Fourier transform (identical to that in Figure 2(A)) is shown in A. Bandpass filtration results in the modified Fourier transform shown in B.

Figure 4. Bandpass filter enhanced sperm head images. The modified Fourier tranform of Figure 3B was inverse Fourier transformed to give the enhanced image seen in A. Regions of the modified Fourier transform containing reflections were selected for inverse Fourier transformation and the remaining areas were set to zero; the resultant image is shown in B. Areas of the structure showing obvious coiling were enlarged, 3 times, and are displayed in the insets.

Figure 5. Deconvoluted sperm head images. The latter half of a sperm head (containing 256 x 200 pixels) was selected for constrained iterative deconvolution (the central panel). Portions were enlarged 3 times to bring out the coiling.

Figure 6. Fluorescently DNA stained Drosophila embryos. A stereo pair showing the embryo after the first 16 nuclear division events is seen in A., while B shows an embryo just before the cellular blastoderm stage. Synchronous mitotic chromosomes are displayed in C.

Figure 7. Image Processing of fluorescently labeled mitotic chromosome arms. A randomly selected chromosome arm from Figure 6C was digitized and is displayed in A. Bandpass filtration using two different sets of parameters gives the results seen in B and C. A tentative interpretation of the architecture of this chromosome arm is presented in D.

Figure 8. Image Processing of High Voltage Electron Micrographs of a Drosophila nuclear structure. The edge of HVEM micrographs of a critical point dried Drosophila tissue culture nucleus is shown in stereo (A). The same image after bandpass filtration is seen in B , with a tenative interpretation depicted in C.

REFERENCES

Agard, D.A. and Stroud, R.M., submitted for publication.

Arp, H. and Lorre, J.L. 1976. Ap. J. 210, 58.

Beer, M. 1976. Analytical Chemistry 48, 93R-95R.

Brenner, N.M. 1969. IEEE Transactions on Audio and Electroacoustics 17, 128-132.

Burgoyne, L.A., Wagar, M.A. and Atkinson, M.R. 1971. Biochem. Biophys. Res. Comm. 39, 254.

Cooley, J.W. and Tukey, J.W. 1968. Math. of Comput. 19, 297-301.

Costa, J.L., Joy, D.C., Maher, D.M., Kirk, K.L. and Hui, S.W. 1979. EMSA 35th, 238-239.

Crowther, R.A. and Klug, A. 1975. Ann. Rev. Biochem. 44, 161-182.

Frieden, B.R. 1975. Topics in Applied Physics 6, 177-248.

Gibbs, A.J. and Rowe, A.J. 1973. Nature 246 509-511.

Henderson, R. and Unwin, P. 1975. Nature 257, 28-32.

Inouè, S. and Sato, H. 1964. in "Molecular Architecture in Cell Physiology", ed. Hayashi, T. and Ezent-Gyorgy, Prentice-Hall, Englewood Cliffs, New Jersey.

Isaacson, M., Johnson, D. and Crewe. 1973. Radiat. Res. 55, 205.

Janssen, P.A. Hunt, R.H. and Plyler, E.H. 1970. J. Opt. Soc. Am. 60, 596-599.

Kuwada, I. 1939. Cytologia 10, 213.

Lorre, J.L. and Lynn, D.J. 1978. "Application of Digital Image Processing Techniques to Astonomy Imagery" JPL Publication, 78, 17.

Laemmli, U.K., Cheng, S.M. Adolph, K.W., Paulson, J.R., Brown, J.A. and Baumbach, W.R. 1977. Cold Spring Harbour Symp. Quant. Biol. 42, 351-365.

Matsura, H. 1938. Cytologia 9, 243.

Nathan, R. in "Pictoral Pattern Recognition" ed. G.C. Cheng (Thompson, Washington, D.C. 1968).

O'Handley, D.A. and Green, W.B. 1972. Proc. IEEE 60, 821.

Sedat, J. and Manuelidis, L. 1977. Cold Spring Harbor Symp. Quant. Biol. 42, 331-350.

Sedat, J., Manuelidis, L. and Agard, D.A. to be submitted.

Tinoco, I. Personal Communication.

Zalokar, M. and Erk, I. 1976. J. de Microscopie et de Biologie Cellulaire 25(2), 97-106.

FIGURE I

FIGURE 2

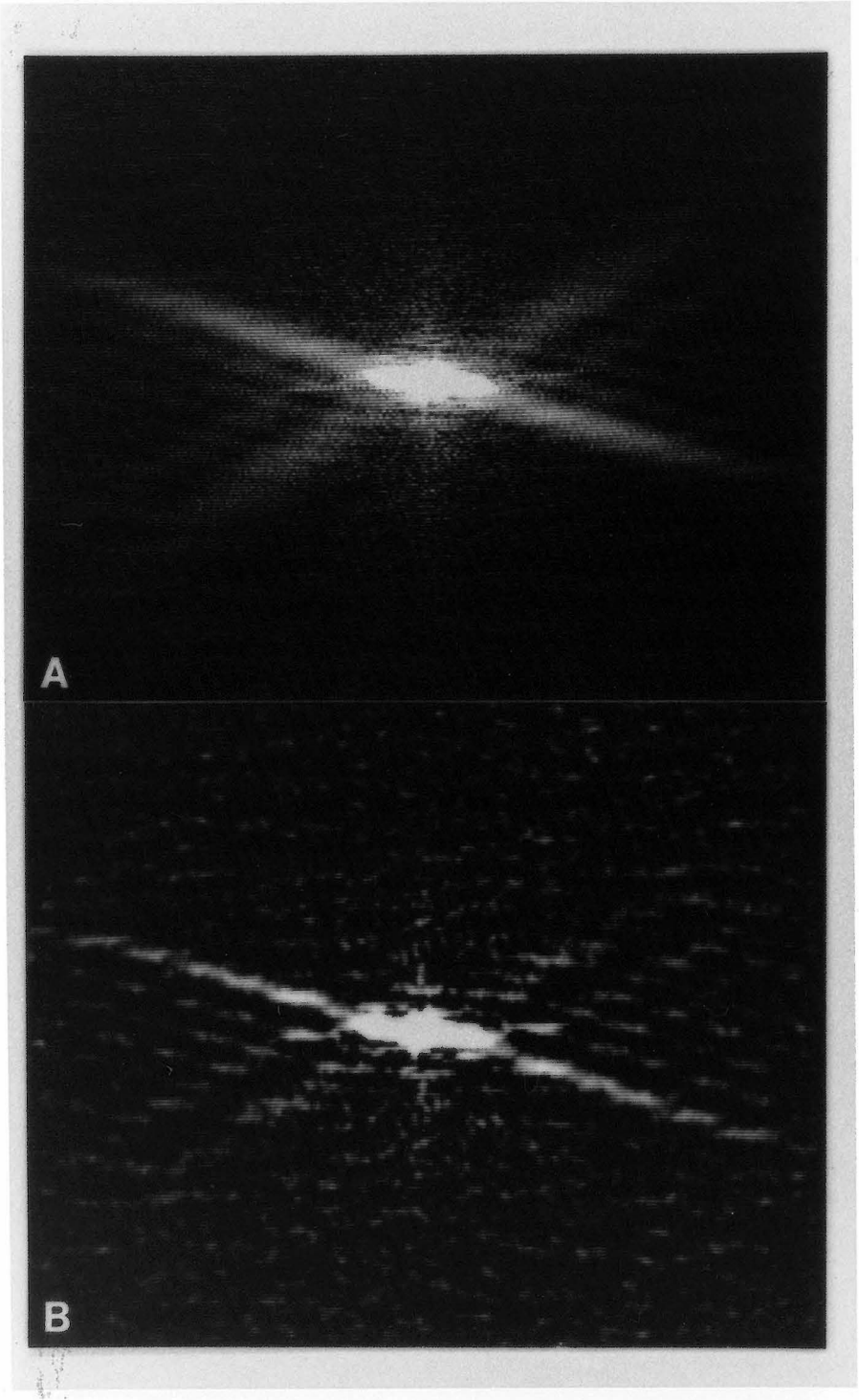

FIGURE 3

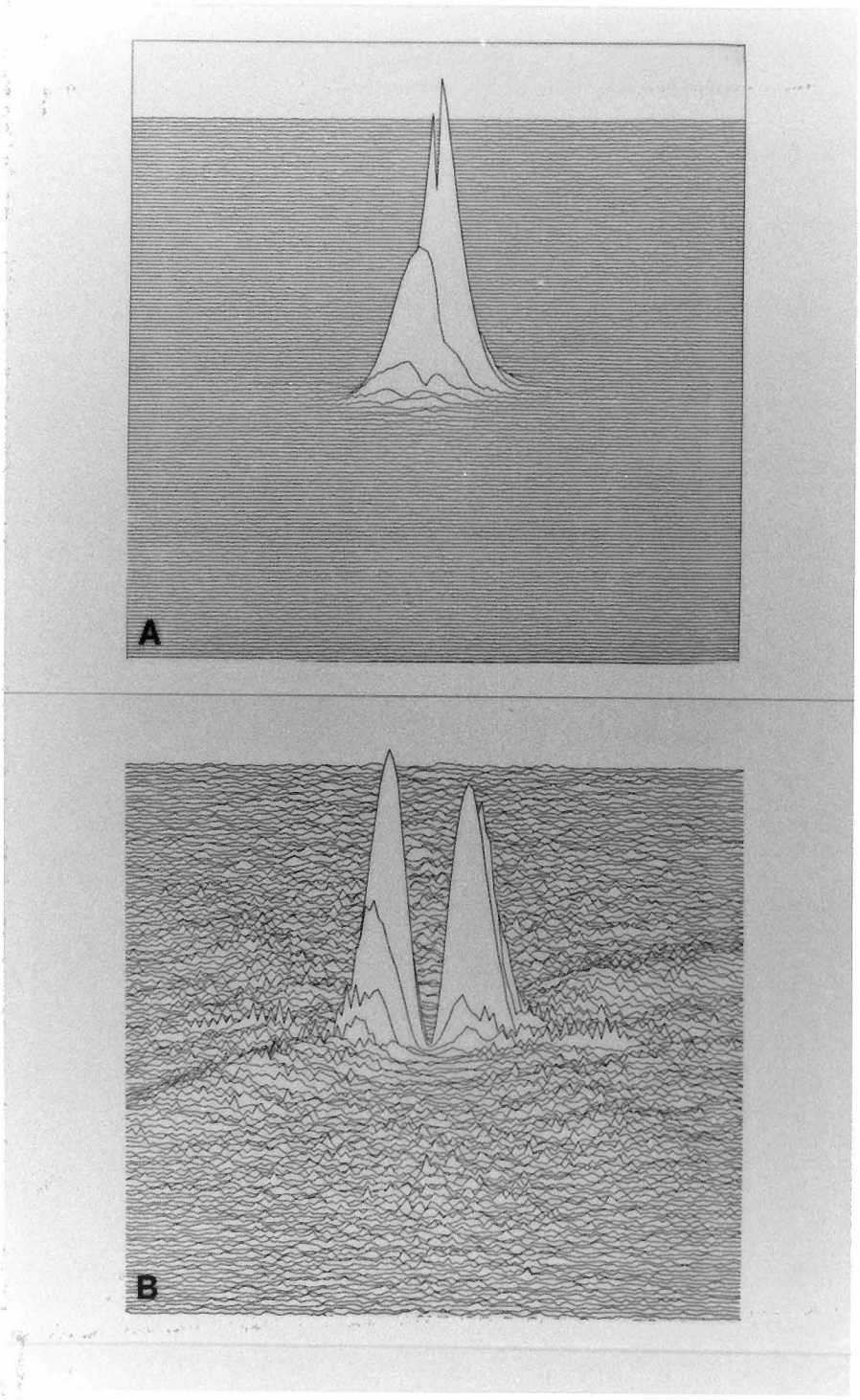

FIGURE 4

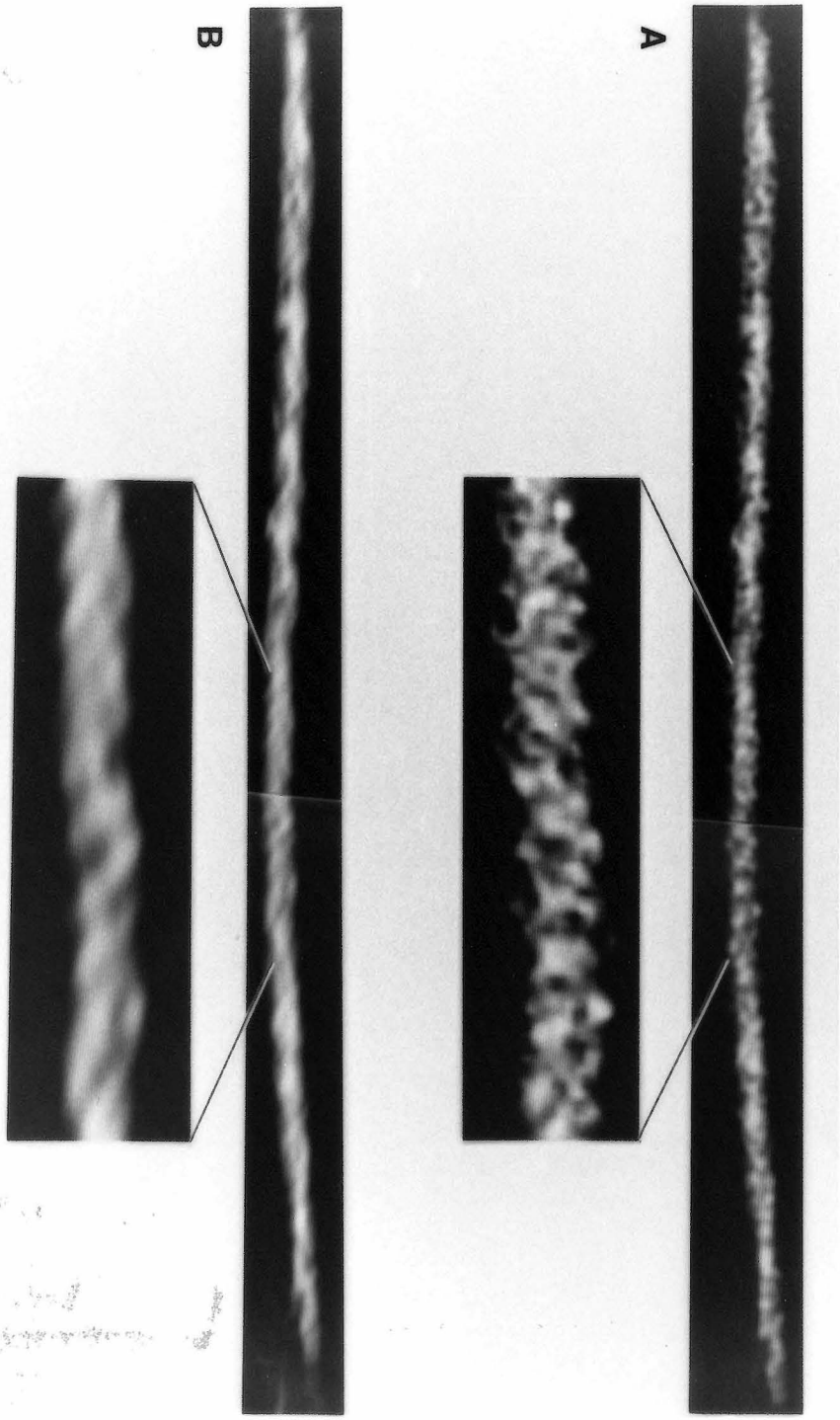

FIGURE 5

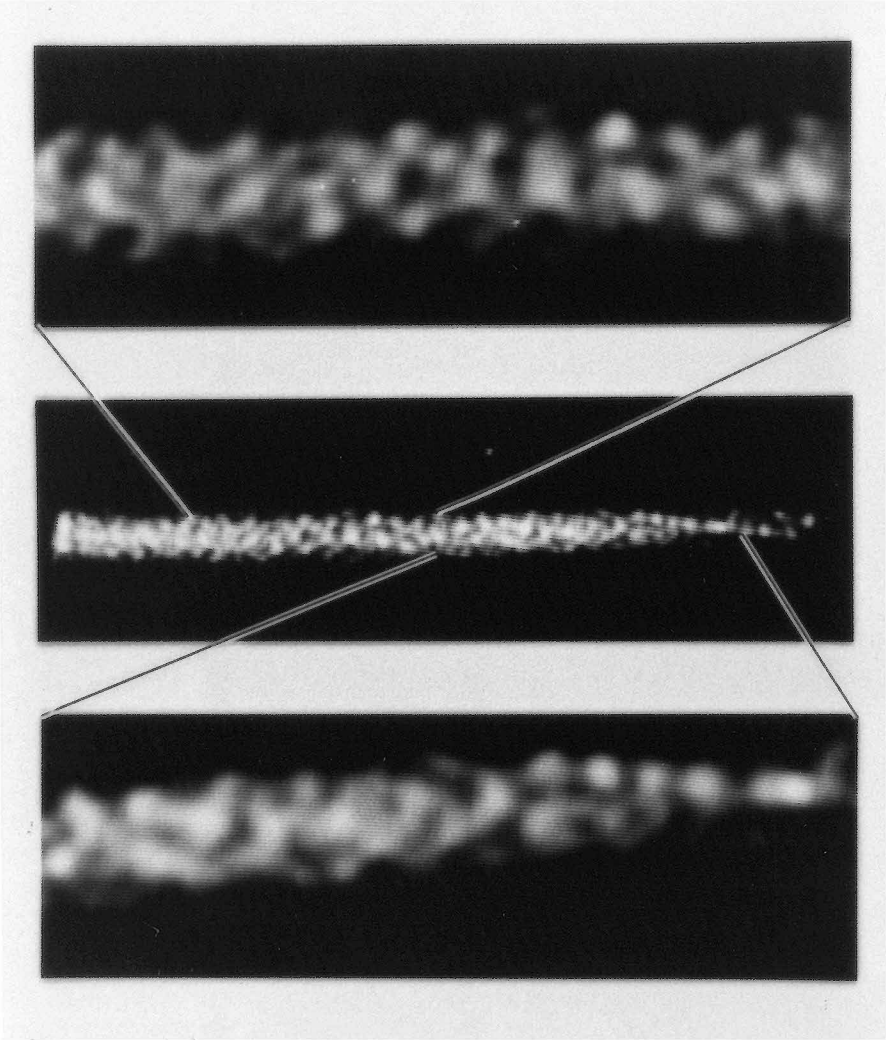

FIGURE 6

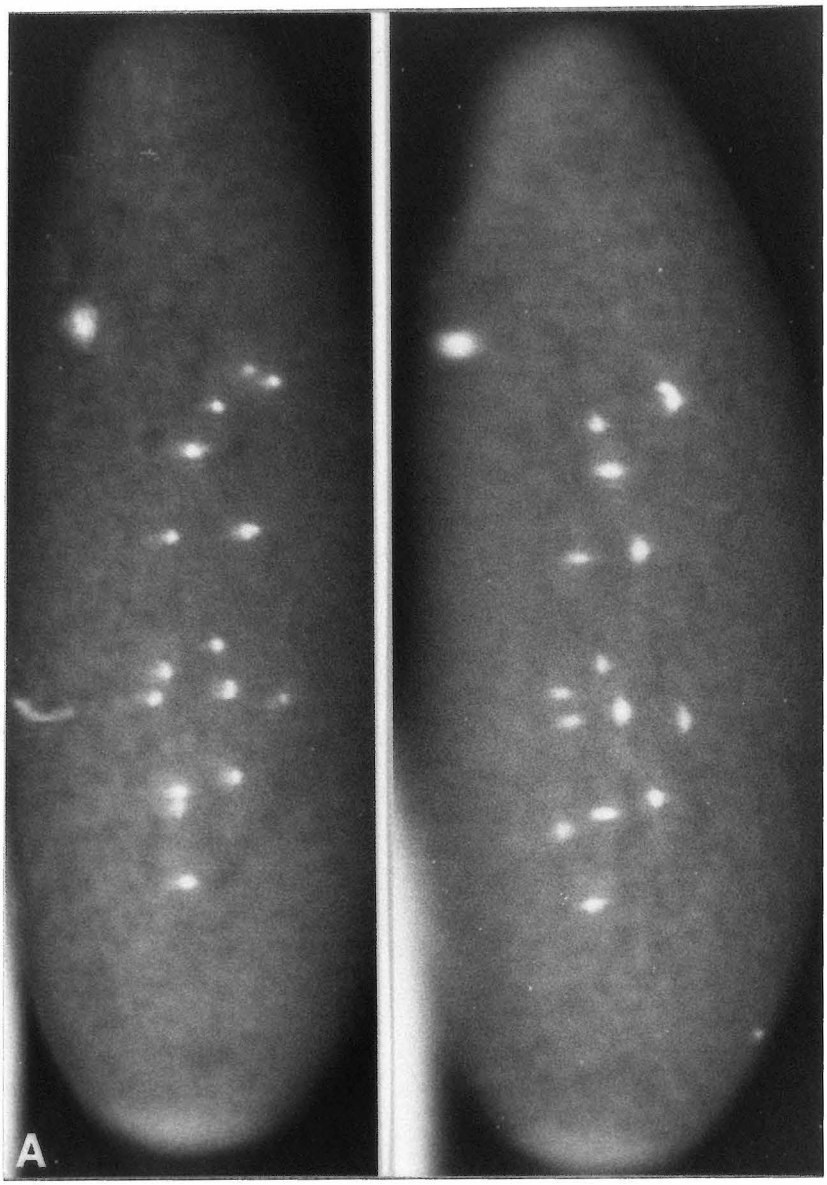

FIGURE 6 cont.

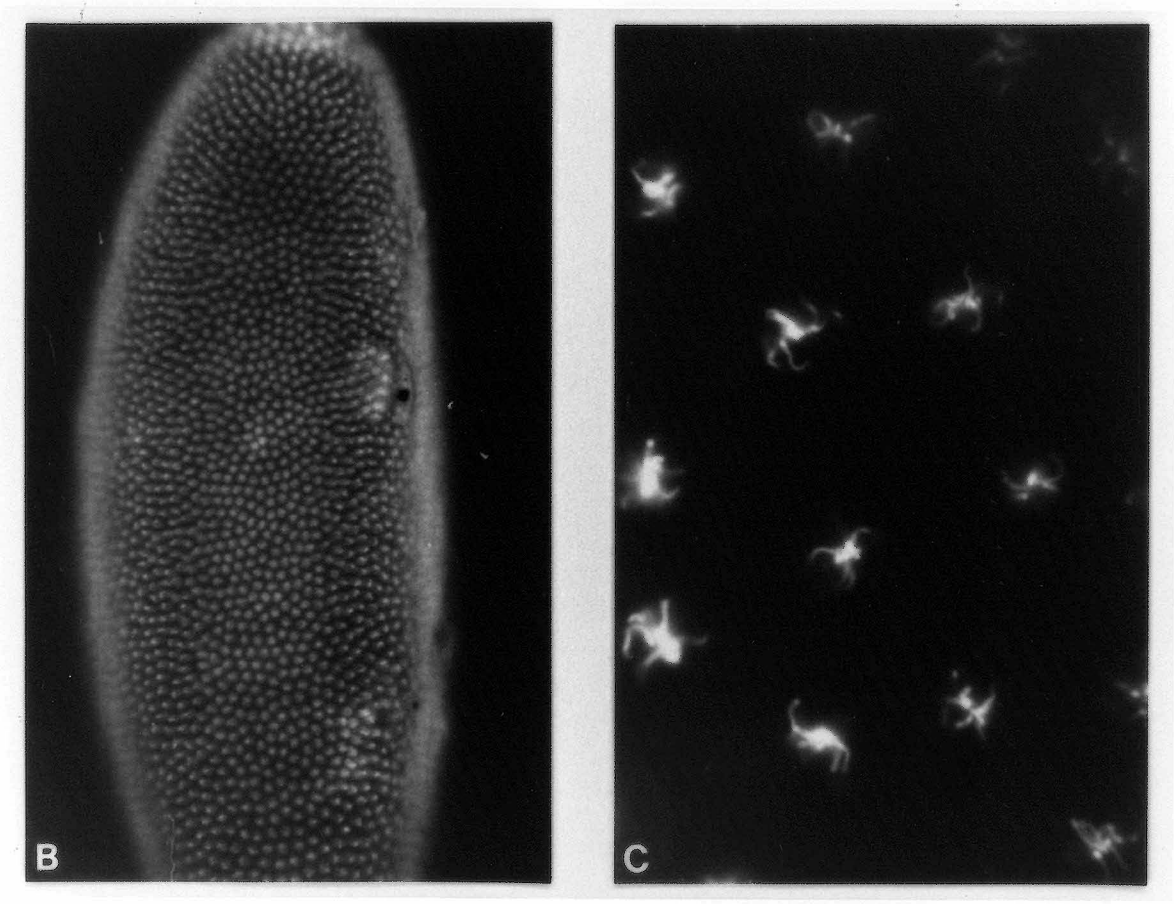

FIGURE 7

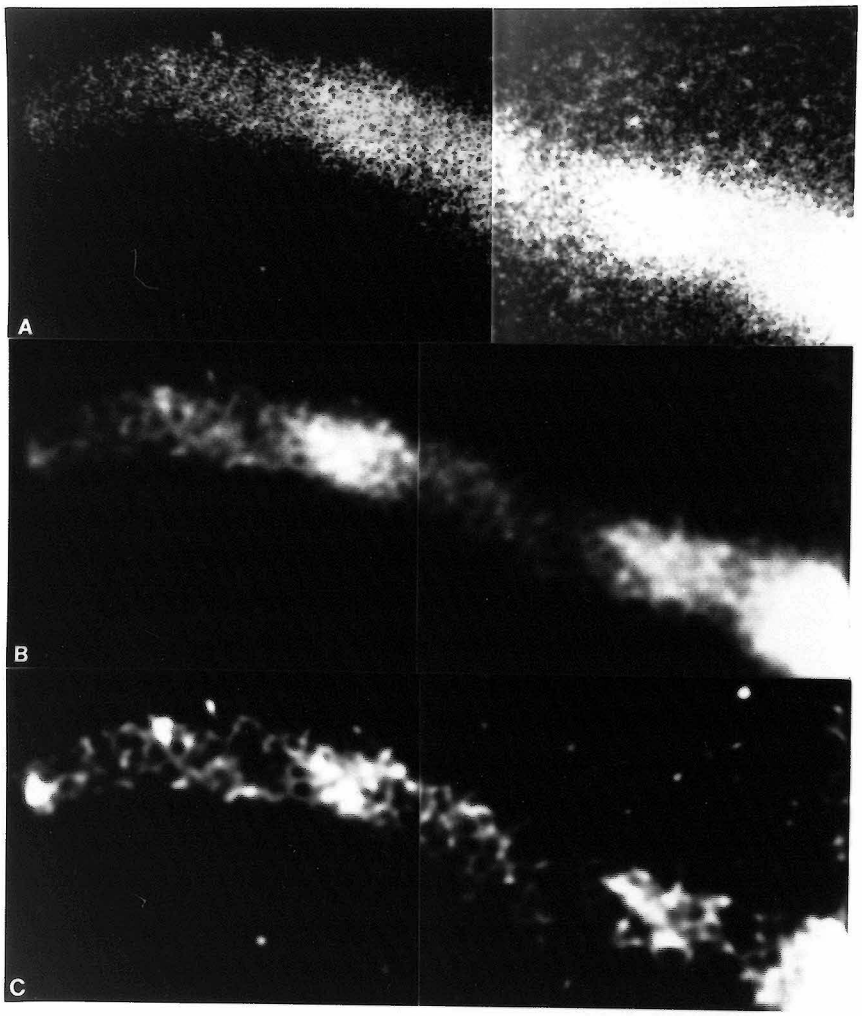

FIGURE 7d cont.

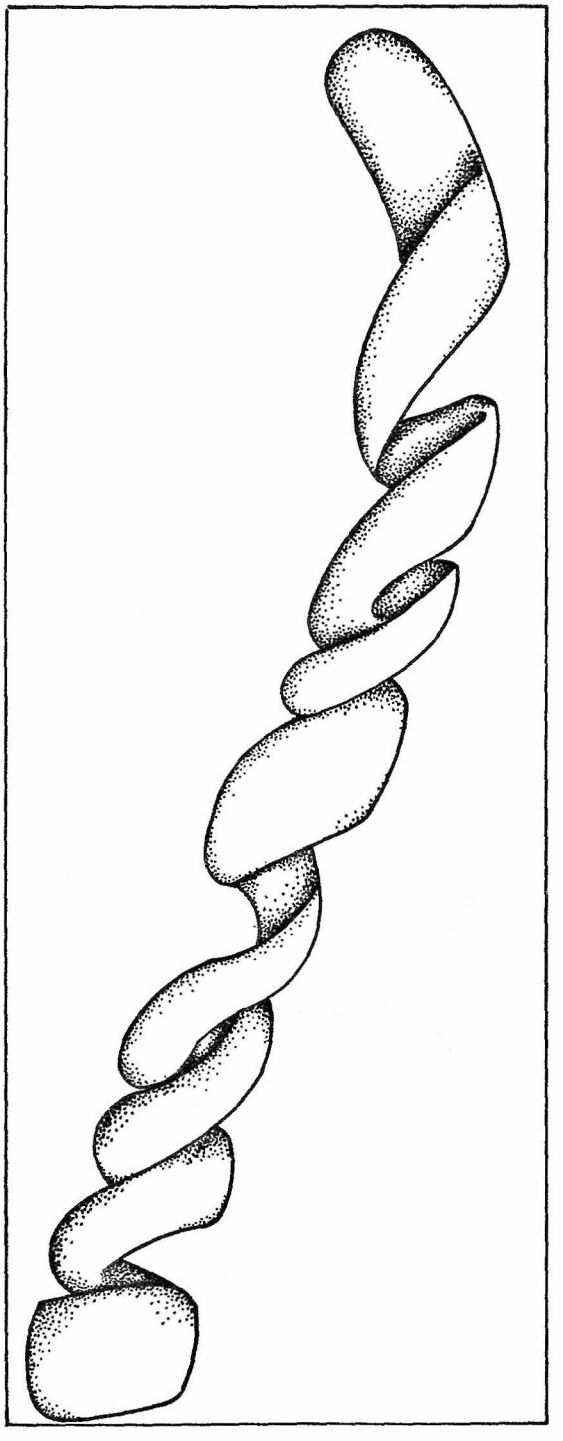

FIGURE 8

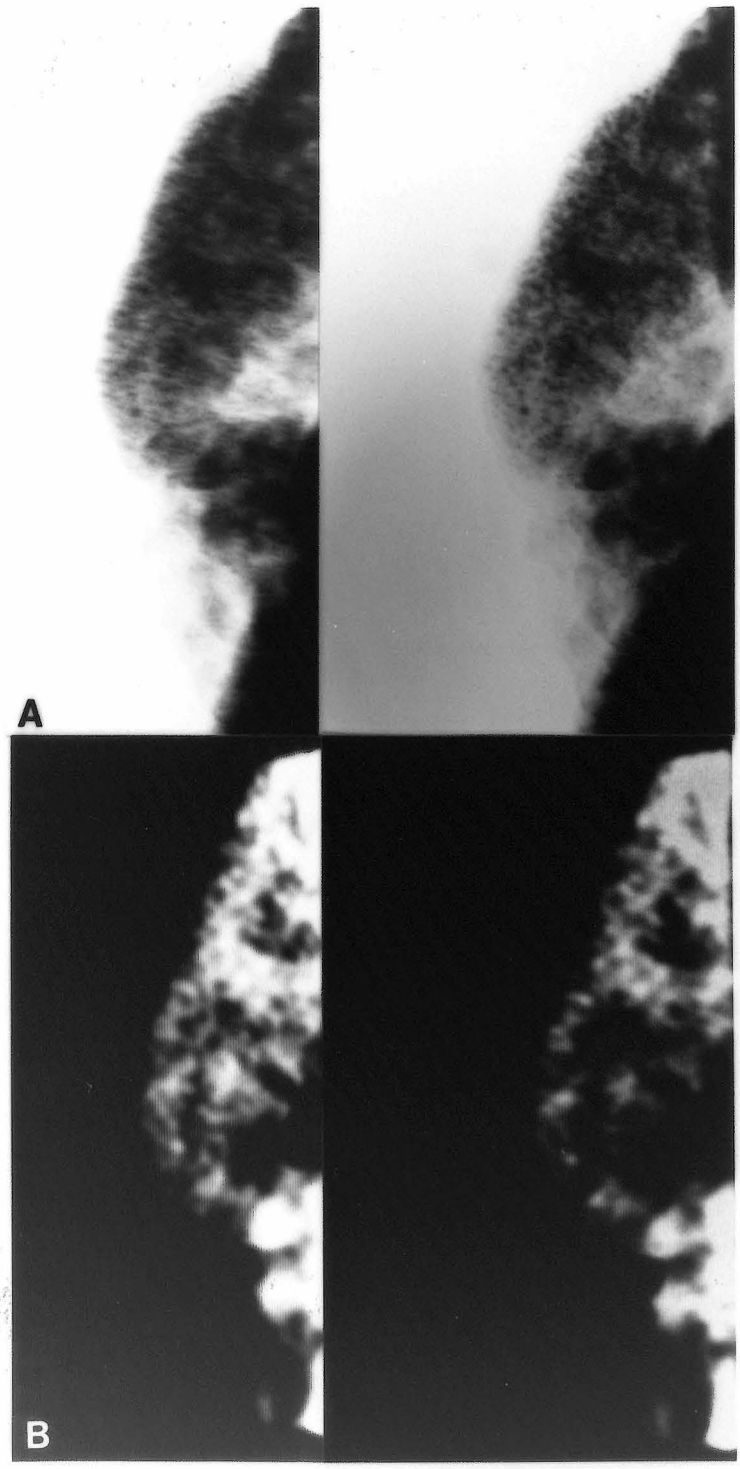

FIGURE 8c cont.

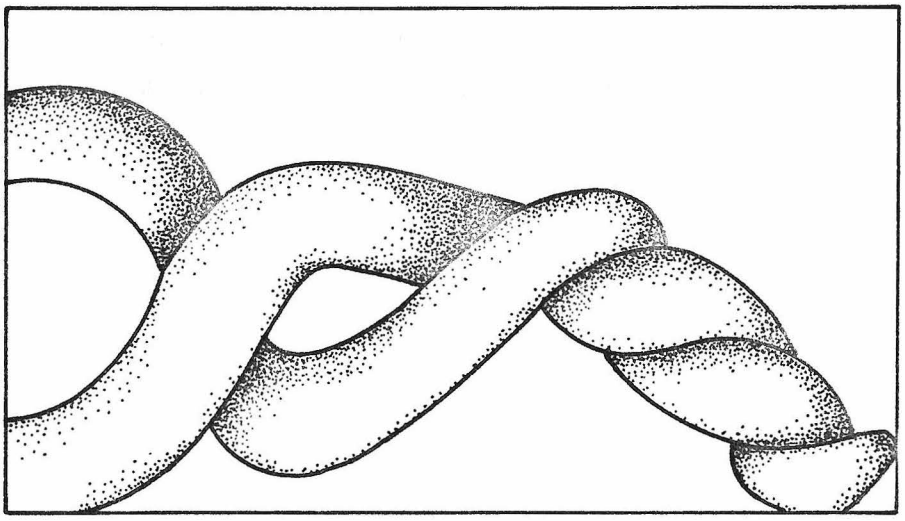

APPENDIX VII

Quantitative Analysis of Electrophoretograms: A Mathematical Approach to Super-resolution

Quantitative Analysis of Electrophoretograms: A Mathematical Approach to Super-Resolution

by

D.A. Agard, R.A. Steinberg* & R.M. Stroud

Department of Biochemistry & Biophysics
University of California
School of Medicine
San Francisco, California
94143

*Biological Sciences Group U-44
University of Connecticut
Storrs, Connecticut
06268

ABSTRACT:

A mathematical method is presented for the quantitative analysis of overlapping spots or bands taken from digitized gel patterns. The procedure is applied to both one and two dimensional gel electrophoretic separations.

INTRODUCTION:

Gel electrophoresis techniques, both one and two dimensional, have become the cornerstone of modern biological and biochemical research. They provide a rapid means of separating and analyzing macromolecules, from mixtures of a few components to whole cell extracts. Ultimately, realization of the full potential of these techniques requires that methods be developed for the accurate quantitative analysis of electrophoretograms. In the past few years several investigators have begun to develop automated techniques for quantitative analysis (1,2,3). This task is especially difficult in the case of two-dimensional gel patterns because of their enormous complexity. The general procedure involves first digitizing the gel electrophoretogram (either a negative or an autoradiograph is suitable) and then analyzing the digital image. The methods currently in use require that spots be rather well resolved for accurate quantitation. Presented here is a mathematical procedure for enhancing the apparent resolution of the gel; thereby separating overlapping peaks. As a digital representation of the gel is also required, this approach is a natural adjunct to analysis procedures already developed.

The method employed is a modified Jansson-VanCittert (4) constrained

iterative deconvolution scheme. By contrast with peak fitting approaches, no knowledge concerning either the number or location of peaks is required; the result is thus completely unbiased. The amount of increased resolution that can be obtained with this procedure depends on how well the band or spot migration properties of the gel can be characterized. Two examples will be considered. The first is an autoradiograph of a two-dimensional gel where it was desired to quantitate two partially unresolved spots (a shoulder on a broad peak). For this example, only a limited resolution increase was required to separate the two components and hence little attempt was made to characterize the behavior of this gel system. For the second example, a one-dimensional agarose gel of restriction enzyme fragments was chosen. As this problem requires a great enhancement of resolution, considerable care was taken to establish the migration behavior of bands on the gel. The approach presented here is a general one, and can be used on data from virtually any electrophoretic or chromatographic procedure.

Theory of the Method

Inherent in any given gel electrophoresis system is an intrinsic resolution limitation that causes bands or spots to have some shape instead of appearing as lines or points. Mathematically (using the one dimensional case for simplicity), the gel pattern can be considered as a convolution of an ideal profile $\rho(x)$ with some smearing function $s(x)$ that serves to broaden and overlap the perfect peaks in a manner to give the observed profile $o(x)$:

$$o(x) = \int \rho(x-u)s(u)du \qquad (1)$$

This is illustrated in figure 1. What is desired is some way to reverse this convolution, thereby deconvoluting $o(x)$ to yield the ideal profile $\rho(x)$. This requires some knowledge of the smearing function $s(x)$. For the two dimensional example $s(x)$ was approximated by a gaussian function, while for the one dimensional experiment $s(x)$ was experimentally determined. Although many techniques exist for accomplishing this deconvolution operation (see reference 5), the best seems to be a modification of the Jansson-Van Cittert iterative constrained deconvolution technique (4).

The presence of noise in the observed profile $o(x)$ can lead to an inaccurately deconvoluted profile. This technique uses the knowledge that $\rho(x)$ must be everywhere positive to help solve this problem. That is, since one knows that negative optical densities are physically meaningless (although they are mathematically allowed), this information can be inserted into the deconvolution procedure. The result is a greatly reduced sensitivity to noise. Similar approaches have been employed in our laboratory for the solution of the one dimensional phase problem in x-ray scattering of membranes (6, 7) and in the solution of the x-ray crystal structure of the snake neurotoxin α-Bungarotoxin (8).

The basic Jansson-Van Cittert algorithm (after Frieden, 5) is:

$$\begin{aligned} &\text{i)} && o_k(x) = \rho^k(x) * s(x) \\ &\text{ii)} && \rho^{k+1}(x) = \rho^k(x) + \gamma(x)[o(x) - o^k(x)] \qquad (2) \\ &\text{iii)} && k = k + 1 \\ &\text{and} && \gamma(x) = 1 - A|o^k(x) - A| \end{aligned}$$

where A is a constant and * denotes the convolution operation of equation

1. In equation 2 the starting point for the refinement is k=0 and $\rho^{o}(x)$ = o(x). The current guess $\rho^{k}(x)$ is smeared by convolution with the gel blurring function s(x)(step i). A new guess, $\rho^{k+1}(x)$, to the correct $\rho(x)$ is then generated by comparison of the broadened $\rho^{k}(x)(= o^{k}(x))$ with the observed gel profile o(x) in step ii. If $o^{k}(x)$ is greater than o(x), as occurs when $\rho^{k}(x)$ is too broad, $\rho^{k+1}(x)$ will be sharpened by subtracting an amount proportional to $o^{k}(x) - o(x)$. The applied correction is modulated by $\gamma(x)$; when $o^{k}(x)$ approaches either the lower or upper boundary limits (ϕ, A/2), the magnitude of the correction approaches zero. The entire procedure is iterated until there is no significant difference between $o^{k}(x)$ and o(x). At this point, $\rho^{k}(x)$ becomes an equivalent to $\rho(x)$. The $\gamma(x)$ function is used to apply both non-negativity and maximum positivity constraints. In practice the parameter A is set to twice some reasonable approximation of the maximum peak height (accurate selection of this parameter is not required).

The original deconvolution method was modified in two important ways: the convolution operation indicated in step i) is actually performed as a multiplication in Fourier transform space, thereby speeding the algorithm about 100 fold, and second the sensitivity to noise was further reduced by smoothing $\rho^{k}(x)$ every 10 iterations. The convolution theorem (see, for example 9) shows that the convolution operation of step i is equivalent to Fourier transforming both $\rho^{k}(x)$ and s(x) according to equation 3 and taking the inverse Fourier transform of their product as

in equation 4.

$$P^k(X) = \int \rho^k(x) e^{2\pi i x X} \, dx \qquad (3)$$
$$S(X) = \int s(x) e^{2\pi i x X} \, dx$$

$$o^k(x) = \int P^k(X) S(X) e^{-2\pi i x X} \, dX \qquad (4)$$

In practice we have used the Fast Fourier transform algorithm developed by Cooley and Tukey (10) to greatly increase the speed of these operations. Also, it is only necessary to calculate S(X) once.

Concomitant with increasing the resolution of the gel profile, occurs an increase in the apparent amount of noise. Thus there must be a trade-off between the degree of resolution enchancement and the maximum noise level that can be tolerated in the resultant profile. For this application, the deconvoluted profile $\rho(x)$ should be a smooth function since small ripples and sharp spikes are more likely to result from errors in the data than from true features. No provision was made for this in the original deconvolution scheme. A simple way of accomplishing this added noise suppression is to smooth $\rho(x)$ by coupling adjacent points.

$$\rho'(x) = \alpha\rho(x) + \beta[\rho(x-1) + \rho(x+1)] + \gamma[\rho(x-2) + \rho(x+2)] \qquad (5)$$

where α, β, γ are adjustable constants and $\alpha+2\beta + 2\gamma = 1$, thus for each point in the profile $\rho(x)$ a new value is computed based on the weighted

sum of it, its first ($\rho(x-1),\rho(x+1)$) and second neighbors ($\rho(x-2)$, $\rho(x+2)$). For maximal efficiency this smoothing operation should only be applied after every 5-10 cycles of the deconvolution scheme. In the examples presented here, α,β and γ were chosen to correspond to a limited gaussian function, and smoothing was applied every 10 cycles.

Quantitative Resolution of Overlapping Spots on A 2-D Gel

As part of a study of the metabolism of regulatory subunits of cyclic AMP-dependent protein kinase in mouse lymphoma cells[1], it was deemed necessary to determine the time course of regulatory subunit phosphorylation in the presence and absence of an analog of cyclic AMP. Spots corresponding to phosphorylated and non-phosphorylated forms of the regulatory subunit had been identified in two-dimensional polyacrylamide gel patterns using cyclic AMP-affinity purification of the species from cells labeled with ^{35}S-methionine (11), but these spots are not well-resolved from contaminating species in gels of whole cell extracts (11, figure 2a,b). Regulatory subunits from control cells could be affinity-purified before running gels to allow quantitation of radioactivity in phosphorylated and non-phosphorylated forms, but such a procedure rests on the untested assumption that recovery of the two forms after purification will be equal. Regulatory subunits from cells stimulated with analogs or inducers of cyclic AMP do not bind efficiently to the affinity resin (R.A.S., unpublished results) rendering pre-purification impracticable for such samples. The experiment

[1] Steinberg, R.A., Agard, D.A., manuscript in preparation.

was therefore performed by running gels of crude extracts of cells pre-labeled with ^{35}S-methionine and chased for various times in non-radioactive media with or without dibutyryl cyclic AMP.[1] Radioactivity in phosphorylated and non-phosphorylated forms of kinase regulatory subunit was quantified using the deconvolution method described above to resolve these spots from contaminants. For comparison, replicate samples from the culture chased without dibutyryl cyclic AMP were affinity-purified and the regulatory subunit species quantified by microdensitometry of two-dimensional gel autoradiograms as previously described (11).

From the patterns of crude extract gels, regions of interest were selected visually and scanned on a Syntex AD-1 flatbed auto-densitometer using an aperture of 54.5 x 109 μ. Half-tone computer representations of scanned areas from two gels are shown in figures 2c,d. From these digital images, areas containing the regulatory subunit spots were selected (boxes in figures 2c,d) and converted to one dimensional profiles by integrating the optical densities across the width of the rectangle. The resultant one dimensional profiles were smoothed using the rapid piecewise spline method of Savitsky (12). These profiles showing the contaminating spot as either the larger peak (early time point) or the shoulder (late time point) became the starting point (o(x)) for the iterative deconvolution procedure (Thick lines, figures 3a, 3b respectively). Resolving the shoulders into separate peaks is a rather simple problem and as such it was not necessary to carefully characterize the smearing function s(x). A gaussian function was assumed for this purpose. The results after 50 cycles of deconvolution are shown as thin lines in figures 3a,3b. Following deconvolution, it was a simple matter to

separate the two peaks and to quantitate the area under each. The total procedure required less than 5 minutes on a small mini-computer. Figure 4 shows a comparison of the regulatory subunit phosphorylation data obtained from gels of crude cell extracts using the deconvolution method with that obtained by microdensitometry of gels of affinity-purified material. On the whole, the agreement between the two sets of data is quite good, and we have preliminary data suggesting that the tendency for the purified subunits to give higher phosphorylation ratios at early time points reflects a purification bias in favor of holoenzyme associated subunits (D.A.A. and R.A.S., unpublished results).

Separation of Overlapping Bands on a 1-D Gel

This experiment was designed to test the limits of mathematically enhanced resolution in a system where the correct answer was known. A mixture of HIND III restriction fragments from digests of PM2 and SV40 DNA was run on an ethidium bromide agarose gel (13) under non-resolving conditions (figure 5). The gel pattern was digitized and smoothed as before. Gels run under resolving conditions (not shown) indicated that the broad peaks I, II, III were each composed of two bands. The PM2 digest alone was also run on the same gel under non-resolving conditions (Figure 6). Several of the bands from this lane were known to contain only a single molecular species and these were used to characterize the smearing function s(x) for the gel. The deconvolution method used here assumes that s(x) is invariant across the gel; because of diffusion effects the bands broaden as they migrate down the gel. A

plot of half-width at half-height of the reference bands as a function of migration distance is shown in figure 7. Using this information, the x-axis was expanded and contracted so that all of the reference bands would be equally broad. One of these bands was chosen for the smearing function s(x). The x-axis of the profile shown in figure 5 was modified in a similar manner to give the starting function o(x). The results after 200 cycles of constrained deconvolution are shown in figure 8. Although it was apparent from the gel trace as well as the gel itself that bands II and III are separated, before processing it was not possible to ascertain that these bands were each composed of two components. After processing, the doublets were well resolved. The shoulder on the first broad peak was also resolved into its component parts. Although non-resolving conditions were utilized to set up this test, similar improvements are possible when trying to separate overlapping peaks from gels run under optimum resolving conditions.

DISCUSSION

A general procedure has been presented for the resolution enhancement of profiles from gel electrophoretograms. The method is fast, simple to use, and can readily be set up on any computing system. The enhanced resolution provided by this technique allows quantitative analysis of overlapping peaks. This can be important when the gel system used is at the limits of its resolution capabilities. As was shown in the two-dimensional example, this procedure obviated the need for purification of the component of interest providing benefits both by a reduction of

labor and elimination of uncontrolled purification biases.

It is felt that such a technique represents a natural addition to existing computer based processing schemes. Computational methods can simplify the task of extracting quantitative information for complex gel patterns. Ultimately, such information will be of great value in the studies of cellular regulation and development where the intensity and position of critical peaks from a whole cell extract must be resolved and compared. Such an approach should also be useful in extending the usable range of DNA sequencing gels. Fortran programs are available upon request.

ACKNOWLEDGEMENTS

We would like to thank M. Sure for running the restriction digest gels, and R. Bornstein for assistance in preparation of this manuscript. This work was supported by the National Institutes of Health Grant GM 24485 and by the National Science Foundation PCM77-25407 (D.A.A. and R.M.S.) as well as by National Cancer Institute Grants CA 24334 and CA 14733 (R.A.S.).

REFERENCES

1. Schumaker, M.F. (1978). Anal. Biochem. 91, 375-393.

2. Garrels, J.I. (1979). J.B.C. 254, 7961-7977.

3. Bossinger, J., Miller, M.J., Vo, K-P., Geiduschek, E.P., Xuong, N-H. (1979) J.B.C. 254, 7986-7998.

4. Jansson, P.A., Hunt, R.H., Plyler, E.K. (1970) J. Opt. Soc. Am. 60, 596-599.

5. Frieden, B.R. (1975) Topics in Applied Physics 6, 177-248.

6. Stroud, R.M. and Agard, D.A. (1979) Biophys. J. 25, 495-512.

7. Ross, M.J., Klymkowsky, M.W., Agard, D.A., and Stroud, R.M. (1977) J.M.B. 116, 635-659.

8. Agard, D.A. & Stroud, R.M. (1980) J.M.B. -submitted.

9. Lipson, H. & Taylor, C.A. (1958) in Fourier Transforms and X-ray Diffraction, G. Bell and Sons, Ltd., London.

10. Cooley, J.W., Lewis, P.A.W., Welch, P.D. (1969). IEEE Transactions on Education 12, 27-34.

11. Steinberg, R.A., O'Farrell, P.M., Friedrich, U., and Coffino, P. (1977) Cell 10, 381-391.

12. Savitsky, A. and Golay, M.J.E. (1964) Anal. Chem. 36, 1627-1639.

13. Pulleyblank, D.E., Shure, M., Tung, D., Vinograd, J., Vosberg, M.P. (1975) Proc. Nat. Acad. Sci. USA 72, 4280-4284.

FIGURE LEGENDS

Figure 1. Illustration of band broadening in a hypothetical gel system. The ideal profile for the four separate molecular species ($\rho(x)$, fine line) is broadened by diffusion within the gel to give the observed profile ($o(x)$, heavy line). Note how the two central peaks overlap so as to be almost completely unresolved.

Figure 2. Autoradiographs of two-dimensional gel patterns for two different points along the time course for regulatory subunit phosphorylation; the phosphorylated regulatory subunits are indicated by arrows in A,B. Panel A corresponds to an early time point and Panel B to a late time point. The outlined regions in A,B were scanned on a computer-controlled densitometer and are displayed in panels C and D. The marked regions in C, D were chosen for further analysis.

Figure 3. The one-dimensional tracing derived from the region marked in figure 2c is shown as a heavy line in a. The resultant profile after 50 cycles of deconvolution is depicted as the fine line in a. The starting (heavy line) and deconvoluted (fine line) profiles for the region outlined in Figure 2d are shown in b. The scales for the axes are arbitrary.

Figure 4. A scatter plot of the phosphorylation time course data comparing values obtained from affinity purified regulatory subunits

with that obtained by deconvolution of gel patterns from crude extracts.

Figure 5. A gel pattern and densitometer tracing for a mixture of PM2 and SV40 DNA run on an ethidium bromide agarose gel is shown. The labeled peaks were chosen for further analysis.

Figure 6. Same as Figure 5 but using PM2 DNA alone. These bands are used as reference bands to determine the smearing function s(x).

Figure 7. A log-log plot of the ratio of peak width to peak height as a function of migration distance through the gel. The values were taken from the data shown in Figure 6.

Figure 8. The profile for the region of Figure 5 containing bands I, II, and III after correction for increased band broadening as a function of migration distance is shown (thick line). The same data after 200 cycles of constrained deconvolution is shown super-imposed (fine line). The doublets in bands II and III are now resolved.

FIGURE I

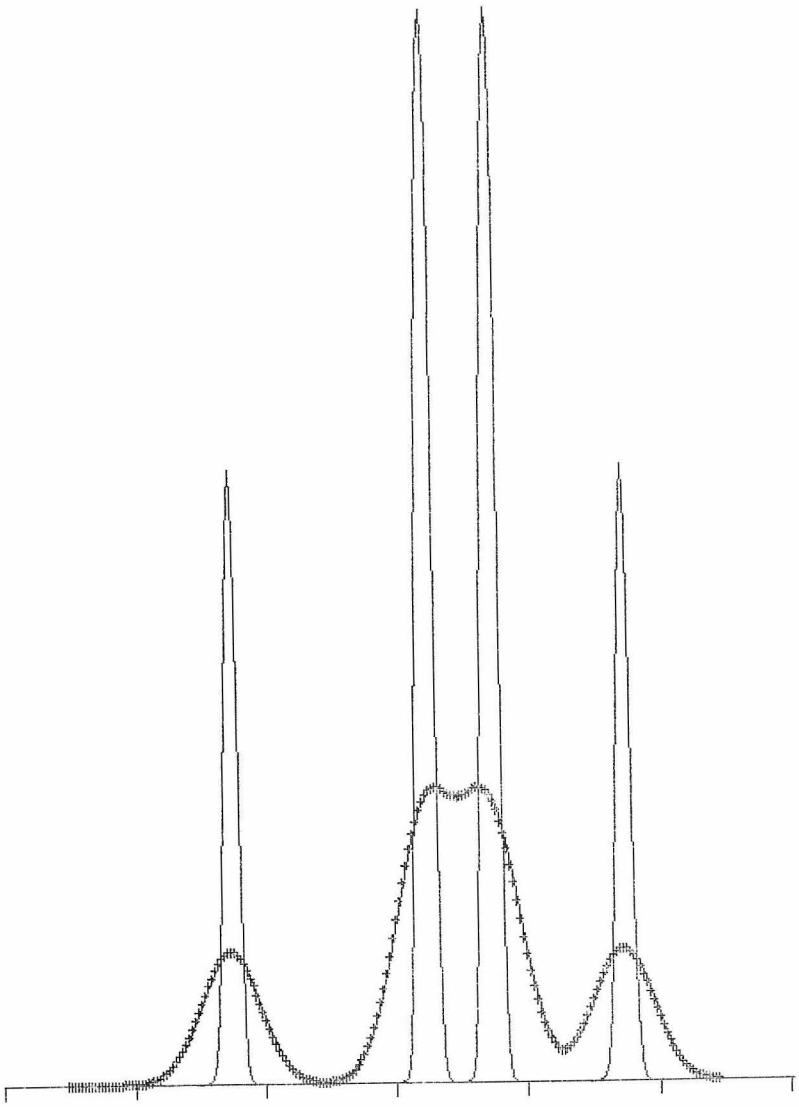

FIGURE 2

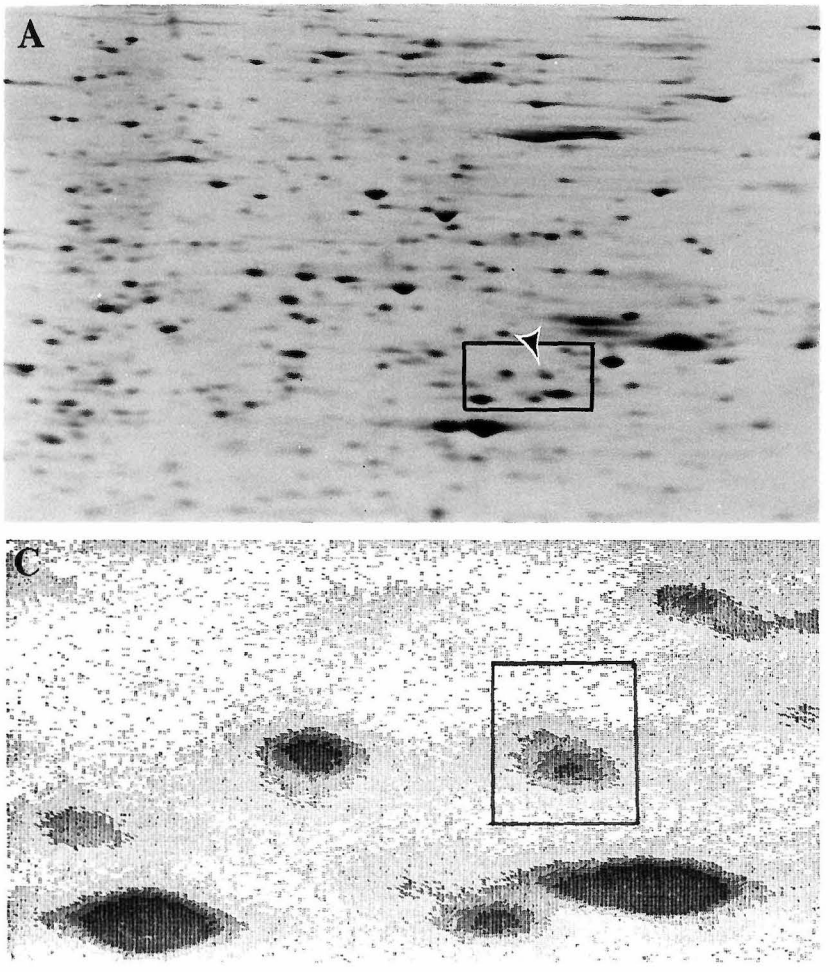

FIGURE 2 cont.

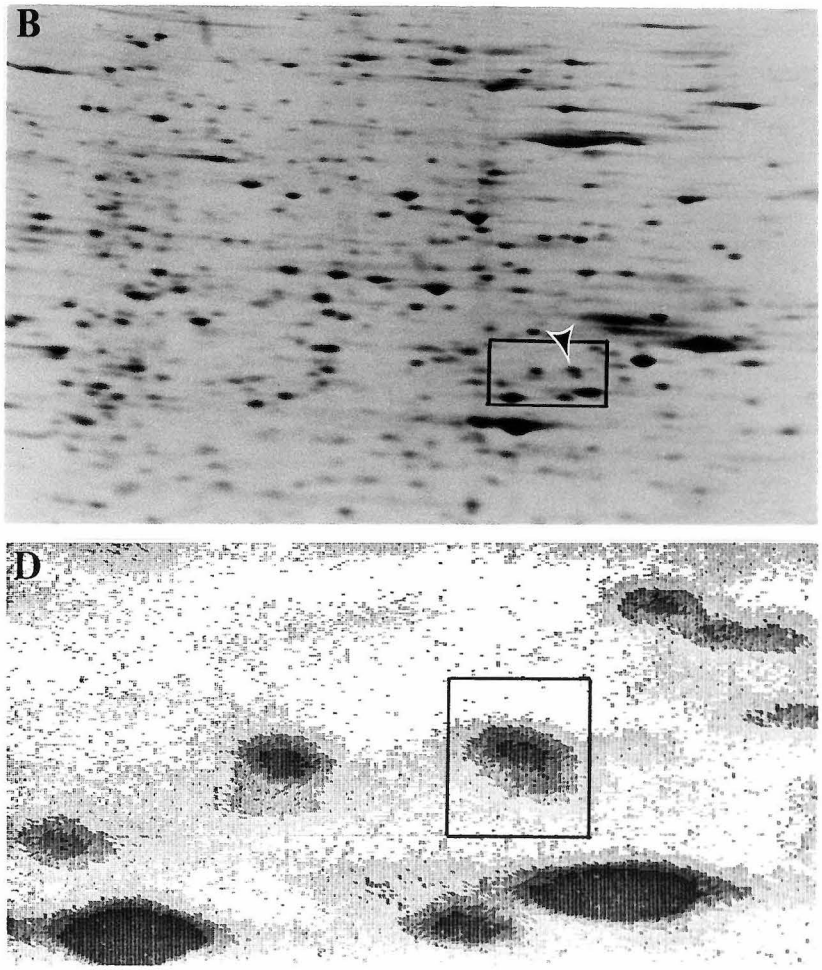

FIGURE 3a

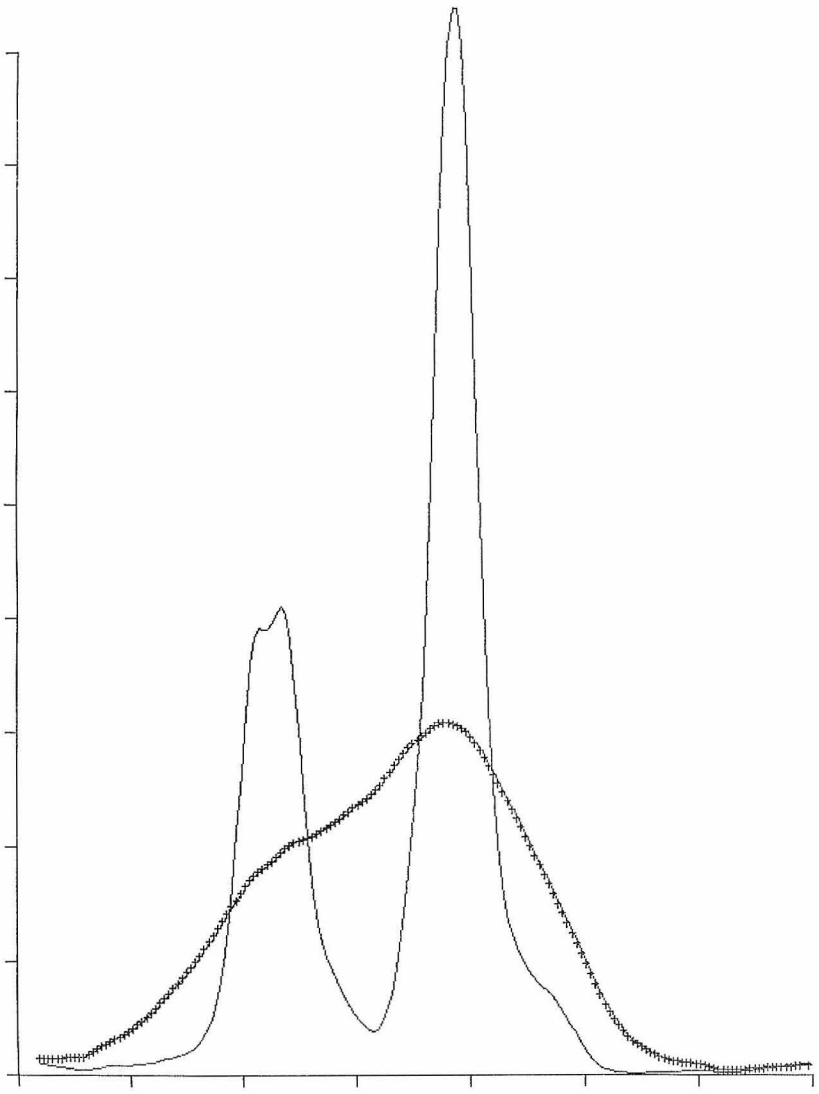

FIGURE 3b

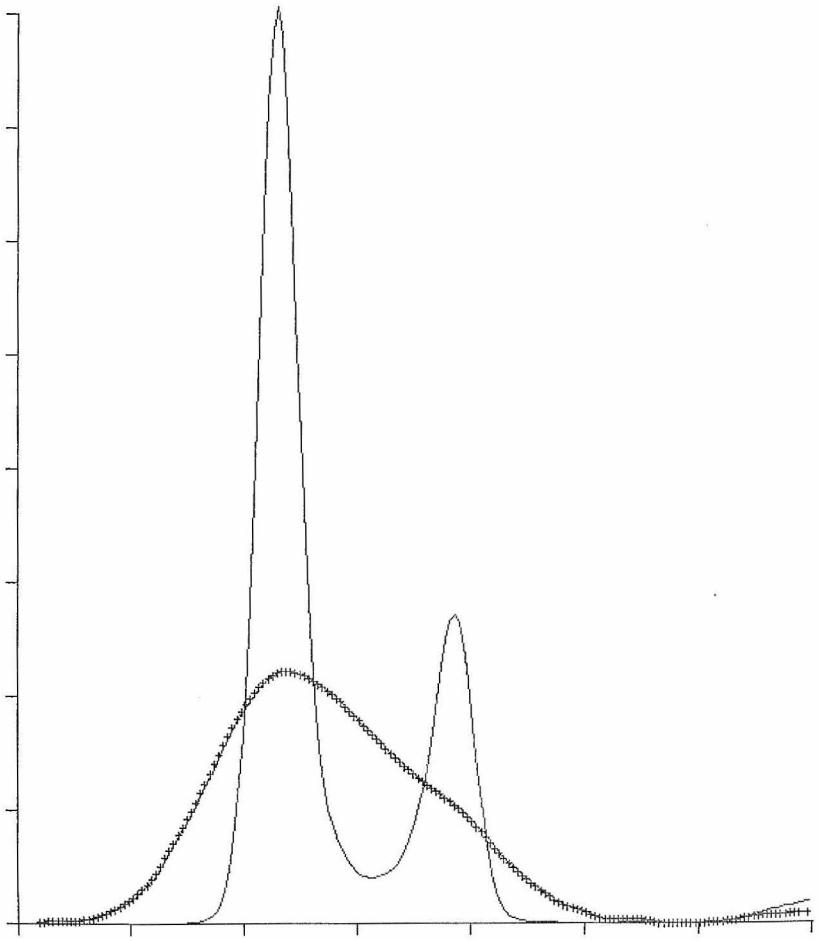

FIGURE 4

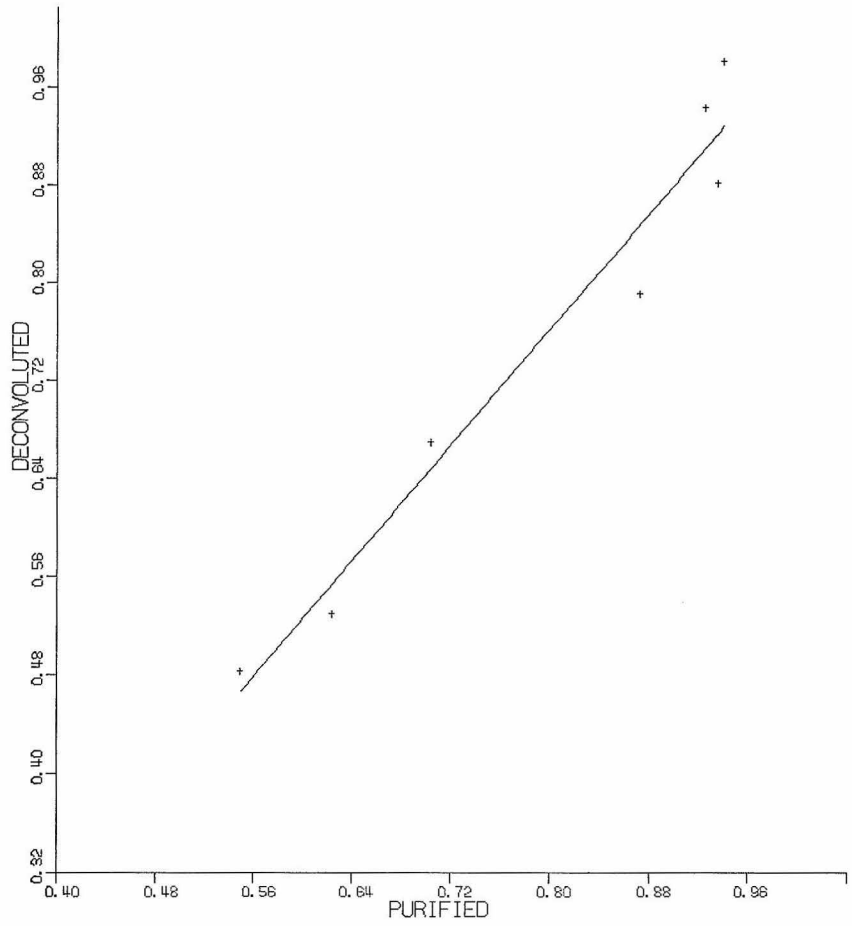
DECONVOLUTED
0.32
0.40
0.48
0.56
0.64
0.72
0.80
0.88
0.96
PURIFIED
0.40
0.48
0.56
0.64
0.72
0.80
0.88
0.96

FIGURE 5

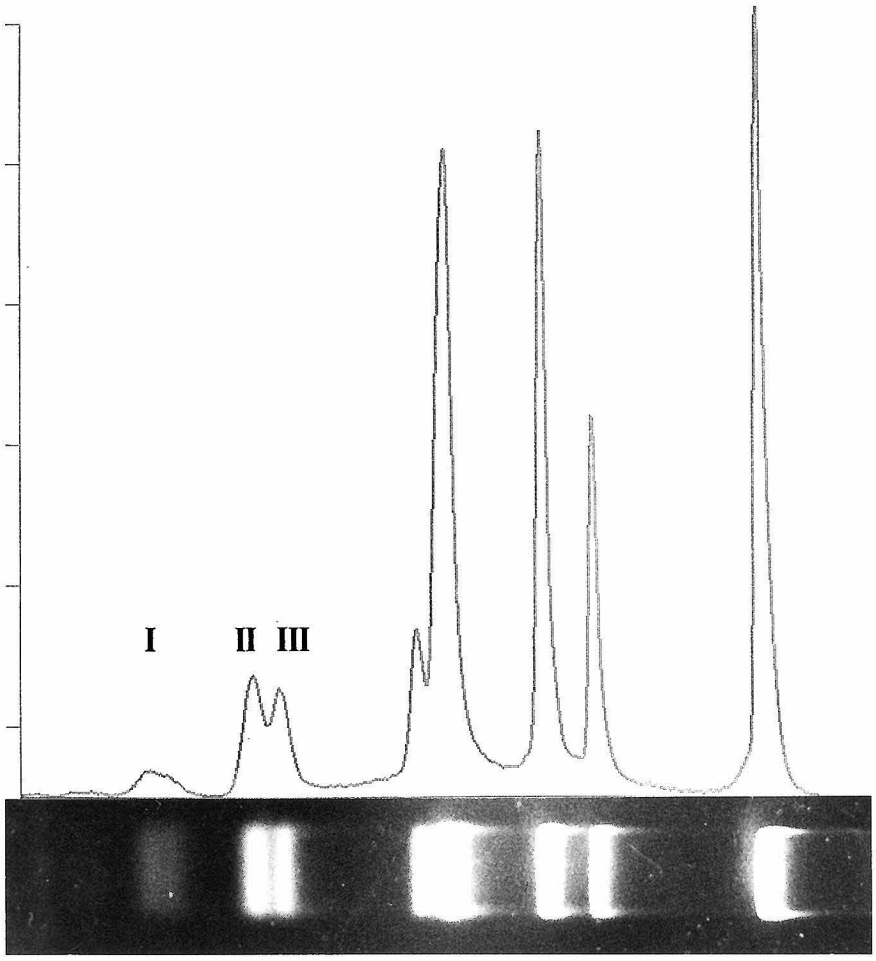

FIGURE 6

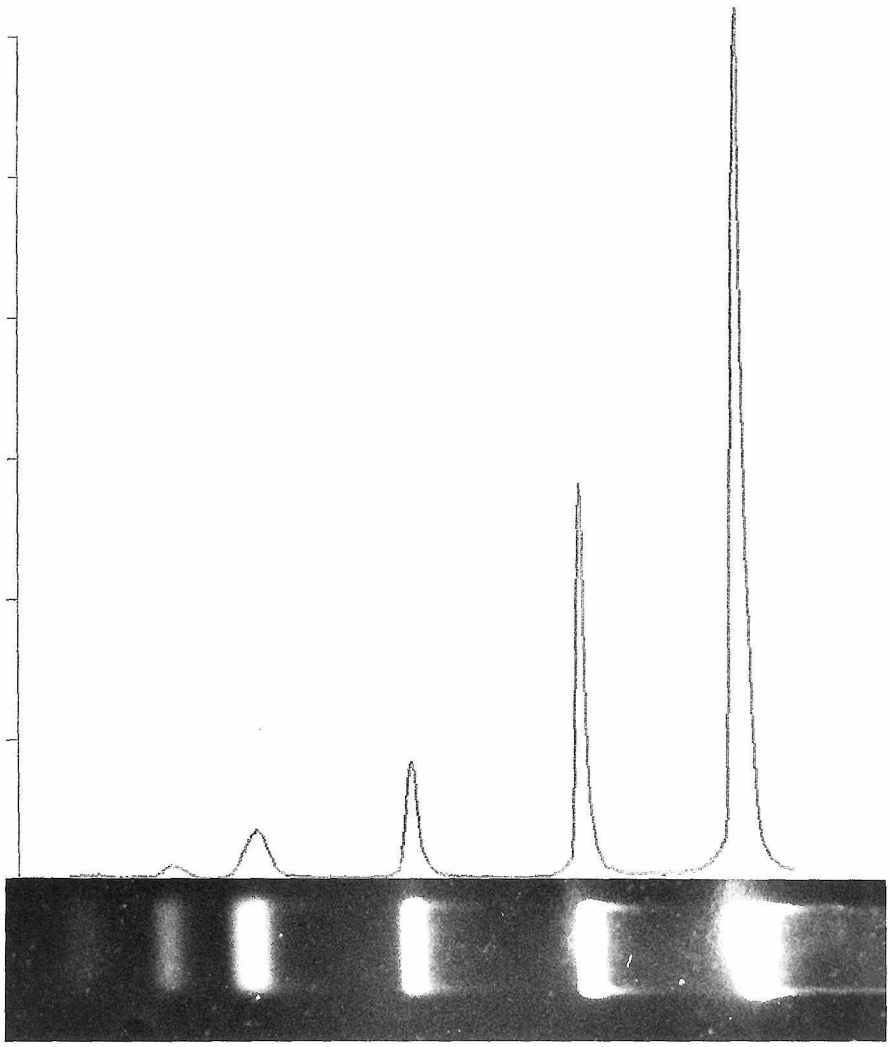

FIGURE 7

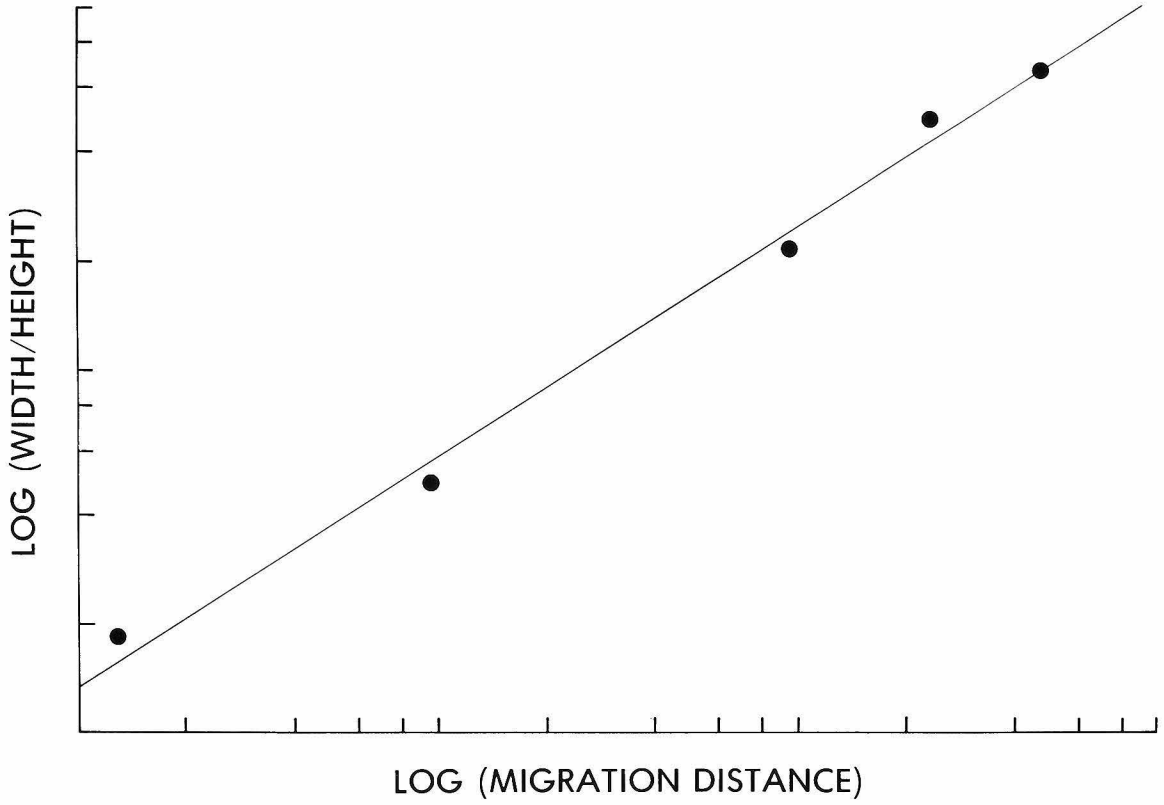

FIGURE 8